

Measuring snow thickness over Antarctic sea ice with a helicopter-borne 2 - 8 GHz FMCW radar.

Natalia Galin

B.E. Electrical Engineering (Hons.),
New South Wales University, 2006

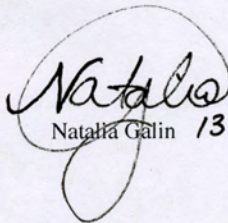
Submitted in fulfilment of the requirements for the
Degree of Doctor of Philosophy
at the University of Tasmania.

Institute for Marine and Antarctic Studies, the University of Tasmania
January 2012

Statement of Declaration

I declare that this thesis contains no material which has been accepted for a degree or diploma by the University or any other institution, except by way of background information and duly acknowledged in the thesis, and to the best of my knowledge and belief no material previously published or written by another person except where due acknowledgement is made in the text of the thesis, nor does the thesis contain any material that infringes copyright.

This thesis may be made available for loan and limited copying in accordance with the *Copyright Act of 1968*


Natalia Galin 13/JAN/12

Abstract

Antarctic sea ice and its snow cover are integral components of the global climate system, yet many aspects of their vertical dimensions are poorly understood, making their representation in global climate models poor. Remote sensing is the key to monitoring the dynamic nature of sea ice and its snow cover. Reliable and accurate snow thickness data from an airborne platform is currently a highly sought after data product. Remotely sensed snow thickness measurements can provide an indication of precipitation levels. These are predicted to increase with effects of climate change, and are difficult to measure as snow fall is frequently lost to wind-blown redistribution, sublimation and snow-ice formation. Additionally, accurate regional scale snow thickness data will increase the accuracy of sea ice thickness retrieval from satellite altimeter freeboard estimates.

Airborne snow-depth investigation techniques are one method for providing regional estimation of these parameters. The airborne datasets are better suited to validating satellite algorithms, and are themselves easier to validate with *in-situ* measurement. The development and practicality of measuring snow thickness over sea ice in Antarctica using a helicopter-borne radar forms the subject of this thesis. The radar design, a 2 - 8 GHz Frequency Modulated Continuous Wave Radar, is a product of collaboration and the expertise at the Centre for Remote Sensing of Ice Sheets, Kansas University.

This thesis presents a review of the theoretical basis of the interactions of electromagnetic waves with the snow and sea ice. The dominant general physical parameters pertinent to electromagnetic sensing are presented, and the necessary conditions for unambiguous identification of the air/snow and snow/ice interfaces by the radar are derived. It is found that the roughnesses of the snow and ice surfaces are dominant determinants in the effectiveness of layer identification in this radar. Motivated by these results, the minimum sensitivity requirements for the radar are presented.

Experiments with the radar mounted on a sled confirm that the radar is capable of unambiguously detecting snow thickness. Helicopter-borne experiments conducted during two voyages into the

East Antarctic sea-ice zone show however, that the airborne data are highly affected by sweep frequency non-linearities, making identification of snow thickness difficult. A model for the source of these non-linearities in the radar is developed and verified, motivating the derivation of an error correcting algorithm. Application of the algorithm to the airborne data demonstrates that the radar is indeed receiving reflections from the air/snow and snow/ice interfaces.

Consequently, this thesis presents the first *in-situ* validated snow thickness estimates over sea ice in Antarctica derived from a Frequency Modulated Continuous Wave radar on a helicopter-borne platform. Additionally, the ability of the radar to independently identify the air/snow and snow/ice interfaces allows for a relative estimate of roughness of the sea ice to be derived. This parameter is a critical component necessary for assessing the integrity of satellite snow-depth retrieval algorithms such as those using the data product provided by the Advanced Microwave Scanning Radiometer - Earth Observing System sensor on board NASA's Aqua satellite.

This thesis provides a description, solution or mitigation of the many difficulties of operating a radar from a helicopter-borne platform, as well as tackling the difficulties presented in the study of heterogeneous media such as sea ice and its snow cover. In the future the accuracy of the snow-depth retrieval results can be increased as technical difficulties are overcome, and at the same time the radar architecture simplified. However, further validation studies are suggested to better understand the effect of the heterogeneous nature of sea ice and its snow cover on the radar signature.

Contents

Statement of Declaration	i
Abstract	iii
Contents	v
List of Figures	xi
List of Tables	xxiii
List of Acronyms	xxv
Acknowledgements	xxvii
1 Introduction	2
1.1 World Climate and the Polar Regions	2
1.1.1 Sea Ice and Climate	3
1.2 Sea Ice Observation	5
1.2.1 Satellite Remote Sensing of Sea Ice Thickness	10
1.2.2 Snow Thickness on Sea Ice Remote Sensing	14
1.3 Outline	18
1.3.1 Chapter Summary	19

2	Introduction to Radar Principles and Summary of Operating Parameters	22
2.1	Overview of FMCW Radar	25
2.2	Operating Design Parameters	28
2.3	Performance Parameters	28
2.3.1	Frequency Resolution: δf	29
2.3.2	Range Resolution: δR	29
2.3.3	Unambiguous Range	30
2.3.4	Operating Range	30
2.3.5	Antenna Gain and 3 dB Beamwidth	32
2.3.6	Active Area	32
2.3.7	Thermal Noise Power Density: N_T	34
2.3.8	Minimum Detectable Signal: MDS	34
2.3.9	Sampling Frequency: f_s	35
2.4	FMCW Distributed Target Radar Range Equation	36
2.4.1	Signal to Noise Ratio: SNR	38
2.4.2	Theoretical Minimum Backscattering Coefficient: σ^0	39
2.5	Summary	41
3	Electromagnetic Wave Interaction with Snow and Sea Ice using RAASTI	43
3.1	Wide Bandwidth and Layered Media	43
3.1.1	Qualitative Considerations	44
3.1.2	Quantitative Considerations	46

3.2	Conditions for Unambiguous Interface Identification	49
3.2.1	Power Splitting at the Boundary of Two Media	49
3.2.2	Modelling the Condition for Snow Layer Identification	52
3.2.3	Effect of Snow Wetness	54
3.3	Sensitivity of Snow Thickness Estimates to Errors in Refractive Index	56
3.4	Backscattering Coefficient Estimation	59
3.4.1	Surface Scatter	61
3.4.2	Volume Scatter	61
3.5	Summary	63
4	Sled-Based Radar Tests - Fast ice, Davis Station, Antarctica	66
4.1	Radar Operating Conditions and Assumptions	66
4.1.1	Experimental Description	68
4.2	The Physical Conditions of Snow on Fast Ice, Davis Station	70
4.3	Results	70
4.3.1	Type I: Snow Pit Analysis	70
4.3.2	Type II: Blizzard Tail Study	79
4.4	Summary	82
5	Development of a Non-linearity Correcting Algorithm	85
5.1	Problem Description	85
5.2	Assumptions	87
5.3	Non-linearities as a Function of Target Range	89
5.3.1	Analysis	89
5.3.2	Non-linearity Characterisation	92
5.3.3	Mitigation	93
5.4	Non-linearity Correction Algorithm	94
5.4.1	Performance Simulation	94
5.5	Results	96
5.6	Summary	98

6	Helicopter-borne Radar Experiments, East Antarctica	102
6.1	Radar Helicopter Platform	102
6.2	Sea Ice Physics and Ecosystem eXperiment, SIPEX'07	106
6.2.1	Crane Experiments	107
6.3	Voyage 1, 2008	110
6.3.1	Experiment Description	111
6.3.2	<i>In-situ</i> Gathered Data Summary	115
6.3.3	Helicopter Flights	118
6.3.4	Radar Operating Conditions and Assumptions	122
6.3.5	Peak Detection	123
6.3.6	Converting peak separation to snow thickness	129
6.3.7	Results	130
6.3.8	System Error Estimate	135
6.4	Summary	135
7	Conclusions and Recommendations	138
7.1	Discussion	139
7.1.1	Suggested Technical Improvements	141
7.2	Related Work and Outlook	142
A	RAdar for Antarctic Snow Thickness Investigation (RAASTI)	145
A.1	Introduction	145
A.2	SIPEX'07, Radar Version 1.0	145

A.2.1	Antennas	146
A.2.2	YIG –Yttrium Iron Garnet Current Controlled Oscillator	151
A.2.3	YIG Main Coil Driver	152
A.2.4	Laboratory Experiments	155
A.3	V1’08, Radar Version 2.0	160
A.3.1	YIG Main Coil Driver	161
A.3.2	YIG Heater Tests	161
A.3.3	Internal Delay Lines	162
A.3.4	Antenna Interference	164
A.3.5	Sled-based Radar Operation	164
A.3.6	Helicopter Boot Vibration Tests	165
A.4	National Instruments	166
A.4.1	Hardware	166
A.4.2	Software	168
A.4.3	RAASTI File Format	171
B	SIPEX’07 RAASTI Flight Summary	174
B.1	Introduction	174
B.2	Flight Details	176
B.2.1	Alpha	176
B.2.2	Bravo/Charlie/Delta	176
B.2.3	Golf	179
B.2.4	Hotel/India/Juliet	179
B.2.5	Mike/November/Oscar	181
B.2.6	Papa	182
B.2.7	Sierra	183
B.2.8	Uniform	184
B.2.9	Victor and Crane Test	184
B.2.10	Yankee/Zulu/Zulu Two	184

C	Hard Disk Drive Anti-Vibration Tests	188
C.1	Results	188
C.2	Discussion	190
D	Characterisation of the 8-Element TEM Horn Antennas	195
D.1	Background	195
D.2	Motivation	195
D.3	Method	195
D.4	Results	198
D.5	Summary	199
E	The Effect of Constant Antenna Gain on UWB Radar Systems.	203
E.1	Overview	203
E.2	Introduction	203
E.3	Problem Setup	204
E.4	Quantitative Analysis and Simulation	205
E.5	Experimental Results	207
E.6	Summary	207
	References	209

List of Figures

1.1	The minimum and maximum sea ice extents in the Arctic and Antarctic respectively. <i>Credit: National Snow and Ice Data Center.</i>	7
1.2	The five sectors/regions into which the Antarctic coast is split (B&A Seas sector is short for: Bellingshausen and Amundsen Seas Sector). Commonly the Indian Ocean and Western Pacific Ocean sectors are combined, collectively referred to as the East Antarctic Sector. <i>Credit: NASA - Goddard Space Flight Center.</i>	8
1.3	Schematic of a floe.	11
2.1	Principal components of a FMCW radar.	23
2.2	The top coordinate axes illustrate the transmit frequency of the FMCW radar up-chirp as a function of time, and the subsequently received frequency delayed by τ seconds. The bottom coordinate axes illustrate the resulting frequency after mixing of the transmitted and received frequencies, where f_d is proportional to the time delay between transmission and reception, τ	24
2.3	High-level FMCW component block diagram.	27
2.4	An illustration of a situation where ambiguities in radar return could occur: the target is further than $\tau > 2T_p$ away, and hence beyond the unambiguous range of the radar.	31
2.5	The active area (range cell limited) within the radar beamwidth limited footprint shown from two perspectives: side on as the helicopter flies over the surface, and when looking down onto the surface.	34
2.6	The detection probability for a sinusoidal signal in white noise (<i>Blake, 1986</i>), adapted from <i>Brooker [2009]</i>	36
2.7	Block diagram of the sweep voltage driving the oscillator to output a chirp. The voltage gain of the system leads to a chirp amplitude of V_t	37
2.8	Receiver chain components and their associated noise, gain, and bandwidth values.	40
3.1	Illustration of the small and large-scale roughness features of a surface. The radar range cells are seen here propagating down onto the surface. The active area of the radar illuminates large-scale surface features that may potentially mask returns from the sub-surface.	45

3.2	The RMS height of the fast ice surface, as derived from laser altimeter data. The graph shows that the surface features are undersampled until the sampling distance is increased to ≈ 50 m.	47
3.3	The same results as 3.2, except on a larger scale, showing the distances of interest, which correspond to the size of the active area of RAASTI.	47
3.4	Transition from specular reflection to rough surface scattering as quantified by g , adapted from <i>Beckmann and Spizzichino</i> [1963].	49
3.5	The auto-correlation length calculated using the laser/INS datasets over fast ice. The approximate distance over which the surface features decorrelate (defined at the $1/e$ level of the auto-correlation function) is ≈ 27 m.	50
3.6	The typical nature of sea ice and its snow cover in Antarctica, illustrating the possibility of scattering and specular reflection being present within the active area. (Photograph taken at an altitude of 80 m.)	50
3.7	The possible ambiguity condition between returns from the air/snow and snow/ice interfaces, where D_n denotes the diameter of the active area.	51
3.8	Return power requirements for the air/snow and snow/ice interfaces for unambiguous identification of the layers. The power received from the snow/ice interface should be greater than that from the air/snow interface.	51
3.9	Reflection and transmission of a plane wave. A is the incident beam arriving at an angle θ_i to, R is the reflected beam, and T is the transmitted beam into the medium at an angle θ_r	53
3.10	Reflection and refraction/transmission at air/snow and snow/ice interfaces.	53
3.11	Snow refractive index as a function of ice refractive index required to satisfy unambiguous relative power requirements.	55
3.12	Ice refractive index as a function of snow refractive index. The areas which satisfy the unambiguous relative power requirement are enclosed within the red lines.	55
3.13	Refractive index at the frequencies 2, 5, and 8 GHz as a function of increasing snow water content. The values demonstrate that equation 3.8 will remain satisfied even with increasing snow wetness, hence the reflection from the snow/ice interface can be expected to be stronger. However, this ignores the increasing power losses of the EM radiation in a wet snow pack, which is further explored in the text.	57
3.14	The absorption length (or the penetration depth) of the EM radiation at 2, 5 and 8 GHz as a function of increasing snow wetness. The large difference in penetration depth over the frequency range indicates that it is likely that a wet snow pack degrades the range resolution of the radar by preventing reflection of the higher frequencies.	58

3.15	σ_0 for fast ice, using the formulation for backscattering coefficient provided by <i>Beckmann and Spizzichino</i> [1963] (pp 88).	61
3.16	Snow volume scattering contribution to the backscattering coefficient as a function of frequency, demonstrating its increased contribution. Consequently, reducing the chances of the radar in receiving returns from the full transmitted bandwidth. . .	63
3.17	Volume scattering sensitivity to changes in: refractive index, grain size and wetness.	64
4.1	An example of a snow pit demonstrating the small vertical scale variability of surface height over decimetre scales. Various features of this snow pit were frequently observed in the sled-based study, such as the large depth hoar crystals and slush layer at the snow/ice interface. Additionally, a layer of dirt, probably blown from the Vestfold Hills appears about 35 mm above the ice surface. . . .	68
4.2	An example snow pit with layering present.	69
4.3	Snow density sampler tool, shown here filled with snow from a snow pit. Collecting a known volume of snow, allows the density of the weighted sample to be calculated.	69
4.4	Pit #1 experiment.	73
4.5	Pit #2 experiment.	74
4.6	Pit #3 experiment.	75
4.7	Pit #4 experiment.	76
4.8	Pit #5 experiment.	77
4.9	Pit #6 experiment.	78
4.10	The radar view of the blizzard tail, created by stacking radar returns recorded every meter. The red line is an example pick of the snow/ice interface.	80
4.11	Radar view of the end of the blizzard tail: full bandwidth. The snow/ice interface is clearly visible.	81
4.12	Radar view of the end of the blizzard tail: 2.2 - 4.1 GHz.	83
4.13	Radar view of the end of the blizzard tail: 4.1 - 5.9 GHz.	83
4.14	Radar view of the end of the blizzard tail: 5.9 - 7.8 GHz.	83

5.1	Spectrogram of raw radar data illustrating the ≈ 2 m smearing in the IF. The identification of the air/snow and snow/ice interfaces is impossible.	86
5.2	Comparison between the ideal and actual transmitted frequency as a function of time.	87
5.3	Spreading in the difference frequency caused by non-linearities in the transmitted chirp, which degrades the frequency resolution of the radar, and also the vertical range resolution.	89
5.4	Piecewise approximations to a non-linear chirp, demonstrating a simplistic example a non-linearity errors that can be present in a linear chirp.	91
5.5	Non-linear chirp effects on the difference frequency. The change in gradient shown in figure 5.4 leads to a change in frequency from f_1 to f_2 , which must be affected by a chirp between them.	92
5.6	Delay line difference frequency spectrum. Ideally it should be a narrow peak, however under non-linearity conditions it is here seen to spread over 1 m.	93
5.7	Simulated radar data of two targets; the ideal difference frequencies, and the difference frequencies derived when corrupted by transmitter non-linearities. The small shift between the ideal peak, and the peak retrieved after application of the non-linearity correcting algorithm occurs due to imprecise knowledge of the target's range by the algorithm. A time-domain window is used to approximately isolate the response from the air/snow and snow/ice surfaces in the waveform corrupted by non-linearities. The center of the window is assumed to be the location of the true target, however this is not always the case and consequently a shift in the peaks results. However as it is only the <i>difference</i> between the air/snow and snow/ice interfaces that is sought, the shift is immaterial for snow thickness extraction purposes.	95
5.8	Non-linearity corrected simulated data of two targets. The red line shows the input data to the algorithm which is corrupted by non-linearities and white noise. The blue line is the effect of the algorithm in compensating for the non-linearities where two peaks (labelled) are seen.	96
5.9	Comparison of algorithm effect on actual radar data. Signal power plotted as a function of helicopter altitude. The red line is the raw data where a signal power is seen to increase from about 53 m, however it is not possible to identify the presence of two surfaces. The blue line is the effect of the non-linearity algorithm correction to this data. Two peaks are clearly visible.	97
5.10	Spectrogram of raw radar data, the vertical axis plots the helicopter altitude in meters, and the horizontal axis is the time in seconds. It is very difficult to distinguish the surfaces if any present in the radar data.	99

5.11	Spectrogram of corrected radar data, the vertical axis plots the helicopter altitude in meters, and the horizontal axis is the time in seconds. The application of the non-linearity correcting algorithm reveals the presence of two surface in parts of the radar data.	99
5.12	Zoomed in spectrogram of corrected radar data, the surfaces are easily picked out by eye.	100
5.13	A plot of the radar IF frequency for one chirp, as a function of voltage and sample number (proportional to time). The spike seen in the plot could be the results of phase jitter (not removed by the algorithm) which is responsible for the vertical lines in spectrograms of Figures: 5.10, 5.11, and 5.12	100
6.1	Schematic of the RAPPLS helicopter instrument arrangement. <i>Courtesy of J.Lieser.</i>	103
6.2	Photograph of the underside of the helicopter during flight. <i>Courtesy of K.Newbery.</i> The black rectangular window in the top right hand side of the helicopter is the laser scanner aperture, the two black rectangular boxes between the skids are the radar transmit and receive antennas, and the exposed box to the top right of the radar antennas is the camera lens.	103
6.3	The IF frequency voltage during a single chirp duration, demonstrating the amplitude suppression with time which is explained in appendix E.	106
6.4	The voltage waveform used to actuate the YIG to chirp up from 2 to 8 GHz and back to 2 GHz respectively. The segment in red identifies the usable segment of the chirp.	107
6.5	The radar inside a cage pallet and attached to the ship's crane for testing. <i>Photo credit: J. Lieser.</i> The radar antennas are secured to the bottom of the cage pallet.	108
6.6	Three individual radar records are shown, with returns due to the air/snow and snow/ice interfaces seen here to be changing their location as the altitude of the cage pallet changed. A large noise component (possibly due to cross-coupling of the antennas) is stationary.	109
6.7	A spectrogram of the stacked radar returns during the crane tests of the radar. Two lines are seen moving across the image, identifiable as the air/snow and snow/ice interface returns, whereas the a large noise signal is stationary during the experiment. The two lines of lower intensity at a large range, seeming to mirror the motion of the bright air/snow and snow/ice peaks are likely to be the 2nd harmonics of the two returns.	110
6.8	Satellite image of Vestfold Hills, with the test site labelled. <i>Photo credit: Australian Antarctic Division, Kingston, Tasmania, Australia.</i>	113

6.9	<i>In-situ</i> experiment outline.	114
6.10	Photograph of the start of Line A at an altitude of 82 m. The image represents an area of 47 x 72 m. The effects of wind on the snow are evident, with sastrugi features ranging from 1 m to 10 m, and in places bare ice is visible. <i>Photo credit: Adam Steer.</i>	115
6.11	Referring to figure 6.9(b), this graph plots the snow thickness over the first half of sampled area: snow thickness measured every 2 m, in the first half of the sample area by 10 groups, spaced 4 m apart. The red profile corresponds to the measurements recorded between the flags over which the helicopter was directed to fly.	116
6.12	Temperature profiles of the snow pack recorded every 5 m, by five groups spaced 8 m apart. The blue line plots the temperature measurements recorded by each group, and the red line corresponds to the average temperature along the center track, demonstrating a small spatial variability of temperature gradients. The centre temperature plot corresponds to the profile between the flags over which the helicopter was directed to fly.	117
6.13	Density of snow pack along Line A, measured every 20 m. The absence of a density sample at 160 m is due to the absence of a snow layer at the site.	117
6.14	A plot of the relative altitude derived from the difference between the laser range and INS altitude, demonstrating the 'dropout' in laser signal when the helicopter flies over the corner reflector placed at the start flag. The absence of the signal in the second Pass may be due to the post-processing of the laser data which picked out only those returns at nadir.	119
6.15	Distribution of the estimated coordinates of the start flag of Line A using the corner reflector position.	120
6.16	Distribution of estimated coordinates of the end flag of Line A.	120
6.17	The flight tracks of the six Passes. The maximum separation between them is 2 - 3 m, as shown in figure 6.18.	121
6.18	The flight tracks of the six Passes plotted in a Cartesian plane with the starting flag at the origin. The red lines show the assumed tracks along which <i>in-situ</i> snow thickness measurements were recorded.	122
6.19	The raw radar data collected over a Pass at 100 m altitude, with the results of the picking algorithm overlaid.	124
6.20	The raw radar data collected over a Pass at 50 m altitude, with the results of the picking algorithm overlaid.	125

6.21	The raw radar data, and the corrected radar data for three consecutive returns showing the same peak location. Additionally, the performance of the non-linearity algorithm is shown: the dotted line represents the un-corrected radar record, where the interface peaks are completely unidentifiable.	126
6.22	Closer demonstration of the results of the picking algorithm, in areas where the eye generally sees two surfaces, the picking algorithm is not successful.	128
6.23	Closer demonstration of the results of the picking algorithm, comparison between a successful and unsuccessful pick result.	128
6.24	Approximate number of range bins calculated across the transect lines, using a changing velocity factor (red line), or a mean velocity factor (blue line).	130
6.25	Snow thickness retrieved from the individual Passes: 1, 2, and 3.	132
6.26	Snow thickness retrieved from the individual Passes: 4, 5, and 6. (Pass 5 snow depth retrieval is poor due to helicopter path deviations from flight line.)	132
6.27	Comparison between the <i>in-situ</i> measured snow thickness, and the average radar derived snow thickness for the passes at 1, 2 and 3.	133
6.28	Comparison between the <i>in-situ</i> measured snow thickness, and the average radar derived snow thickness for the Passes 4 and 6. (Pass 5 is excluded from the average due to its high deviation from the flight path.)	133
6.29	Scatter plot of the <i>in-situ</i> measured snow thickness versus the radar derived snow thickness. A linear least-squares fit to the data points is overlaid. It could be expected for the gradient of this line to be 1.0, and offset to be zero. However this is not the case. The smaller gradient value indicates that the radar under-estimates the snow thickness, which could be explained by the presence of undetected icy layers in the snow pack, or salinity at the bottom of the snow pack which was not measured. The bias value of 29.409 mm is less than the radar range resolution, and consequently the result of the resolving capacity of the radar system.	134
6.30	As in figure 6.29, the gradient deviation from 1.0 is the result of the radar underestimating the snow thickness. The differences between the two regression curves for the two lines (A and B) could be indicative of the differences in snow properties such as density and grain size, which were not measured separately for the two lines. In future experiments, it would be preferable to measure the density profile of both (or more) lines and if the salinity of the snow pack.	134
6.31	Error in helicopter data estimates as a function of averaging interval.	136
6.32	Estimated roughness (as RMS height) derived from the radar data for the air/snow and snow/ice interfaces.	136

A.1	RAASTI v1.0, the SIPEX'07 radar block diagram.	146
A.2	Original YIG main coil driver, <i>courtesy of CReSIS</i>	147
A.3	Modified YIG main coil driver, <i>courtesy of P.Jansen (STS-AAD), adapted from MicroLambda Inc.</i>	147
A.4	Frequency response: original YIG main coil driver.	148
A.5	Frequency response: modified YIG main coil driver.	148
A.6	Custom designed 8 - element TEM horn array for helicopter operation, shown here within radome (Pelican TM 1700 case).	149
A.7	Custom designed 8 - element TEM horn array in radome, attached between helicopter skids.	149
A.8	Technical drawing of the antenna mounts for helicopter operation. <i>Courtesy of S.Whiteside, AAD</i>	150
A.9	Array antennas attached to cage pallet for crane tests.	151
A.10	Close-up: Array antennas attached to cage pallet for crane tests.	151
A.11	Schematic of the YIG driver.	154
A.12	YIG driver response to step input (voltage versus time).	154
A.13	YIG driver response to ramp input (voltage versus time).	155
A.14	YIG long term frequency drift. (YIG output monitored through a “divide-by-four” circuit.)	156
A.15	Power at the output of the transmit power amplifier.	157
A.16	Attenuation in IF observed at higher frequencies.	157
A.17	LNA sensitivity test results.	158
A.18	Frequency response of the IF amplifier.	159
A.19	RAASTI v2.0, the V1'08 radar block diagram.	160

A.20	The initial layout of the updated YIG mail coil driver. (Used during SIPEX'07.)	161
A.21	The final layout of the updated YIG mail coil driver. (Used during V1'08.)	161
A.22	YIG case temperature during first flight.	163
A.23	Delay lines used in testing.	163
A.24	Internal delay line distortion test.	164
A.25	Sled-based radar operation. <i>Photo courtesy K.Newbery.</i>	165
A.26	Accelerometer measured vibrations inside the boot of the helicopter. (<i>Courtesy: K. Newbery, STS - AAD</i>).	166
A.27	Radar system setup, front.	167
A.28	Radar system setup, back.	167
A.29	RAASTI GUI.	170
A.30	RAASTI file format.	171
B.1	Location of flights made during SIPEX'07. <i>Image courtesy of J.Lieser.</i>	175
B.2	Hard disk performance in the helicopter running on ground power.	177
B.3	Hard disk performance during flight.	177
B.4	Expected sharp return, seen here at approximately 145 m.	178
B.5	“Diffuse return”, seen here at approximately 85 m.	178
B.6	Kinks in the 2ohm voltage, and affect on radar return.	179
B.7	Apparent return of the radar at high altitude.	180
B.8	First signs of “broadband” noise.	180
B.9	Changes made to the YIG driver voltage waveform.	181
B.10	Broadband noise present at on return, even at high radar altitude.	182

B.11 Broadband noise present when running on ground power with receive antenna port disconnected.	182
B.12 Absence of broadband noise when running from a ship source of AC.	183
B.13 YIG and YIG driver, illustrating the loose component.	183
B.14 Significant contribution of broadband noise, almost covering the full radar spectrum.	184
B.15 Crane test results.	185
B.16 Helicopter hover over marked area.	186
C.1 Anti-vibration mount, side 1.	189
C.2 Anti-vibration mount, side 2.	189
C.3 Internal PATA, <i>on ground</i>	191
C.4 Internal PATA, <i>in flight</i>	191
C.5 External SATA (A), <i>on ground</i>	192
C.6 External SATA (A), <i>in flight</i>	192
C.7 External SATA (B), <i>on ground</i>	193
C.8 External SATA (B), <i>in flight</i>	193
D.1 Model of a single element of the antenna array, <i>Gunbatar</i> [2007].	196
D.2 Single antenna element, <i>Gunbatar</i> [2007].	196
D.3 Antenna array assembled and installed in the radome.	197
D.4 Antennas in radomes, mounted between the skids of the Squirrel helicopter. . . .	197
D.5 Antenna with radome mounted on testing frame.	198
D.6 Antenna without radome mounted on testing frame (bore sight).	199
D.7 Antenna Gain (dB) versus Frequency (GHz).	200

D.8	Antenna full 3dB beamwidth (degrees) of antenna versus Frequency (GHz). . . .	200
D.9	Antenna Gain (dB) versus Frequency (GHz) - blue (with radome), red (without radome).	201
D.10	Antenna 3dB beamwidth (degrees) versus Frequency (GHz) - blue (with radome), red (without radome).	201
E.1	Variation of A_{eff} as a function of frequency and chirp period.	205
E.2	RMS power as a function of centre frequency.	206
E.3	Comparison of the rectangular and A(t) (“amplitude suppression”) windows. . . .	207
E.4	Amplitude modulation effects on the IF frequency.	208

List of Tables

1.1	Approximate of values of thicknesses and densities for snow, and sea ice in Antarctica.	14
2.1	Radar design parameters.	28
2.2	The expected radar performance parameters.	29
2.3	Antenna parameters.	32
3.1	Rayleigh conditions for specular reflection.	48
3.2	Experimentally derived viewing conditions.	48
3.3	Error in snow pack thickness calculations as a function of error in density for dry snow (n_{ds}) and wet snow (n_{ws}). (Refractive index calculated after <i>Galley et al.</i> , 2009.)	59
3.4	Sensitivity of wet snow refractive index to error in density, for 2, 5, and 8 GHz. Snow wetness taken as 0.65%. (Refractive index calculated after <i>Galley et al.</i> , 2009.)	60
4.1	Comparison between the <i>in-situ</i> measured and radar estimated snow thickness pit measurements (theoretical radar range resolution of 32.5mm).	71
5.1	Sensitivity of gradient error to target range.	91
6.1	Helicopter antenna parameters, measured at the NASA antenna testing facility. .	105
6.2	The mean and range of snow thickness values measured <i>in-situ</i> over the ten sample tracks of Line A.	116
6.3	Coordinates of the start and end flags of Line A.	119
6.4	Approximate helicopter viewing conditions.	123
6.5	<i>In-situ</i> measured snow density, and calculated corresponding velocity factor. . . .	129
A.1	Delay Line Lengths	164
A.2	RAASTI File Format	172
B.1	Flight summary.	174
C.1	Summary of HDD write speed performance.	190
D.1	Antenna testing points.	198
E.1	Window performance parameters.	207

List of Acronyms

IPPS	1 Pulse Per Second	AAD	Australian Antarctic Division
ACFR	Australian Center for Field Robotics	ADA	Anomalous Diffraction Approximation
ADC	Analog to Digital Converter	AMSR-E	Advanced Microwave Scanning Radiometer for EOS
ARISE	Antarctic Remote Ice Sensing Experiment	ASIRAS	Airborne SAR/Interferometric Altimeter System
BW	Band Width	CRISIS	Center for Remote Sensing of Ice Sheets
CRF	Chirp Repeat Frequency	CRI	Chirp Repeat Interval
EM	Electromagnetic	EMI	Electromagnetic Interference
ESA	European Space Agency	FAT32	File Allocation Table (32-bit)
FFT	Fast Fourier Transform	FIFO	First In First Out
FMCW	Frequency Modulated Continuous Wave	GPS	Global Positioning System
GSFC	Goddard Space Flight Center	GUI	Graphical User Interface
HDD	Hard Disk Drive	IF	Intermediate Frequency
INS	Inertial Navigation System	IPPC	Intergovernmental Panel on Climate Change
IPY	International Polar Year	LaRA	Laser/Radar Altimeter
LNA	Low-Noise Amplifier	LPF	Low-Pass Filter
MDS	Minimum Detectable Signal	NA	Not Available
NASA	National Aeronautics and Space Administration	NCOM	INS proprietary protocol
NI	National Instruments	NMEA	National Marine Electronics Association 0183
NTFS	New Technology File System	PATA	Parallel - Attachment Packet Interface
PRF	Pulse Repetition Frequency	RAASTI	RAdar for Antarctic Snow Thickness Investigation
RADAR	RAdio Detection And Ranging	RAPPLS	RAdar-Aerial Photography-Pyrometer-Laser Scanner
RF	Radio Frequency	RMS	Root Mean Square
SATA	Serial - Attachment Packet Interface	SIPEX'07	Sea Ice Physics and Ecosystem eXperiment 2007
SNR	Signal to Noise Ratio	STS	Science Technical Support
SWE	Snow Water Equivalent	TEM	Transverse Electromagnetic
UDP	User Datagram Protocol	UWB	Ultra Wide Band
YIG	Yttrium-Iron-Garnet		

Acknowledgements

Everything in Nature is simple; it is realising how simple it is that can be hard.

I am grateful to Duncan Wingham for making the hardest things simple.

To my family :)

Chapter

1

Introduction

1.1 World Climate and the Polar Regions

World politics, economics and science is in a progressive shift towards recognising the important impacts that anthropogenic greenhouse gases have on our planet. Science has stepped heavily into the public arena with information that is not simply novel and fascinating, but of a predictive quality, the core of scientific endeavour. The reaction of the world on all levels is a fascinating development to observe, and science must continue to examine and study the Earth's climate; refining its conclusion and improving the integrity of its message.

Understanding which factors of our changing climate are due to natural causes and which are anthropogenic is currently a topical question for science. Established in 1988, the Intergovernmental Panel on Climate Change (IPCC) aims to provide an assessment of the current knowledge of climate change, the causes of these changes, and predictions for future change. Encompassed in these aims is the necessity to quantify global sea level rise. The polar regions contain a large portion of the Earth's water reserves. If the ice caps of both Greenland and Antarctica were to melt sea level would rise by some 70 m, (*Rignot and Thomas, 2002*).

It has also long been predicted that changes in the climate will be most pronounced at the polar regions. For example, the *Manabe and Stouffer, [1980]* climate model demonstrated larger surface warming in the polar regions when compared to the rest of globe, under conditions of increasing greenhouse gas emissions. Recent modeling studies (e.g. *Holland and Bitz, 2003*) offer further support to the view of the importance that the polar regions play in Earth's climate system. The term *polar amplification* is now frequently used to describe the predicted sensitivity of the polar regions to changes in global climate.

The presence of sea ice is one key reason that the polar regions are sensitive to changes in climate (*Xie et al., 1994; Wu et al., 1999; Houghton et al., 2001*). Sea ice may cover up to 11% of the

world's oceans, and while not significantly contributing directly to sea level rise, sea ice has a pronounced affect on the role that the polar regions play in the global climate (*Chapman and Walsh, 1993; Curry et al., 1995*). Sea ice is recognised as a cryospheric component that must be included in coupled climate models if they are to capture decadal variability (*Washington and Parkinson, 2005*).

1.1.1 Sea Ice and Climate

Sea ice is formed from the coagulation of ice crystals in polar ocean waters. As described by *Allison et al., [1993]* in calm waters crystals of frozen water will form smooth sheets of ice called *nilas*, while in the presence of waves force these crystals to form discs of ice called *pancakes*. Under continuous wave action, these pancakes will be aggregated into increasingly pancakes, finally forming a consolidated sea ice cover. Further growth of the sea ice may occur from the underside of the sea ice via accretion of ice crystals from the water, or via accumulation of a thick snow layer. In instances when this snow cover is heavy enough to depress the sea ice below the water line, flooding of the snow, which subsequently refreezes add to the total ice thickness.

During its formation and subsequent growth, sea ice expels highly salty water (brine) back into the ocean. This saltier and hence denser water sinks, contributing to formation of water masses such as the Antarctic Bottom Water (e.g. *Foster and Carmack, 1976*). These denser waters are recognised as an important source of ocean ventilation, and global overturning circulation (*Aagaard and Carmack, 1989; Rintoul et al., 2002*). The subsequent melting of sea ice leads to the presence of a fresher surface layer, and just as its formation contributed to driving the thermohaline circulation, the melting of sea ice acts to inhibit it.

The presence of sea ice on the water surface acts as a physical barrier separating the atmosphere and ocean, affecting the momentum (e.g. *Martinson and Wamser, 1990*), and chemical exchanges (e.g. *Gleitz et al., 1995*) that exist between them. Sea ice dramatically alters the heat and radiation budgets of the ocean and atmosphere (e.g. *Jordan et al., 1999*). The role that sea ice plays in the polar climate is largely driven by the markedly greater reflectivity that sea ice has to incident solar radiation (*Brandt et al., 2005*) when compared with the open ocean. In the summer months, when the sun is constantly above the horizon, the sea ice cover has an insulating effect on the ocean. It acts to prevent up to 80% of the sun's rays from entering the water and increasing its

temperature. In the winter months however, sea ice acts to prevent heat from leaving the relatively warmer ocean waters. During these months large temperature differences can exist between the atmosphere ($\approx -40^\circ\text{C}$) and the ocean (at -1.8°C for salty waters). Thereby heat fluxes can transfer energy at rates of more than $800\text{W}/\text{m}^2$ between open ocean and the atmosphere, whereas the presence of sea ice is able to reduce this energy loss to less than $30\text{W}/\text{m}^2$, (*Maykut, 1978; Parkinson, 1997*).

Sea ice has also an important role to play in the ecological processes of the polar regions (*Eicken, 1992; Nicol et al., 2000*), supporting a diverse array of micro and mega fauna. Harboring large concentrations of bacteria, and algae both within the brine channels (*Smetacek and Nicol, 2005*) that are created during sea ice growth (through which the brine is expelled as sea ice grows), and on its underside. These algal ecosystems are an important source of food for the large number of krill that they nourish, and which contribute for example, some 25% of the total primary production in the Southern Ocean (*Arrigo and Thomas, 2004*). The thickness of sea ice has a direct influence on its ability to sustain algal communities, due to the effect it has on the penetration of photosynthetically active radiation which is required for their sustenance (*McMinn et al., 1999*).

Snow on Sea Ice

A snow cover compounds the effect that sea ice in its interaction with the atmosphere and ocean (*Ledley, 1993; Fitchefet, 2000; Massom, 2001*). Snow has an even higher albedo than sea ice (*Allison et al., 1993*), and only a thin cover of snow is all that is needed for it to reflect most of the incoming solar radiation. As sea ice can be viewed as an insulating blanket on the ocean, snow plays this same role for sea ice. Snow has a thermal conductivity an order of magnitude less than sea ice (*Maykut and Untersteiner, 1971*). The oft-used values for the thermal conductivity of sea ice and snow are 2 and $0.3\text{ W}/\text{m}/\text{K}$ respectively, and more recent studies have measured the thermal conductivity of snow to be even less at $0.16\text{ W}/\text{m}/\text{K}$ (*Massom, 1997; Sturm, 1998*). A layer of snow acts to prevent melt of sea ice in the summer months, and thermodynamic growth during the winter months (*Eicken et al., 1994*). Furthermore, the effect of even a thin snow cover can be quite dramatic, for example a 10 cm snow cover can all but eliminate the available photosynthetically active radiation penetrating the ice (*Meiners, 2002*).

Due to its insulating properties, a snow cover can reduce growth of sea ice by accretion. However, particularly in the Southern Ocean snow loading is often large enough to depress a floe below the

water line, the subsequent re-freezing of the wet snow will contribute to the total sea ice thickness (Maksym and Jeffries, 2000). This process of flooding and refreezing of snow forms meteoric ice, widely recognised as playing an important role in the response of the Southern Ocean to warming temperatures (Fichefet and Morales Maqueda, 1999). On the one hand it is predicted that warmer ocean waters will support a thinner sea ice cover, and on the other hand warming temperatures could lead to increasing net precipitation leading to increases in snow ice formation (Eicken *et al.*, 1994; Manabe *et al.*, 1991), and consequently a possibility of the overall thickening of the Antarctic sea ice cover (Zhang, 2007).

1.2 Sea Ice Observation

Since the 1970s, satellite data has contributed to the study of many features of the polar regions. To date, satellite data has been used to routinely derive for example, sea ice concentration, extent, motion, deformation, and surface temperature (e.g. Zwally *et al.*, 1983; Gloersen *et al.*, 1992; Emery *et al.*, 1997; Comiso and Parkinson, 2004). These data have been used to improve our understanding of how the polar regions are interacting with the ocean and atmosphere processes (e.g. Rayner *et al.*, 2003).

In the Northern Hemisphere, sea ice covering the Arctic Ocean extends to the North Pole, and is confined by land masses of Eurasia and North America (figure 1.1). The sea ice extent in the Arctic will vary annually between 6.9 to 15.3 million square kilometers (Parkinson and Cavalieri, 2002). This confined sea ice is likely to survive from one year to the next (referred to as *multi-year* sea ice), and as a consequence can reach average thicknesses of 2 m or more (Laxon *et al.*, 2003). Characteristically, it supports a relatively even, thin snow cover (≈ 0.3 m, Warren *et al.*, 1999) due to low precipitation and seasonal melting of the snow pack.

In contrast, the sea ice cover over the Southern Ocean, surrounding the Antarctic continent is geographically unbounded (figure 1.1). The geographically unconstrained sea ice extent varies significantly more than its counterpart in the Arctic. Its yearly extent reported to fluctuate between 3.1 to 18.2 million square kilometers (Cavalieri and Parkinson, 2008). The exposure of the Antarctic sea ice to warmer maritime weather, and frequent storms means that the sea ice is mostly seasonal, with few areas (such as the Weddell Sea, figure 1.2) where the sea ice cover may survive the summer months. Consequently, the sea ice is thinner (≈ 0.9 m, Worby *et al.*, 2008a), and due

to frequent precipitation supports a thicker snow cover, which oft-times is enough to depress the sea ice below the water line (*Massom et al.*, 2001).

The seasonal growth and decay of sea ice in Antarctica represents one of the greatest seasonal changes on Earth, and its variability is strongly coupled with the Earth's climate system (*Yuan and Martinson*, 2000). The seasonal variability oscillates between a minimum in February of 3 to 4 million square kilometers, where what remains of the sea ice is largely concentrated in the Weddell, Amundsen and Bellingshausen Seas (see figure 1.2) which contain the rare examples of multi-year sea ice in Antarctica; to the September maximum when the sea ice cover surrounds the waters around the continent completely, covering some 8% of the Southern Hemisphere, and on occasion extending as far North as 55° South (*Gloersen et al.*, 1992).

Antarctic sea ice is on average thinner than its Arctic counter part, which is largely attributed to greater oceanic heat flux, and to its geographically unconstrained nature, which allows frequent removal from the coast by winds and currents. A recently published climatology of sea ice: *Worby et al.*, [2008a] compiled from available ship-based observations estimates the large-scale mean thickness of sea ice to be less than a meter. However, large regional and seasonal variability is observed between the six sectors (into which the Antarctic coast is conventionally divided, see 1.2). Annually, the thickest ice is found mainly in the Weddell, and parts of the Bellingshausen and Amundsen Seas, as well as in parts of the Ross Sea. Whereas thinner ice, is found to occur in the Indian and Pacific Ocean sectors. Regionally, Ross Sea is found to have on average thicker ice during almost all seasons, except during Spring time, when the largest Antarctic polynya opens, and produces large volumes of thin ice.

In contrast, *in-situ* measurements have found that Antarctic snow thickness is generally thicker than its Arctic counter part, and of greater seasonal and regional variability. A review of the snow properties on Antarctic sea ice by *Massom et al.*, [2001] finds that the mean snow thickness varies from 200 to 490 millimeters seasonally and regionally. This distribution is attributed to variability in precipitation regimes, redistribution by persistently strong winds (*Andreas and Claffey*, 1995), as well as the age of the underlying sea ice (older sea ice is generally observed to have the thickest snow cover). This is to be compared with the Arctic, where snow thickness will vary between 0.26 and 0.42 m at the end of the accumulation season (*Warren et al.*, 1999). The flooding of snow, and subsequent reduction in the albedo and increase in thermal conductivity is a prevalent feature in

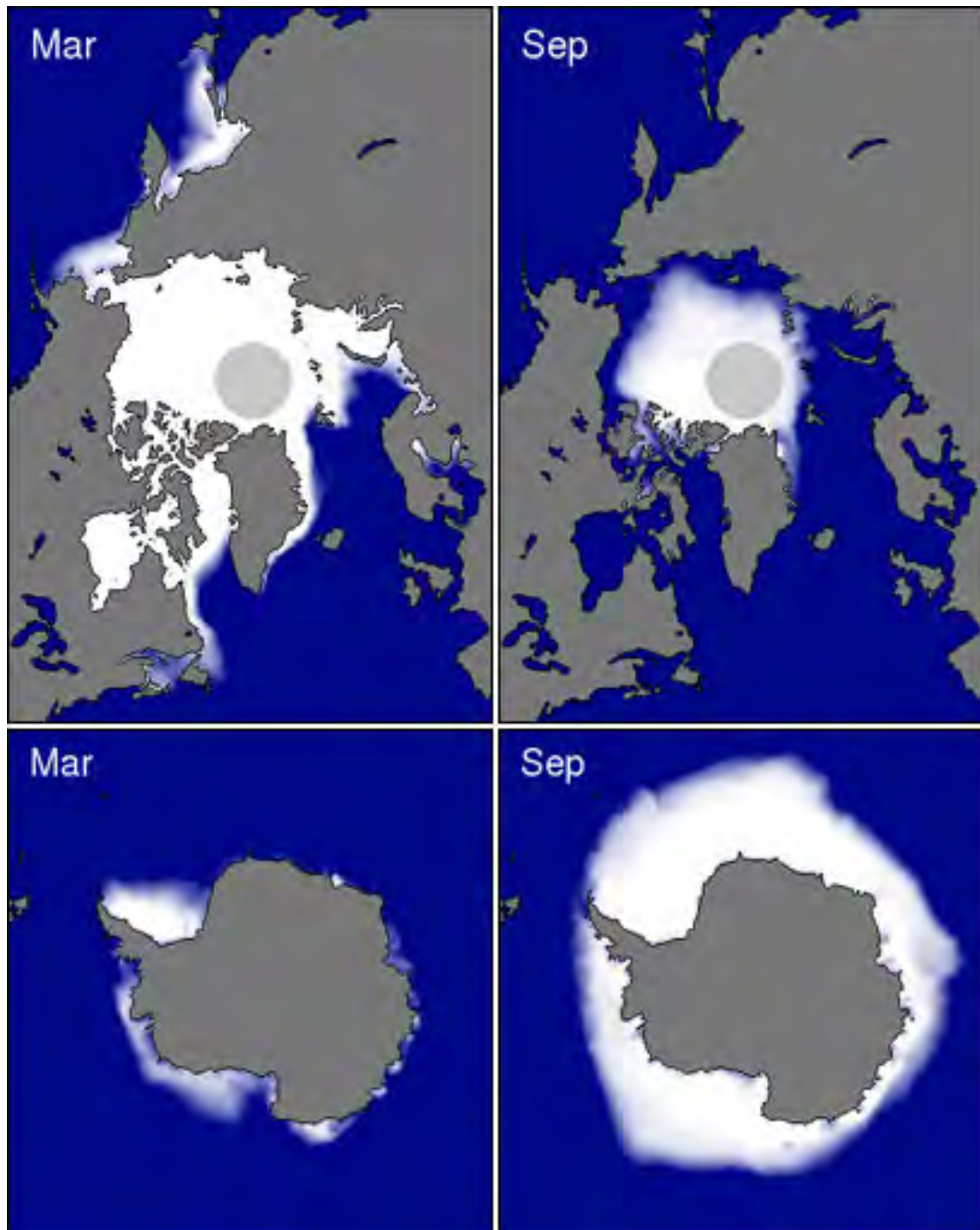


Figure 1.1: The minimum and maximum sea ice extents in the Arctic and Antarctic respectively. *Credit: National Snow and Ice Data Center.*

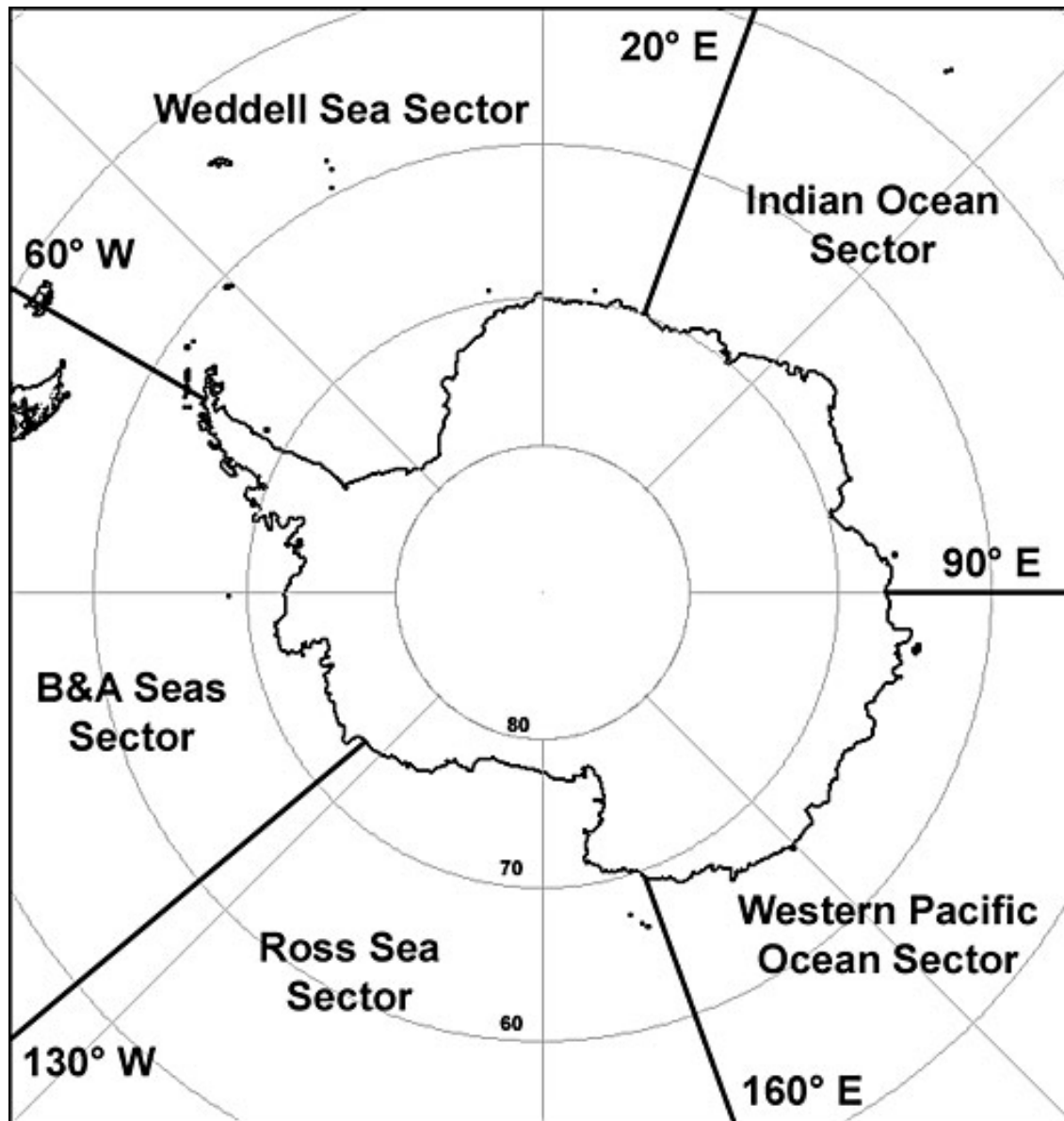


Figure 1.2: The five sectors/regions into which the Antarctic coast is split (B&A Seas sector is short for: Bellingshausen and Amundsen Seas Sector). Commonly the Indian Ocean and Western Pacific Ocean sectors are combined, collectively referred to as the East Antarctic Sector. *Credit: NASA - Goddard Space Flight Center.*

the Southern Ocean. Such events frequently lead to snow-ice formation, whose contribution to the total ice thickness has been found to vary from 8 - 38 % (*Massom et al.*, 2001).

Observations of Trends in Sea Ice Thickness

Sea ice cover is known to have not only annual cycles and interannual cycles, but predictions have also been made as to the possible secular trends in sea ice volume which may be affected by the changing climate (*Bitz et al.*, 2001). Sea ice thickness, and distribution affect the exchange of heat between the atmosphere and ocean, the freshwater budget, and ultimately the large-scale polar climate conditions (*Holland et al.*, 2006). In order to understand the large-scale mechanism and quantify the relationship between changes in climate and the sea ice cover of the polar regions, the trends in volume (not just extent and concentration) must be understood. Volume changes in sea ice can be written thus:

$$\frac{\partial V}{\partial t} = A \frac{\partial \bar{h}}{\partial t} + \bar{h} \frac{\partial A}{\partial t} \quad (1.1)$$

where V is the total volume of sea ice, A is the areal cover, \bar{h} is the areally averaged thickness, and t is the time variable.

In the Arctic decadal trends or rather the decline in both extent and thickness of sea ice have been observed. There is evidence that the changing climate has led to significant sea ice depletion in the Arctic. The extent of the Arctic sea ice has been reported to decline at a rate of 32900 ± 6100 square kilometers per year (*Parkinson and Cavalieri*, 2002) over a 20 year period (1979 - 1999). Additionally, declassified submarine logs of upward looking sonar measurements under sea ice in the Arctic have allowed such trends in thickness of sea ice to be assessed. For example, *Rothrock et al.*, [1999] use this submarine data to find that the thickness of sea ice in the Arctic has decreased by 1.3 m from 1980 to 2000. Satellite data support these findings, *Laxon et al.*, [2003] report a decreasing trend in sea ice thickness of 67 ± 19 millimeters per year during the 1992 - 2001 period, calculated from satellite radar altimeter (ERS-1 and ERS-2) retrievals.

In Antarctica however, whereas surface air temperatures have been observed to increase since the 1950s (*Jacka and Budd*, 1998), the trend in sea ice extent also shows a significant increase of 11200 ± 4200 square kilometers per year (*Zwally et al.*, 2002) over the same 20 year period (1979 - 1999). A more recent study (*Cavalieri and Parkinson*, 2008) extends this time series to 2006, finding that this increase in sea ice cover is indeed increasing. They note however, that

the response of different Antarctic sectors is quite varied, and that the derived trends depend on the averaging time interval, concluding that such results are suggestive of the fact that the secular trends are not yet being captured by the available time series.

Unlike in the Arctic no large-scale submarine sonar data exist in the Southern Ocean, and currently sea ice thickness measurements in Antarctica are mostly limited either regionally or temporally (e.g. *Worby et al.*, 1999; *Worby et al.*, 2001; *Haas*, 1998). The single existing sea ice climatology in Antarctica has only recently been compiled from the aggregation of a large number of ship based observations by *Worby et al.*, [2008a]. Prior to this, the absence of a sea ice thickness climatology for the Southern Ocean has forced the assumption that $\frac{\partial h}{\partial t} = 0$ (*Van de Berg et al.*, 2005). Satellite observations of sea ice in Antarctica have been attempted from both laser (*Zwally et al.*, 2008), and radar (*Giles et al.*, 2008b) altimeters. However, currently both methods are not yet constrained enough to provide reliable estimates of sea ice thickness. To date large-scale estimates of changes in sea ice thickness in the Antarctic must be based on model output alone (*Shepherd et al.*, 2010).

While the response of the Arctic to changes in the climate are by no means solved, there is a disparity in the information available between the two polar regions, which is by no means a reflection of their relative importance. As in the Arctic (*Perovich et al.*, 2003; *Holland et al.*, 2008), there is a great interest in understanding the volume and consequently mass balance changes of the sea ice cover in Antarctic. However, modelling studies of the sea ice mass balance for the Southern Ocean (*Vancappenolle et al.*, 2009) have only the visual ship-based observations of ice thickness available to them, which have no temporal resolution.

There is no doubt that remote sensing is the most suitable tool to assess and grapple with the effects that the changing climate is having on the large-scale thickness and extent of sea ice. To better understand and quantify the role that sea ice plays in the Earth's climate it is necessary to improve on the current satellite techniques of monitoring sea ice and to reduce uncertainties in available measurements.

1.2.1 Satellite Remote Sensing of Sea Ice Thickness

The methodology of satellite remote sensing of sea ice thickness is based on the assumption that Archimedes' principle is applicable to floes that comprise the sea ice cover. When applying

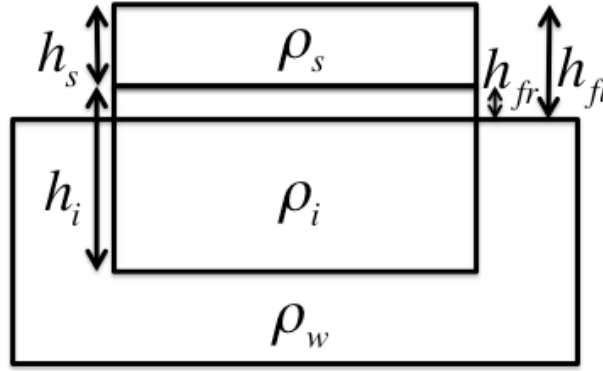


Figure 1.3: Schematic of a floe.

Archimedes' principle to a floe it is assumed that the integrated hydrostatic pressure (of the displaced water) over the submerged area of sea ice exerts a force that is balanced by the integrated force of gravity that pulls on the floe. In such cases the floe is assumed to be in *hydrostatic equilibrium*. Figure 1.3 shows a simple schematic of a floe under hydrostatic equilibrium. While the sea ice may not be hydrostatic equilibrium at scales of meters due to local density variations, on scales of satellite sensors, for areal averages greater than hundreds of meters, this assumption necessarily holds because gravitational forces greatly exceed those of sheer stresses in the ice.

As the radar or laser satellite altimeter illuminates the floe, it records the range between itself and the sea ice. The altimeter measured surface elevation is then used to infer the freeboard of the sea ice, which is then used to estimate the submerged portion. Two important assumptions are made during this inference, that: the densities and surfaces of both the sea ice and snow volumes are constant, on both horizontal and vertical scales within the satellite footprint. At this point the distinction between laser and radar altimetry must be made. In the case of the laser altimeter (e.g. ICESat), the signal will reflect from the top surface whether it is snow or sea ice. Consequently, climatology data, or assumptions of snow loading must be made in ice thickness estimation. While in the case of the radar altimeter (e.g. ENVISAT) it is assumed that the radar signal will penetrate the snow cover (Beaven *et al.*, 1995), and hence measure the freeboard directly. Consequently, the simple algebraic relationship between sea ice thickness and its freeboard is different between the radar and laser altimeter measurements:

$$h_{i,radar} = h_{fr} \frac{\rho_w}{\rho_w - \rho_i} + h_s \frac{\rho_s}{\rho_w - \rho_i}, \quad (1.2)$$

$$h_{i,laser} = h_{fl} \frac{\rho_w}{\rho_w - \rho_i} - h_s \frac{\rho_w - \rho_s}{\rho_w - \rho_i}. \quad (1.3)$$

(The simplicity of these equations is a direct result of the mentioned assumptions of uniform density and surface features of the snow and sea ice. However, as figure 1.3 attempts to illustrate, neither the snow cover, freeboard, nor the underlying sea ice surfaces are smooth (not to mention varying in density). The presence of these features has a particularly greater impact on the radar altimeter return, due to its relatively greater footprint, and vertical range resolution compared with the laser altimeter. The biases that this averaging and these assumptions will introduce into freeboard elevation retrieval is yet to be investigated.)

As previously mentioned, neither radar nor laser measurements of Antarctic sea ice are currently yielding satisfactory estimates of its thickness. Radar altimetry estimates of sea ice elevation are found to underestimate the sea ice thickness when compared with the ship-based climatology (*Giles et al.*, 2008b), and this has led to questioning of the assumption that the radar signal penetrates the snow pack in Antarctica. Further, a recent study of the penetration of radar frequencies into the snow in Antarctica has shown that more often than not, the signal reflects from an internal boundary within the snow pack: *Willat et al.*, [2010]. Whereas laser altimeter data is currently lacking snow thickness estimates of sufficient spatial resolution (*Zwally et al.*, 2008). Both techniques are pointing to lack of knowledge of snow thickness as the primary source of error in attempts to retrieve sea ice thickness.

What is the error made in sea ice thickness if we have no knowledge of snow thickness? Using equations 1.2 and 1.3, the error in ice thickness will be (substituting the average values in table 1.1):

for the radar altimeter,

$$\Delta h_{i,radar} = -h_s \frac{\rho_s}{\rho_w - \rho_i} \quad (1.4)$$

$$\approx -h_s \frac{360}{1023.8 - 900} = -2.9h_s, \quad (1.5)$$

for the laser altimeter,

$$\Delta h_{i,laser} = +h_s \frac{\rho_w - \rho_s}{\rho_w - \rho_i} \quad (1.6)$$

$$\approx +h_s \frac{1023.8 - 360}{1023.8 - 900} = +5.4h_s. \quad (1.7)$$

The above equations, show that a lack of knowledge of snow cover could lead to an error in the total sea ice thickness by approximately three times its snow cover thickness in the case of the radar altimeter, and five times in the case of the laser altimeter. For example (for the laser altimeter) using the long-term mean thickness of sea ice, of 0.87 ± 0.91 m (Worby *et al.*, 2008), and snow depth mean values ranging from $0.02 - 0.49 \pm 0.16$ m (Massom *et al.*, 2001) the error made in sea ice thickness (when assuming that this snow is actually sea ice) is: $(0.1 - 2.5) \pm 0.8$ m, introducing a positive bias into sea ice thickness estimates, and consequently volume trends. Considering that even a thin layer of sea ice may be covered with snow (Massom *et al.*, 2001), to improve satellite estimates of sea ice thickness, it is imperative to have a method for measuring its snow cover.

Giles *et al.* [2007] find that the greatest error made in sea ice thickness estimation from either a radar or laser altimeter is due to snow thickness uncertainty (with the error almost doubling for the case of laser altimeter). Adapting their method for Antarctic sea ice, we estimate the error in thickness incurred due to uncertainty in snow thickness and density values. Assuming that the uncertainties in measurements of the thicknesses and densities are uncorrelated, to a first order, the uncertainty in sea ice thickness (given the uncertainties in these other variables) can be written as:

for radar altimeter retrieval,

$$\begin{aligned} \varepsilon_{h_i}^2 = & \varepsilon_{h_{fr}}^2 \left(\frac{\rho_w}{\rho_w - \rho_i} \right)^2 + \varepsilon_{h_s}^2 \left(\frac{\rho_s}{\rho_w - \rho_i} \right)^2 + \varepsilon_{\rho_s}^2 \left(h_s \frac{1}{\rho_w - \rho_i} \right)^2 \\ & + \varepsilon_{\rho_w}^2 \left(h_{fr} \frac{1}{\rho_w - \rho_i} - h_s \frac{\rho_w}{(\rho_w - \rho_i)^2} - h_s \frac{\rho_s}{(\rho_w - \rho_i)^2} \right)^2 \\ & + \varepsilon_{\rho_i}^2 \left(h_{fr} \frac{\rho_w}{(\rho_w - \rho_i)^2} + h_s \frac{\rho_s}{(\rho_w - \rho_i)^2} \right)^2, \end{aligned} \quad (1.8)$$

for the laser altimeter retrieval,

$$\begin{aligned} \varepsilon_{h_i}^2 = & \varepsilon_{h_{fl}}^2 \left(\frac{\rho_w}{\rho_w - \rho_i} \right)^2 + \varepsilon_{h_s}^2 \left(-\frac{\rho_w - \rho_s}{\rho_w - \rho_i} \right)^2 + \varepsilon_{\rho_s}^2 \left(h_s \frac{1}{\rho_w - \rho_i} \right)^2 \\ & + \varepsilon_{\rho_w}^2 \left(h_{fl} \frac{1}{\rho_w - \rho_i} - h_s \frac{1}{\rho_w - \rho_i} - h_{fl} \frac{\rho_w}{(\rho_w - \rho_i)^2} + h_s \frac{\rho_w - \rho_s}{(\rho_w - \rho_i)^2} \right)^2 \\ & + \varepsilon_{\rho_i}^2 \left(h_{fl} \frac{\rho_w}{(\rho_w - \rho_i)^2} - h_s \frac{\rho_w - \rho_s}{(\rho_w - \rho_i)^2} \right)^2. \end{aligned} \quad (1.9)$$

Substituting estimates of the means and uncertainties of the thicknesses and densities summarised

in table 1.1, the above equations become:

for the radar altimeter retrieval,

$$\begin{aligned}\varepsilon_{h_i}^2 &= \varepsilon_{h_f}^2(68.3) + \varepsilon_{h_s}^2(8.4) + \varepsilon_{p_s}^2(2.9 \times 10^{-6}) + \varepsilon_{\rho_w}^2(3.3 \times 10^{-4}) + \varepsilon_{\rho_i}^2(1.5 \times 10^{-4}) \\ &\approx 0.06 + \mathbf{0.19} + 0.04 + 8.2 \times 10^{-5} + 3.8 \times 10^{-3},\end{aligned}\quad (1.10)$$

for the laser altimeter retrieval,

$$\begin{aligned}\varepsilon_{h_i}^2 &= \varepsilon_{h_f}^2(68.4) + \varepsilon_{h_{ps}}^2(28.7) + \varepsilon_{p_s}^2(2.9 \times 10^{-6}) + \varepsilon_{\rho_w}^2(1.3 \times 10^{-4}) + \varepsilon_{\rho_i}^2(1.5 \times 10^{-4}) \\ &\approx 0.03 + \mathbf{0.65} + 0.04 + 3.2 \times 10^{-5} + 3.8 \times 10^{-3}.\end{aligned}\quad (1.11)$$

From the above calculations it is again clear that in both the radar and laser altimeter retrieval, uncertainty in snow thickness contributes the greatest error to sea ice thickness estimates. The above expressions also show that if we want to detect changes in sea ice thickness of the order of tens of centimeters (using the 67 millimeter trend estimated by *Laxon et al.*, [2003] as an upper bound estimate of the possible secular trend in sea ice thickness in Antarctica) it is clear that methods for both sea ice thickness retrieval and snow thickness must be improved. If we consider that the sole error in sea ice thickness retrieval was snow thickness uncertainty, then using equations 1.8 and 1.9, the error in snow thickness estimation must be less than 35 millimeters.

Parameter	Mean Value [m]	Reference	Error Estimate [m]	Reference
Ice freeboard (h_{fr})	0.11 m	$h_{fi} - h_s$	0.03 m	<i>Giles and Hvidegaard</i> , 2006
Freeboard (h_{fi})	0.32 m	<i>Zwally et al.</i> , 2008	0.02 m	<i>Kwok et al.</i> , 2004
Snow depth (h_s)	0.21 m	<i>Massom et al.</i> , 2001	0.15 m	<i>Massom et al.</i> , 2001 ¹
Ice density (ρ_i)	900 kg m ⁻³	<i>Worby et al.</i> , 2008	5 kg m ⁻³	<i>Wadhams et al.</i> , 1992
Snow density (ρ_s)	360 kg m ⁻³	<i>Massom et al.</i> , 2001	120 kg m ⁻³	<i>Massom et al.</i> , 2001
Water density (ρ_w)	1023.8 kg m ⁻³	<i>Wadhams et al.</i> , 1992	0.5 kg m ⁻³	<i>Wadhams et al.</i> , 1992

Table 1.1: Approximate of values of thicknesses and densities for snow, and sea ice in Antarctica.

1.2.2 Snow Thickness on Sea Ice Remote Sensing

In the Arctic, where the sea ice is usually covered with dry snow, the assumption that the radar signal penetrates the snow cover (*Beaven et al.*, 1995) while not yet proven *in-situ*, has been useful in retrieving sensible ice thickness estimates from radar and laser altimetry data (*Laxon et*

al., 2003; *Kwok and Cunningham*, 2008). In contrast, snow depth on Antarctic sea ice has been particularly difficult to estimate with radar and laser altimeters. The assumption that the radar signal penetrates the snow pack is under question (*Giles et al.*, 2008b; *Willatt et al.*, 2010). It is known from field observations that the snow cover of sea ice is of variable thickness, may be rough, saline, wet and constantly changing (*Massom et al.*, 2001). Such a diverse array of physical properties of snow has a major impact on its dielectric properties to which remote sensing methods are sensitive.

Density, salinity and wetness will determine the dielectric properties of the snow pack and the penetration depth of radar signal. The radar signal will generally reflect from dielectric contrasts (*Feynman*, 1963), and for the Southern Ocean snow this is not necessarily at the snow/ice interface. Studies of the snow pack in Antarctica demonstrate that it is highly heterogeneous, *Massom et al.*, [2001] observing density variability from 240 to 600 kg m⁻³ across a single floe, and frequently subject to flooding. Flooding events of the snow pack could potentially lead to wicking of brine into the snow pack causing radar signal reflection to occur other than at the snow/ice interface. Additionally, the presence of icy layers within the snow pack introduces dielectric contrasts which may complicate the radar return.

Observations of snow cover on sea ice in Antarctica motivate the statement (although speculative): that the dielectric properties of this snow cover are likely to change significantly between locations only several meters apart. Such conditions place high demands on a remote sensing instrument aimed at retrieving snow thickness over sea ice.

Other than model output (*Fichefet and Morales Maqueda*, 1999; *Fichefet et al.*, 2000), climatology based on extensive compilation of ship based observations of sea ice and its snow thickness in Antarctica (*Worby et al.*, 2008a), the only existing large-scale snow depth product comes from the passive AMSR-E instrument on the Aqua satellite (*Comiso et al.*, 2003; *Markus and Cavalieri*, 1998). The AMSR-E snow product is provided on a daily basis over the whole Antarctic region at 25 km grid scales, with a precision for snow estimation of 50 millimeters. However, recent studies have shown it to be inaccurate. *Worby et al.*, [2008b], and *Massom et al.*, [2003] describe results from an extensive set of experiments conducted during a 2003 voyage in Antarctica to validate satellite sea ice data products: ice concentration, surface temperature, and snow thickness cover. It was found that AMSR-E significantly underestimates the snow thickness, and its performance

is dramatically degraded by the roughness of the underlying sea ice (*Powell et al.*, 2005; *Stroeve et al.*, 2006).

The benefits of developing a reliable, repeatable method/instrument for regional studies of snow cover thickness over sea ice in Antarctica are: for satellite snow thickness retrieval validation, sea ice thickness retrieval, and also for understanding further the nature and extent of the heterogeneity of snow thickness. Improving our knowledge of sea ice thickness distribution will allow us to refine models of the polar regions (*Holland and Bitz*, 2003), which will provide us with better predictive tools for looking into the future.

However, the large-scale coverage of satellites is difficult to validate satisfactorily with *in-situ* data (*Worby et al.*, *in prep.*), considering that it is not only challenging to achieve coincident measurements with satellite overpasses, but that the methodology of combining the large averages of a highly heterogeneous snow cover with that of a single *in-situ* measurement is unknown. To address this, research has been directed to developing sled and air-borne remote sensing techniques, these are easier to validate with *in-situ* data, and are themselves better suited to regional scale coverage that in turn can be used to validate and/or assist satellite retrievals.

Giles et al., [2007], present the first quantitative analysis of airborne data combining laser and radar altimeters to retrieve snow depth over sea ice. The data was gathered on an opportunistic flight over the Fram Strait in the Arctic, during the LaRA (Laser Radar Altimetry) campaign of 2002. Although the snow depth estimated from the difference in range measured by the laser and radar altimeters compares well with the expected climatology, validation of this method with *in-situ* data is absent (it was not possible).

Leuschen et al., [2008], present results of the same laser/radar altimeter instruments of flights over the Bellingshausen Sea, Antarctica during the 2004 Antarctic AMSR-E Sea Ice field campaign. The paper presents results that show reasonable estimates of snow thickness, however, it is still not clear that the radar reflections came from the snow/ice interfaces. This experiment too, was not able to collect *in-situ* data for direct comparison and validation of the airborne measurements.

A single radar system that potentially is able to simultaneously provide the range to the air/snow and snow/ice interfaces is one based on the Frequency Modulated Continuous Wave (FMCW)

radar principle. Such radars have been extensively and successfully used for snow depth studies (*Marshall and Koh, 2008*). The ability of the FMCW technique to obtain an air/snow and snow/ice interface return from a single waveform eliminates the need for cross-calibration with a laser altimeter, and is robust to aircraft altitude changes, as both air/snow and snow/ice interface returns will undergo the same range shifts.

Until now, FMCW radar operation has been conclusively demonstrated to work from a sled-based platform (*Koh et al., 1996; Kanagaratnam et al., 2007; Holmgren et al., 1998*), and airborne experiments have been performed over ice sheets and in mountain regions (*Rink et al., 2006; Marshall et al., 2008a; Willyard, 2006*). However, only a few such instruments have been employed for snow depth research in Antarctica.

A 2 - 8 GHz FMCW radar for snow thickness study of Antarctic sea ice was first proposed by *Gogineni et al., [2003]*. The precision of such an instrument for snow thickness retrieval is estimated to be 25 millimeters. A series of experiments measuring snow thickness using this radar from a sled platform were made in 2003 during the Australian-led ARISE cruise (*Massom et al., 2003*). Preliminary results demonstrating the capacity of this radar to extract snow thickness with a high degree of accuracy: *Kanagaratnam et al., [2007]*. The understanding that the necessary regional coverage for satellite calibration and validation cannot be provided by a sled-based radar, motivates this work to discuss the steps necessary to achieve airborne operation.

In parallel to the development of a snow thickness radar at the Center for Remote Sensing of Ice Sheets (CReSIS), Kansas University, the European Space Agency designed and built ASIRAS (Airborne SAR/Interferometric Altimeter System, *Lentz et al., 2002*) for the purpose of validating the CryoSat satellite (*Wingham et al., 2006*). In principle, the ASIRAS radar altimeter should provide insight into the snow thickness retrieval over sea ice (*Makynen and Hallikainen, 2009*). However, as the CryoSat mission does not include measurement of Antarctic sea ice thickness as one of its primary mission goals, ASIRAS was not flown in Antarctica until 2008-2009 (*Helm et al., 2009*). Further flights of ASIRAS are however planned to include sea ice in the Antarctic region, and these data will no doubt advance research in this area.

In 2006, an airborne version of the 2 - 8 GHz FMCW radar was flown during the NASA Arctic 2006 AMSR-E validation Campaign (*Cavalieri and Markus, 2001*). The flights were made

coincident with projected AMSR-E passes. Unfortunately, there was difficulty encountered collecting data, technical difficulties with the radar prevented successful identification of the air/snow and snow/ice interfaces. System adjustments eventually improved the radar resolving capacity (Willyard, 2006; Wade, 2008), however transect results from the experiment are not yet publicly available.

Based on the experience and lessons learned from the above-mentioned experiments, this thesis outlines the collaborative work undertaken by CReSIS and University of Tasmania to adapt a 2 - 8 GHz FMCW radar for helicopter-borne operation. The Australian icebreaker - *RSV Aurora Australis* is capable of carrying up to three helicopters and is already frequently used by the Australian Antarctic Division (AAD) during science and resupply voyages into East Antarctica. This ease of access motivated the development of a helicopter-borne radar for snow thickness estimation in the pack ice zone.

1.3 Outline

The objective of this thesis has been to take an existing FMCW radar system, mount it to a helicopter, and use *in-situ* data to validate its performance for estimating of snow cover thickness over Antarctic sea ice. The field work was conducted during the Sea Ice Physics and Ecosystem eXperiment of 2007, (SIPEX'07) voyage and at the Australian Antarctic Davis Station in 2008. The FMCW radar was loaned to the Australian Antarctic Division (AAD) by the Centre for Remote Sensing of Ice Sheets (CReSIS), Kansas University. It had been previously been reported to successfully retrieve snow thickness from a sled-based platform (Kanagaratnam *et al.*, 2007).

This work involved the integration of a wide range of disciplines, and operated at the interface between engineering and science. It involved the theoretical study of interactions of the snow and sea ice media with electromagnetic radiation, design and development of a radar system, adaptation of the radar instrument to airborne operation and its construction and installation in a helicopter. The thesis work also included: the design of a suite of experiments (airborne, sled-based, and *in-situ* methods for validation studies), the operation of the radar during flight trials, processing of the data, the development of new signal processing algorithms for data extraction from the radar signal, and finally the interpretation of the snow thickness derived from the data.

This thesis is composed of five chapters where most of the theoretical and experimental work is presented, and an equal number of appendices, which comprise the laboratory work conducted in

the construction and experimentation of the radar. In the description of the thesis chapters and appendices to follow the reader is asked to alternately refer to chapters and appendices.

1.3.1 Chapter Summary

Chapter 2 of this thesis begins with a brief overview of the principle behind FMCW radar operation, and what separates it from the more common pulse radar. The basic design of the radar provided is largely due to experience of the CReSIS group (who have long been recognised as the experts in the field of polar remote sensing). Subsequently, translation of the design parameters into the expected operational performance characteristics (in order to contextualise the limitations of the radar) motivate the review made in the third chapter.

It was necessary to alter the design of the radar in various areas, to adapt it (in hardware and software) to the stringent performance requirements of helicopter-borne snow thickness estimation. The evolution of the radar design, the laboratory work performed to determine its operational capacity, description of the operating software written, and evolution of the data structures conducted at the AAD are described in *Appendix A*.

Provided with the radar performance summary, *Chapter 3* presents the necessary conditions for unambiguous detection the air/snow and snow/ice interfaces. Additionally it contains a summary of the physical characteristics of sea ice and its snow cover, and how they map to dielectric constants. The main issues regarding the use of radar systems for measuring snow thickness are explored, in particular: how are EM waves scattered from snow and ice interfaces? and what can be determined about the air, snow, and ice from the radar observations?

The first field trials of the radar were performed during the Sea Ice Physics and Ecosystem eXperiment of 2007 (SIPEX'07). However, during this voyage the radar was found to be affected by helicopter vibrations. *Appendix B* provides a summary of the flights, problems encountered and the steps taken to remedy the problems. In order to reconfirm the operational ability of the radar (as it had now been modified) a sled mount was constructed at the AAD and experiments of the radar from a sled-based platform performed during the second field trials of the radar on a voyage in 2008 (V1'08). These experiments are described in *Chapter 4*, and the radar is found to operate correctly and detect the snow thickness with reasonable accuracy.

It was identified that the vibrations of the helicopter that were corrupting the radar data during the SIPEX'07 voyage were mainly affecting the hard-disk drives of the radar, preventing data from actually being recorded. In order to address this problem collaboration was established with the Australian Centre for Field Robotics (ACFR) who provided the design of anti-vibration mounts for the hard-disk drives (HDD). The experimental trial of these mounts and subsequent improvement in data collection of the radar is described in *Appendix C*.

The solution to the vibration problem allowed sufficient radar data to be collected for validation purposes. However, a new problem was encountered: the data collected from helicopter-borne experiments during V1'08 was found to be corrupted by inherent systematic signal error in the radar itself. This compromised the possibility of extracting snow thickness information. *Chapter 5* presents a description of the nature of the error and the derivation and results of a non-linearity correction algorithm that was designed to overcome this problem. Application of this algorithm to the radar data demonstrated that the radar was receiving air/snow and snow/ice returns, making interface extraction a tractable problem.

In order to characterise the radar system used during the helicopter experiments it was necessary to understand the performance of the antennas used during the flights. As the antennas were designed in-house at CReSIS, only the theoretical performance characteristics were initially known. In 2009, tests of the antennas in the anechoic chamber at the NASA/Goddard Space Flight Centre were conducted. *Appendix D* describes the experimental performance of the antennas. The results of the antenna tests motivated and provided the explanation for the large loss in signal in the radar at increasing frequency, and a brief study of this effect was made and is described in *Appendix E*.

Chapter 6 summarises the problems from the helicopter-borne experiments during the SIPEX'07 voyage, and the solutions developed before the V1'08 voyage. Successful application of the algorithm developed in chapter five is applied to the radar data collected in V1'08. Finally, a description of the validation method with coincident *in-situ* data collected for the areas flown by the helicopter is presented.

Chapter 7 summarises the conclusions of this work, provides recommendations for future work, as well as summarising the current status of research efforts in progress.

Chapter

2

Introduction to Radar Principles and Summary of Operating Parameters

One goal of radar systems as the acronym on which the term is based implies is: RAdio Detection And Ranging (*Kingsley and Quegan, 1999*). In its simplest form it is a system that uses electromagnetic (EM) radiation to detect the presence of an object and then determine the range to the detected object.

There are multiple means by which radars do this. For instance, pulse radar systems use the time interval between the transmission and reception of an emitted pulse, while Frequency Modulated Continuous Wave (FMCW) systems convert the time delay between transmission and reception into a frequency that carries both detection and ranging information.

FMCW radars have long been used for the purpose of snow thickness estimation (*Marshall and Koh, 2008*). In 2003, a 2 - 8 GHz FMCW radar was first proposed for the study of snow on Antarctic sea ice by *Gogineni et al., 2003*. In 2003 such a radar was demonstrated to estimate snow thickness in Antarctica from a sled-based platform, *Kanagaratnam et al., 2007*. Following this experiment, in 2006 an airborne version was flown as part of the NASA Arctic 2006 AMSR-E validation Campaign (*Cavalieri and Markus, 2001*), however due to technical problems with the radar the experiment was not successfully completed. A new version of the radar was build in 2007, and CReSIS supplied this radar to the author for helicopter borne operation.

The principal idea of FMCW is based on the known fact that the product of two harmonics is equivalent to the sum of two sinusoids whose frequencies are the difference and sum of two the harmonics' frequencies:

$$\cos(2\pi f_1 t) \cos(2\pi f_2 t) = \frac{1}{2} (\cos(2\pi t(f_1 - f_2)) + \cos(2\pi t(f_1 + f_2))) . \quad (2.1)$$

Figure 2.1 illustrates the main components of FMCW radar. A chirp signal is generated and transmitted from the antenna and its reflection is subsequently received. The transmitted chirp

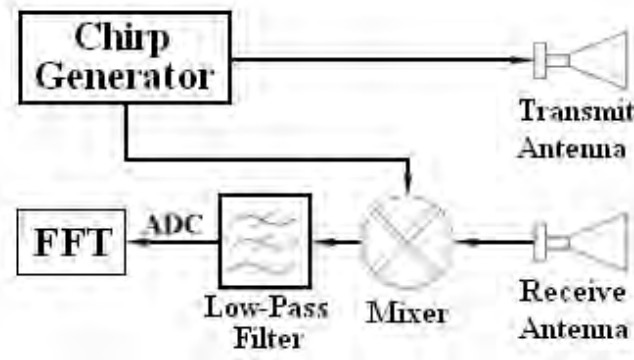


Figure 2.1: Principal components of a FMCW radar.

and reflected signal are mixed to provide the difference and sum components. The low pass filter extracts only the difference component, which is then passed on to a Fast Fourier Transform (FFT) block. The FFT acts as a bank of correlators that detect the frequency value.

The function of the radar specific to the purposes of this work is to detect the presence, and thickness of the snow cover on sea ice using the FMCW method.

RAASTI (RAdar for Antarctic Snow Thickness Investigation) was loaned by the Centre for Remote Sensing of Ice Sheets (CReSIS) to the Australian Antarctic Division (AAD) during 2007 and 2008 for fitting and operation from a helicopter. Therefore, there is no justification made here for the radar design parameters as they are based on the expertise and experience of the CReSIS group. However, the performance parameters unique to RAASTI are derived. This is done by applying established radar operation principles and equations, such as those of *Skolnik*, [1970], *Kingsley and Quegan*, [1999], and *Brooker*, [2005]. The derivation of these performance parameters is done in order to contextualise the operation and limits of RAASTI.

In other words, RAASTI's performance characteristics are calculated *given* its design parameters.

This chapter presents a brief overview of the application of the FMCW principle for radar operation and the use of the components shown in Figure 2.1. Additionally, the radar range equation, and signal-to-noise ratio (SNR) at the output of the FFT are derived. Finally, the chapter concludes with an estimate of the minimum detectable signal level, and this estimate is in turn used to approximate the minimum backscattering coefficient to which RAASTI is sensitive.

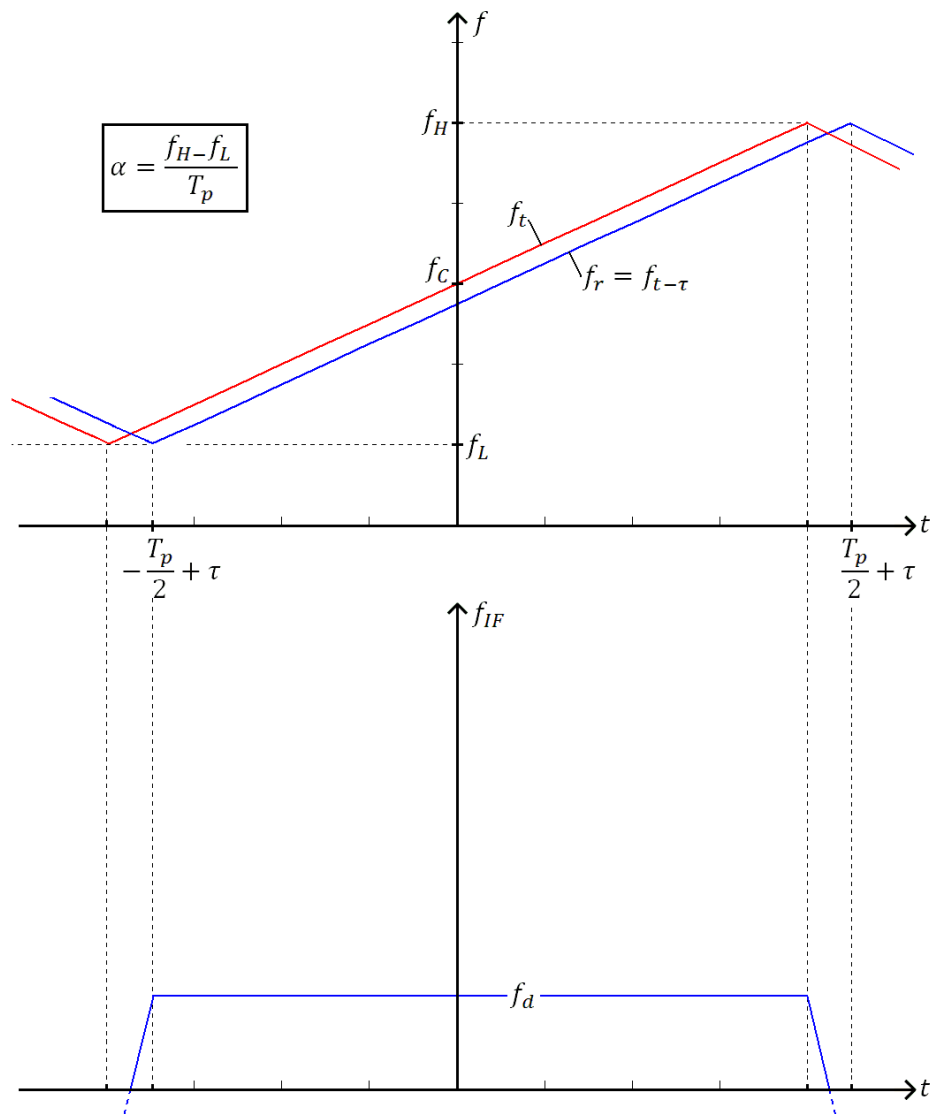


Figure 2.2: The top coordinate axes illustrate the transmit frequency of the FMCW radar up-chirp as a function of time, and the subsequently received frequency delayed by τ seconds. The bottom coordinate axes illustrate the resulting frequency after mixing of the transmitted and received frequencies, where f_d is proportional to the time delay between transmission and reception, τ .

2.1 Overview of FMCW Radar

Though the frequency modulation applied to the transmitted signal can be of any nature, in this radar a linear modulation in frequency (commonly referred to as a “linear chirp”), from f_L to f_H is applied (Skolnik, 1970; Stove, 1992). Referring to figure 2.2, the instantaneous transmitted frequency is:

$$f_t(t) = f_c + \alpha t \text{ [Hz]}, -T_p/2 \leq t \leq T_p/2, \quad (2.2)$$

where f_c is the centre frequency [Hz], and α is the chirp gradient [Hz/s] which is equal to the ratio of the total frequency excursion, divided by the chirp duration:

$$\alpha = \frac{f_H - f_L}{T_p} \text{ [Hz/s]}. \quad (2.3)$$

Assuming constant (and normalised) amplitude, the transmitted signal is characterised by a linear frequency modulated voltage at the output of the oscillator, which can be expressed as:

$$s_t(t) = \mathcal{R}e \left\{ \exp \left(j2\pi \left(f_c t + \frac{1}{2} \alpha t^2 \right) \right) \right\} \text{ [V]}, \text{ valid for } -T_p/2 \leq t \leq T_p/2. \quad (2.4)$$

As this chirp is being generated and transmitted, it is also being reflected from an object within the antenna beam and simultaneously received by the radar. Essentially, the signal received is a replica of the transmitted signal, but delayed in time:

$$s_r(t) = \mathcal{R}e \left\{ \exp \left(j2\pi \left(f_c(t - \tau) + \frac{1}{2} \alpha (t - \tau)^2 \right) \right) \right\} \text{ [V]}, \quad (2.5)$$

valid for $-T_p/2 + \tau \leq t \leq T_p/2 + \tau$,

where τ [s] is the round trip time delay for a signal travelling from the radar to the target and back. In order to extract the frequency component, which is proportional to target range, the signal received is multiplied by the signal transmitted:

$$s_{mix}(t) = s_t(t) \times s_r(t) \text{ [V]}. \quad (2.6)$$

This calculation determines the intermediate frequency (IF, which is comprised of the difference and sum components, as conceptually demonstrated by equation 2.1.

A low-pass filter removes the sum component. The low-pass filter is also used to limit the

maximum range from which the radar can receive a signal, serving as an anti-aliasing filter before the Analog to Digital Converter (ADC). This is discussed in detail in section 2.3.4.

The IF after mixing and low-pass filtering is:

$$s_{IF}(t) = \mathcal{R}e \left\{ \exp \left(j2\pi \left(f_c\tau + \alpha t\tau - \frac{1}{2}\alpha\tau^2 \right) \right) \right\} \text{ [V]}, \quad (2.7)$$

valid for $-T_p/2 + \tau \leq t \leq T_p/2$,

where the phase component $2\pi\alpha t\tau$, contains the difference frequency that is proportional to the target's range. The value of this difference frequency is extracted by the FFT operation. Since the remaining two phase terms: $f_c\tau$ and $-\frac{1}{2}\alpha\tau^2$ in the above equation are not time dependent, they present a constant phase offset in the signal, and can be ignored. Differentiating the time dependent phase term to find the frequency:

$$\begin{aligned} \omega_d &\equiv 2\pi\alpha t\tau, \\ f_d &\equiv \frac{1}{2\pi} \frac{d}{dt} (2\pi\alpha t\tau), \\ f_d &= \alpha\tau \text{ [Hz]}. \end{aligned} \quad (2.8)$$

Thus, for a given slope α , the further the object is from the radar the greater the difference frequency between the transmitted and received signals.

As distinct to methods used in pulse radar, in which the *time* between the pulse transmitted and the pulse received is proportional to the target's range, in FMCW radar it is the difference frequency that is proportional to the range. This is demonstrated by the following relationship:

$$R = \frac{c}{2} \cdot \frac{f_d}{\alpha} \text{ [m]}, \quad (2.9)$$

derived from equation 2.8 where τ was substituted by:

$$\tau = \frac{2R}{c}, \quad (2.10)$$

where R is the range of the target [m], and c is the speed of light *in vacuo* ($\approx 3 \times 10^8 \text{ ms}^{-1}$).

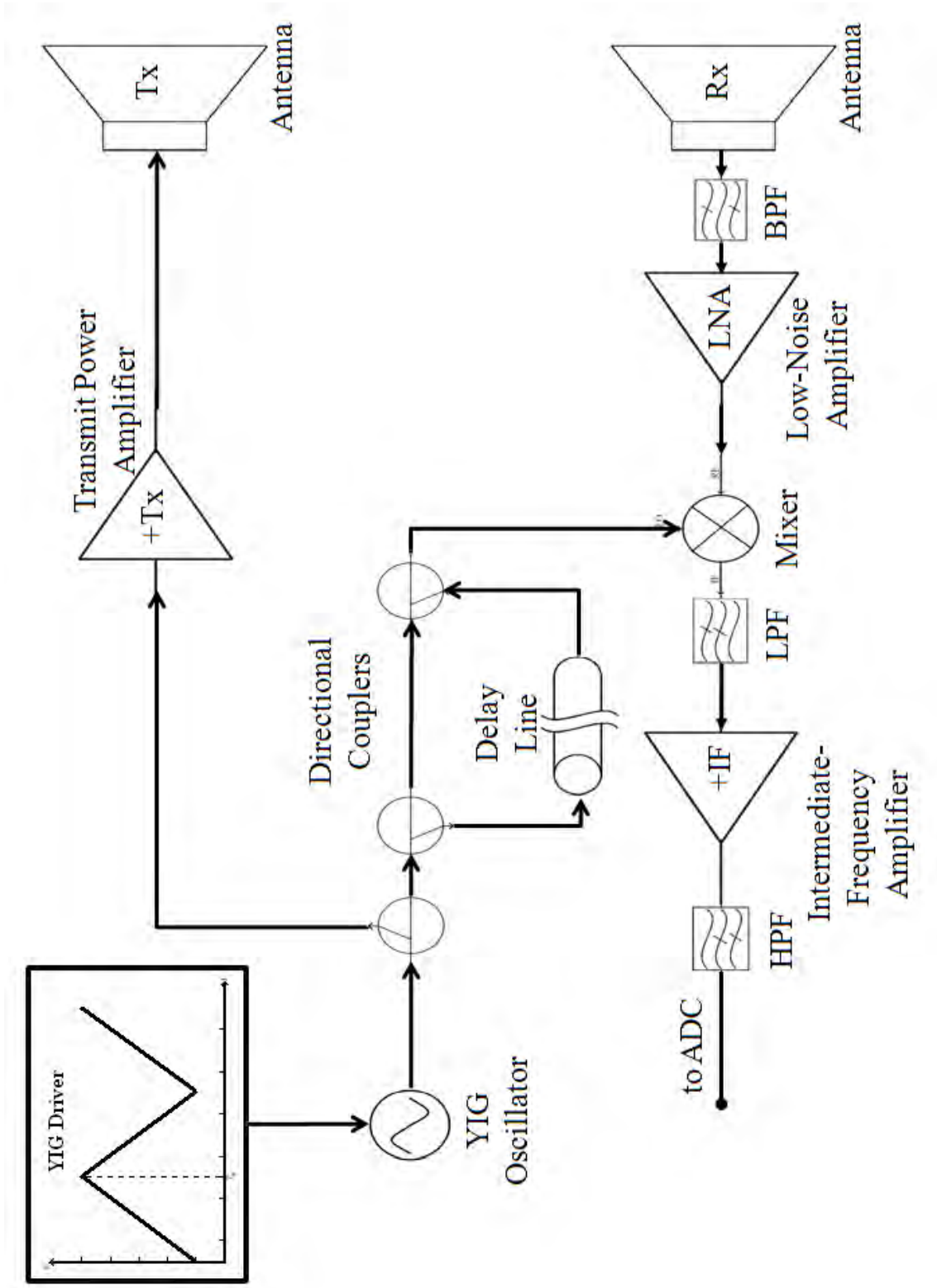


Figure 2.3: High-level FMCW component block diagram.

2.2 Operating Design Parameters

Table 2.1 provides a summary of the design parameters of the FMCW radar received from CReSIS. In order to adapt to the requirements of helicopter operation and to improve range resolution RAASTI underwent both hardware and software modifications. Appendix A provides a technical description of the development of the radar undertaken by the author (with assistance from the AAD Science Technical Support (STS) staff).

The final operational design of RAASTI's RF (Radio Frequency) section is provided by the block diagram in figure 2.3. The main components of the FMCW radar previously presented can be identified, with the main differences being the inclusion here of a delay line (providing a reference target, to be explained in chapter 5), and the FFT operation being performed by a digital block not shown here.

Description	Symbol	Value	Unit
Operating Frequency	Δf	2 - 8	GHz
Median Frequency	f_c	5	GHz
Sweep Time	T_p	1.25	ms
Frequency Sweep Rate	α	4800	GHz/s
Sweep Type		Triangular	Continuous
Chirp Repeat Frequency	CRF	400	Hz
Transmit Power	P_t	30	dBm
Antenna 3dB Beamwidth			
- along track	θ	> 80	degrees
- across track	ψ	8	degrees
Antenna Gain	$G_{rx}; G_{tx}$	10	dBi
Low Pass Filter	f_{LFP}	5	MHz
High Pass Filter	f_{HFP}	1	MHz
Sampling Frequency	f_s	12.5	MHz
ADC		12	bits
Operating Speed (Helicopter)			
- min	v_{min}	20	m/s
- max	v_{max}	35	m/s

Table 2.1: Radar design parameters.

2.3 Performance Parameters

Parameters describing RAASTI's expected performance summarised in table 2.2. A brief explanation of how these values are derived, using standard radar principles, is provided in the subsections 2.3.1 - 2.3.9.

Description	Symbol	Value	Unit	Section
Frequency Resolution	δf	800	Hz	2.3.1
Range Resolution	δR	25	mm	2.3.2
Unambiguous Range	R_u	750	km	2.3.3
Operating Range				2.3.4
- minimum	R_{min}	31.25	m	
- maximum	R_{max}	156.25	m	
Active Area				2.3.6
- min range	A_{min}	4.9	m^2	
- max range	A_{max}	24.5	m^2	
Minimum Detectable Signal	MDS	-138	dBm	2.3.8
Backscattering Coefficient				2.4.2
- min range	$\sigma_{R_{min}}^0$	-107	dB	
- max range	$\sigma_{R_{max}}^0$	-87	dB	

Table 2.2: The expected radar performance parameters.

2.3.1 Frequency Resolution: δf

The difference frequency resulting from a target reflecting the incident signal is found by equation 2.8. Under ideal conditions this frequency is a truncated sinusoidal tone, which exists over the time interval: $-T_p/2 + \tau \leq t \leq T_p/2$. Usually τ is $\ll T_p$, and hence the truncated tone can be assumed to exist for $\approx T_p$. The finite duration of the tone necessarily applies a limit to the accuracy with which its frequency can be calculated. Likewise implicit in the process (prior to frequency analysis) is a time-domain convolution performed with a rectangular window, which causes the spectrum to become a sinc function¹. As such, the best possible frequency resolution using the 3 dB half-power points of the sinc function, is (*Kingsley and Quegan, 1999*):

$$\begin{aligned}
 \delta f &\equiv 1/T_p, \\
 &= 1 / (1.25 \times 10^{-3}[\text{s}]) , \\
 &= 800[\text{Hz}].
 \end{aligned} \tag{2.11}$$

2.3.2 Range Resolution: δR

In FMCW radar, the chirp slope/gradient (i.e. α) facilitates a mapping between the frequency and distance/spatial domains. Range resolution is defined as the minimum distance between two

¹Defined: $\text{sinc}(x) \equiv \frac{\sin(x)}{x}$

objects necessary to clearly distinguish one from the other. This distance can be derived from equation 2.9, and using the frequency resolution calculated in the previous section, is found to be equal to:

$$\begin{aligned}
 \delta R &= \frac{1}{2} \frac{c}{\alpha} \delta f, \\
 &= \frac{1}{2} \times \frac{3 \times 10^8 [\text{ms}^{-1}]}{4800 \times 10^9 [\text{Hz s}^{-1}]} \times 800 [\text{Hz}], \\
 &= 0.025 [\text{m}].
 \end{aligned} \tag{2.12}$$

Equivalently, the range resolution can be derived as a function of the chirp bandwidth (determined by the total frequency excursion of the chirp) (*Brooker, 2005*):

$$\begin{aligned}
 \delta R &= \frac{c}{2\Delta f}, \\
 &= \frac{c}{2(f_H - f_L)}, \\
 &= \frac{3 \times 10^8 [\text{ms}^{-1}]}{2 \times 6 \times 10^9 [\text{Hz}]}, \\
 &= 0.025 [\text{m}].
 \end{aligned} \tag{2.13}$$

2.3.3 Unambiguous Range

The unambiguous range of a FMCW radar is usually far beyond the sensitivity of the radar itself; it is included here for purposes of completeness. Unambiguous range is defined as the range from which a return will be an integer multiple of a chirp away (see figure 2.4), and is given by:

$$\begin{aligned}
 R_{unamb} &\leq c \cdot (2 \cdot T_p), \\
 &= 3 \times 10^8 [\text{ms}^{-1}] \times 2 \times 1.25 \times 10^{-3} [\text{s}], \\
 &= 750 [\text{km}].
 \end{aligned} \tag{2.14}$$

2.3.4 Operating Range

In practice, the range to which the radar is sensitive is determined by the instrument design and usually controlled by the *high-pass* (HPF) and *low-pass* (LPF) *filters* applied to the IF signal.

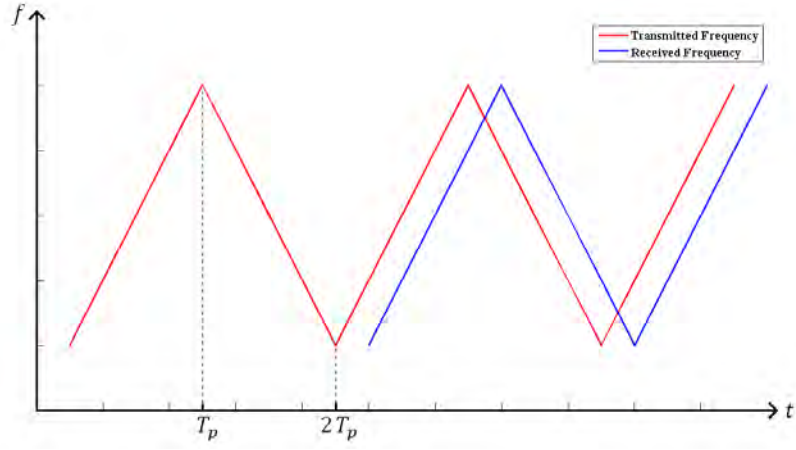


Figure 2.4: An illustration of a situation where ambiguities in radar return could occur: the target is further than $\tau > 2T_p$ away, and hence beyond the unambiguous range of the radar.

These two filters determine the possible values of difference frequencies passed on to the FFT from the mixer output. By limiting the possible values of difference frequencies passed to the FFT, the two filters effectively determine the minimum (R_{min}) and maximum (R_{max}) range that the radar can detect.

The minimum operating range (R_{min}), as determined by the used in RAASTI, which has a 3dB cut-off point at 1 MHz is:

$$\begin{aligned}
 R_{min} &= f_{LPF} \cdot \frac{1}{\alpha} \cdot \frac{c}{2}, \\
 &= 1 \times 10^6 [\text{Hz}] \times \left(\frac{1}{4.8 \times 10^{12} [\text{Hz s}^{-1}]} \right) \frac{3 \times 10^8 [\text{ms}^{-1}]}{2}, \\
 &= 31.25 [\text{m}].
 \end{aligned} \tag{2.15}$$

The maximum operating range (R_{max}), as determined by RAASTI's HPF, which has a 3dB cut-off point at 5 MHz is:

$$\begin{aligned}
 R_{max} &= f_{HPF} \cdot \frac{1}{\alpha} \cdot \frac{c}{2}, \\
 &= 5 \times 10^6 [\text{Hz}] \times \left(\frac{1}{4.8 \times 10^{12} [\text{Hz s}^{-1}]} \right) \frac{3 \times 10^8 [\text{ms}^{-1}]}{2}, \\
 &= 156.25 [\text{m}].
 \end{aligned} \tag{2.16}$$

2.3.5 Antenna Gain and 3 dB Beamwidth

Appendix D provides a summary of the tests performed to characterise the performance of the 8-element array of horns designed at CReSIS that were used during helicopter-borne operation of RAASTI. The results of the tests provided a better understanding of RAASTI's performance limitations. The test results are summarised in table 2.3.

The tests demonstrated that the functional bandwidth of the antennas is 4 GHz, instead of the expected 6 GHz. This resulted in a degradation of the range resolution capability of the radar. Additionally, the large beamwidth of the antennas may lead to difficulties in clearly identifying the air/snow and snow/ice interfaces.

	Theoretical	Measured
Bandwidth	6 GHz (2 - 8 GHz)	4 GHz (2 - 6 GHz)
Gain	10 dBi	10 dBi
Beamwidth (3dB)		(<i>maximum</i>)
- along track (θ)	80 degrees	> 80 degrees
- across track (ψ)	8 degrees	8 degrees

Table 2.3: Antenna parameters.

2.3.6 Active Area

Active area is defined as the ground area illuminated by the radar from which signals are integrated into a single range bin². This area can also be considered as the area of ambiguity, indicating that all sources of variability within this area are integrated into a single value.

Using the antenna 3dB beamwidth in the along and across-track directions from section 2.3.5, the area that the transmitted chirp spreads over as it travels to the distributed target is equal to an ellipse whose origin is at the nadir point, and has radii of:

$$r_{3dB-alongtrack} = R \tan \frac{\theta}{2}, \quad (2.17)$$

$$r_{3dB-acrosstrack} = R \tan \frac{\psi}{2}. \quad (2.18)$$

As the chirp travels its wavefront does not cover this area simultaneously. Within this beamwidth the nadir point is reached first. The extremities of this area are illuminated by the transmitted chirp

²This can be thought of as a single pixel in the image seen by the radar.

wavefront only some time later. Using the fact that the range can be measured with only range resolution accuracy, this effectively segments the beamwidth illuminated area into discrete *range cells*, see figure 2.5. Hence, the area of the first range cell is given by the area of the central ellipse (which in this case reduces to a circle):

$$A_1 = \pi \cdot x_1^2 \text{ [m}^2\text{]},$$

where:

$$x_1 = y_1 = \sqrt{(R + \delta R)^2 - R^2} \text{ [m]}, \quad (2.19)$$

For the minimum and maximum operating range of the radar this area is found to be equal to:

$$A_1(R_{min}) = 4.91, \text{ [m}^2\text{]}, \quad (2.20)$$

$$A_1(R_{max}) = 24.55. \text{ [m}^2\text{]}. \quad (2.21)$$

Subsequent range-cell areas are given by the areas of the surrounding annuli:

$$A_n = \pi (x_n \cdot y_n - x_{n-1} \cdot y_{n-1}) \text{ [m}^2\text{]},$$

where for the along-track direction the range-cell dimension, x_n [m], is given by:

$$x_n = \sqrt{(R + n\delta R)^2 - R^2} \text{ [m]}, \quad (2.22)$$

and due to the narrower beamwidth in the across-track direction the range-cell dimension, y_n [m], is given by:

$$y_n = \min \begin{cases} \sqrt{(R + n\delta R)^2 - R^2} \text{ [m]} \\ R \tan \frac{\psi}{2} \text{ [m]} \end{cases} \quad (2.23)$$

The above equations (2.22 and 2.23) demonstrate that with increasing range the active area increases, and this plays an important role in determining the average physical and statistical properties affecting the nature of reflection.

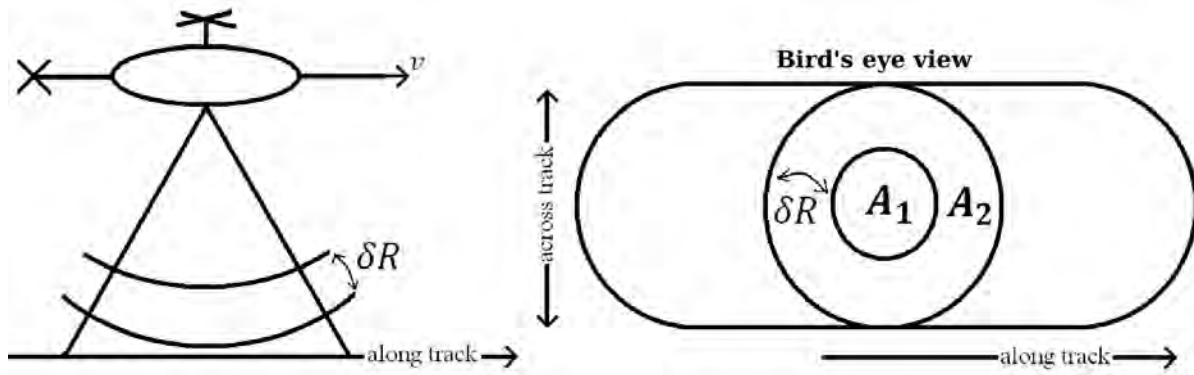


Figure 2.5: The active area (range cell limited) within the radar beamwidth limited footprint shown from two perspectives: side on as the helicopter flies over the surface, and when looking down onto the surface.

2.3.7 Thermal Noise Power Density: N_T

The thermal noise power quantifies the power of white noise present in all components due to an above-zero Kelvin temperature, and is given by (Brooker, 2009):

$$\begin{aligned}
 N_T &= 10 \log_{10} (k \cdot T) \text{ [W/Hz]}, \\
 &= -229 + 25, \\
 &= -204[\text{dBW/Hz}], \\
 &= -174[\text{dBm/Hz}],
 \end{aligned}
 \tag{2.24}$$

where k is Boltzmann's constant ($1.3806503 \times 10^{-23} \text{ m}^2 \text{ kgs}^{-2} \text{ K}^{-1}$); T is the operating temperature in Kelvin [K].

2.3.8 Minimum Detectable Signal: MDS

The MDS which the radar is capable of receiving is limited by the noise level present at the radar's receiver. A radar's MDS is determined by the thermal noise power within a single range bin (frequency resolution) of the receiver (Brooker, 2009), and is given by:

$$N_{rx} = N_T \cdot \beta_{FFT} \text{ [W]}, \tag{2.25}$$

where N_T is the thermal noise density, and β_{FFT} is the receiver range bin. The range bin width of RAASTI's receiver is 800 Hz. Frequently to decrease the side-lobe level, a window (such as

the Hamming) is applied to the signal prior to frequency detection. RAASTI's receiver range bin is widened in this way by the application of a Hamming window, having a widening factor of 1.3 (Harris, 1978). As such, N_{rx} is found to be equal to:

$$\begin{aligned} N_{rx} &= -174 + 30, \\ MDS &\equiv -144 \text{ [dBm]}. \end{aligned} \tag{2.26}$$

Required Signal Level: $MDS = S_{det}$

It is instructive to calculate an approximate value for the minimum required signal level for a given false-alarm rate (P_{fa}), and detection probability (P_d), (Brooker, 2009). Assuming relaxed requirements: detection probability of 0.5 and false-alarm rate of 10^{-2} , figure 2.6 shows that the signal level must be at least 6.0 dB above the noise floor. This requirement increases the MDS calculated in equation 2.26. Consequently for successful detection, the signal level must be at least:

$$\begin{aligned} S_{det} &= N_{rx} + 6.0, \\ &= -138 \text{ [dBm]}. \end{aligned} \tag{2.27}$$

2.3.9 Sampling Frequency: f_s

Section 2.3.4 noted that a radar's maximum operating range is determined by its LPF. This essentially sets the maximum possible difference frequency, and by the sampling theorem twice this frequency is the minimum sampling rate for the ADC:

$$f_s > 2 \cdot f_{IF(LPF)}. \tag{2.28}$$

However for future design, it should be noted here that only the *difference* in returns between the air/snow and snow/ice interfaces are of interest for snow *thickness* calculations. Over sea ice in Antarctica, this can safely be assumed to never exceed 5 m. This assumption give a *relative* difference frequency of 160 kHz. Hence, an IF signal with a 5 MHz bandwidth leads to a large

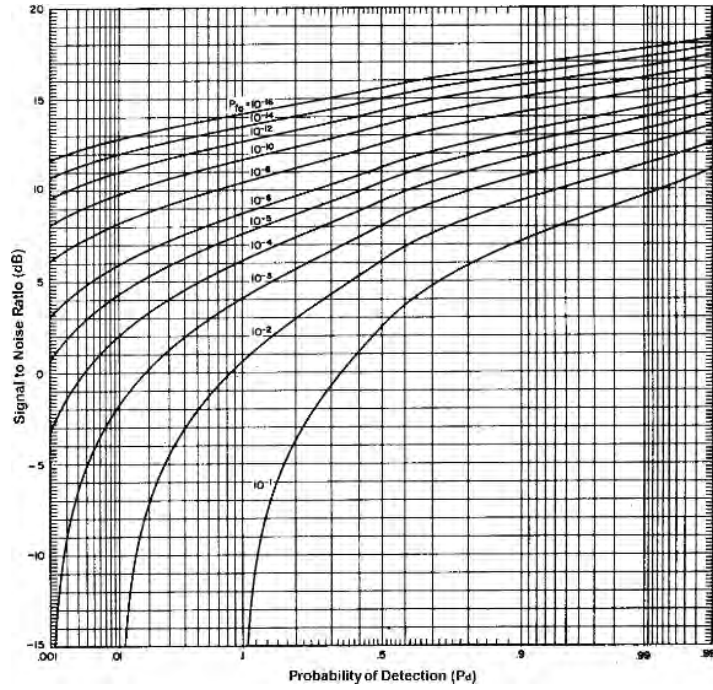


Figure 2.6: The detection probability for a sinusoidal signal in white noise (Blake, 1986), adapted from Brooker [2009].

amount of redundancy in terms of the overall range examined. Exploitation of this oversampling factor can be used to decrease the noise floor in the received signal, as well as the data storage requirements.

2.4 FMCW Distributed Target Radar Range Equation

The radar range equation expresses the value of power received as a function of radar operating and performance parameters. A summary of its derivation applicable to RAASTI, assuming a distributed target is presented here³. The transmitted chirp, in volts can be written as:

$$s_t(t) = V_t \cos(2\pi f_c t + \pi \alpha t^2) \text{ [V]}, \quad (2.29)$$

valid over the chirp duration period $(-T_p/2 < t < T_p/2)$, where V_t is the voltage gain of the radar system, whose variation with time is shown in figure 2.7.

The instantaneous power at the transmit antenna port during generation a single chirp (T_p) is equal

³For a more general description refer to Skolnik [1970], or Ulaby *et al.* [1986a].

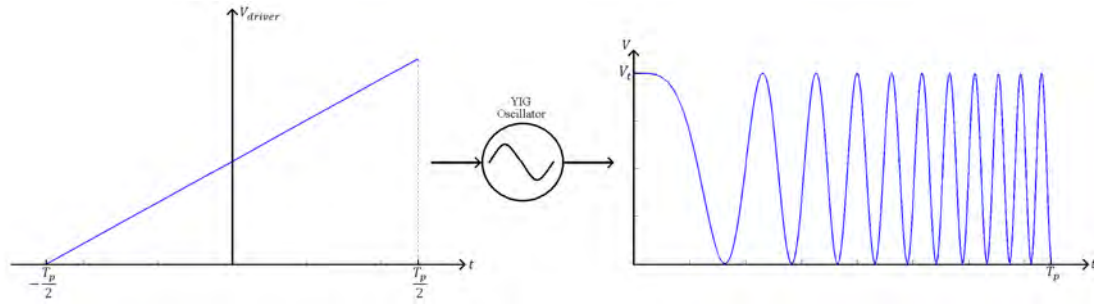


Figure 2.7: Block diagram of the sweep voltage driving the oscillator to output a chirp. The voltage gain of the system leads to a chirp amplitude of V_t .

to:

$$P_t(t) = s_t(t)^2 / R_\Omega \text{ [W]}, \quad (2.30)$$

where R_Ω is the input impedance of the antenna (with a coupled antenna this is usually 50Ω).

This power is convolved with the antenna's impulse response and radiated into space. As it travels the signal power suffers from spreading loss, with the power density at the distributed target, at a range R equal to:

$$S_{\text{inc}} = P_t(t) \cdot G_t \cdot \frac{1}{4\pi R^2} \text{ [W/m}^2\text{]}. \quad (2.31)$$

Subsequently this power is scattered by the distributed target. The area from which a single tone will be reflected is range-cell limited, with the first range-cell area equal to:

$$A_1 = \pi \cdot [(R + \delta R)^2 - R^2] \text{ [m}^2\text{]}. \quad (2.32)$$

Assuming a level of surface roughness the effectiveness of the scattering is determined by the backscattering coefficient, σ^0 . Consequently, the power scattered by the target is:

$$P_{\text{tar}} = S_{\text{inc}} \cdot (A_1 \cdot \sigma^0) \text{ [W]}. \quad (2.33)$$

The scattered signal undergoes additional spreading loss on its path towards the receive antenna, and the power density at the receive antenna is:

$$S_{\text{ant}} = P_t(t) \cdot G_{\text{tx}} \cdot \frac{1}{4\pi R^2} \cdot (A_1 \cdot \sigma^0) \cdot \frac{1}{4\pi R^2} \text{ [W/m}^2\text{]}. \quad (2.34)$$

This power is then intercepted by the effective area of the receive antenna, A_{eff} , (defined as:

$\frac{\lambda^2}{4\pi} G_{rx}$, see *Balanis*, [1977]), and the received power is therefore:

$$P_r(t - \tau) = P_t(t) \cdot G_{tx} \cdot \frac{1}{4\pi R^2} \cdot (A_1 \cdot \sigma^0) \cdot \frac{1}{4\pi R^2} \cdot A_{eff} [\text{W}]. \quad (2.35)$$

Equation 2.35 is the radar range equation for a distributed target for FMCW radar⁴.

Additional losses to the received power level are due to cable loss, component insertion loss etc. However, these losses were controlled by the inclusion of small valued attenuators between components in the radar to facilitate coupling, limit feedback and signal reflection. Consequently system losses are minimal and not included here.

2.4.1 Signal to Noise Ratio: SNR

In order to calculate the SNR at the output of the FFT, the signal power and noise constituents are traced through the radar components, beginning with the receive antenna.

Figure 2.8 shows the receiver chain with the respective component gains, losses and changing signal bandwidths. After quantisation, an N-point FFT is taken and consequently a *coherent power gain* of: $G_{coh} \equiv \frac{N^2}{2}$, is applied to the signal, and a *dc gain* of: $G_{dc} \equiv \frac{N}{2}$, is applied to the noise, (*de Wit*, 2005). This results in the power of the frequency peak corresponding to the single tone and the noise floor at the output of the FFT to be respectively:

$$P_{FFT} = G_{coh} \cdot G_{rx} \cdot P_r [\text{W}], \quad (2.36)$$

$$N_{FFT} = G_{dc} \cdot G_{rx} \cdot N_T \cdot \beta_{FFT} [\text{W}]. \quad (2.37)$$

where G_{rx} is the gain of the overall receiver chain.

⁴To paraphrase *Skolnik* [1970]:

The badge of a novice in the FM-radar field is a carefully worked out performance appraisal based only on the application of the radar range equation.

Hence, it is acknowledged that the analysis of the influence of phase noise on the signal noise floor, the possibility of small signal suppression, and interference is neglected, but is not necessary for a first-order estimation of the radar behaviour.

Hence, the SNR at the output of the FFT is:

$$\begin{aligned} SNR_{FFT} &= P_{FFT}/N_{FFT}, \\ &= N \cdot \frac{P_r}{N_T \cdot \beta_{FFT}}. \end{aligned} \quad (2.38)$$

Quantisation Noise

The quantisation noise of the ADC may be a limiting factor on the achievable SNR of the system. The signal-to-quantisation-noise ratio of an ideal ADC is defined (*Proakis and Manolakis* [2004], pp. 756) as:

$$SNR_Q = 6.02N + 16.81 - 20\log_{10}\left(\frac{R}{\sigma_x}\right) \text{ [dB]}, \quad (2.39)$$

$$= 6.02 \times 12 + 16.81 - 20\log_{10}(10/4), \quad (2.40)$$

$$\approx 69 \text{ [dB]}, \quad (2.41)$$

where N is the number of bits, and R is the range of the ADC, and σ_x^2 is the signal power. It should be noted here, that although this derivation is for an ideal ADC, it is useful in that it provides an upper bound on the SNR.

2.4.2 Theoretical Minimum Backscattering Coefficient: σ^0

The minimum detectable backscattering coefficient can now be approximated by determining conditions for which the SNR_{FFT} satisfies the probability of detection, and false-alarm rate as discussed in section 2.3.8. For this to occur, the following relationship must hold:

$$SNR_{FFT} > 6.0 \text{ [dB]}. \quad (2.42)$$

Using this condition⁵, and the values provided in tables 2.1, and 2.2, the minimum backscattering coefficient to which RAASTI is sensitive can be approximated. It is calculated to vary over R_{min}

⁵For the SNR_{FFT} , using an $N = 14001$ point FFT (as used in the signal processing algorithms written for the radar).

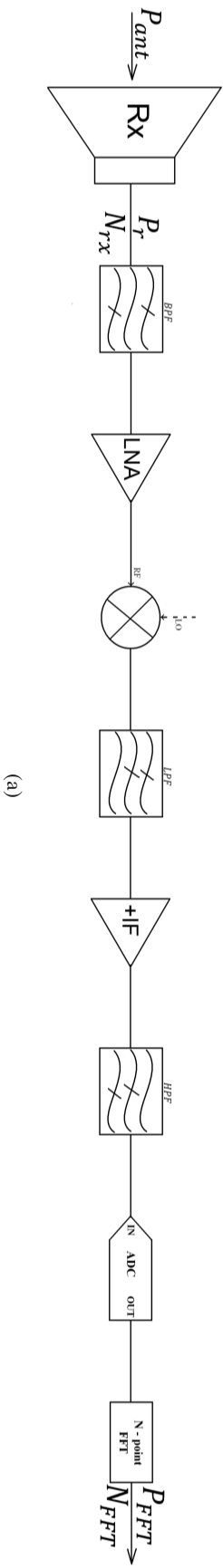


Figure 2.8: Receiver chain components and their associated noise, gain, and bandwidth values.

to R_{max} , as:

$$\sigma_{R_{min}}^0 > -107 \text{ [dB]}, \quad (2.43)$$

$$\sigma_{R_{max}}^0 > -87 \text{ [dB]}. \quad (2.44)$$

If targets for any reason have lower backscattering than the values derived above, they become lost in the noise floor. This result is particularly important for further analysis of the radar viewing conditions provided in the next chapter where the conditions necessary for unambiguous detection of the air/snow and snow/ice interfaces are explored.

2.5 Summary

This chapter provided an overview of the operating principle, parameters and performance characteristics of the FMCW radar (RAASTI) used in helicopter-borne experiments over sea ice in Antarctica for the purpose of measuring snow thickness. The design parameters of the radar are presented in table 2.1, based on these values the expected performance parameters of the radar are derived. The values of the performance parameters are summarised in table 2.2. These values (in table 2.2) constrain the operating altitude, speed of the radar, the area of illumination of the radar and the expected vertical range resolution. These values will be used in the following chapter to estimate how RAASTI *sees* the sea ice and its snow cover, and how it is expected to detect the snow thickness.

Chapter

3

Electromagnetic Wave Interaction with Snow and Sea Ice using RAASTI

This chapter considers the nature of the interactions of the EM radiation transmitted by RAASTI with the snow and sea ice media. The dielectric properties and the physical properties that drive the dielectric signatures of snow and sea ice are summarised. This is presented in order to contextualise the interpretation of the return signal, as well as to understand the limit to the information that can be extracted from it.

It is demonstrated that the radar is theoretically capable of unambiguously detecting and resolving the air/snow and snow/ice interfaces, and the conditions for achieving this in practice are summarised. It will be shown that when imaging highly deformed surfaces with RAASTI, unambiguous identification of the air/snow and snow/ice interfaces is only possible when the reflected power from the snow/ice interface is greater than that from the air/snow interface.

3.1 Wide Bandwidth and Layered Media

It follows from Maxwell's equations that EM waves will reflect from a sharp change in refractive index, usually indicative of a boundary separating two media. However, what is meant by *sharp*? Conventionally, a boundary is assumed to be sharp when the refractive index changes within a distance that is small compared to the wavelength of incident radiation (*Feynman*, 1963). This leads to a complication when applied to RAASTI as the transmitted frequency spans 2 octaves: what is sharp at 2 GHz ($\lambda = 150$ mm) is not necessarily sharp at 8 GHz ($\lambda = 37.5$ mm).

Additionally, depending on the nature of surface fluctuations, the interaction of the radar radiation will be affected by the size and scale of the fluctuations relative to the wavelength of the EM radiation. *Beckmann and Spizzichino* [1963] state this very concern in their study of surfaces: "... the same surface may be rough for some wavelengths and smooth for others; or for the same wavelength it may be either rough or smooth for different angles of incidence."

These two sources of heterogeneity: refractive index changes within the snow media, and the surface/boundary characteristics of the air/snow and snow ice interfaces will affect the sensitivity and resolving performance of the radar. A study of the changes in the refractive index and nature of scatter within the snow and from the sea ice, and associated behaviour as the radar sweeps from 2 - 8 GHz is outside the scope of this thesis¹. As such, it was judged sufficient to present the various electromagnetically significant values at three discrete frequencies: 2, 5 and 8 GHz.

3.1.1 Qualitative Considerations

The interaction of the radar signal with a surface boundary can often be described by surface features that are either due to:

- small scale “roughness”,
- large scale “undulations” in surface topography.

(With the size distinction determined by comparison of the features to the wavelength of the radar signal.)

Roughness characteristics will affect the nature of the scattering. Depending on the degree of roughness, the signal may interact with the boundary in a specular manner, be completely lost within the surface cavities (black-body), or display behaviour between these two extremes. To determine the region of operation, the distinction between a smooth or rough surface must be quantified. *Beckmann and Spizzichino* [1963] differentiate between a smooth and rough surface as follows: “... a surface will scatter energy of an incident plane wave into various directions, whereas a surface that reflects in a specular manner will be called smooth.”.

The main effect of roughness is to determine the directivity of scattered energy. For a backscattering radar which only observe scattered energy in the direction of the receiver, surfaces of increasing roughness will tend to decrease the receive power as the signal is scattered over a wide range of angles.

¹This complication is only recently being explored, e.g. *Taylor* [2001], where it is addressed in some detail.

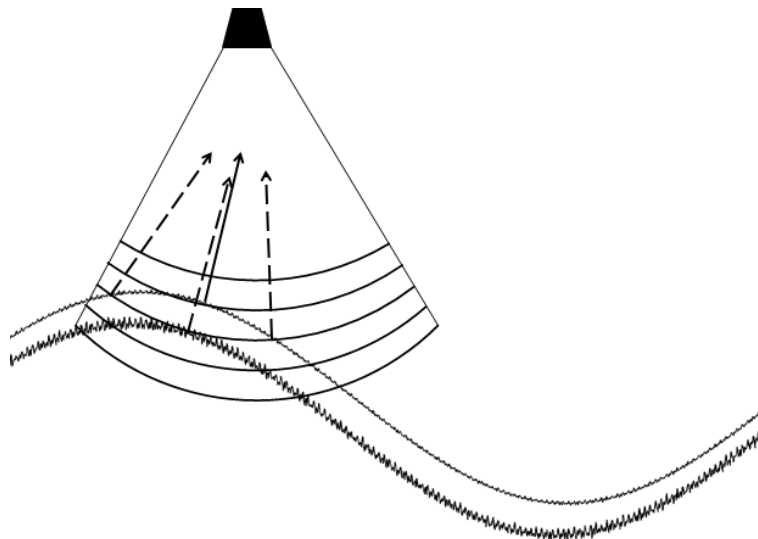


Figure 3.1: Illustration of the small and large-scale roughness features of a surface. The radar range cells are seen here propagating down onto the surface. The active area of the radar illuminates large-scale surface features that may potentially mask returns from the sub-surface.

The second characteristic, refers to the effects of surface topography on the distribution of the radar signal in the vertical range resolution space. As an illustrative example of this, consider a surface characterised by large-scale undulations; if the active area of a radar covers these variations in surface height, the reflected signal may come from both the surface and subsurface. Figure 3.1 demonstrates a return signal arising from the surface, and sub-surface in the same range cell, and consequently affecting the capacity of the system to detect the sub-surface layer.

Conversely, if the surface studied is of a low spatial frequency, such that these changes in height are not present within the active area of a radar there will be no ambiguity between a return arriving from the surface with a return due to the subsurface interface reflection. (This condition is also noted by *Yankielun* [1992] when examining the returns of a FMCW radar for profiling freshwater ice.)

It is clear that the nature of the surface is independent of the instruments used to measure it. The difference between the sizes of the small- and large-scale features for a particular radar being determined by the wavelength used, and its viewing aperture. In the sections to follow, the scales of surface roughness as seen by RAASTI are quantified.

3.1.2 Quantitative Considerations

Specular reflection, in which the Fresnel formulae describe the relationship between reflected and refracted waves, is characteristic of smooth surfaces, and is different to scattering in two distinct ways: the reflection from the surface is coherent² and it is focused³. There is no ambiguity in returns from the air/snow and snow/ice interface under specular reflection conditions as off-angle reflections are directed away from the receiving aperture of the radar. Therefore it is important to gauge the *degree of specularity* of the surfaces under study at the frequencies of interest. This will provide an estimate of the maximum possible power reflected from the interfaces, and hence for a first order estimate of the expected received signal power to be made.

Frequently, Rayleigh conditions are used to gauge the possibility of specular reflection occurring at an interface (*Beckmann and Spizzichino, 1963*). The Rayleigh conditions for specular reflection require that the root-mean-square difference (RMS or standard deviation) of the surface height be less than $\lambda/8$ over the first Fresnel zone (*Beckmann and Spizzichino, 1963*).

Thus guided, the values for these conditions are calculated over three frequencies spanning the used bandwidth. As the Fresnel zone area is a function of range, it is calculated for three nominal operating heights of the radar: 30, 100, and 150 m. These values are summarised in table 3.1. The laser data gathered in a helicopter-borne exercise during a voyage to Antarctica in 2008 (courtesy of *Lieser, 2008*), are used to estimate the actual surface roughness conditions. Figure 3.2 plots the calculated standard deviation in surface height as a function of increasing sample distance, and figure 3.3 presents the same data on a larger scale over the 0 - 10 m interval (closer to the radar active area radius). These data are used to estimate the RMS height at a given active area diameter, and the surface conditions for three nominal operating heights are summarised in table 3.2.

A comparison of the two tables 3.1 and 3.2 leads to the conclusion that at higher altitudes, the Rayleigh conditions are may not be satisfied. In order to capture the degree to which the surface appears smooth at the frequencies used, the *specular reflection coefficient reduction factor* as given by *Skolnik [1970]*:

$$\sqrt{g} \equiv 2\pi \frac{\sigma}{\lambda}, \quad (3.1)$$

is calculated, where σ is the standard deviation of surface height.

²Meaning that all reflected waves undergo the same phase change.

³The area from which specular reflection occurs is strictly defined by the first Fresnel zone.

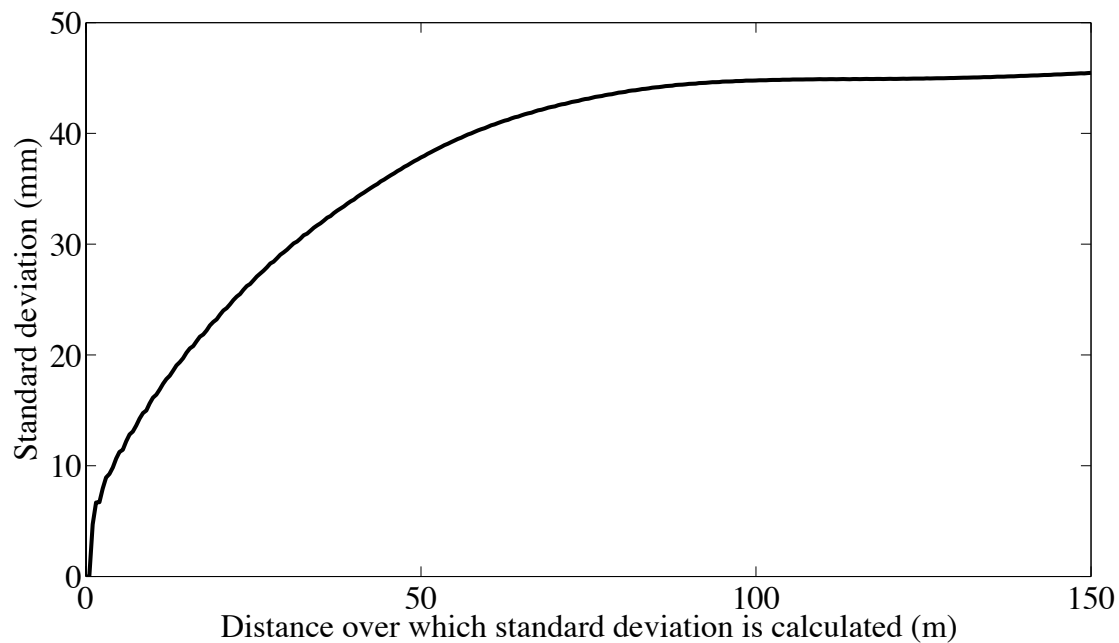


Figure 3.2: The RMS height of the fast ice surface, as derived from laser altimeter data. The graph shows that the surface features are undersampled until the sampling distance is increased to ≈ 50 m.

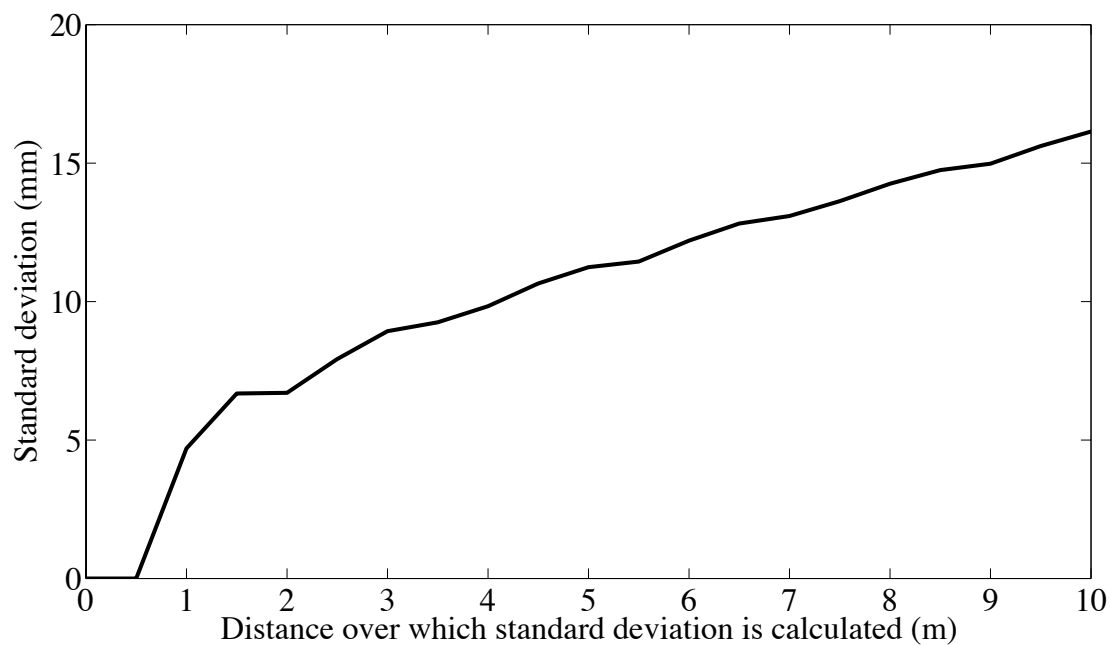


Figure 3.3: The same results as 3.2, except on a larger scale, showing the distances of interest, which correspond to the size of the active area of RAASTI.

Frequency (GHz)	2	5	8
$\lambda/8$ (mm)	18.8	7.5	4.69
Altitude (m)	30	100	150
First Fresnel Zone (m^2)	0.89	3.88	6.13

Table 3.1: Rayleigh conditions for specular reflection.

Altitude (m)	30	100	150
Standard Deviation (mm)	4.70	9.83	12.2
Active Area (m^2)	4.91	15.71	24.55

Table 3.2: Experimentally derived viewing conditions.

Figure 3.4 illustrates the nature of scattering that an incident EM wave will undergo, losing directivity in reflection due to an increase in surface roughness, as quantified by g . By convention, it is assumed that for specular reflection $g \approx 0$, whereas for rough surfaces $g \gg 1$. Using the experimentally derived standard deviation values, the value of g for the snow surface is calculated to be:

$$g_{100m} = \{0.17, 1.06, 2.71\},$$

given for 2, 5, and 8 GHz respectively (the values provided above are at a nominal operating height of 100 m).

g is a “rule-of-thumb” quantity used for a first-order estimate of potential directivity of the surface as a function of its *vertical* roughness characteristics, i.e. standard deviation of surface height. Another important quantifier of small-scale surface roughness is the correlation length of the *horizontal* surface features, which is a measure of the range of angles over which the scatter from the surface will occur. Referring to the laser data, and applying the auto-correlation function, the approximate distance over which the surface features decorrelate is found to be ≈ 27 m (defined by the distance at which the auto-correlation function decreases by $1/e$) see 3.5.

The long correlation length coupled with a relatively low RMS height leads to the hypothesis that returns will be restricted to a small region around the radar’s nadir point, and that large scale undulations in the surface will not interfere with the identification of the air/snow and snow/ice returns. However, cases of higher surface roughness and lower correlation length (when flying over deformed ice such as shown in figure 3.6), may occur and the effect of large-scale features on the radar signal require consideration. In such cases, the radar may receive scattered returns from

both the air/snow and snow/ice interfaces in the same active area. Fortunately, even under such circumstances, it may be possible to unambiguously identify the air/snow and snow/ice returns. The conditions necessary for this are explored in section 3.2.

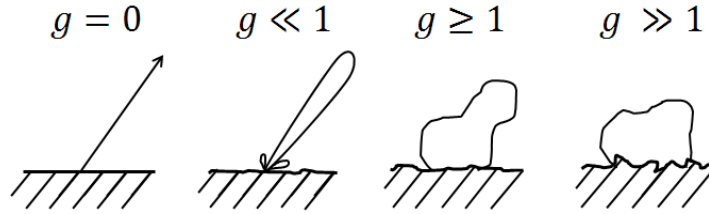


Figure 3.4: Transition from specular reflection to rough surface scattering as quantified by g , adapted from *Beckmann and Spizzichino* [1963].

3.2 Conditions for Unambiguous Interface Identification

The air/snow interface return is unambiguous since it can safely be assumed to correspond to the first peak in the radar return waveform. The snow/ice interface however, is not as clearly identifiable. Considering the possibility of large-scale surface deformation (due to ridging for example), coupled with a wide antenna beamwidth⁴, a situation may arise whereby a return from the surface of an off-nadir range cell occurs in the same range bin as the return from the snow/ice interface (figure 3.7). In such instances, in order to identify the return from the snow/ice interface it is required that the power level of the snow/ice interface be higher than that coming from the air/snow interface, that is:

$$P_{s/i} > P_{a/s}. \quad (3.2)$$

This condition is illustrated by figure 3.8, and if it is not met the return from the snow/ice interface cannot be clearly distinguished from off-nadir air/snow returns (*Gogineni and Prescott*, 2001).

3.2.1 Power Splitting at the Boundary of Two Media

The refractive index is the sole parameter affecting the distribution of power between the reflection and transmission of incident EM radiation at the interface of two media⁵. Calculating its value

⁴If the radar were *beamwidth limited* (*Webster* 1999) this ambiguity condition could not exist.

⁵Ignoring cases where the wavelength is comparable to the size of the particles comprising the medium, large crevices and porous media, and/or gradual changes in refractive index constituting

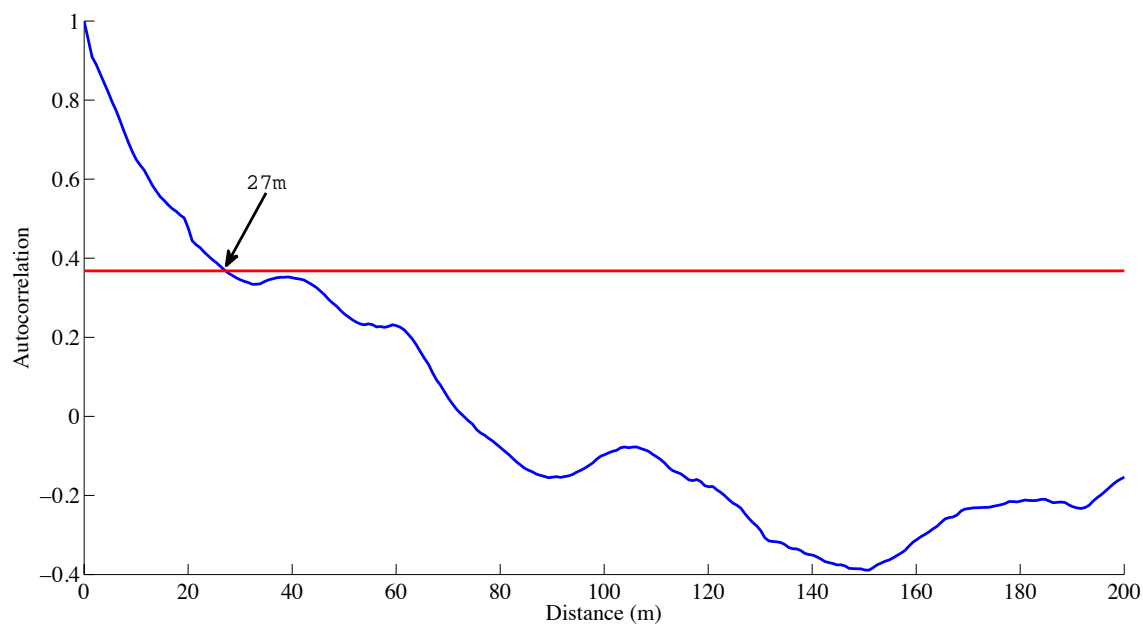


Figure 3.5: The auto-correlation length calculated using the laser/INS datasets over fast ice. The approximate distance over which the surface features decorrelate (defined at the $1/e$ level of the auto-correlation function) is ≈ 27 m.

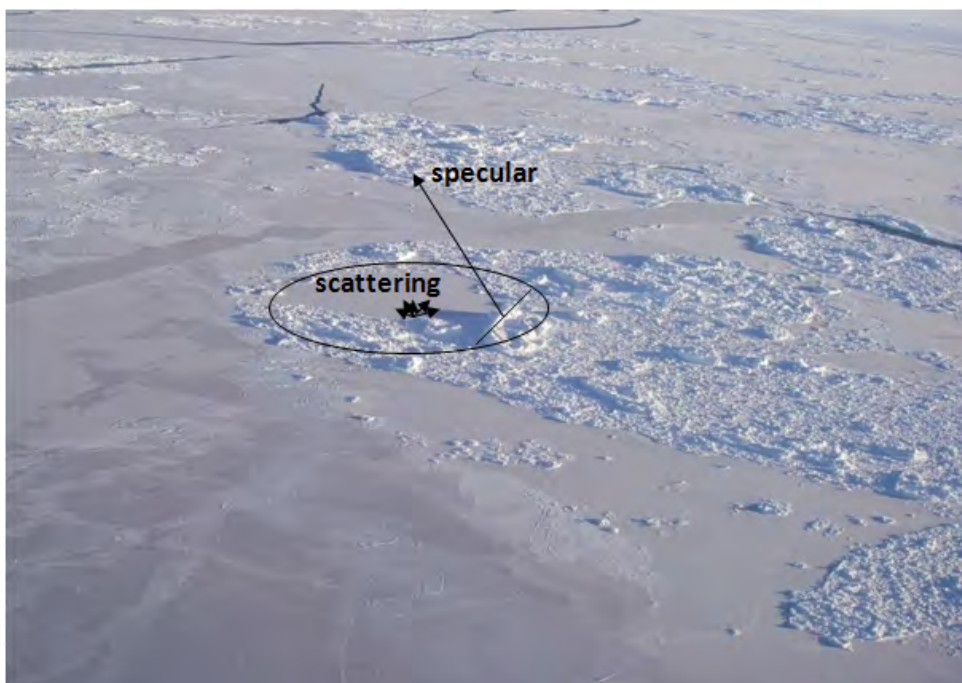


Figure 3.6: The typical nature of sea ice and its snow cover in Antarctica, illustrating the possibility of scattering and specular reflection being present within the active area. (Photograph taken at an altitude of 80 m.)

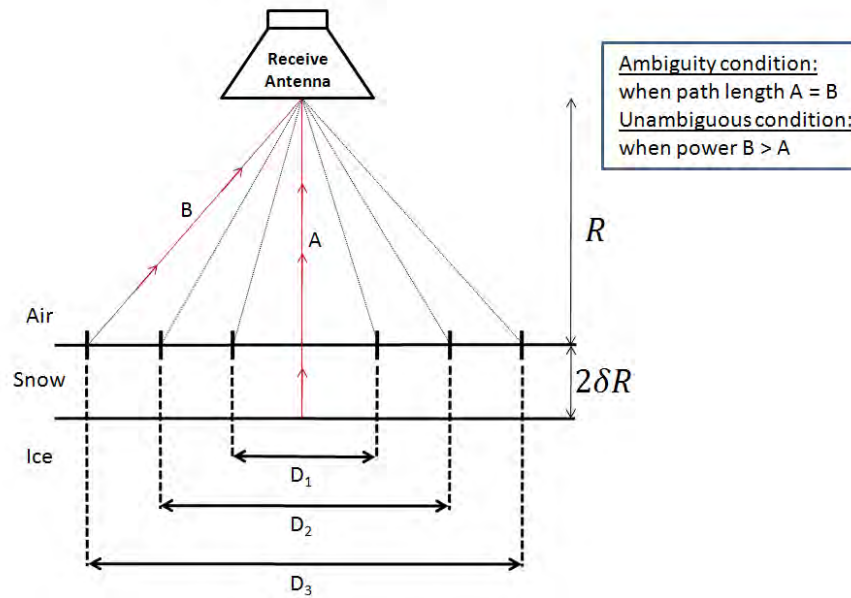


Figure 3.7: The possible ambiguity condition between returns from the air/snow and snow/ice interfaces, where D_n denotes the diameter of the active area.

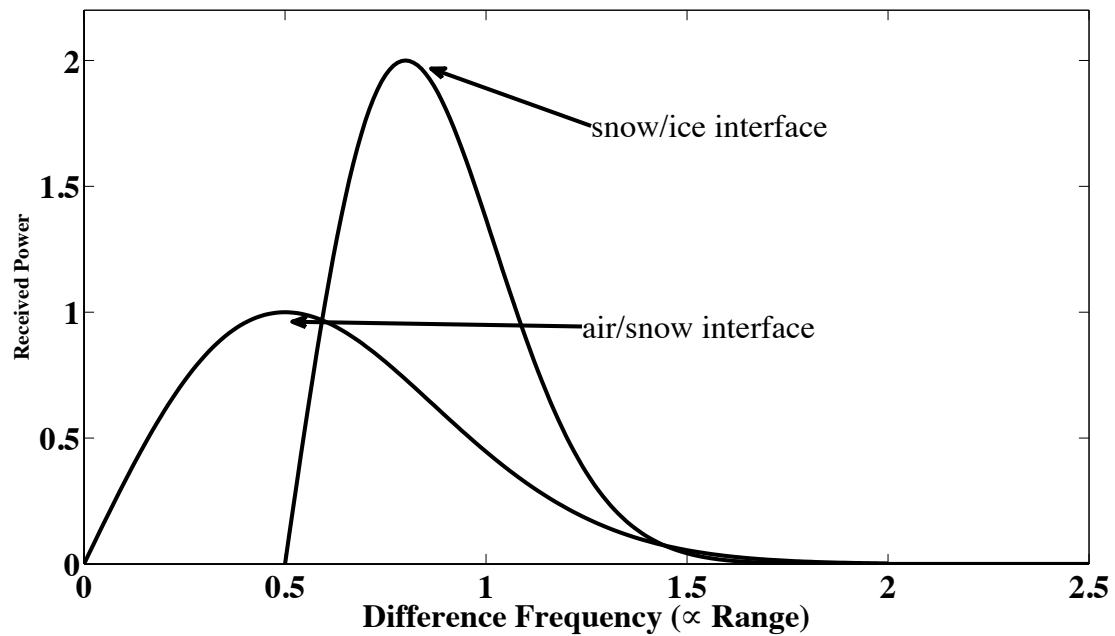


Figure 3.8: Return power requirements for the air/snow and snow/ice interfaces for unambiguous identification of the layers. The power received from the snow/ice interface should be greater than that from the air/snow interface.

allows the upper bound of the expected power returned from the air/snow and snow/ice interfaces to be quantified.

A plane wave incident on the boundary of two homogeneous media of different dielectric properties is split into two waves: a transmitted wave continuing into the second medium, and a reflected wave propagating back into the first medium (*Born and Wolf*, 1965). The *Fresnel formulae* relate the amplitude of the incident wave to the amplitudes of the transmitted and reflected components respectively, see figure 3.9:

$$\begin{aligned} T_{\parallel} &= \frac{2n_1 \cos \theta_i}{n_2 \cos \theta_i + n_1 \cos \theta_r} A_{\parallel}, \\ T_{\perp} &= \frac{2n_1 \cos \theta_i}{n_1 \cos \theta_i + n_2 \cos \theta_r} A_{\perp}, \\ R_{\parallel} &= \frac{n_2 \cos \theta_i - n_1 \cos \theta_r}{n_2 \cos \theta_i + n_1 \cos \theta_r} A_{\parallel}, \\ R_{\perp} &= \frac{n_1 \cos \theta_i - n_2 \cos \theta_r}{n_1 \cos \theta_i + n_2 \cos \theta_r} A_{\perp}, \end{aligned} \quad (3.3)$$

where the subscripts \parallel and \perp refer to the components of the wave parallel and perpendicular to the plane of incidence respectively; A is the amplitude of the incident wave onto the interface of the two media; T is the amplitude of the transmitted wave into the second medium; R is the amplitude of the reflected wave; θ_i and θ_r are the angles of incidence, and refraction respectively, measured from a normal to the surface; and n_1 and n_2 are the refractive indices of the two media. Under conditions of normal incidence (where $\theta_i = \theta_r = 0$) and single polarisation, the above formulae reduce to:

$$T = \frac{2n_1}{n_2 + n_1}, \quad (3.4)$$

$$R = \frac{n_2 - n_1}{n_2 + n_1}. \quad (3.5)$$

3.2.2 Modelling the Condition for Snow Layer Identification

Provided that the refractive index is the sole parameter affecting the distribution of power between the reflection and transmission of incident EM radiation at the interface of two media, the upper gradual progression from one media to the other. The possibility of their effect on the signal (i.e. volume scattering, explored in section 3.4.2) must be acknowledged, but a detailed analysis is outside the scope of this thesis.

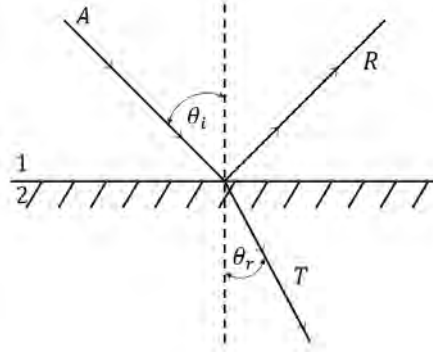


Figure 3.9: Reflection and transmission of a plane wave. A is the incident beam arriving at an angle θ_i to R is the reflected beam, and T is the transmitted beam into the medium at an angle θ_r .

bounds of the reflected powers from the air/snow and snow/ice interfaces can be derived. Referring to figure 3.10 the reflected powers from the two interfaces are expressed as:

$$P_{a/s} = (R_{a/s})^2 P_{inc}, \quad (3.6)$$

$$P_{s/i} = (1 - (R_{a/s})^2) P_{inc} (R_{s/i})^2 (1 - (R_{a/s})^2), \quad (3.7)$$

where P_{inc} is the power incident at the air/snow interface and $R_{a/s}$ and $R_{s/i}$ are the Fresnel reflection coefficients (at nadir incidence) at the air/snow and snow/ice interfaces respectively. This formulation and equations ignore possible coherent interactions of the incident EM radiation within the snow, which (if present) will make the reflectivity of the snow sensitive to its thickness. This this approach is justified on the basis of the comparably dominant scattering by snow grains. (Models (Nghiem *et al.*, 1995a) of sea ice interaction with EM radiation demonstrate that this effect may be present, however, it has not yet been isolated (Nghiem, *et al.*, 1995b).)

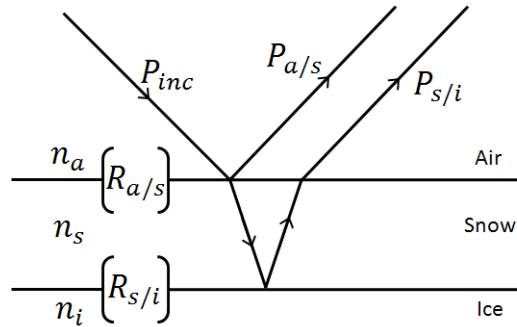


Figure 3.10: Reflection and refraction/transmission at air/snow and snow/ice interfaces.

Combining these expressions with equation 3.2, yields the condition for unambiguous

identification of the return from the snow/ice interface:

$$(R_{a/s})^2 \leq (1 - (R_{a/s})^2)(R_{s/i})^2(1 - (R_{s/i})^2),$$

or equivalently,

$$(R_{a/s})^2 = K(1 - (R_{a/s})^2)(R_{s/i})^2(1 - (R_{s/i})^2), \quad (3.8)$$

where K is introduced here to model the relative power factor. $K < 1$ for equation 3.2 to be satisfied. This equation summarises the condition necessary for unambiguous identification of the two interfaces.

Quantification of the relationship (equation 3.8) allows for an assessment of the region of its validity to be made. The refractive index of air is conventionally equal to unity, and the range of likely values for n_s and n_i are found in literature (*Ulabiy et al.*, 1986b; *Hallikainen et al.*, 1986; *Frolov and Macheret*, 1999) to be:

$$n_s : 1.2 \rightarrow 2.0$$

$$n_i : 3.1 \rightarrow 3.5.$$

Figure 3.11 plots the necessary values of the refractive index of ice, given the refractive index of snow for equation 3.8 to be satisfied. The values of K are chosen as: 1.0 (as the upper bound on the condition) and 0.15 as this leads to an ≈ 8 dB difference between the power returns of the air/snow and snow/ice interfaces. This is in line with the findings of *Gogineni et al.* [2009].

The solutions plotted in figure 3.11 demonstrate that is not unrealistic to assume a higher power return from the snow/ice interface than from the air/snow interface. However, the degree of sensitivity of this condition should be qualified. Figure 3.12 illustrates how a slight change in the refractive index of snow could necessitate an unrealistically high refractive index of ice in order to maintain resolution ability. This could potentially lead to conditions where the underlying surface becomes undetectable.

3.2.3 Effect of Snow Wetness

The effect of wetness on the refractive index of snow must be considered when dealing with the Antarctic sea ice and its snow cover. In contrast to the Arctic, snow on Antarctic sea ice is subject

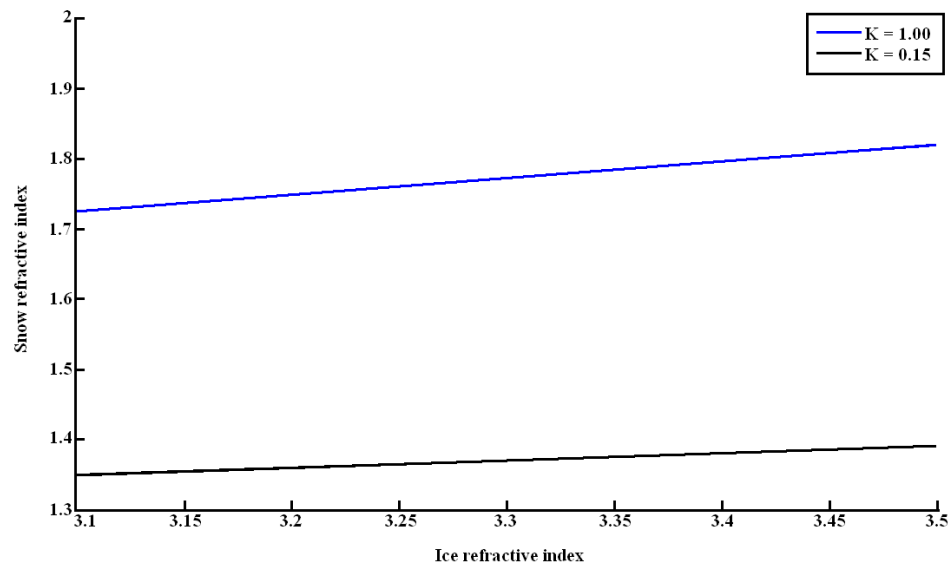


Figure 3.11: Snow refractive index as a function of ice refractive index required to satisfy unambiguous relative power requirements.

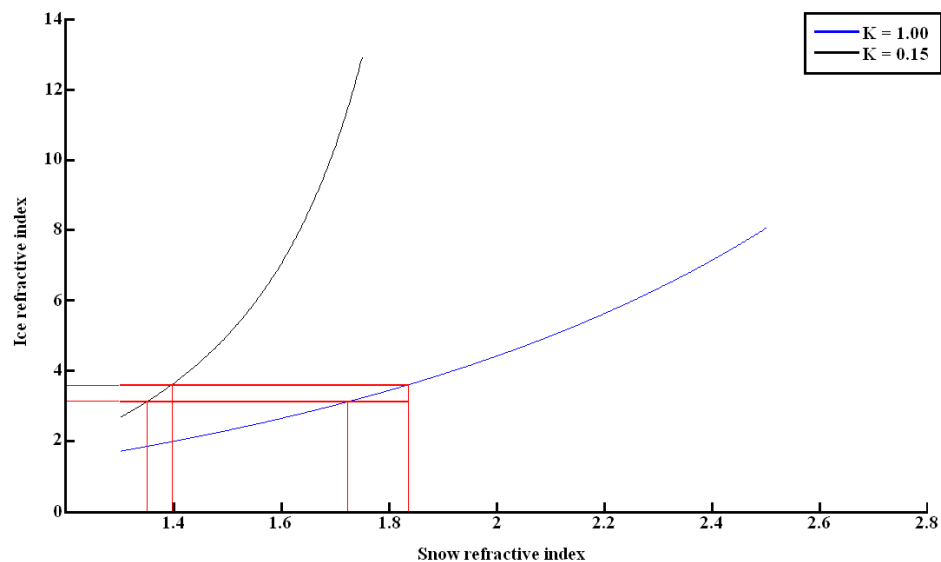


Figure 3.12: Ice refractive index as a function of snow refractive index. The areas which satisfy the unambiguous relative power requirement are enclosed within the red lines.

to warmer atmospheric temperatures and has a higher chance of flooding (*Massom et al.*, 2001). Using *Galley et al.*, [2009], expression for refraction index, figure 3.13 demonstrates the change in refractive index as a function of snow wetness. The figure shows that even a relatively large wetness of 10% still keeps the refractive index within bounds required for higher reflection to occur from the snow/ice interface, at the frequencies explored here. This ignores the power loss experienced by the EM radiation in a wet snow pack.

The imaginary part of the refractive index is no longer negligible for wet snow, and this has the effect of reducing the penetration depth of the radiation. The absorption length (or depth in this case), approximated by *Rees*, [2006] is:

$$l_a \approx \frac{\sqrt{\epsilon'}}{2\pi\epsilon''}\lambda, \quad (3.9)$$

where ϵ' and ϵ'' are the real and imaginary parts of the complex dielectric constant, and quantify the EM energy stored, and energy loss in the medium respectively. Their relationship to the complex refractive index can be found in *Born and Wolf*, 1965 pp613.

Figure 3.14 summarises the changes in absorption length of the snow as a function of increasing water content, calculated for a nominal snow density of $300\text{kg}/\text{m}^3$. This plot shows that the water content of snow may prevent correct detection of the air/snow and snow/ice interfaces. This can be the result of either the EM radiation being completely absorbed by the snow pack, thereby no power is reflected, or if only a portion of the incident frequencies are reflected hence the receive bandwidth is decreased (i.e. vertical resolution suffers), and hence the snow layer is not resolvable.

3.3 Sensitivity of Snow Thickness Estimates to Errors in Refractive Index

Provided with a 6 GHz radar bandwidth, the best (theoretical) range resolution of RAASTI is 25 mm (*in vacuo*). However, RAASTI is an instrument that measures the *time* separation between returns. Hence, the refractive index is used to estimate the velocity of propagation of the EM waves in the media, in order to map time to distance. The velocity of propagation in a medium as a function of the refractive index is given by:

$$v = \frac{c}{n}. \quad (3.10)$$

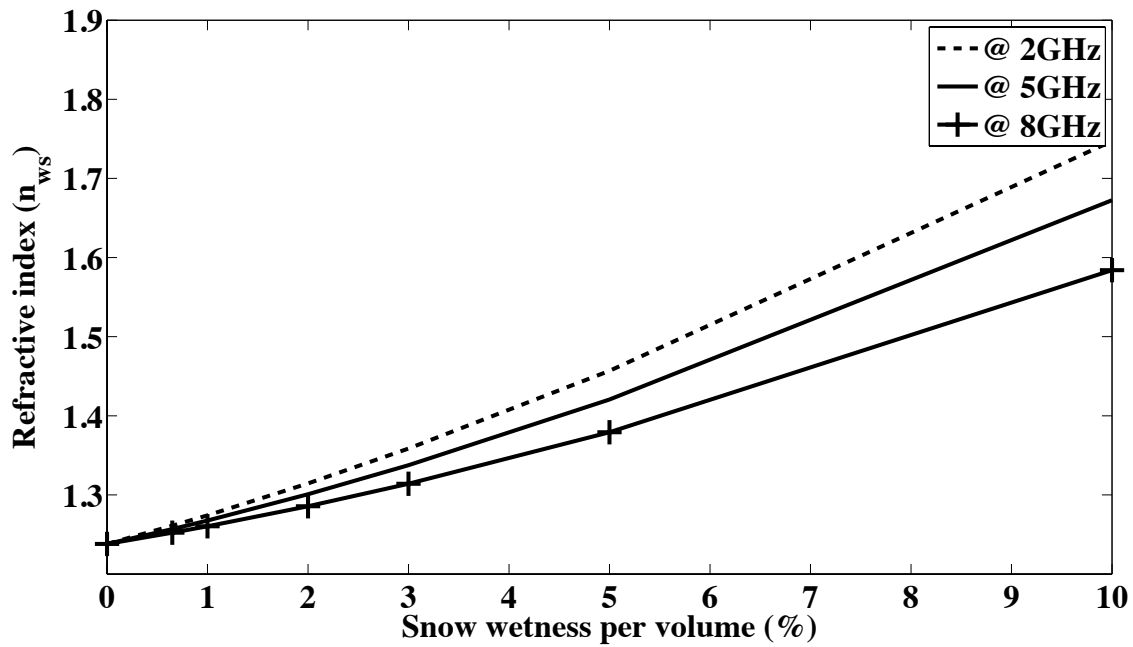


Figure 3.13: Refractive index at the frequencies 2, 5, and 8 GHz as a function of increasing snow water content. The values demonstrate that equation 3.8 will remain satisfied even with increasing snow wetness, hence the reflection from the snow/ice interface can be expected to be stronger. However, this ignores the increasing power losses of the EM radiation in a wet snow pack, which is further explored in the text.

Knowledge of the refractive index is imperative to accurately deriving the snow layer thickness, hence it is necessary to gauge the sensitivity of the radar to errors in estimates of the refractive index.

In dry snow, the density of the snowpack is considered the dominating factor affecting the refractive index (*Hallikainen et al.*, 1986; *Galley et al.*, 2009). An average snow density value of 300kgm^{-3} results in a refractive index of 1.24 (calculated after *Galley et al.*, 2009). Table 3.3 summarises the percentage error in distance as a function of increasing error in density.

However, as snow over sea ice in Antarctica is frequently wet, similar calculations (using equations for refractive index provided by *Galley et al.* [2009]) are also provided here for the average snow and sea ice conditions. As wet snow will be a dispersive media, table 3.4 summarises the calculated refractive index for wet snow as a function of the frequencies: 2, 5, and 8 GHz. (Average snow wetness of 0.65% (*Massom et al.*, 2001) is combined with a nominal snow density of 300kgm^{-3} is used in calculating the values in the table.) Fortunately, as the results in table 3.4 show, wetness

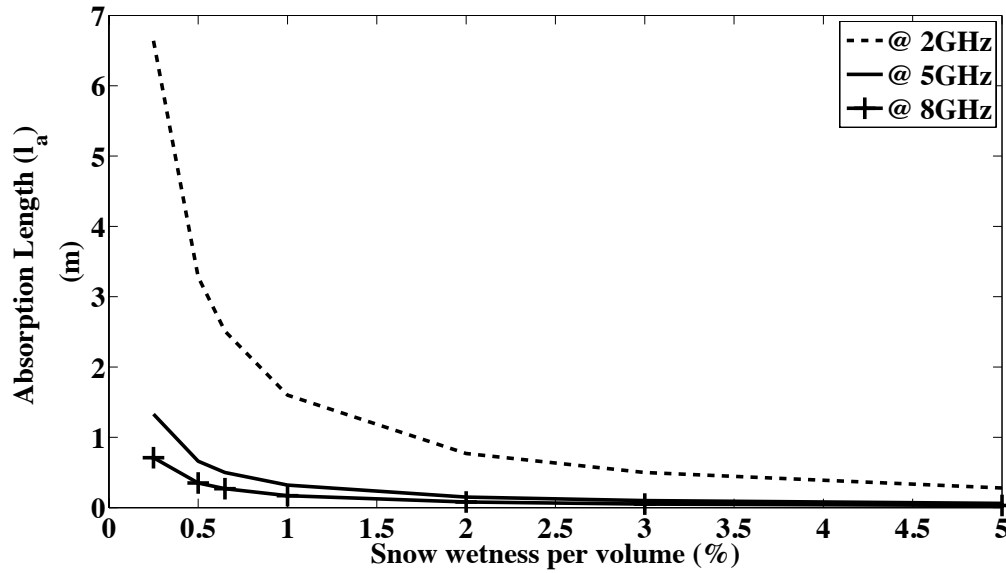


Figure 3.14: The absorption length (or the penetration depth) of the EM radiation at 2, 5 and 8 GHz as a function of increasing snow wetness. The large difference in penetration depth over the frequency range indicates that it is likely that a wet snow pack degrades the range resolution of the radar by preventing reflection of the higher frequencies.

does not have a strong dispersive effect on the refractive index over these frequencies. However, as the last row of table 3.3 however shows there is increasing error made in distance calculations under wet snow conditions.

The values in table 3.3 demonstrate that the error in refractive index due to even a 90% error in density is small. This can be explained by the relatively large and dominating factor of the propagation velocity⁶, combined with the relatively thin snow thickness over sea ice⁷, resulting in a high tolerance for error in density measurements when the snow thickness is relatively shallow. This has important implications for the many layered (and hence of variable density) snow pack present on sea ice in Antarctica, i.e. it may not always be necessary to quantify the density of each layer.

The measurement of the density and wetness of the snow pack is subject to commission and omission errors. A commission error may be committed when, due to the heterogeneous nature of the snow pack, density measurement of each layer in the snow may not be feasible (for example,

⁶Similar results are mentioned by *Marshall et al.* [2008b].

⁷Taken here to be 1 m, as a conservative estimate.

thin crusty layers with the largest density are ignored), and/or wetness measurements with the required vertical resolution into the snow profile are not made. The values in tables 3.3 and 3.4 demonstrate that sampling every layer in the snow pack is not necessary under dry snow conditions, however, in cases where a wet snow pack is expected, accurate knowledge of density becomes more important in conversion of radar delay time to thickness. In addition, the advantage of regional-scale remote sensing of snow thickness would be compromised if the values in these tables showed that the density and wetness estimates of the snow pack needed to be known with high accuracy in order to avoid large errors in snow thickness estimates. The values in table 3.3 show that for a dry snow pack a 90% error in density contributes approximately a 20% error to snow thickness (for example, if the snow thickness is 20 cm, this gives a 4 cm error in snow thickness, which is just above RAASTI's vertical range resolution), consequently there is some tolerance to omission error in *in-situ* sampling of snow density. Notably, under wet snow conditions density estimates become more important, and if it is suspected that the snow to be studied will have liquid water content, then more regular sampling of snow density may be required.

It should also be noted that the effect of wetness coupled with an increase in salinity within the snow is not considered. The change in refractive index according to changes in salinity are being studied in depth (*Goldsetzer et al.*, 2009). Under these conditions, dispersion and additional power loss of the EM signal do occur (*Marshall and Koh*, 2008a). This could further contribute to ambiguity in interface identification, and further work in this area is necessary.

$\rho = 300\text{kgm}^{-3}$	ρ	$\rho + 33\%$	$\rho - 33\%$	$\rho + 50\%$	$\rho - 50\%$	$\rho + 90\%$	$\rho - 90\%$
n_{ds}	1.24	1.32	1.16	1.36	1.12	1.47	1.02
error in distance (%)	0	6.64	6.50	10.1	9.79	18.4	17.4
$n_{ws}(5\text{GHz})$	1.26	1.34	1.18	1.38	1.14	1.48	1.05
error in distance (%)	0	6.06	6.72	8.95	10.5	15.2	20.2

Table 3.3: Error in snow pack thickness calculations as a function of error in density for dry snow (n_{ds}) and wet snow (n_{ws}). (Refractive index calculated after *Galley et al.*, 2009.)

3.4 Backscattering Coefficient Estimation

The previous sections considered the upper bound on the power distribution between air/snow and snow/ice interfaces assuming smooth surface conditions. In this section, the effect of roughness

$\rho = 300 \text{ kg m}^{-3}$	2 GHz	5 GHz	8 GHz
$n_{ws}(+33\%)$	1.34	1.34	1.33
$n_{ws}(-33\%)$	1.18	1.18	1.17
$n_{ws}(+50\%)$	1.38	1.38	1.38
$n_{ws}(-50\%)$	1.14	1.14	1.13
$n_{ws}(+90\%)$	1.49	1.48	1.48
$n_{ws}(-90\%)$	1.05	1.05	1.04

Table 3.4: Sensitivity of wet snow refractive index to error in density, for 2, 5, and 8 GHz. Snow wetness taken as 0.65%. (Refractive index calculated after Galley *et al.*, 2009.)

on the reflected power is considered.

Under rough surface conditions, the backscattering coefficient captures the amount of reflected signal power (Ulaby *et al.*, 1982a). The oft-quoted (Kim *et al.*, 1984) empirical model for the backscattering coefficient of snow covered ice (Ulaby *et al.*, 1982b), neglecting the ice volume contribution, is:

$$\sigma^0(\theta) = \sigma_{a/s}^0(\theta) + T_{a/s}^2(\theta) \left[\sigma_{sv}^0(\theta') + \frac{1}{L^2(\theta')} \cdot \sigma_{s/i}^0(\theta') \right], \quad (3.11)$$

where $\sigma_{a/s}^0(\theta)$ is the backscattering coefficient for the *snow surface* (i.e. air/snow interface); $\sigma_{sv}^0(\theta')$ is the backscattering coefficient for the *snow volume*; $\sigma_{s/i}^0(\theta')$ is the backscattering coefficient for the *ice surface* (i.e. the snow/ice interface); $T_{a/s}(\theta)$ is the Fresnel transmission coefficient at the air/snow interface; $L(\theta')$ is the propagation loss through the snow; θ is the incidence angle; and θ' is the refraction angle into the snow. This equation aggregates the surface and volume scattering contributions into a single backscattering component and represents the total backscattered power that is received by the radar over the chirp duration.

In order to measure snow thickness, RAASTI must be sensitive to the *time delay* of the backscattering component over the chirp duration. RAASTI must identify the time delay between the air/snow interface component ($\sigma_{a/s}^0$) and the snow/ice interface component ($\sigma_{s/i}^0$). Under conditions of high surface deformation, when large-scale roughness features may be present within RAASTI's active area, unambiguous identification of the air/snow and snow/ice interfaces is possibly only if the snow/ice interface has a higher backscattering component than the air/snow interface.

In the next section, an estimate of the backscattering coefficient is made.

3.4.1 Surface Scatter

Using the expression for a backscattering coefficient derived in *Beckmann and Spizzichino* [1963] (pp 88) and using the estimated values for surface roughness (see section 3.1.2), figure 3.15 plots the approximate values of $\sigma_{air/snow}^0$ and $\sigma_{snow/ice}^0$ at a nominal operating height of 100 m over fast ice. (Since these calculations were made for fast ice conditions, the snow/ice surface is modelled to be slightly less rough than the air/snow surface.) This approximation demonstrates that the backscatter from the air/snow interface may be lower than from the snow/ice interface, at least over fast ice areas.

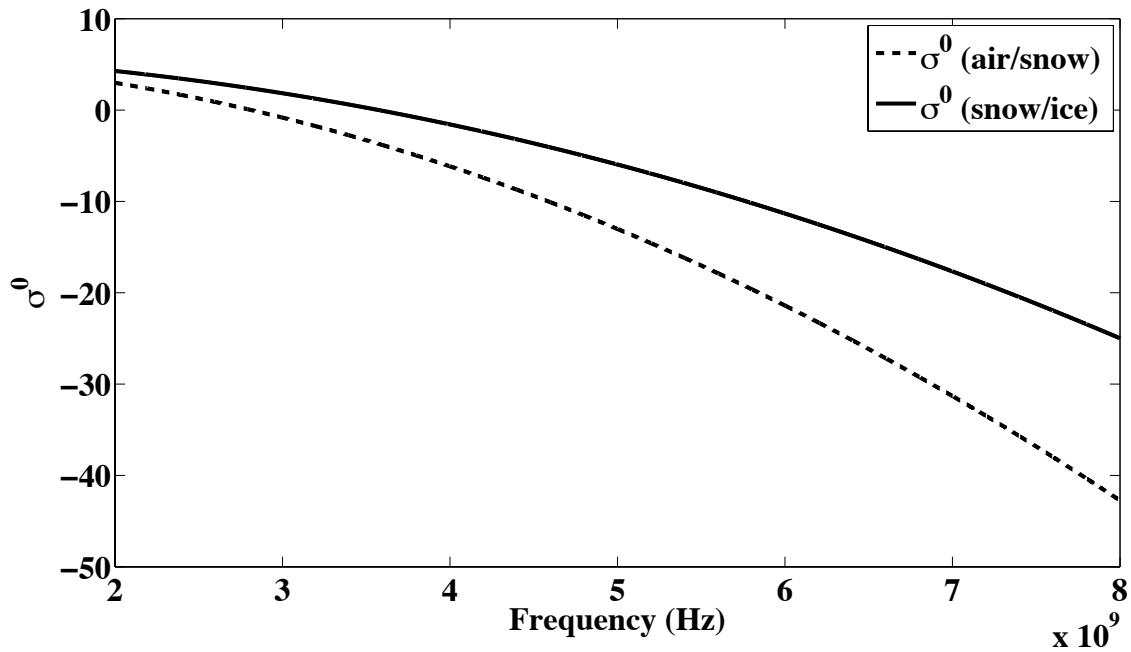


Figure 3.15: σ_0 for fast ice, using the formulation for backscattering coefficient provided by *Beckmann and Spizzichino* [1963] (pp 88).

3.4.2 Volume Scatter

The previous section showed that the refractive index and backscattering coefficient difference between the air/snow and snow/ice interfaces may lead to unambiguous detection. However, volume scatter may prevent this. Volume scattering will contribute to ambiguity in returns, as the

return due to volume scatter can occur at any time between the detection of the air/snow interface and the snow/ice interface return.

Volume scattering is present when the medium is non-homogeneous and thereby contains possible scattering centres. Generally, for the scattering centres to be influence EM radiation they must be of a comparable in size to the wavelength of the radiation. In the case of RAASTI, between: 150 mm - 37.5 mm. In the snow cover of sea ice, grain sizes (for example depth hoar) can reach millimetre dimensions (*Massom et al.*, 2001). However, most likely it is conglomerated snowflakes that form scattering centres comparable to the wavelengths used. This can occur for example, when warm temperatures are present during a snow fall event and individual snowflakes clump together into larger centimetre scale flakes that then fall to form the snow pack. In such situations significant volume scattering may occur; for example *Barber et al.* [1998] observe that volume scattering becomes a significant component at frequencies exceeding 5.3 GHz.

Approximating the backscattering component contributed by the snow pack volume as:

$$\sigma_{sv}^0 = \frac{\sigma_{sc} \cos(\theta)}{2 \cdot \sigma_{ext}}, \quad (3.12)$$

(adapted from *Krishnan* [2007]), where σ_{sc} , and σ_{ext} are the scattering and extinction cross-sections, and θ is the angle of incidence of the snow conglomerates respectively.

The expressions for the scattering and extinction cross-sections are taken from *Chylek et al.* [1993], where the anomalous diffraction approximation (ADA) of *van de Hulst* [1957] is used, to approximate individual fluffy snowflakes as horizontally oriented hexagonal plates. As interaction between the individual scatterers is not considered, these expressions are used here to provide a rough estimate for the backscattering volume component. The ADA is a method by which the scattering properties of *large*⁸, *soft*⁹ particles may be estimated without recourse to lengthy exact calculations.

Figure 3.16 plots the estimated contribution of volume backscatter as a function of frequency, and compares it to the backscattering contribution due to surface scattering from fast ice and its

⁸Determined by the size parameter: $x = k \times a$, where k is the wavenumber, and a is the conglomerate radius. In this case the size parameter is ≈ 1 , i.e. the radar signal is subject to Mie scattering.

⁹Particles whose relative refractive index is close to one are considered *optically soft*.

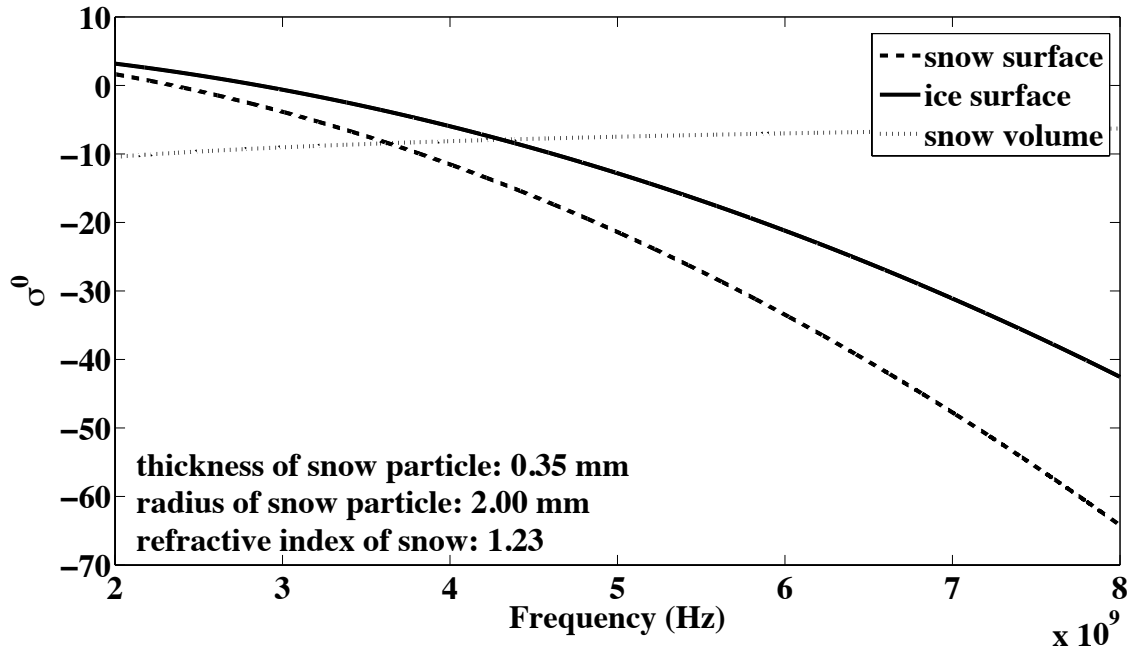


Figure 3.16: Snow volume scattering contribution to the backscattering coefficient as a function of frequency, demonstrating its increased contribution. Consequently, reducing the chances of the radar in receiving returns from the full transmitted bandwidth.

snow cover, demonstrating that volume backscatter can lead to ambiguity in detection at higher frequencies.

The dependence of volume scattering on small changes in refractive index, grain size and wetness is simulated and displayed in figure 3.17. These calculations demonstrate that volume scattering is more sensitive to changes in refractive index than grain size and wetness individually. In future work it may become possible to distinguish the exact contribution of volume scattering to the total power received by the radar with accurate knowledge of the snow surface characteristics. This may enable remote sensing studies of the snow structure and morphology.

3.5 Summary

The possibility and likelihood of unambiguously detecting and resolving the air/snow and snow/ice interfaces are described, and the necessary conditions for unambiguous detection are quantified.

Calculations of surface roughness using laser data gathered over fast ice in Antarctica have demonstrated that while specular reflection is unlikely, the surface does not have large-scale

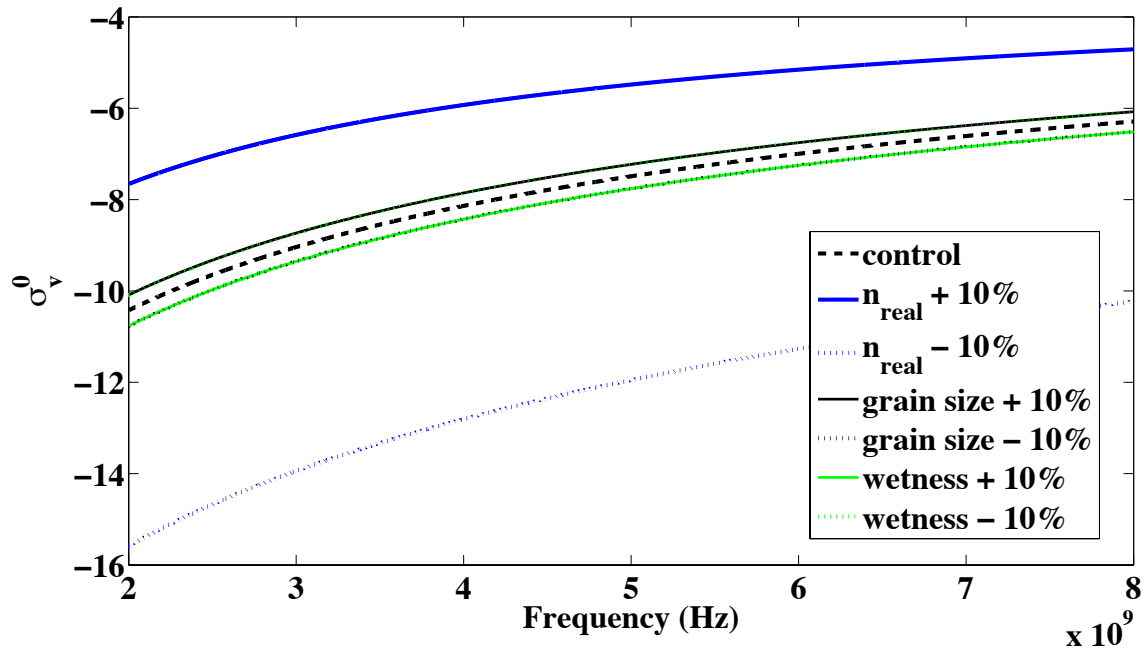


Figure 3.17: Volume scattering sensitivity to changes in: refractive index, grain size and wetness.

roughness features that interfere with the identification of the air/snow and snow/ice interfaces. It is argued that in areas of high deformation, identification of the two interfaces may still be possible if the power from the snow/ice interface is greater than that from the air/snow interface.

Approximations of the backscattering coefficient demonstrated that, on average, the condition that the scattered power from the snow/ice interface be greater than the scattered power from the air/snow interface is satisfied.

For the successful operation of RAASTI the surface and subsurface roughness features are critical.

Chapter

4

Sled-Based Radar Tests - Fast ice, Davis Station, Antarctica

Thus far, the frequencies employed by RAASTI have been assumed to penetrate a dry snow pack. However, it is not obvious that they necessarily will, given the actual dynamic nature and structural characteristics of snow cover on sea ice. Chapter 3 presented the conditions for unambiguous identification of the interfaces, and argued that these conditions could be met for snow over sea ice. Nonetheless, it remains extremely difficult to predict the nature of radar returns¹ air/snow and snow/ice interfaces (Axelsson, 1978; Moore and Williams, 1957).

To better understand RAASTI's mode of operation, and the behaviour and nature of the return signal, the radar was prepared for sled-based experiments. These experiments removed the uncertainties of motion and noise associated with helicopter operation and enabled a controlled study of the variation in returns from snow over fast ice in the vicinity of the Australian Antarctic Station, Davis, (68°35' S, 77°58' E). The sled platform provided a controlled environment in which *in-situ* measurements could be taken directly under the area viewed by the radar.

4.1 Radar Operating Conditions and Assumptions

Two assumptions were made when operating the radar from a sled-based platform. Firstly, that the system non-linearities could be ignored, and secondly, that incident signals were subject to specular reflection. The first assumption is justified by considering the small separation between the radar antennas and the surface. In sled-based operation, the received signal arrives with such a small (nanosecond) time delay from the transmitted signal that large non-linearities can be tolerated before the frequency deviation is > 800 Hz (i.e. able to encroach on a neighbouring range bin). This concept is explored in more detail in chapter 5.

¹For instance the changes in: return peak width, power level (due to uncertainties in the instrument phase noise properties), and antenna beamwidth changes with frequency, and the reality of the highly heterogeneous structure of the sea ice and its snow cover, are difficult to quantify when aiming for clear mathematical expressions with tractable solutions.

The second assumption is justified by an examination of the surface conditions sampled by the RAASTI's active area. The two horn antennas (*ETS-Lindgren*) used in these experiments, have a 60° beamwidth. Assuming that they are co-located², and using the results from chapter 2, the active area is calculated as:

$$\begin{aligned} A &= \pi \cdot x_1^2, \\ &= \pi(0.28)^2 \approx 0.25 \text{ [m}^2\text{]}. \end{aligned}$$

As such, the RMS height that can be expected over this area is less than 5 mm. Since these surface roughness features satisfy the Rayleigh conditions, it may be concluded that the viewing surface is likely to appear specular in sled-based operations.

Justification for the second assumption is not based on the case that the nature of the surface changes depending on type of radar used and its height from the ground. The argument here is that depending on the height of the radar, the active area (*spot* on the ground seen by the radar) changes. This change in the size of the illuminated area on the ground alters the spatial sampling frequency of the radar. In chapter 3, the laser sampling of the surface demonstrated that sampling over areas less than 50 m, undersamples the surface. Consequently, a spot size of 0.25 m^2 will considerably under-sample the surface, and in this case the surface will appear *smooth*, given the low vertical height distribution relative to the radar wavelengths. As an example, figure 4.1 provides a snap shot of the vertical distribution of surface height changes over a horizontal distance of approximately 250 mm.

²Being approximately 300 mm apart, and 1.6 m from the ground, this is a fair assumption (see appendix A).



Figure 4.1: An example of a snow pit demonstrating the small vertical scale variability of surface height over decimetre scales. Various features of this snow pit were frequently observed in the sled-based study, such as the large depth hoar crystals and slush layer at the snow/ice interface. Additionally, a layer of dirt, probably blown from the Vestfold Hills appears about 35 mm above the ice surface.

4.1.1 Experimental Description

Two types of experiments were conducted from the sled-based radar platform:

Type I A series of static tests in which the radar reflections from a single area were recorded and snow thickness measured. *In-situ* measurements of snow density and layer thickness were made.

Type II The sled was drawn over a transect, and the radar signature and *in-situ* snow thickness recorded every meter.

The thickness measurements were made with a folding measuring rule (see figure 4.2), and density samples were taken with a sampling tool shown in figure 4.3.



Figure 4.2: An example snow pit with layering present.



Figure 4.3: Snow density sampler tool, shown here filled with snow from a snow pit. Collecting a known volume of snow, allows the density of the weighted sample to be calculated.

4.2 The Physical Conditions of Snow on Fast Ice, Davis Station

The sled tests were conducted during the late spring/early summer. Consequently, relatively warm air temperatures ($\approx 0^\circ\text{C}$) were experienced and occasional positive air temperatures were recorded. These conditions could have lead to melting/decay of the fast ice around Davis Station or as proposed by *Crocker and Wadhams* [1989], a product of swell penetration, as overnight the complete fast ice cover (having an average thickness of 1.5 m) disappeared. Frequent winds blowing over the Vestfold Hills during blizzard conditions deposited dirt, as well as fresh, sticky snow on the fast ice. The snow studied in these experiments was often only lightly packed on the surface, comprising of large depth hoar crystals. Moreover, slush at the ice interface was frequently observed.

4.3 Results

4.3.1 Type I: Snow Pit Analysis

Six experiments were conducted, all nearby the Australian Antarctic Station - Davis. Even within the close geophysical proximity of the experiments (no more than 1 km apart - although GPS coordinates were not recorded), a large variety of snow pack density and stratigraphy was observed. Figures 4.4, 4.5, 4.6, 4.7, 4.8, and 4.9 present a summary of the *in-situ* measurements as well as the radar recorded signatures as a function of distance³, and *in-situ* conditions recorded for the six snow pit studies. The air/snow and snow/ice interfaces were expected to correspond to the greatest changes in refractive index. Consequently, two strong peaks in the radar data are expected to indicate their presence, and the separation of the peaks to indicate the thickness of the snow layer.

Table 4.1 summarises the estimates of snow thickness measured *in-situ* and the snow thickness derived from data collected by the radar. The snow pack thickness estimated from the radar compares well with the *in-situ* measurements. Considering that the vertical range resolution is theoretically 32.5 mm^4 , the agreement between the values is reasonable. The discrepancies, and observations regarding the relative amplitude are explained below on a case by case basis:

³The return from the metal plate occurs between 6 m and 7 m, which is much greater than the height of the antennas above the surface due to additional delay that the signal suffers from the cables connecting the antennas, and radar internal component delay.

⁴Provided with a 6 GHz bandwidth, as section 2.3.2 calculates, the vertical range resolution is 25 mm. Consequently, when a Hamming window is applied to the data this increases by 1.3 to: 32.5 mm.

Pit #:	<i>In-situ</i> depth (mm)	Radar derived depth (mm)
1	63.5	63.0
2	169.0	118.0
3	123.5	127.0
4	148.0	149.0
5	745.0	642.0
6	153.0	147.0

Table 4.1: Comparison between the *in-situ* measured and radar estimated snow thickness pit measurements (theoretical radar range resolution of 32.5mm).

Pit #1 The radar performed well, reporting a snow thickness well within the range resolution limits. This was a result of a well-packed and dense snow cover, coupled with a dry and solid underlying ice surface. However, a comparison of the Fresnel coefficient term (R^2), which captures the theoretical percentage power that should be reflected at the air/snow and snow/ice interfaces, with the actual relative power levels of the two peaks identified as the relevant returns, indicates that the radar signal suffered a greater than anticipated power loss. This can be explained either by unaccounted scattering or, since the snow thickness is comparable to the wavelengths used (5 GHz is a 60 mm wavelength), by the influence of thin-film effects (*Born and Wolf*, 1965), and related phenomena requiring further study.

Pit #2 The radar waveform does not display a peak that can be identified as the snow/ice layer. Hence, a comparison is provided between the radar return from the untouched snow surface, and the radar return from the same surface, but with the snow cleared. The absence of reflection can be explained by the fact that the surface layer was found to be wet, with large snow grains and hence likely to have absorbed all incident radiation.

Pit #3 The *in-situ* and radar measurements are within the range resolution. The minor discrepancy is explained by signal reflection from an unobserved density change at the bottom of the snow layer before reaching the ice surface. The layering present in the snow pack was measured with a rule, but density samples were not taken due to time constraints during the experiment.

Pit #4 The *in-situ* and radar measurements are within the range resolution. An internal peak is seen at a distance of 58 mm away from the air/snow peak in the radar return, but this is not corroborated by visual evidence. This could be due to an unobserved density change.

Pit #5 The last visually recorded layer is not detected by the radar, and this is explained by the fact that the bottom was found to be wet and slushy and hence impenetrable to the radar signal. This likely resulted from the increasingly warmer weather conditions experienced later in the study.

Pit #6 The *in-situ* and radar measurements are within the range resolution; the relatively small difference is likely due to the presence of a slushy bottom layer.

In general it was observed that *in-situ* measurements visually identified layers in the snow pits, which were frequently not detected by the radar. This is likely due to the fact that the thickness of the layers was comparable to the wavelengths used. However, with increasing frequency (smaller wavelength) such layering should be detected, as reported by *Marshall et al.* [2008b] and *Koh et al.* [1996].

In future work, enabling this radar with a capacity for detecting not only the thickness of the snow, but also layering within the snow pack would allow for increased understanding of the nature of snow accumulation. Potentially allowing for a judgement to be made on recent weather, and wind conditions.

Pit # 1: 18th November, 2008

Air temperature: -4.2°C

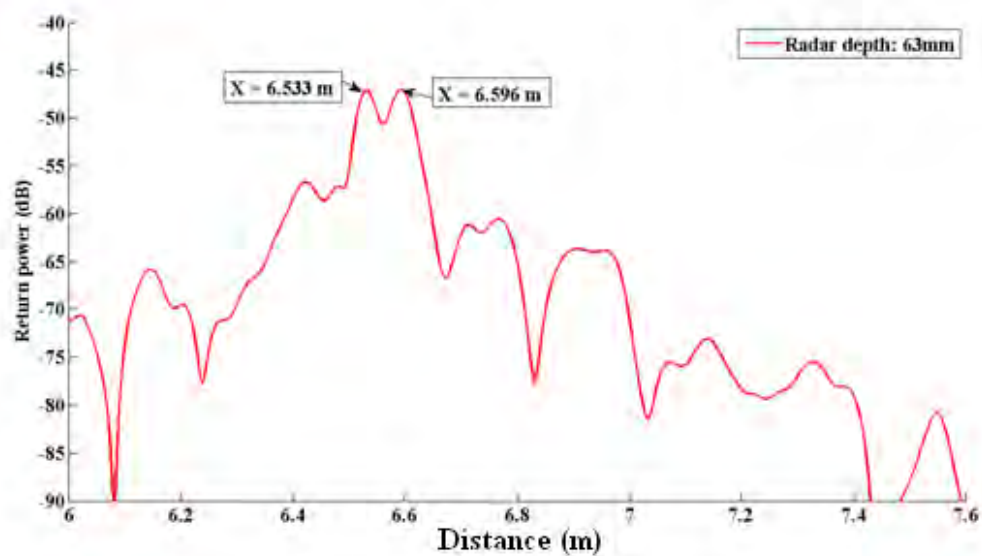
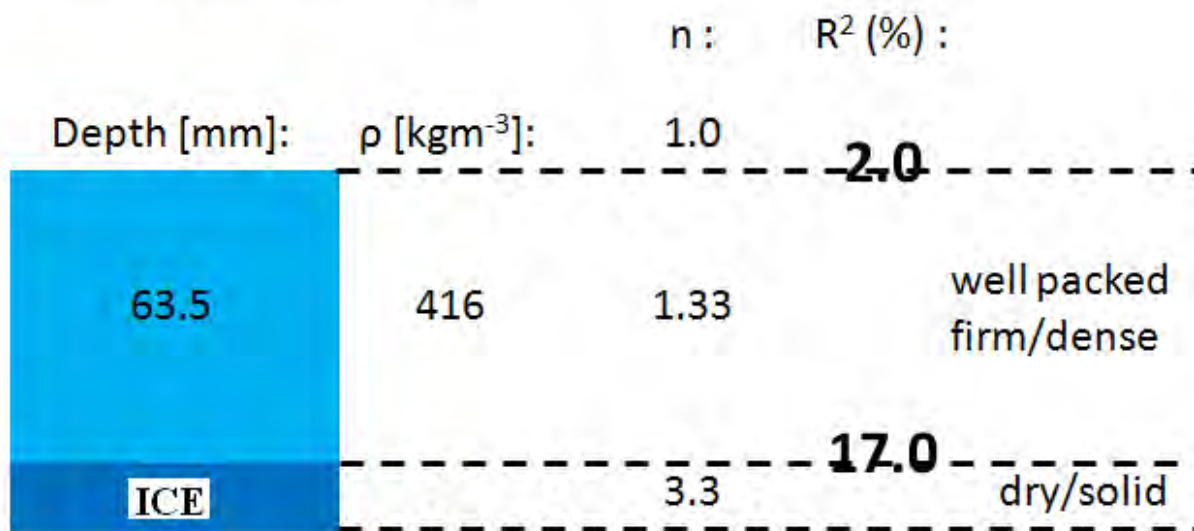


Figure 4.4: Pit #1 experiment.

Pit # 2: 21st November, 2008

Air temperature: +1.2°C

		n :	R ² (%) :
Depth [mm]:	ρ [kgm ⁻³]:	1.0	2.22
13.8	440	1.35	0.21
45.0	581	1.48	0.08
110.0	493	1.40	16.34
ICE		3.3	

dirt layer

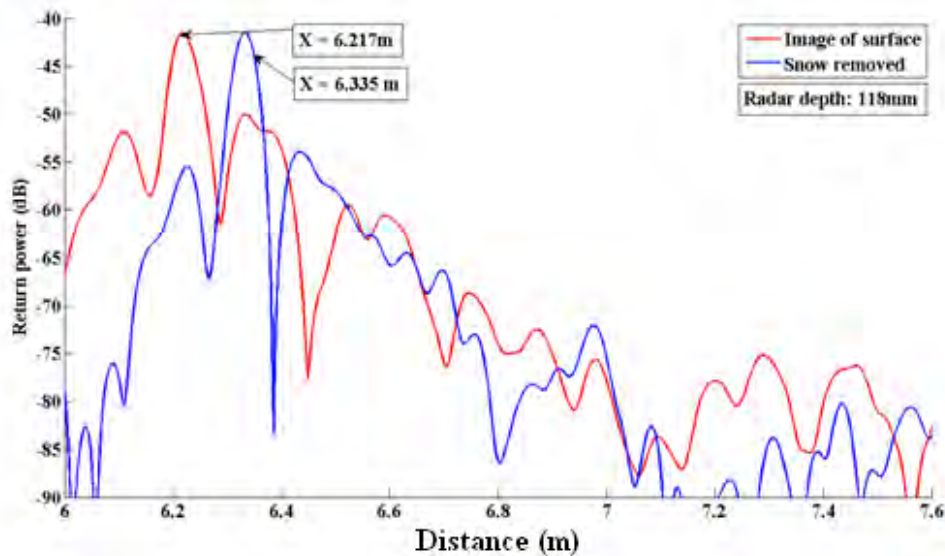


Figure 4.5: Pit #2 experiment.

Pit # 3: 23rd November, 2008
Air temperature: -0.2°C

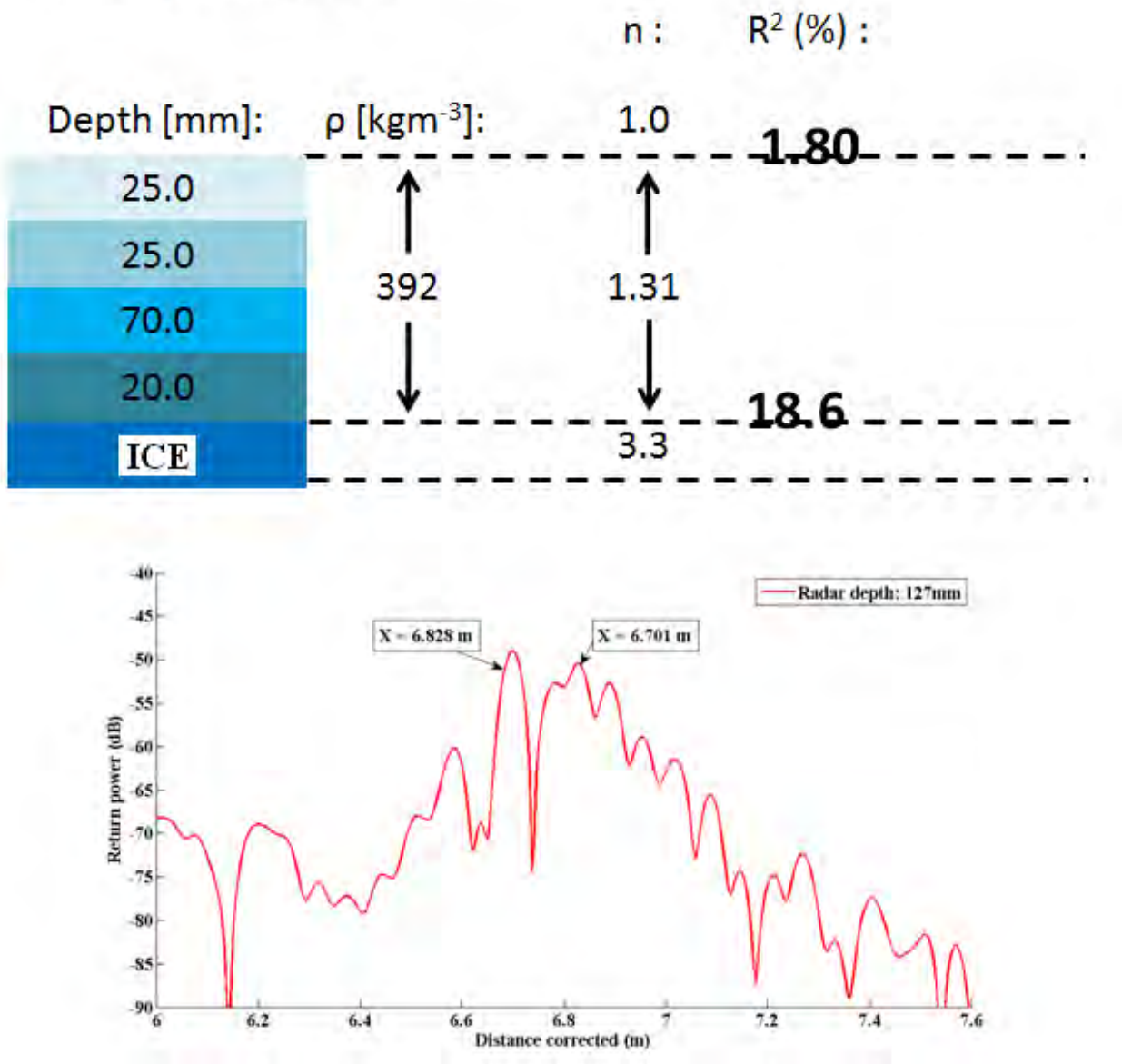


Figure 4.6: Pit #3 experiment.

Pit # 4: 23rd November, 2008

Air temperature: -0.1°C

		n :	R ² (%) :
Depth [mm]:	ρ [kgm ⁻³]:	1.0	1.7
110.0	373	1.30	0.013
38.0	410	1.33	18.1
ICE		3.3	

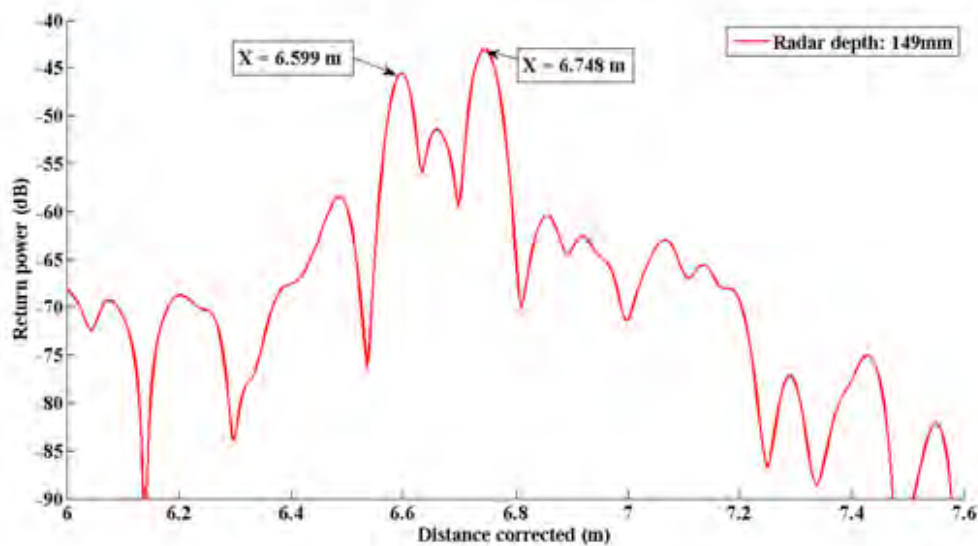


Figure 4.7: Pit #4 experiment.

Pit # 5: 25th November, 2008
Air temperature: +0.5°C

		n :	R ² (%) :
Depth [mm]:	ρ [kgm ⁻³]:	1.0	1.41
240.0	335	1.27	0.07
440.0	426	1.34	
65.0	667	1.55	0.53
ICE		3.3	13.02

wet/slushy
layer

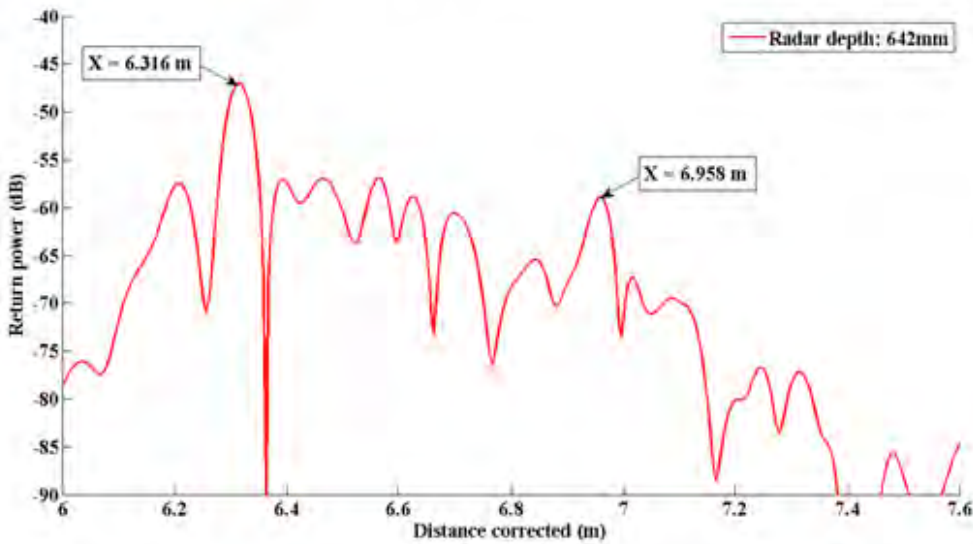


Figure 4.8: Pit #5 experiment.

Pit # 6: 26th November, 2008

Air temperature: +0.6°C

		n :	R ² (%) :
Depth [mm]:	ρ [kgm ⁻³]:	1.0	2.32
93.0	443	1.36	0.05
60.0	378	1.30	18.9
ICE		3.3	

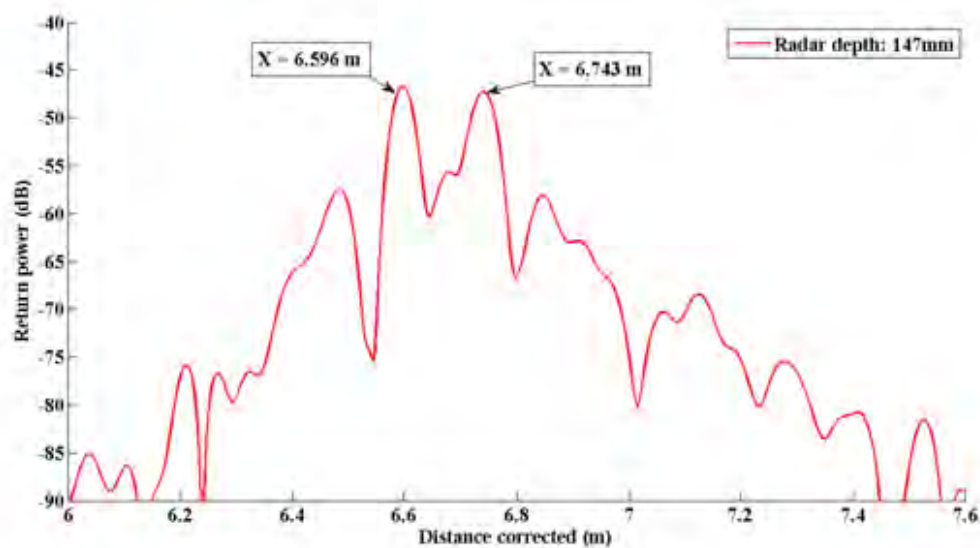


Figure 4.9: Pit #6 experiment.

4.3.2 Type II: Blizzard Tail Study

In all Type I experiments the *in-situ* measurements allowed for easier localisation of the peaks corresponding to air/snow and snow/ice interfaces in the radar return. This *a priori* knowledge of where to look for a snow/ice peak in the radar signal may have forced a conclusion that the radar was operational. To eliminate this possibility, RAASTI was drawn along a 50 m transect over a snow mound that had formed behind an island during a blizzard. At every meter, the radar signature was captured and snow thickness data measured *in-situ* with a ruler.

Figure 4.10 presents these data as a stacked spectrogram, along the x-axis are two radar returns for each meter, and along the y-axis are the FFT range bins (proportional to snow thickness). A single refractive index of 1.35 is used to convert the free-space distance to snow depth, and the red line represents *in-situ* measured depth. A simple peak-picking algorithm was written in MATLAB to detect the air/snow and snow/ice peaks in the radar data based on their relative power levels. A correlation of 0.92 is found between the radar derived and *in-situ* measured depths.

The blizzard tail data shows a strong power return at the air/snow interface, and a considerably weaker return at the snow/ice interface. As previously mentioned, this is likely accounted for by the wetness and possible salinity of the snow pack⁵. However, it also poses the question of whether or not the full signal bandwidth manages to penetrate the snow pack, be reflected from the snow/ice interface, and reach the receiver above the noise floor of the radar. Both penetration and reception of the full transmitted bandwidth is necessary to achieve the expected vertical range resolution.

⁵Wetness of the snow was observed, but neither the wetness nor the salt content of the snow directly measured.

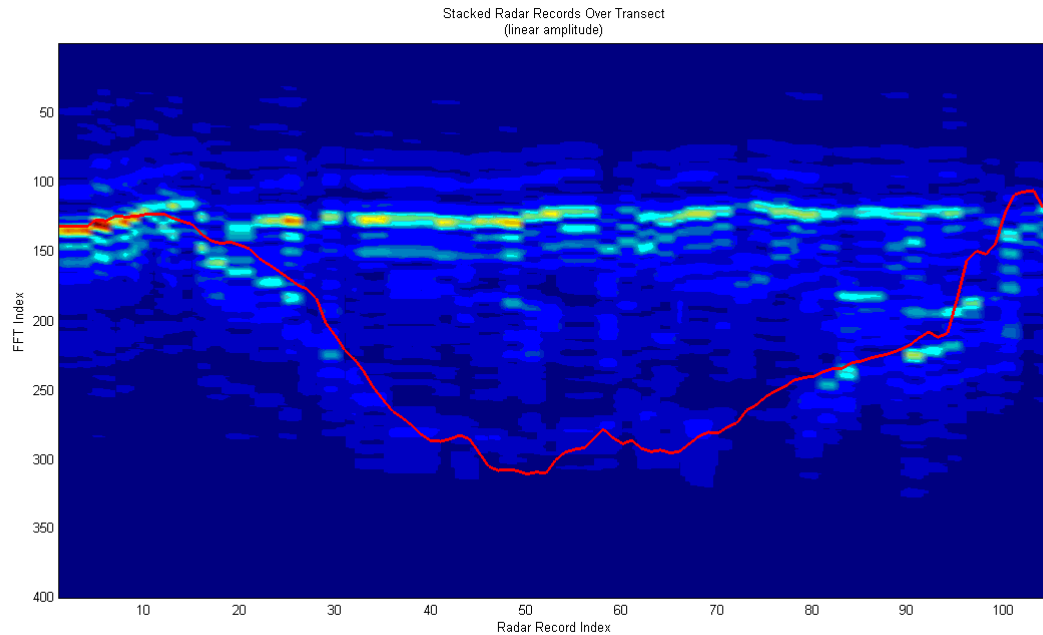


Figure 4.10: The radar view of the blizzard tail, created by stacking radar returns recorded every meter. The red line is an example pick of the snow/ice interface.

Usable Bandwidth

To confirm that the received bandwidth of the radar contains data from the air/snow and snow/ice interface reflections, the return signal was split into smaller bandwidths and the spectrograms compared. This test validated the employment of the whole bandwidth of the radar in resolution calculations.

In future experiments, careful calibration of the radar transmit power across the full bandwidth would make it possible to use the returns from separate frequency bands to study the penetration depth of the signal into snow pack. This would allow for estimation of snow pack, since snow wetness strongly affects the power level of the return signals.

Figure 4.11 plots the radar return when the complete transmitted bandwidth is processed, while figures 4.12, 4.13, and 4.14 show the same data but processing only 2.2 - 4.1; 4.1 - 5.9; 5.9 - 7.8 GHz of the bandwidth respectively. Comparing the layers present in the figures demonstrates that indeed the full bandwidth of the radar contains information from the air/snow and snow/ice reflections. Additionally, as has previously been reported by *Marshall et al.* [2008b], higher

frequencies are more sensitive to layering within the snow pack. In this case, when the bands are individually studied, the reflections from the layers are strong enough to be clearly observed.

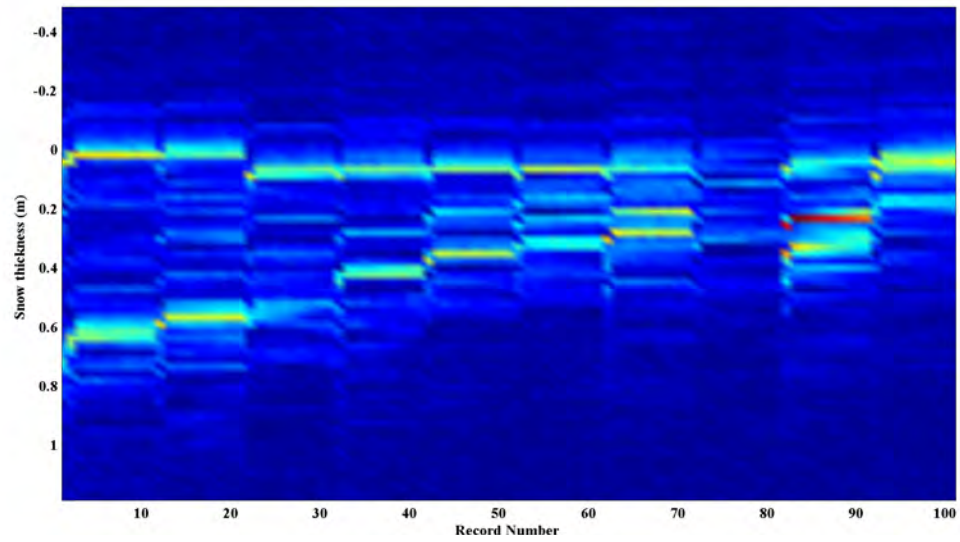


Figure 4.11: Radar view of the end of the blizzard tail: full bandwidth. The snow/ice interface is clearly visible.

4.4 Summary

This chapter presents the results of six sled-based experiments that demonstrate two important features of RAASTI's operating capacity. Firstly, they demonstrate a sufficient level of agreement between measured and estimated snow thickness data. Secondly, they show the penetration of the full transmitted bandwidth into the snow pack, a measure that is important for range resolution estimation. Exact correspondence between the *in-situ* measured and radar estimated snow thickness results, however, should not be expected. The two methods cannot be expected to achieve one-to-one correspondence. The loss of power level in the returned signals was greater than theoretically anticipated (using the Fresnel formula). This observation is likely explained by snow wetness and possible salinity, neither of which were measured in these experiments but should be studied in future work.

These sled-based results also highlight the need for improved understanding of the interaction of the 2 - 8 GHz radiation (at 150 - 37.5 mm wavelength) with snow pack which is of comparable depth to the wavelengths. The questions to be answered are: if snow is capable of displaying a thin-film effect, whereby destructive interference will occur at wavelengths matching the snow thickness, what is the effect on the chirp waveform? Is it strong enough to be detected? How do icy layers which are usually < 37.5 mm in thickness affect the signal? Is this a strong enough signature to be detected?

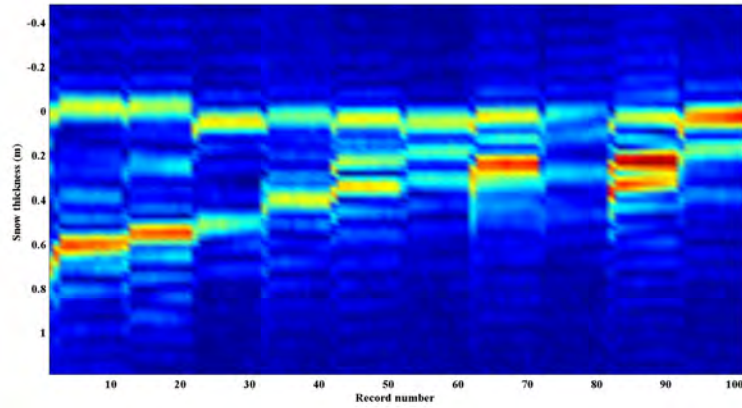


Figure 4.12: Radar view of the end of the blizzard tail: 2.2 - 4.1 GHz.

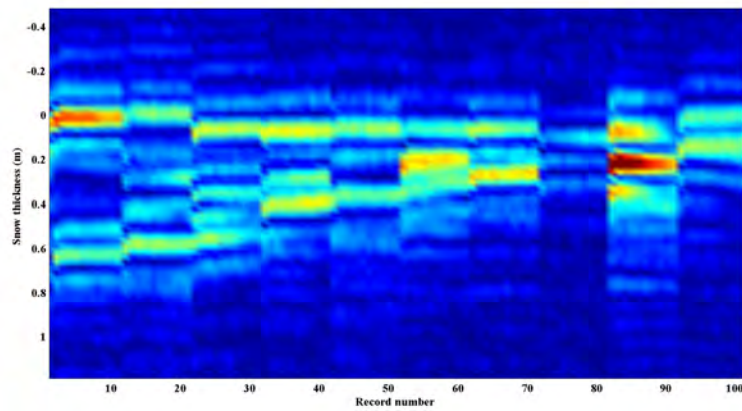


Figure 4.13: Radar view of the end of the blizzard tail: 4.1 - 5.9 GHz.

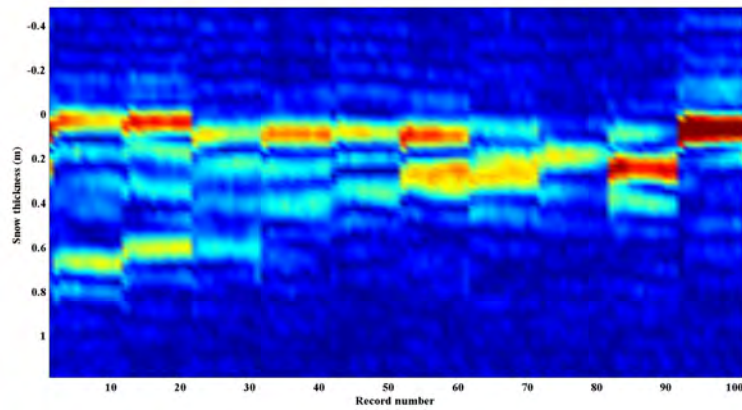


Figure 4.14: Radar view of the end of the blizzard tail: 5.9 - 7.8 GHz.

Chapter

5

Development of a Non-linearity Correcting Algorithm

In FMCW radar as the frequency generator sweeps from 2 - 8 GHz during radar operation, systematic and random phase errors present in the generator degrade the linearity integrity of the sweep (*Griffiths*, 1991). The radar data collected from a helicopter-borne platform is found to be highly corrupted by this noise, which causes spreading of the detected difference frequency for each target. Figure 5.1 provides one example of this, a spectrogram of radar data collected over sea ice from a helicopter, where a loss in distinction of the reflections from the air/snow and snow/ice interfaces can be seen. The similarity and repeated features in this spectrogram lead to the conclusion that they are a product of a systematic error source. It is impossible to identify the air/snow and snow/ice reflection lines with fine resolution as the frequency spread causes a range ambiguity over at least 2 m. Consequently, before any attempts can be made to extract the air/snow and snow/ice interface information this error must be corrected.

This chapter presents a description and results of the application of a non-linearity correcting algorithm developed to assist in the analysis and information extraction from the radar signal. Firstly, a description is provided of the nature of the error in the radar signal. Secondly, using this information a model of the error is presented which naturally leads to an algorithm for correcting these errors. Finally, the results of the application of the correction method to raw radar data are presented and discussed.

5.1 Problem Description

The bandwidth of a radar system is defined as: $BW = f_H - f_L$ (*Harmuth*, 1981), i.e. the difference between the highest and lowest frequencies accepted by the receiver. This bandwidth sets the theoretical limit to the achievable range resolution of a radar, related to the bandwidth by: $\delta R = c/(2BW)$.

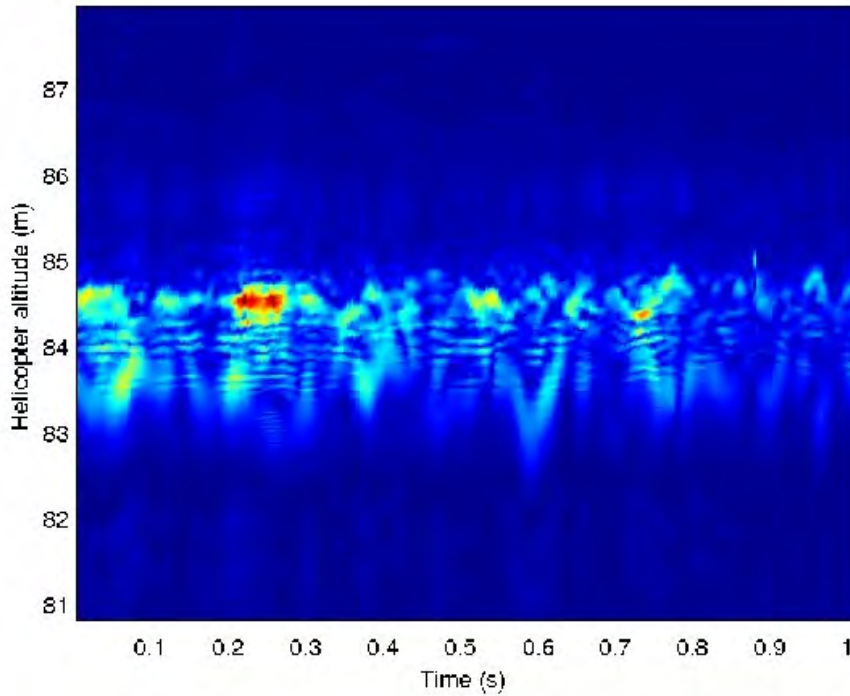


Figure 5.1: Spectrogram of raw radar data illustrating the ≈ 2 m smearing in the IF. The identification of the air/snow and snow/ice interfaces is impossible.

By nature of the processing involved in FMCW radar, this bandwidth is provided by a linear sweep (also referred to as a *linear chirp*) of frequencies between f_L and f_H (see section 2.1). Unlike pulse or step frequency radar architectures, it is the degree of linearity of this sweep that affects how closely the actual resolution approaches the theoretical. For the best possible performance, all the frequencies within the bandwidth must be present, and the transition from one to the other must be in a strict linear fashion.

As the frequency generator sweeps from f_L to f_H , a large non-linearity is imparted on the transmitted signal. This signal is subsequently reflected from the medium, received by the radar, and mixed with the transmitted signal. The mixing of the two non-linear chirps is what consequently leads to “smearing” observed in the radar data. This smearing makes it difficult to accurately determine the location of the air/snow and snow/ice interfaces. Figure 5.2 compares the idealised linear transmitted frequency as a function of time in order to achieve the theoretical range resolution, with the actual frequency non-linearities imparted on the linear sweep (as derived from the radar during operation, see section 5.3.3).

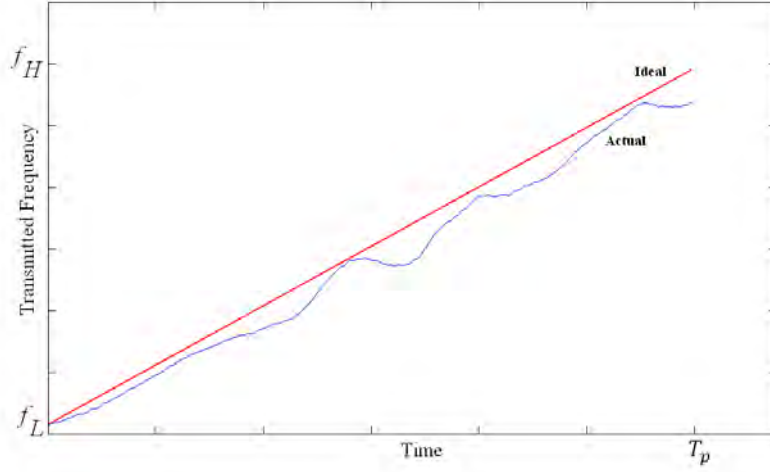


Figure 5.2: Comparison between the ideal and actual transmitted frequency as a function of time.

5.2 Assumptions

The algorithm presented here is derived under the assumption that the smearing of the radar return signal is dominated by errors generated by the oscillator (frequency or chirp generator) of the radar. This implies that the error is contained in the transmitted signal only which is then reflected from the target, received, mixed with the original transmitted signal and digitised.

Conventionally, the errors in the oscillator leading to non-linear variations in the transmitted signal are captured by a phase error term $\epsilon(t)$ (Griffiths, 1991), and FMCW radar signals under these error conditions are frequently written as:

1. Transmitted signal:

$$s_t(t) = \mathcal{R}e \left(\exp(j2\pi(f_L t + \frac{1}{2}\alpha t^2 + \epsilon(t))) \right), \quad (5.1)$$

2. Received signal:

$$s_r(t) = s_t(t - \tau), \quad (5.2)$$

3. IF signal:

$$s_{IF}(t) = \mathcal{R}e \left(\exp(j2\pi(f_c \tau + \alpha t \tau - \frac{1}{2}\tau^2 + \epsilon(t) - \epsilon(t - \tau))) \right), \quad (5.3)$$

defined for $0 \leq t \leq T_p$, where f_L is the start frequency, α is the chirp gradient given by BW/T_p , τ is the delay to the target given by $2R/c$, and $\epsilon(t)$ is the phase error term, or the time dependent

phase non-linearity. In the above formulation this phase error term $\epsilon(t)$ in essence combines all the possible sources of error that lead to deviations of the chirp from a linear frequency function (or quadratic phase function). This aggregation of errors into a single term does not reflect contribution of possible sources of error, making it difficult to extract or model the nature of the non-linearities. Hence $\epsilon(t)$ is only a coarse, high level model of the nature of the non-linearities. In this form it is the *effect* of the non-linearities generated by the oscillator that are modelled, and not the *cause*. This is similar to looking at a situation where a constant force is applied to a mass to cause continuous acceleration. Noticing that the acceleration is not constant the non-linearities detected in the acceleration are modelled, instead of modelling the non-linearities present in the force.

It is possible to gain deeper insight into the problem with a model that is closer to the physical source or *cause* of the non-linearities. Consequently, it is proposed here to represent the non-linearities as affecting the gradient of the frequency, making α time dependent:

$$\alpha(t) \equiv \alpha(1 + \epsilon(t)), \quad (5.4)$$

where $\epsilon(t)$ is now a continuous small perturbation about 0, leading to deviations in the frequency gradient. Consequently, the new expressions for the transmitted and received frequencies are:

1. Transmitted frequency:

$$f_t(t) = f_L + \alpha(t)t, \quad (5.5)$$

2. Received frequency:

$$f_r(t) = f_t(t - \tau), \quad (5.6)$$

3. IF frequency:

$$f_{IF}(t) = \alpha\tau + \underbrace{\alpha t(\epsilon(t) - \epsilon(t - \tau))}_{\text{chirping term}} + \underbrace{\alpha\tau\epsilon(t - \tau)}_{\text{spread term}}, \quad (5.7)$$

where $\epsilon(t)$ is now the *frequency* non-linearity error term.

With a perfectly linear system, the frequency due to a single target would lead to only the first term ($\alpha\tau$) being present in equation 5.7. The additional terms now present allow for an assessment of the effect that the non-linearities have on the ideal response. It is observed that the non-linearities introduce *chirping* as characterised by the middle term, and cause *spreading* about the target frequency (last term). The culmination of these effects leads to a broadening of the resulting

difference frequency as illustrated in figure 5.3. The next section will further illustrate the effect that these terms have on the ideal response.

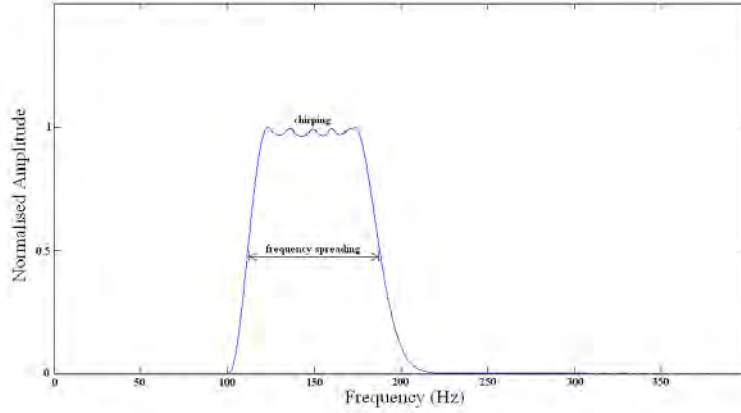


Figure 5.3: Spreading in the difference frequency caused by non-linearities in the transmitted chirp, which degrades the frequency resolution of the radar, and also the vertical range resolution.

5.3 Non-linearities as a Function of Target Range

This section further explores the nature of the two components due to the non-linearity arising from the modified model presented, as well as demonstrating the effect of these components on the radar signal for targets at different ranges. It is shown that for close-range targets, a large frequency error can be tolerated without any correction, supporting the observation that the given radar is able to measure snow depth from a sled-based platform (target range $< 1.6\text{m}$) whereas from a helicopter platform (target range $> 50\text{ m}$) the data become unusable without some form of correction.

5.3.1 Analysis

The simplest example of a non-linearity error is a single change in gradient that can be approximated by a piecewise continuous linear curve, as shown in figure 5.4. In this case the transmitted frequency is written as:

$$f_t(t) = \begin{cases} f_L + \alpha_1 t, & 0 \leq t < \frac{T}{2} \\ f_L + \alpha_1 \frac{T}{2} + \alpha_2 (t - \frac{T}{2}), & \frac{T}{2} \leq t < T \end{cases} \quad (5.8)$$

where α_2 represents a small shift in the chirp gradient during the chirp duration. The received frequency $f_r(t)$ being a delayed version of $f_t(t)$, is:

$$f_r(t) = f_t(t - \tau) = \begin{cases} f_L + \alpha_1(t - \tau), & \tau \leq t < \frac{T}{2} + \tau \\ f_L + \alpha_1 \frac{T}{2} + \alpha_2(t - \frac{T}{2} - \tau), & \frac{T}{2} + \tau \leq t < T + \tau \end{cases} \quad (5.9)$$

After the mixing process, the IF frequency will be:

$$f_{IF}(t) = f_t(t) - f_r(t) = \begin{cases} f_L + \alpha_1(t - \tau), & 0 \leq t < \tau \\ \alpha_1 \tau, & \tau \leq t < \frac{T}{2} \\ \alpha_1(t + \frac{T}{2} - \tau) + \alpha_2(t - \frac{T}{2}), & \frac{T}{2} \leq t < \frac{T}{2} + \tau \\ \alpha_2 \tau, & \frac{T}{2} + \tau \leq t < T \\ f_L + \alpha_1 \frac{T}{2} + \alpha_2(t - \frac{T}{2} - \tau), & T \leq t < T + \tau \end{cases} \quad (5.10)$$

It can be seen that the first and fifth terms (of equation 5.10) are in the GHz region, and hence will be either naturally or intentionally filtered from the IF signal. The second and fourth terms are the difference frequency components due to the target reflection. Under non-error conditions (i.e. when there is no shift in gradient) they would be equal, their inequality is the result of the shift in gradient. The third term represents a *chirping* period between the two frequencies provided by the second and fourth terms. Figure 5.5 plots the time domain IF signal as a function of time (over a single chirp interval), demonstrating the two difference frequency components ($f_1 = \alpha_1 \tau$ and $f_2 = \alpha_2 \tau$) and the chirping interval between them.

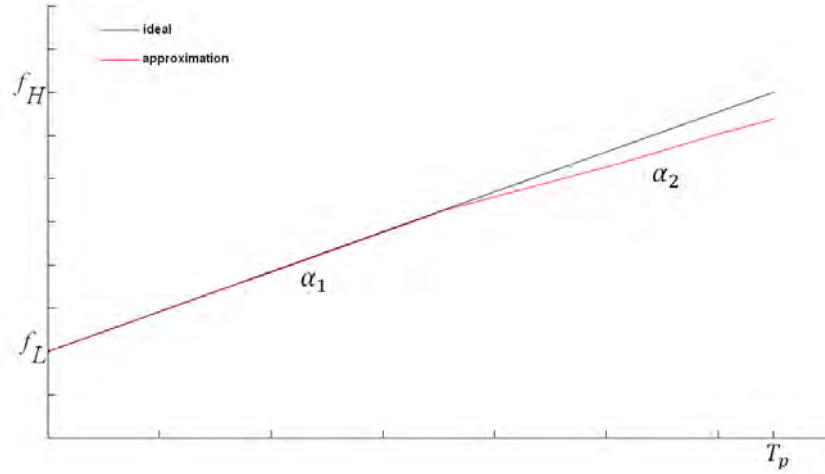


Figure 5.4: Piecewise approximations to a non-linear chirp, demonstrating a simplistic example a non-linearity errors that can be present in a linear chirp.

If the minimal frequency resolution is δf (which is 800Hz, in the case of this particular radar, section 2.3.1), the tolerated deviation in gradient from α_1 before there is a noticeable effect on the difference frequency can be calculated from:

$$\begin{aligned}\alpha_1\tau - \alpha_2\tau &> \delta f, \\ \Delta\alpha\tau &> \delta f.\end{aligned}\tag{5.11}$$

Table 5.1 summarises these results for increasing target range, showing that the smaller τ is, the greater tolerance there is to the difference between α_1 and α_2 . Hence, while the non-linearity in the transmit signal was the same for sled-based and helicopter-borne radar operation, due to the fact that there was only a small separation between the transmit and receive signals in the sled-based experiments, the IF was not visibly corrupted by noise.

Range (m)	1	10	100
$\tau(= 2R/c)$ (ns)	6.7	66	666
$\Delta\alpha$ (GHz/s)	120	12	1.2

Table 5.1: Sensitivity of gradient error to target range.

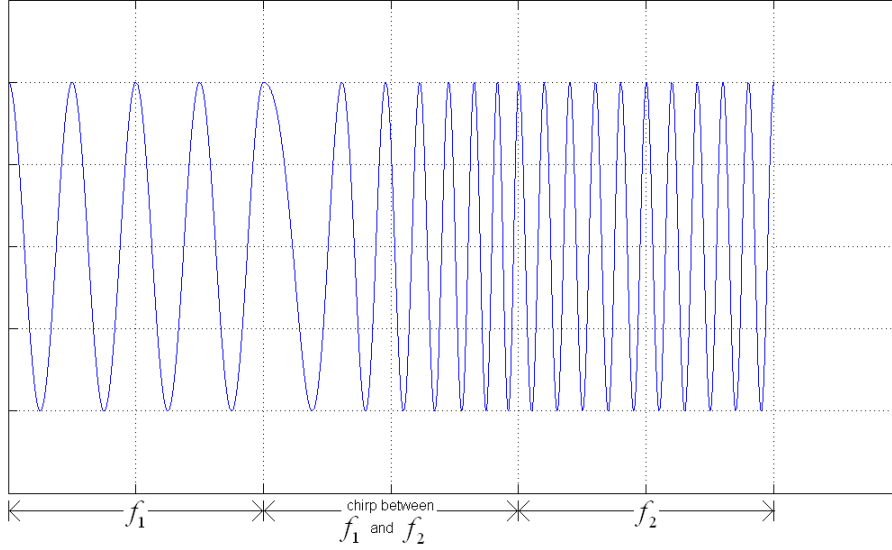


Figure 5.5: Non-linear chirp effects on the difference frequency. The change in gradient shown in figure 5.4 leads to a change in frequency from f_1 to f_2 , which must be affected by a chirp between them.

5.3.2 Non-linearity Characterisation

$\epsilon(t)$ is defined as the non-linearity function that characterises the non-linearities exhibited by α due to the YIG oscillator frequency stability and temperature characteristics. The assumption that $\epsilon(t)$ is a non-linearity function applied to α which moves about 0, implies that the difference term or chirping function (of equation 5.7) for the IF frequency could be seen as approaching zero and relatively non-influential on the rest of the expression. The dominant terms in the expression are thus the first and last terms. Hence the approximation is made that the general form of the IF frequency affected by non-linearities in the gradient is:

$$f_{IF}(t, \tau) = \alpha\tau + \underbrace{\alpha t(\epsilon(t) - \epsilon(t - \tau))}_{\text{chirping function} \rightarrow 0} + \alpha\tau\epsilon(t - \tau) \quad (5.12)$$

$$\approx \alpha\tau(1 + \epsilon(t - \tau)) \quad (5.13)$$

This is the non-linearity characterisation allowed for by the model, which is used to correct the systematic error in the radar signal. Writing f_{IF} as a function of both t and τ reflects the fact that, as the range between the radar and target increases (i.e. as τ increases) the effect of the error increases.

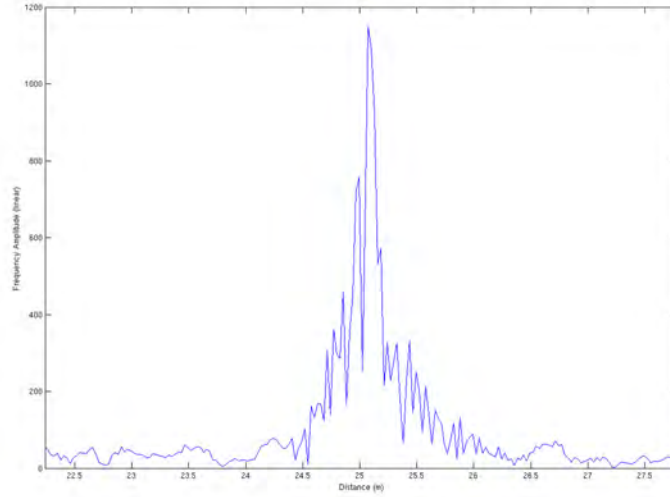


Figure 5.6: Delay line difference frequency spectrum. Ideally it should be a narrow peak, however under non-linearity conditions it is here seen to spread over 1 m.

5.3.3 Mitigation

The only way to correct for non-linearities in a radar retrospectively (in post-processing) is to have knowledge of their nature. The level of accuracy with which the non-linearities are known sets the upper bound on the performance capacity of any correcting algorithm. In order to quantify the non-linearities, a reference target was inserted into the radar system. A semi-rigid copper coaxial cable provides a reference target at approximately 25 m. Figure 5.6 shows the smearing of the radar return at the delay line, due to the non-linearities in the radar frequency generator. Using this information the non-linearities at that range are expressed as:

$$f_d(t, \tau_{ref}) = \alpha \tau_{ref} (1 + \epsilon(t - \tau_{ref})), \quad (5.14)$$

where τ_{ref} is the time delay associated with the delay line.

As it is known that the cable provides a target at a range of 25 m (noting the decrease in propagation velocity), $\alpha \tau$ is calculated for the delay line, and the error term isolated.

5.4 Non-linearity Correction Algorithm

The reference target provided by the delay line allows for the non-linearity effect to be captured at that specific range.

Whereas the reflection of interest will be at a different range, with the expression for the error at an arbitrary target (τ_T) being:

$$f_d(t, \tau_T) = \alpha \tau_T \epsilon(t - \tau_T). \quad (5.15)$$

Hence, one final approximation in the algorithm is made, by again exploiting the assumption that $\epsilon(t)$ is a slowly-varying function, i.e. that the errors experienced by the arbitrary target are similar to those of the delay line but are stretched in proportion to the target range:

$$\alpha \tau_T \epsilon(t - \tau_T) \approx \alpha \tau_T \epsilon(t - \tau_{ref}). \quad (5.16)$$

(If $\epsilon(t)$ was neither affected by the scattering/reflection process nor by the delay line, then this algorithm would not be necessary.)

This same approximation is used in the non-linearity correcting algorithm presented by *Vossiek et al.* [1996]. However, the non-linearity correcting algorithm they present is based on altering the IF sampling interval to compensate for the non-linearities of the transmitter. In contrast the algorithm presented here uses the above approximation to de-convolve the non-linearities from the target response. The following section tests this approximation.

5.4.1 Performance Simulation

In order to test this algorithm, a MATLAB[®] model was created. Two ideal targets located close to each other were simulated and a reference target was added to simulate the delay line. (The error function applied to the simulated returns was derived from the actual error found in the radar delay line.)

Figure 5.7 shows the simulation results where the ideal difference frequencies present in the mixed signal are compared with the difference frequencies after the non-linearities are imparted on the simulated transmitted signal. The figure demonstrates that due to the spreading caused by the

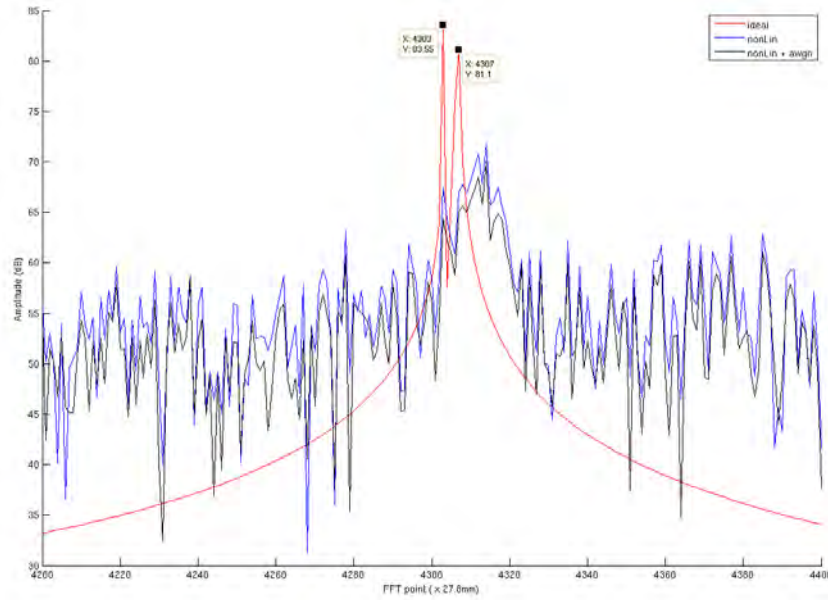


Figure 5.7: Simulated radar data of two targets; the ideal difference frequencies, and the difference frequencies derived when corrupted by transmitter non-linearities. The small shift between the ideal peak, and the peak retrieved after application of the non-linearity correcting algorithm occurs due to imprecise knowledge of the target's range by the algorithm. A time-domain window is used to approximately isolate the response from the air/snow and snow/ice surfaces in the waveform corrupted by non-linearities. The center of the window is assumed to be the location of the true target, however this is not always the case and consequently a shift in the peaks results. However as it is only the *difference* between the air/snow and snow/ice interfaces that is sought, the shift is immaterial for snow thickness extraction purposes.

non-linearity applied, it is unclear where the two targets are located. The non-linearity correcting algorithm was then applied to this data and the result is presented in figure 5.8. The results show that using the delay line response it is possible to correct the non-linearities experienced by the reflections from the air/snow and snow/ice interfaces. (The temporal shift between the two peaks after correcting for non-linearities is an artefact of zero padding in the non-linearity correcting algorithm, due to imprecise knowledge of the exact target range.)

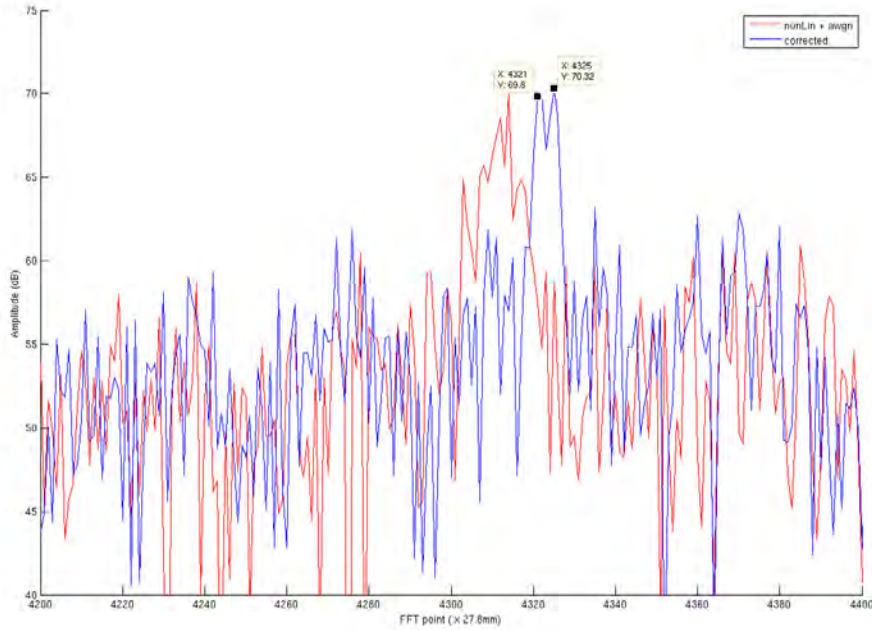


Figure 5.8: Non-linearity corrected simulated data of two targets. The red line shows the input data to the algorithm which is corrupted by non-linearities and white noise. The blue line is the effect of the algorithm in compensating for the non-linearities where two peaks (labelled) are seen.

5.5 Results

Applying this algorithm to the helicopter-borne radar data shows a marked improvement in the capacity for identification of the air/snow and snow/ice interfaces. Figure 5.9 is one example, where radar data are compared pre- and post-algorithm processing, showing that after application of the algorithm peak extraction becomes a tractable problem. The presence of two peaks above the noise-floor in the radar data is remarkable when compared with the degenerate nature of the raw radar signal. Furthermore, the appearance of the two peaks is not an artefact of the algorithm since no assumption is made of how many (if any) peaks must be present in the data. The rise in the noise floor of the signal around the two peaks is due to the localised nature of the algorithm which corrects for the error at a specific target only, degrading the error further at other locations.

Figures 5.10 and 5.11 (maintaining the same vertical and horizontal scales) compare the raw and processed radar data to further demonstrate the effect of the algorithm. This is applied to radar records stacked to show nine seconds of flight time, for a flight conducted over fast-ice in East

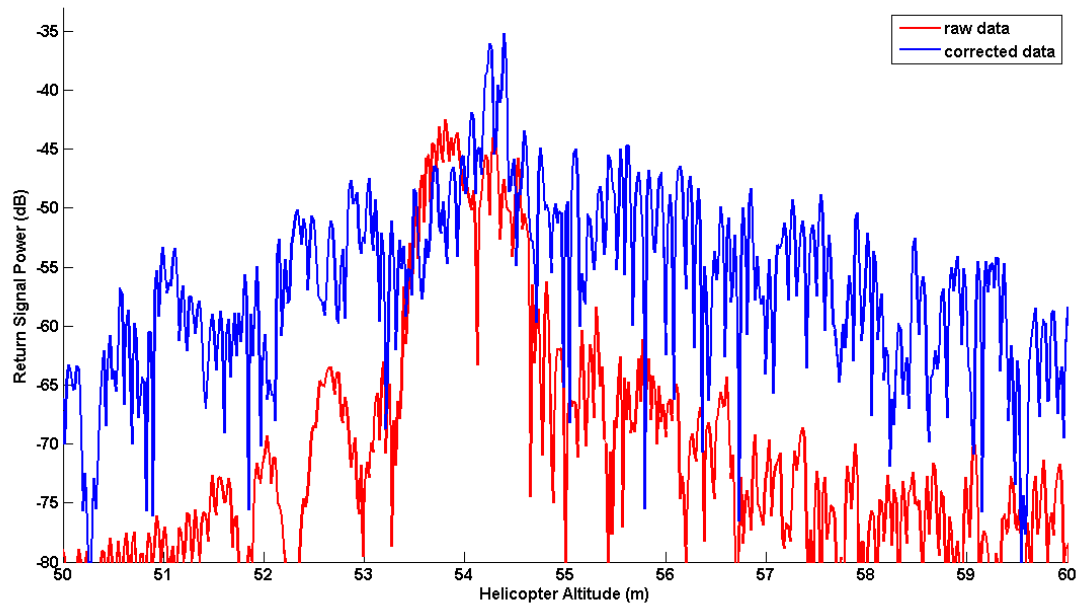


Figure 5.9: Comparison of algorithm effect on actual radar data. Signal power plotted as a function of helicopter altitude. The red line is the raw data where a signal power is seen to increase from about 53 m, however it is not possible to identify the presence of two surfaces. The blue line is the effect of the non-linearity algorithm correction to this data. Two peaks are clearly visible.

Antarctica, 2008. Figure 5.12 provides a zoomed in version of the corrected data where it becomes apparent that the radar receives returns from the air/snow and snow/ice interfaces which can be traced along the nine second flight. The fading observed in the signal between four and seven seconds is not an artefact of the algorithm, but could be explained by the presence of icy/hard surfaces of the wind packed snow. These significantly limit penetration of the radar signal into the snow pack, hence the absence of a distinct second surface. Alternatively, it may be due to the presence of very dry fluffy snow which is almost invisible to the radar (reflecting very little power) hence only the snow/ice interface is detected. In this particular case, it is likely that icy layers are the cause of the fading, as the data is collected over fast ice, where *in-situ* measurements detected many hard wind-packed layers.

The vertical excursions of the signal present in these figures are due to helicopter altitude variation. These may be corrected with accurate synchronisation of the radar and laser instruments however, this was not possible in these experiments as the radar signal is synchronised with the laser at second intervals only.

The interference in the radar signal present in the spectrogram as bright vertical lines (e.g. at approximately 5.5 seconds in figure 5.10) is considered to be due to a jitter of the phase in the time domain signal. Figure 5.13 is a time domain plot of the IF signal as a function of chirp time showing the presence of this jitter in phase the cause of which is not yet understood, but could be the result of helicopter vibration.

5.6 Summary

The development of an algorithm for non-linearity correction of the systematic frequency error generated by the oscillator is an essential element of this work. The algorithm was motivated by a new model for capturing the non-linearities in the chirp waveform. It is argued that this model captures the nature of the error generated in the oscillator. A study is made of the effect of these errors on the received signal with increasing range. The results of the study explain why the same radar can perform well from a sled-based platform, and at the same time data collected from a higher altitude platform is not usable without significant post-processing efforts.

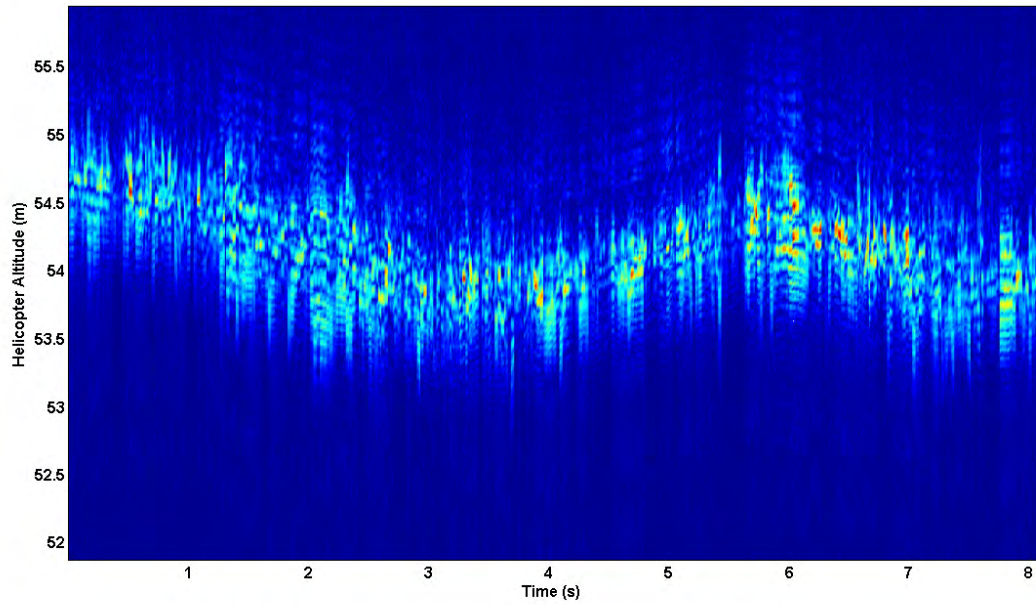


Figure 5.10: Spectrogram of raw radar data, the vertical axis plots the helicopter altitude in meters, and the horizontal axis is the time in seconds. It is very difficult to distinguish the surfaces if any present in the radar data.

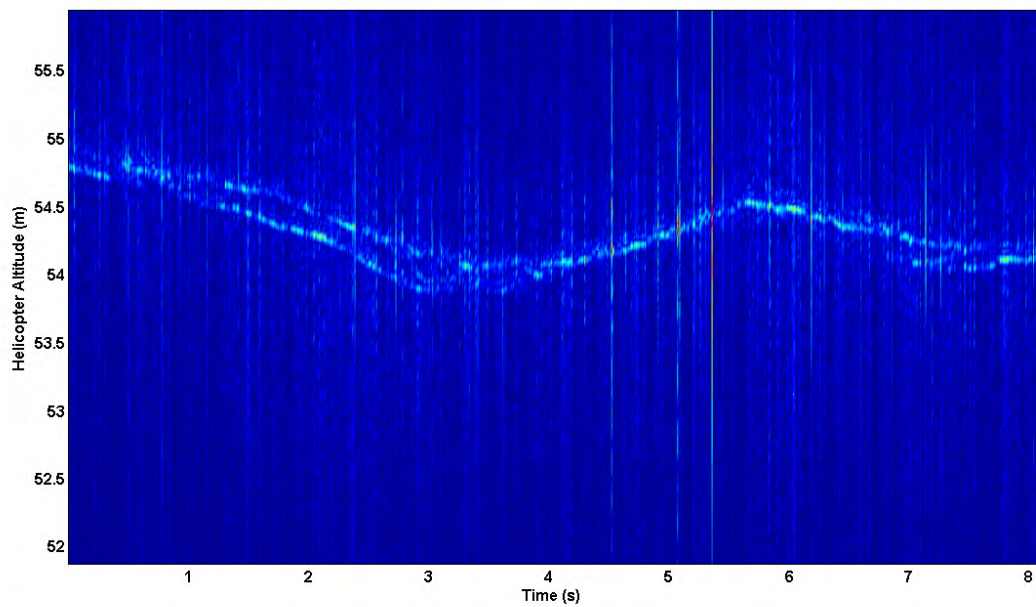


Figure 5.11: Spectrogram of corrected radar data, the vertical axis plots the helicopter altitude in meters, and the horizontal axis is the time in seconds. The application of the non-linearity correcting algorithm reveals the presence of two surface in parts of the radar data.

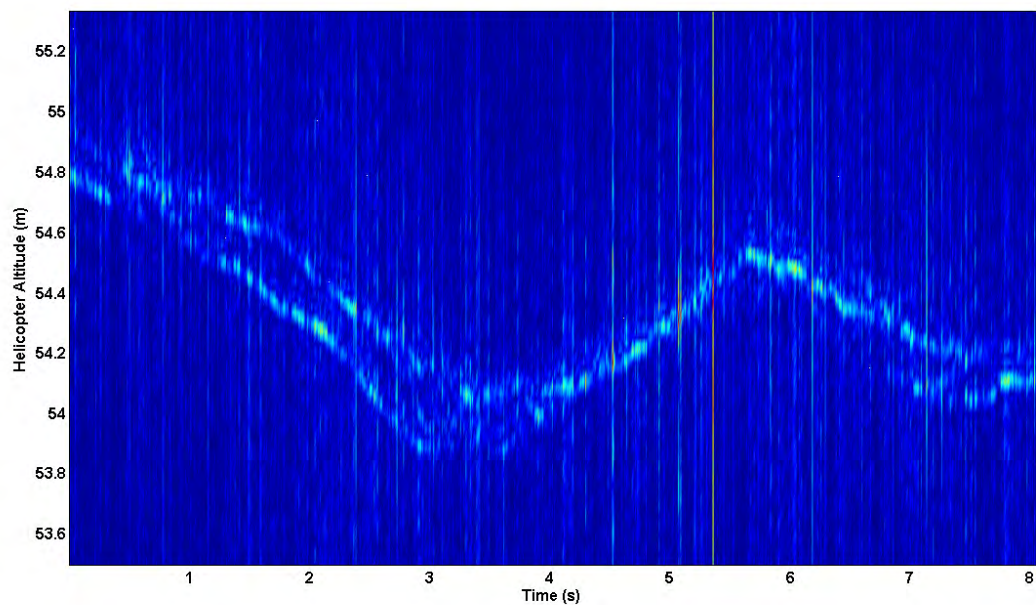


Figure 5.12: Zoomed in spectrogram of corrected radar data, the surfaces are easily picked out by eye.

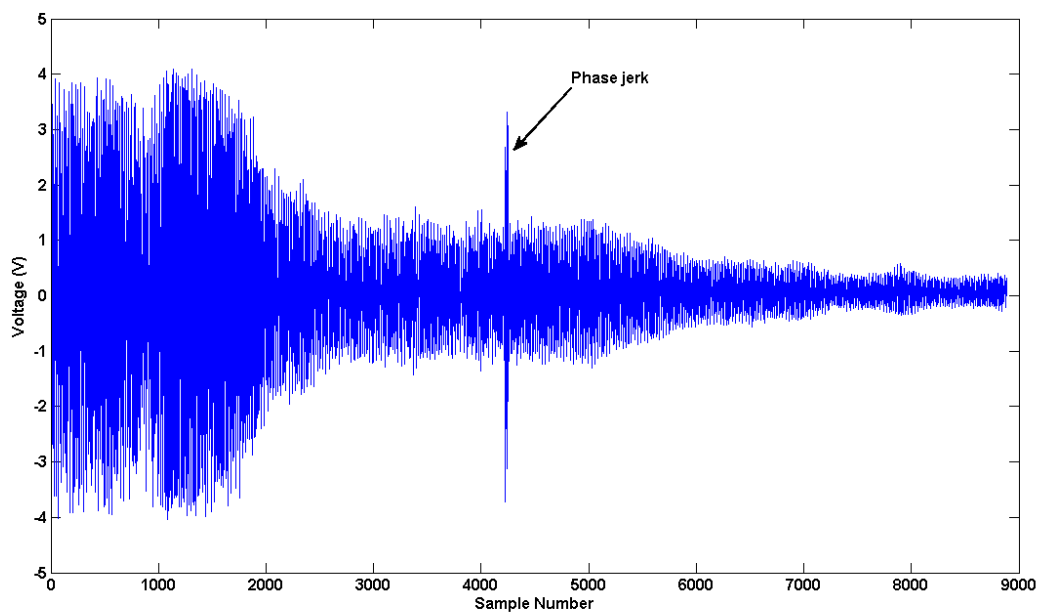


Figure 5.13: A plot of the radar IF frequency for one chirp, as a function of voltage and sample number (proportional to time). The spike seen in the plot could be the results of phase jitter (not removed by the algorithm) which is responsible for the vertical lines in spectrograms of Figures: 5.10, 5.11, and 5.12

Chapter

6

Helicopter-borne Radar Experiments, East Antarctica

This chapter presents the first *in-situ* validated snow thickness estimates derived from FMCW radar on a helicopter platform. The results presented here are summarised in *Galin et al. (in press)*.

Two voyages into the East Antarctic sea ice zone were made with the aim of testing the radar: SIPEX'07, and V1'08. Unfortunately, due to an overwhelming number of technical problems during the SIPEX'07 voyage, the radar data gathered was unusable for validation purposes. Appendix B details the flights conducted, difficulties encountered and solutions attempted. A brief summary of these errors, methods to prevent their recurrence and future recommendations are provided in section 6.2.

The data presented in this thesis confirming the operational ability of snow thickness estimation using an airborne FMCW radar is from the V1'08 voyage. These flights however, were made over fast ice: sea ice which is for the winter season *fast* to the coast, and hence can be expected to be smoother¹, but also to have a thinner cover of snow.

6.1 Radar Helicopter Platform

The radar, together with a laser altimeter, differential INS and camera, were installed into the instrumentation helicopter². As a unit, these instruments were named RAPPLS - or the Radar, Aerial Photography, Pyrometer, and Laser System (RAPPLS). Figure 6.1 is a schematic of the helicopter illustrating the location of the equipment.

The relative position of the three sensors is shown in figure 6.2; the black rectangular window in the top right hand side of the helicopter is the laser scanner aperture, the two black rectangular

¹Smoother ice implies a greater probability of contributions of specular reflection. However, this is not always the case, *Giles et al. [2008a]* finding that fast-ice is in areas rough.

²Eurocopter AS-350 BA "Squirrel".

boxes between the skids are the radar transmit and receive antennas, and the exposed box to the top right of the radar antenna is the camera lens. The presence of a laser and digital camera together with the radar, allowed for a multi-faceted survey of the surface conditions. Appendix A provides details of the design and integration of the radar system with the helicopter, including hardware and software design, and results of laboratory tests of the instruments.

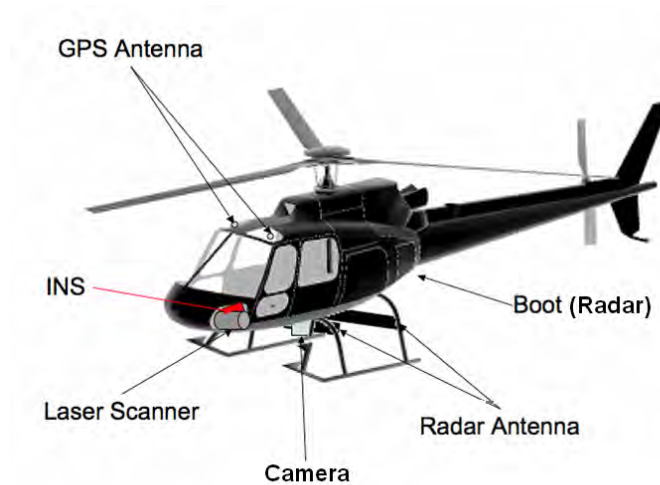


Figure 6.1: Schematic of the RAPPLS helicopter instrument arrangement. *Courtesy of J.Lieser.*



Figure 6.2: Photograph of the underside of the helicopter during flight. *Courtesy of K.Newbery.* The black rectangular window in the top right hand side of the helicopter is the laser scanner aperture, the two black rectangular boxes between the skids are the radar transmit and receive antennas, and the exposed box to the top right of the radar antennas is the camera lens.

Timing Information Distribution and Instrument Synchronisation

The three sensors on board the helicopter and the INS/GPS system were connected to a common Ethernet (1000BASE-T) network. In order to retrieve coincident data from the three sensors their timing had to be synchronised to INS time. This was achieved as follows:

The camera time was updated using NMEA time packets provided by the INS. This alone would have led to a one second uncertainty between the shutter closure time, and the NMEA packet information. However, the actual shutter closing time was logged, and this allowed for a one millisecond timing accuracy to be achieved (*K.Newbery, 2011*). Synchronisation of laser time was achieved by directly routing a 1PPS signal from the INS to the laser control computer, allowing it to synchronise to the one second trigger. The INS proprietary protocol (NCOM) was used to set the absolute time of the laser control computer. This allowed for the laser to timestamp its events with the corresponding INS timing record.

The radar timing synchronisation was complicated by the fact that the computer dedicated to running the radar software and tasked with triggering the transmission, reception, accumulation, processing and storage of the received data was not based on a hard real-time operating architecture. Due to severe timing constraints in writing the software, the radar software ran in a Windows XP environment. This made precise synchronisation with the INS difficult. To overcome possible timing errors, the radar software was instructed to synchronise its system clock with the timing packets supplied by the INS at the beginning of every radar flight. The 1PPS trigger, also routed to the radar, allowed the radar clock to be accurate to within a second of the other instruments. Finally, in order to achieve sub-second timing accuracy, the INS was directed to broadcast UDP packets containing information of the milliseconds within a second (at a 250 Hz rate) between each 1PPS trigger. These were received and processed by the radar control computer and recorded with each radar record.

These efforts gave assurance of ten millisecond accuracy between all instrument timestamps.

Operating Vertical Range Resolution of the Radar

Designed and built by CReSIS (*Gunbatar, 2007*), the antennas of the helicopter radar system are 8-element exponentially tapered TEM horns developed to operate from 2 - 8 GHz. Thorough testing

of these could only be undertaken after the field experiments had been conducted. The anechoic chamber tests were conducted at the NASA/Goddard Space Flight Centre antenna facility. The results of these experiments are summarised in appendix D, and the most relevant specifics provided in table 6.1.

The significance of these tests was two-fold. Firstly, they explained why the IF amplitude tapered strongly with increasing frequency (see figure 6.3). Much like a rectangular or Hamming window, the taper effect resembled an application of a time domain window to the data. As explored in appendix E, it resulted in a loss of SNR and a slight degradation of the achievable range resolution.

Most importantly, however, the tests allowed for the antenna bandwidth to be measured, found to be limited to 4 GHz rather than the 6 GHz range for which they were designed. This condition limited the vertical range resolution to a *theoretical minimum* of 37.5 mm.

The operating vertical range resolution of the radar was further degraded due to considerations of YIG output frequency stability and noise level. Figure 6.4 shows the waveform used to actuate the YIG; the driver circuit used 0 - 10 V to drive the YIG oscillator to sweep from approximately 2 to 8 GHz. Each up and down chirp was performed at a 400 Hz rate, and this waveform was repeated at a 335 Hz frequency. The usable portion of the chirp is marked in red, and corresponds to a bandwidth, and consequently an expected vertical resolution of:

$$BW = (6.000 - 2.588) = 3.4120 \text{ [GHz]}, \quad (6.1)$$

$$\delta R = 43.93 \text{ mm}. \quad (6.2)$$

Gain	10 dBi
Operating Frequency	2 - 6 GHz
Bandwidth	4 GHz
Beamwidth, 3dB	
- across track	8°
- along track	> 80°

Table 6.1: Helicopter antenna parameters, measured at the NASA antenna testing facility.

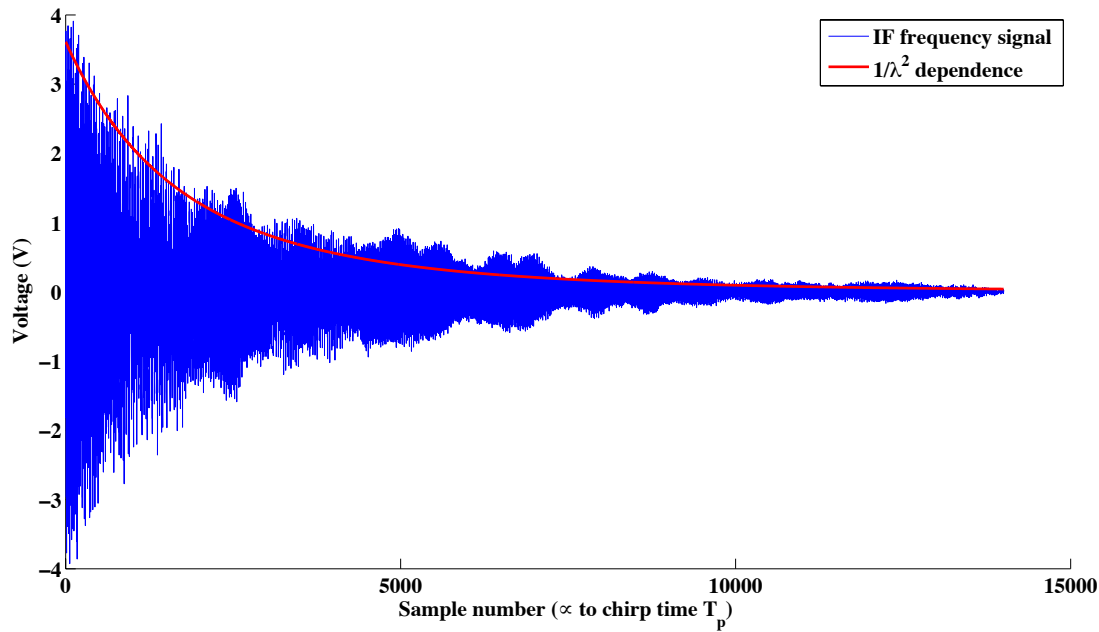


Figure 6.3: The IF frequency voltage during a single chirp duration, demonstrating the amplitude suppression with time which is explained in appendix E.

6.2 Sea Ice Physics and Ecosystem eXperiment, SIPEX'07

The SIPEX'07 experiment was held during a seven week period between September - October 2007. The *RSV - Aurora Australis* was in the East Antarctic sea ice zone between 110°E and 130°E gathering a suite of data related to the physics and ecology of sea ice and its interaction with the atmosphere and ocean.

The decision to install RAASTI in the boot of the helicopter was driven by restrictions and difficulty in obtaining necessary aircraft permits for its placement inside the cabin. Unfortunately, this resulted in significant complications with the performance of the radar during the SIPEX'07 experiment.

RAPPLS flew 19 times with the radar onboard. It was determined after the initial data analysis that the collection rate was significantly below requisite levels during these airborne operations. The cause was found to be related to the vibrations inside the boot of the helicopter - they were affecting RAASTI's hard-disk drives, the only moving components located inside the radar. By way of comparison, under laboratory conditions a data rate of 40 Mbytes/s could successfully be

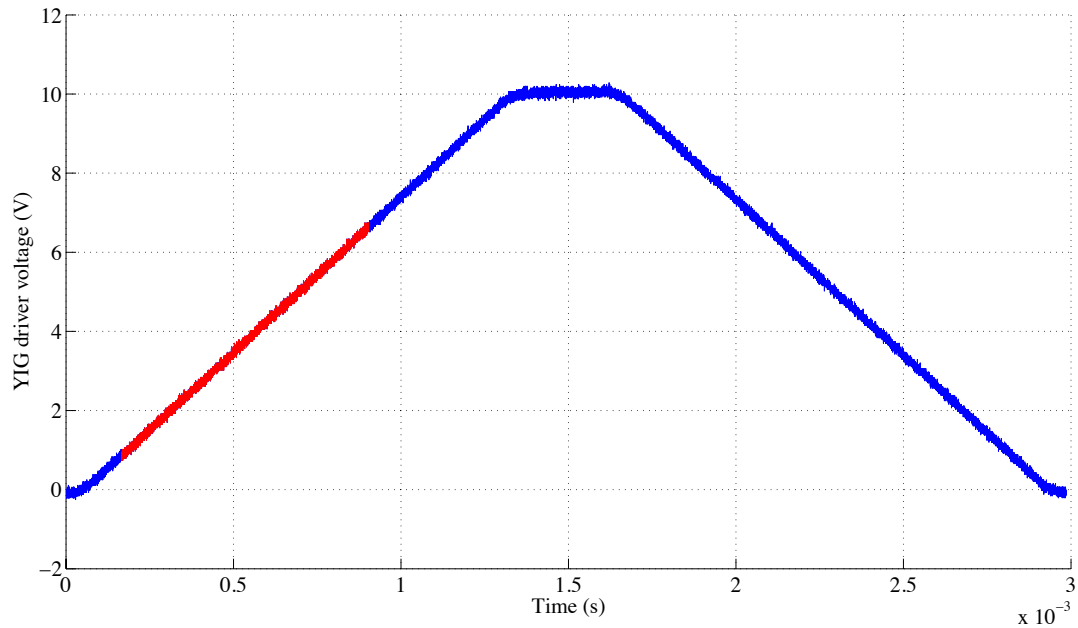


Figure 6.4: The voltage waveform used to actuate the YIG to chirp up from 2 to 8 GHz and back to 2 GHz respectively. The segment in red identifies the usable segment of the chirp.

sustained; this dropped to approximately 3 Mbytes/s in flight conditions and was determined to be an unacceptable rate of data acquisition.

In order to enable even minimal data to be gathered during the numerous flights, only ten of the 335 chirps transmitted per second could be recorded. Considering that at its lowest maintainable speed the helicopter flies 200 m in approximately ten seconds, the data gathered at this reduced rate did not provide sufficient information for validation purposes. The suite of problems and debugging successes during the flights of SIPEX'07 are documented in appendix B.

6.2.1 Crane Experiments

Due to vibration issues encountered during airborne experiments, another approach was needed to test if the radar itself was operating correctly. In order to determine if the radar was operational, that is, sensitive to air/snow and snow/ice interfaces, it was removed from the helicopter and attached to a cage pallet, as shown in figure 6.5. Using the ship's aft crane, the cage pallet was swung over the side of the ship, and was slowly raised, and lowered over the snow-covered sea ice.



Figure 6.5: The radar inside a cage pallet and attached to the ship's crane for testing. *Photo credit: J. Lieser.* The radar antennas are secured to the bottom of the cage pallet.

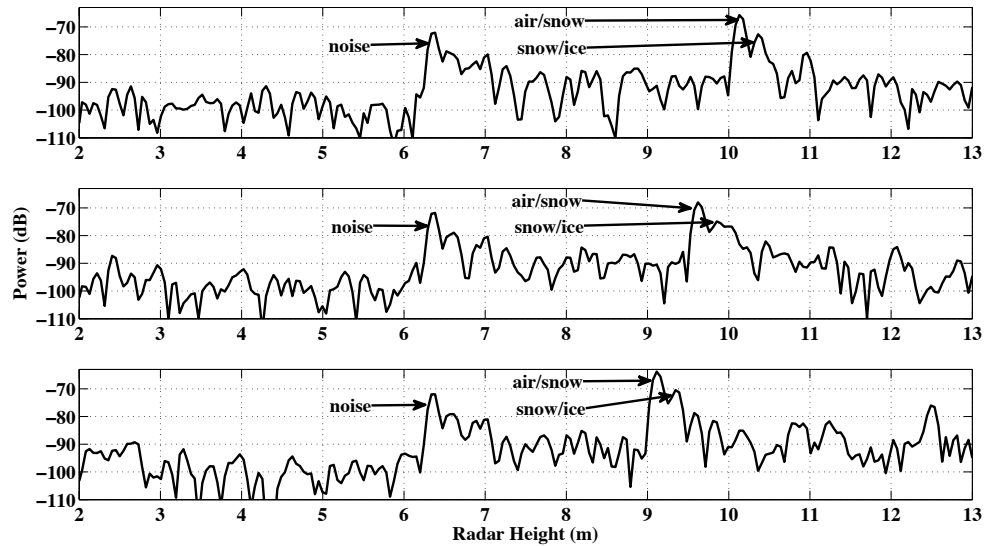


Figure 6.6: Three individual radar records are shown, with returns due to the air/snow and snow/ice interfaces seen here to be changing their location as the altitude of the cage pallet changed. A large noise component (possibly due to cross-coupling of the antennas) is stationary.

This novel method enabled a clearer distinction to be made between radar returns due to the surface, due to subsurface properties, and returns due to noise. It was anticipated that signals indicating air/snow and snow/ice interfaces would change in range, while maintaining constant relative separation. Noise components were expected to remain static. *Galin et al.* [2008], summarises the results of the crane experiment, which demonstrated that the radar was indeed operational. Figures 6.6 and 6.7 show the radar return recorded. The air/snow and snow/ice interface returns are easily identifiable from the background noise.

In the crane experiment, converting the time delay between the two observed peaks in the radar return directly to distance (i.e. no correction is made for the change in EM propagation speed due to the snow) provided a thickness estimate of 120 mm, whereas the *in-situ* average was found to be 150 mm. Unfortunately density samples of the snow were not taken. However, assuming a dry snow pack with 300 kg/m^3 density leads to a snow thickness of approximately 150 mm. Due to logistical difficulties only one such crane experiment was conducted during the voyage, and consequently detailed error analysis of the radar from a crane platform is not possible.

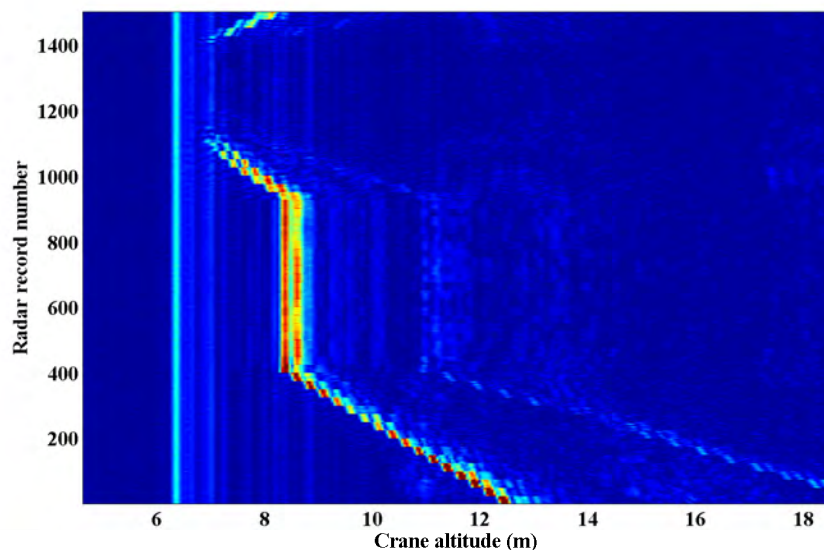


Figure 6.7: A spectrogram of the stacked radar returns during the crane tests of the radar. Two lines are seen moving across the image, identifiable as the air/snow and snow/ice interface returns, whereas a large noise signal is stationary during the experiment. The two lines of lower intensity at a large range, seeming to mirror the motion of the bright air/snow and snow/ice peaks are likely to be the 2nd harmonics of the two returns.

6.3 Voyage 1, 2008

Two main sources of error were observed during SIPEX'07:

- the effect of vibrations on the hard-disk drives and its contribution to the sustainable data rate and,³
- the non-linearity of the frequency generator.

The first problem was successfully addressed in collaboration with colleagues at ACFR, who had developed an anti-vibration mount for hard-disk drives for their all-terrain vehicles. This mount was built and demonstrated to minimise the effect of vibration on the hard disk drives, allowing

³Technology moves at a lightening pace. Three years ago when these experiments were undertaken, solid-state drives with the required storage capacity were far beyond the reach of the thesis budget. Since then, they have become cheaper and faster, and in future, vibration problems affecting the storage media are no longer seen to be an issue.

for the required data rate to be maintained. Appendix C summarises the results of flight tests demonstrating this improvement.

The non-linearity of the oscillator proved a significant impediment to the ability of the radar to resolve closely spaced layers, directly affecting the achievable vertical range resolution. The non-linearity of the oscillator is mostly affected by its internal temperature (*Leier, 2008*). To stabilise its internal temperature, the YIG is equipped with an internal heating element and controller. In theory should maintain the YIG core temperature at $80^{\circ} \pm 1^{\circ}$. This internal heating leads to a temperature gradient between the YIG case and the ambient temperature of the outside environment. To facilitate YIG core temperature stability and prevent constant heat loss, the oscillator and its driver were placed inside an insulated case and the temperature of the case was recorded (see section A.3.2). However, subsequent laboratory experiments determined that this approach was not able to eliminate YIG non-linearities in their entirety.

In anticipation of this an assessment of the literature on non-linearity correction in chirp radars was made. This led to the conclusion that knowledge of the non-linearities was the best available solution. Following the example of *Meta et al. [2007]*, a delay line was included in the transmit/receive loop of the radar. This reference target allowed for the non-linearities to be captured. Consequently, application of a non-linearity algorithm, described in the previous chapter for the air/snow and snow/ice peaks to be identified.

Having implemented the above-mentioned modifications, the radar successfully collected data during the first voyage of the *RSV - Aurora Australis* to the East Antarctic zone in 2008. However, on this voyage due to logistical problems encountered it was not possible to collect data over pack ice, and only fast ice flights were made. The following sections present the validation results of snow thickness retrievals from the helicopter-borne data collected using the FMCW radar over fast ice.

6.3.1 Experiment Description

Figure 6.8 shows a satellite image of the Vestfold Hills area (nearby Davis Station) where the flight tests were conducted. The experimental flights were made over a marked area of 200 m x 80 m, approximately 100 m away from the ship. *In-situ* snow thickness measurements were taken

every 2 m, snow temperature every 10 m, and snow density every 20 m. Figure 6.9(a) is a basic schematic of the marked area designated by ten flags (marked as diamonds on the figure). A map of the recorded snow depth (in mm) is shown in figure 6.9(b).

Lines A and B were made between flags 2 and 7, and 4 and 9 respectively. Standard octahedral radar reflectors (460 mm \times 460 mm) were placed at each of these four flags. The purpose of the corner reflectors was to use their high reflectivity and isotropic radiating characteristics to identify the precise time at which the radar was flown over them.

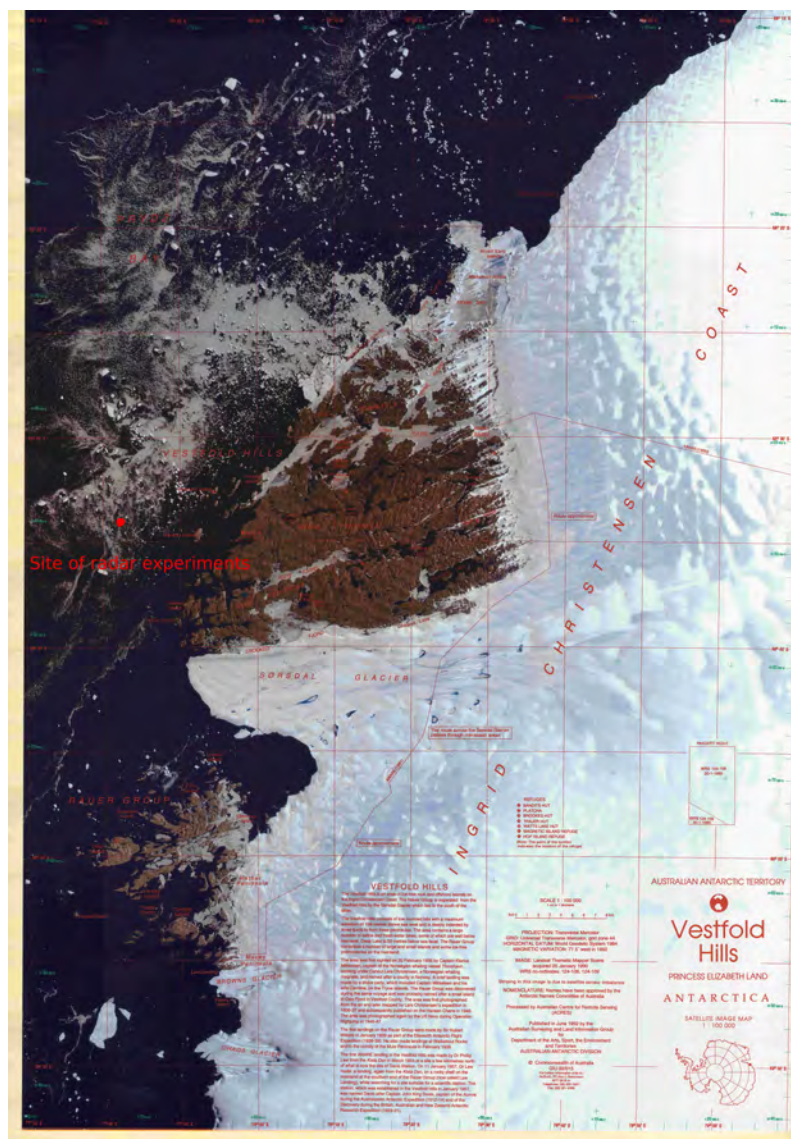
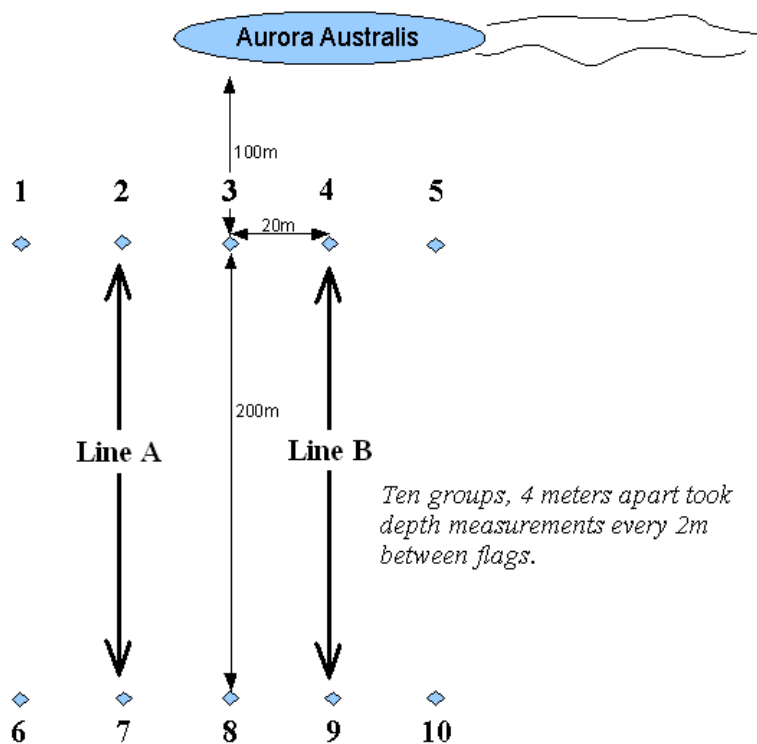
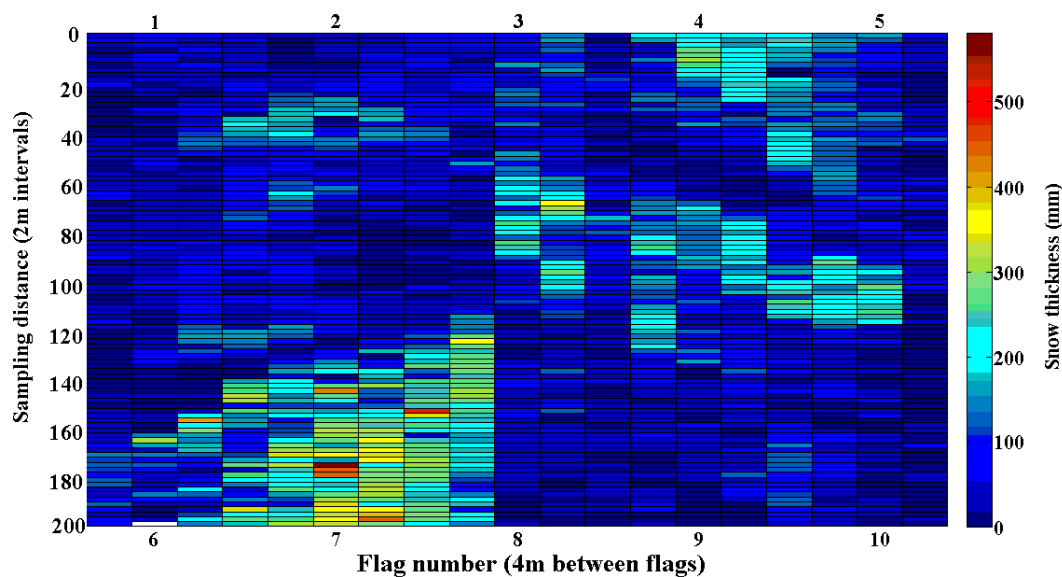


Figure 6.8: Satellite image of Vestfold Hills, with the test site labelled. *Photo credit: Australian Antarctic Division, Kingston, Tasmania, Australia.*



(a) Schematic of the area near the ship where *in-situ* experiments were performed.



(b) *In-situ* measured snow depth distribution map over the experimental area.

Figure 6.9: *In-situ* experiment outline.

6.3.2 *In-situ* Gathered Data Summary

The snow measured over the designated area was very shallow, at a maximum depth of 350 mm it would extend to a maximum of 8 range-bins in the radar resolution space. One range-bin error (due to random error in the system) results in a 13% error in snow thickness, considering the resolution of the radar to be 43.93 mm. Consequently, the presented snow thickness retrievals from the helicopter-borne data will be presented over *Line A*, where the greatest variation in snow thickness is observed.

Figure 6.10 is a photograph of the start of *Line A* (with the start flag visible), taken from an altitude of 82 m. It shows a smooth snow surface which has formed sastrugi in places, while in other areas the snow layer has completely been removed showing a smooth ice surface. The *in-situ* snow thickness measurements made of the first half of the sampled area are plotted in figure 6.11, and mean values provided in table 6.2. The measurements were taken every 2m by ten groups of people spaced 4 m apart. The red snow thickness line represents the snow depth measurements coincident with the flags over which the helicopter was directed to fly.



Figure 6.10: Photograph of the start of *Line A* at an altitude of 82 m. The image represents an area of 47 x 72 m. The effects of wind on the snow are evident, with sastrugi features ranging from 1 m to 10 m, and in places bare ice is visible. *Photo credit: Adam Steer.*

Track #	Mean (mm)	Range (mm)
1	25.7	0 - 125
2	65.0	0 - 270
3	97.6	0 - 270
4	105.6	0 - 255
5	92.4	0 - 250
6	84.1	0 - 305
7	81.2	0 - 260
8	39.6	0 - 180
9	89.4	0 - 350
10	76.5	0 - 260

Table 6.2: The mean and range of snow thickness values measured *in-situ* over the ten sample tracks of Line A.

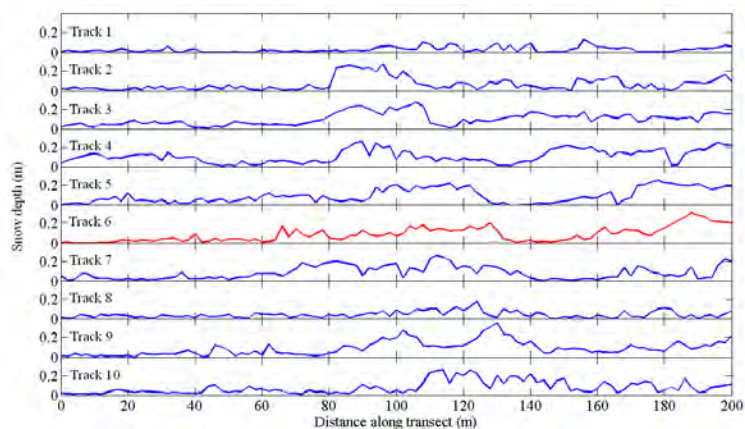


Figure 6.11: Referring to figure 6.9(b), this graph plots the snow thickness over the first half of sampled area: snow thickness measured every 2 m, in the first half of the sample area by 10 groups, spaced 4 m apart. The red profile corresponds to the measurements recorded between the flags over which the helicopter was directed to fly.

Figures 6.12 and 6.13 summarise the temperature of the snow and the corresponding density for Line A. The temperature of the snow was consistently well below freezing, and consequently the snow pack was assumed dry. Direct measurements of snowpack wetness were not taken.

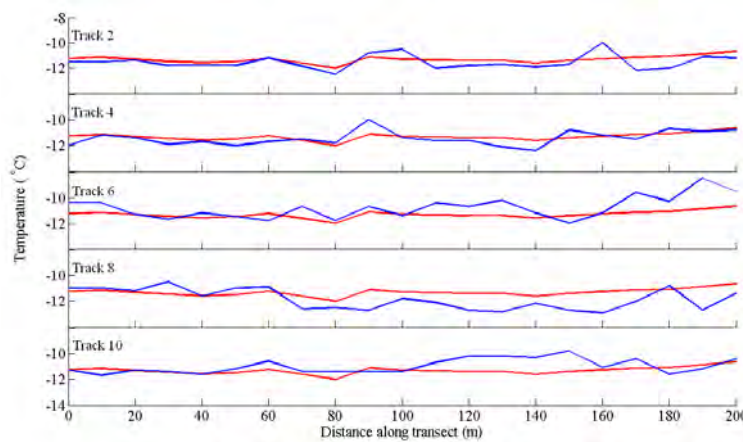


Figure 6.12: Temperature profiles of the snow pack recorded every 5 m, by five groups spaced 8 m apart. The blue line plots the temperature measurements recorded by each group, and the red line corresponds to the average temperature along the center track, demonstrating a small spatial variability of temperature gradients. The centre temperature plot corresponds to the profile between the flags over which the helicopter was directed to fly.

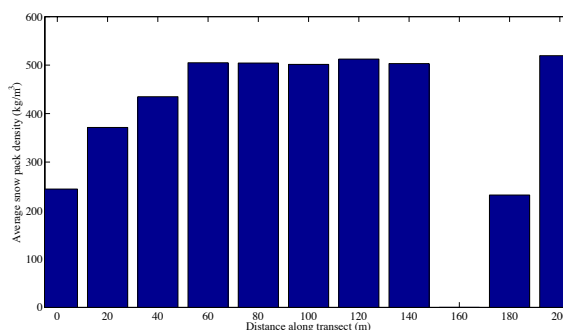


Figure 6.13: Density of snow pack along Line A, measured every 20 m. The absence of a density sample at 160 m is due to the absence of a snow layer at the site.

6.3.3 Helicopter Flights

The radar was flown over Line A six times - three times each at the two altitudes. Flights were repeated in order to minimise the possibility of the radar data being corrupted by biases, due to systematic and/or random errors as well as errors in any post processing algorithms - the use of which was anticipated.

In the validation analysis that follows, the data presented consists of three flights at nominal altitudes of 100 m (referred to as Pass 1, 2, and 3), and three flights at nominal altitudes of 50 m (referred to as Pass 4, 5, and 6). The comparison between the two altitudes was intended to gauge the relative contribution of the errors in the helicopter operations (such as off-nadir pointing), as well as the effect of different scales of surface roughness sampled by a changing active area of the radar.

Localisation of the Passes

In order to locate the start and end of the Passes it is necessary to locate the coordinates of the flags between which the helicopter flew for Line A (flags 2 and 7 in figure 6.9(a)). Since GPS coordinates of the flags were not recorded, the absolute localisation of the flags and flight lines in space and time is not possible. However, relative localisation is possible and is sufficient for our analysis due to the small distances involved.

It was expected that the radar data would contain a clear signature of the corner reflectors, however this signal is not identifiable in the radar data. Fortunately, examination of the laser data revealed spikes in the laser returns that corresponded to the corner reflectors. Figure 6.14 shows an example of the elevation profile for Passes 1, 2 and 3, with a dip indicating a lack of return for this point i.e. the presence of a corner reflector. This method allowed only the start flag to be located. The absence of a corner reflector spike for the Pass 2 may be a product of the data post-processing, whereby only points originating from nadir were kept.

The GPS location of the flag at the end of the 200 m Line A transect could not be derived in this manner, as there was no record of the corner reflectors in the laser data. However, since the transect is known to be 200 m long, it was possible to approximate the location of the end flag using INS data, which provided the total forward distance travelled by the helicopter and its heading.

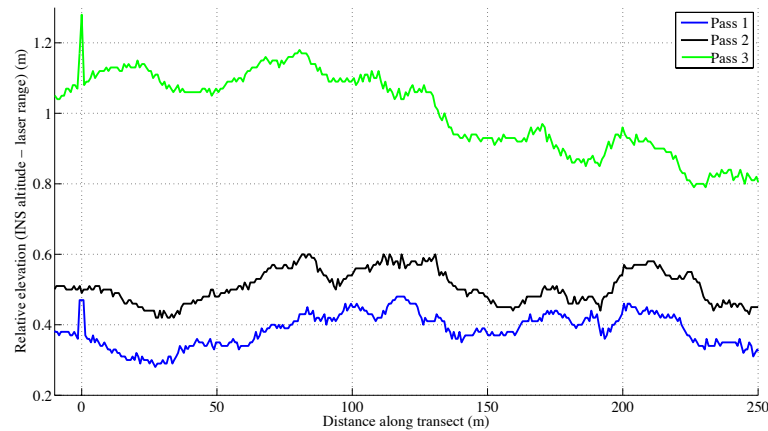


Figure 6.14: A plot of the relative altitude derived from the difference between the laser range and INS altitude, demonstrating the 'dropout' in laser signal when the helicopter flies over the corner reflector placed at the start flag. The absence of the signal in the second Pass may be due to the post-processing of the laser data which picked out only those returns at nadir.

A summary of the start and end flag GPS locations for the six Passes are provided in table 6.3. The GPS coordinates are specified to six decimal places as this is the required relative accuracy if localisation to meter is required. Figures 6.15 and 6.16 plot the distribution on a Cartesian plane of the start and end flag coordinates with the origin defined as their mutual mean location. The figures demonstrate that the start and end of the six Passes are located to within 2-3 m of one another.

Pass #	Start Flag	Stop Flag
1	-68.575713, 77.686651	-68.573888, 77.689787
2	<i>n/a</i>	-68.573883, 77.689865
3	-68.575695, 77.687783	-68.573872, 77.689832
4	-68.575703, 77.687686	-68.573879, 77.689745
5	<i>n/a</i>	-68.573885, 77.689812
6	-68.575703, 77.687658	-68.573883, 77.689731
Mean	-68.575704, 77.687744	-68.573882, 77.689785

Table 6.3: Coordinates of the start and end flags of Line A.

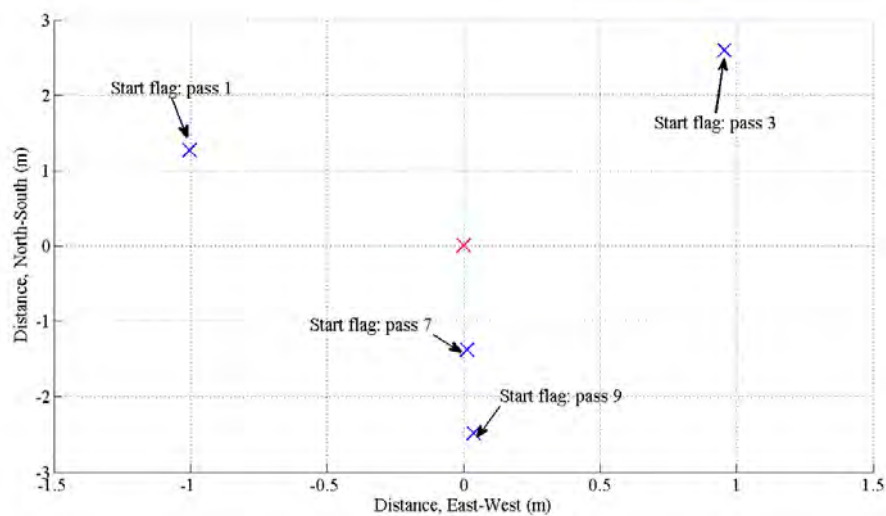


Figure 6.15: Distribution of the estimated coordinates of the start flag of Line A using the corner reflector position.

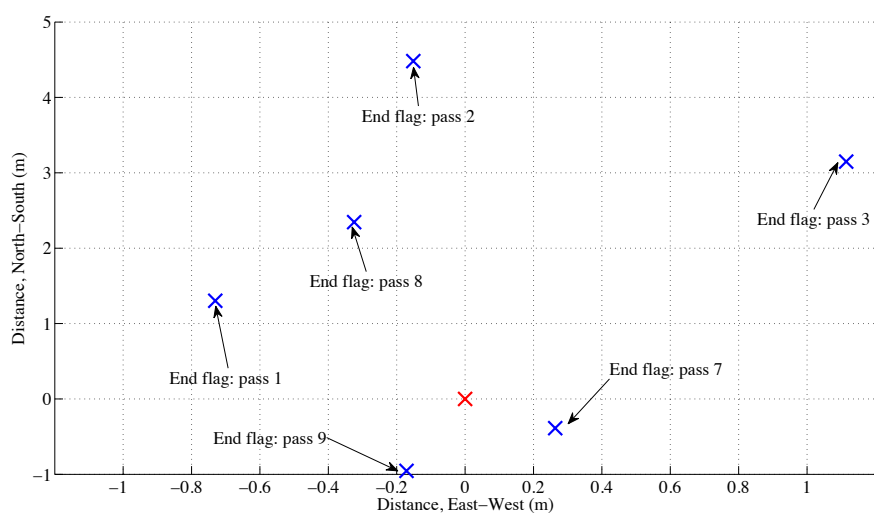


Figure 6.16: Distribution of estimated coordinates of the end flag of Line A.

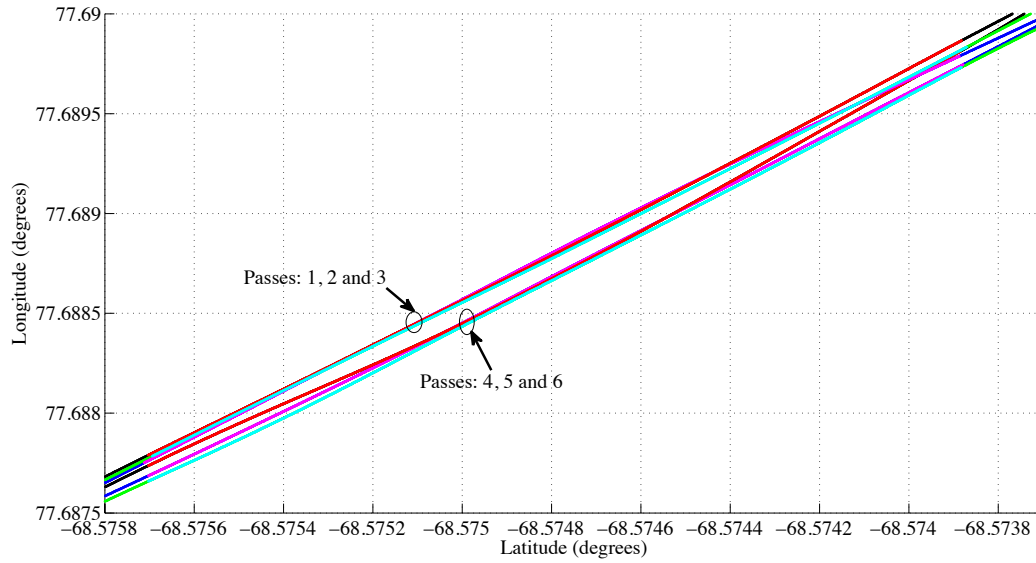


Figure 6.17: The flight tracks of the six Passes. The maximum separation between them is 2 - 3 m, as shown in figure 6.18.

Data gathered between these flag locations were extracted from the INS, laser and radar logs. The localisation of the six Passes is shown in figure 6.17, which plots the latitude and longitude of the flight tracks, and highlights the location of the six Passes. The separation seen between them is calculated to be approximately 2 m. Figure 6.18 plots the tracks of the helicopter for the six Passes on a Cartesian plane. The origin of this coordinate system is defined as the starting flag, the y-axis points to the end flag. This figure demonstrates that for the purposes of the current examination, the helicopter flew a direct path between the start and end-flags. The small deviation from a direct line-of-sight path may need to be re-considered during comparison with the *in-situ* data since the measured snow thickness spatial distribution varied between the sampling groups (spaced 4 m apart).

In summary, considering that the start and end of the six Passes was localised, and the flight path between them retrieved, it was thus meaningful to look for a correlation between the *in-situ* measured snow thickness data and the data retrieved from the radar for these Passes.

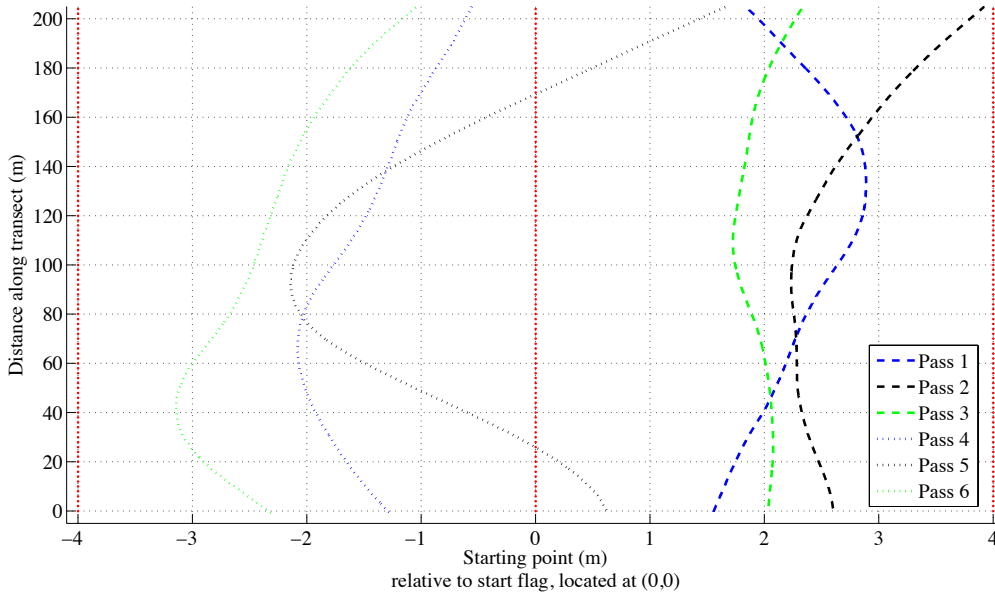


Figure 6.18: The flight tracks of the six Passes plotted in a Cartesian plane with the starting flag at the origin. The red lines show the assumed tracks along which *in-situ* snow thickness measurements were recorded.

6.3.4 Radar Operating Conditions and Assumptions

An estimate of the roughness conditions of the over-flown surfaces are provided by the laser altimeter. The laser range measurements are used for approximating the average standard deviation of surface height at 50 m and 100 m altitude. As discussed in chapter 3, the size of the sample area should be specified when calculating the statistical properties such as standard deviation. This is due to the fact that the active area of the radar (varying from 11.8 m^2 to 23.6 m^2 over the altitudes 50 m to 100 m) under-samples the surface roughness. This fact is illustrated in figure 3.2, which shows that the helicopter operating range places the active area of the radar at the changing slope of the curve.

It is unlikely that the actual snow surface has statistical properties that may be characterised as ergodic, whereby a single set of measurements can be used to approximate the ensemble statistics. This view is supported by the observed changes in mean snow thickness between the ten sampled lines. However, to make progress with the measurements, the laser data is used to determine the average expected standard deviation, and this is found to be: 9.5 mm and 10.5 mm respectively for the two altitudes. Provided that the usable frequency range is between 2 - 6 GHz, the Rayleigh

conditions for specular reflection require the standard deviation to be less than 18.75 - 6.25 mm over the active area. Table 6.4 provides a summary of the helicopter viewing conditions.

These results coupled with the fact that the correlation length of the surface is approximately 27 m, imply that the angle over which scattering would occur is $\approx 10[mm]/27[m] \times 180/\pi = 0.02^\circ$. Hence, near specular returns are to be expected in most cases, and unlikely that large-scale features will lead to ambiguities in the identification of the two interfaces.

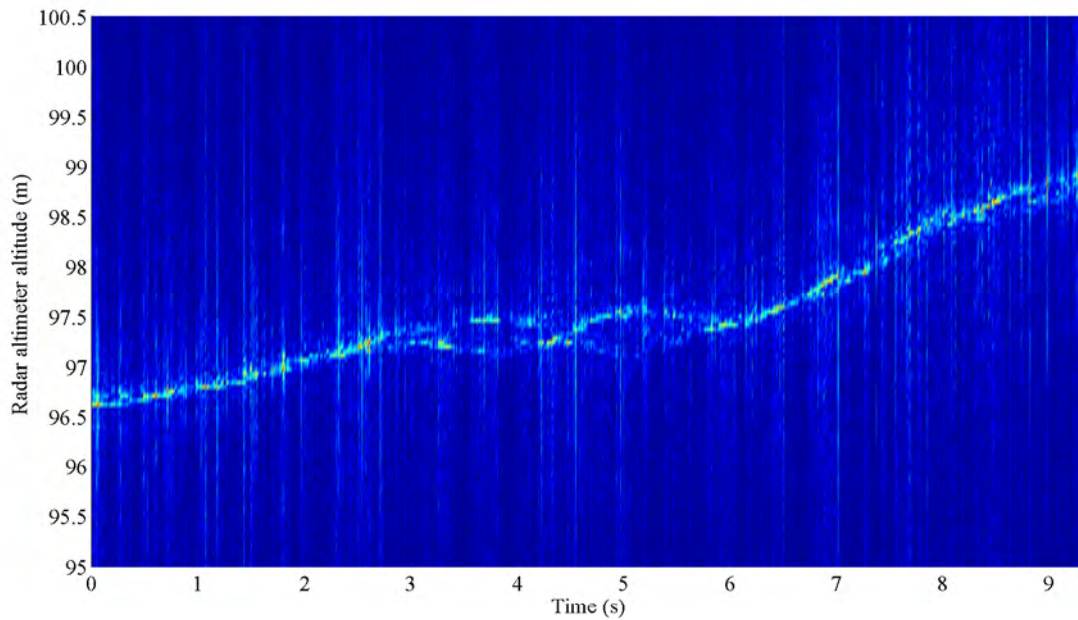
Altitude [m]	Active Area Radius [m]	Laser Derived RMS Height [mm]
50	1.9	9.5
100	2.7	10.5

Table 6.4: Approximate helicopter viewing conditions.

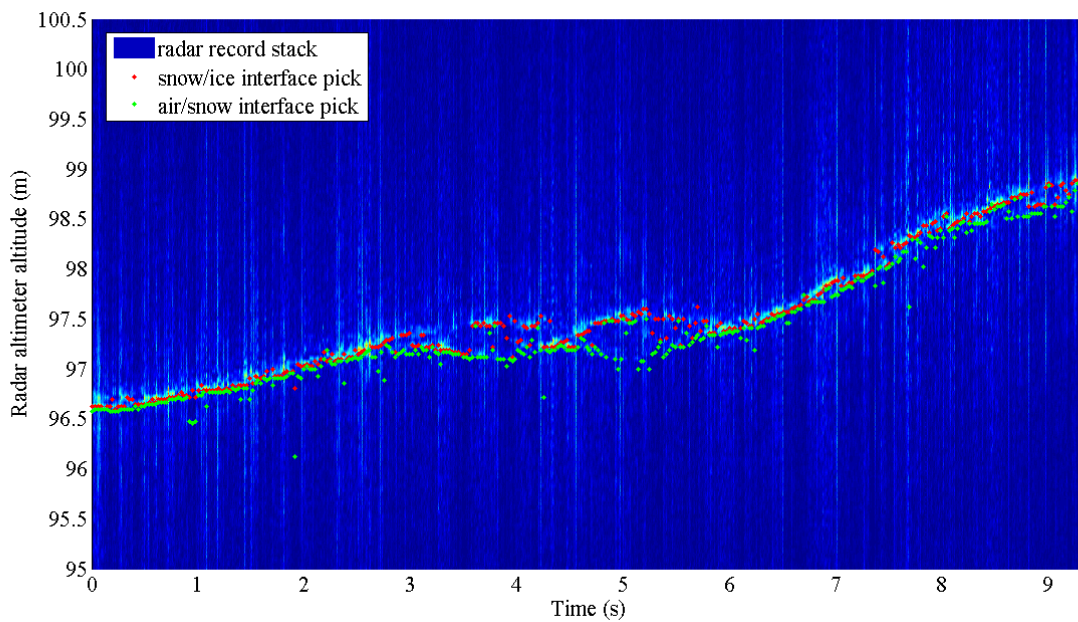
6.3.5 Peak Detection

Once the flights suitable for validation purposes were identified, the non-linearity correcting algorithm was applied to the three Passes at 100 m and three Passes at 50 m altitudes. This extracted peaks arising from reflections at the air/snow and snow/ice interfaces. Figures 6.19(a) and 6.20(a) show examples of Passes at both altitudes following application of the non-linearity correction algorithm. The snow thickness profile is evident.

To automatically extract the peaks corresponding to the air/snow and snow/ice interface a very basic selection criteria was applied. The algorithm had no learning capacity to follow the trend of a peak from one radar record to the next: that is, it was a peak selection rather than peak tracking algorithm. The first peak was identified as having the largest amplitude in the power versus frequency radar record, and the second peak was located as the one having an earlier arrive time (closer range), but also with an amplitude no less than 10 dB below the first peak (after *Gogineni et al.*, 2009).

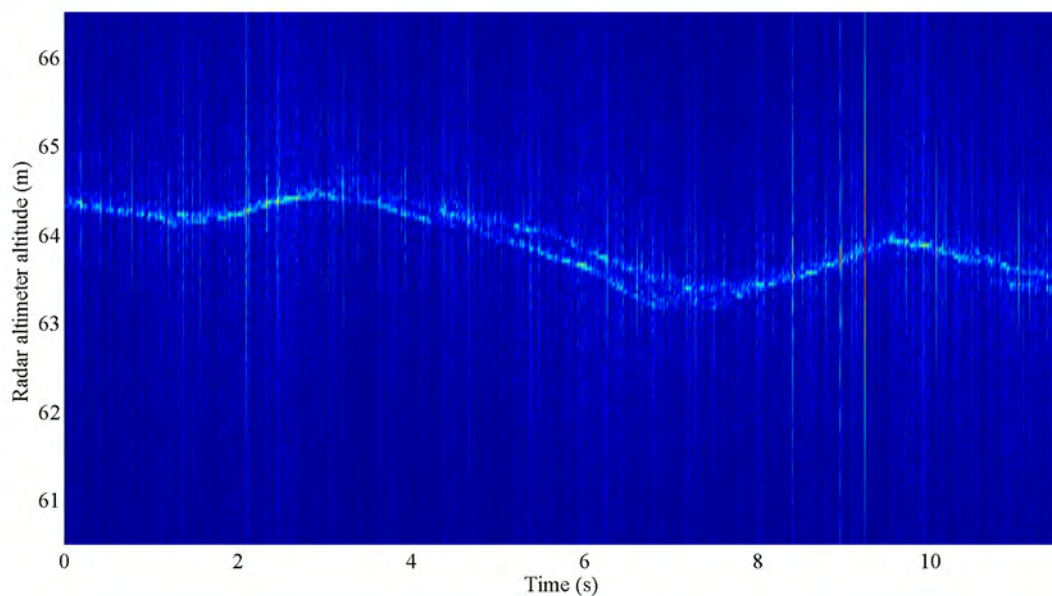


(a) A spectrogram of the radar returns for a Pass at 100 m nominal altitude.

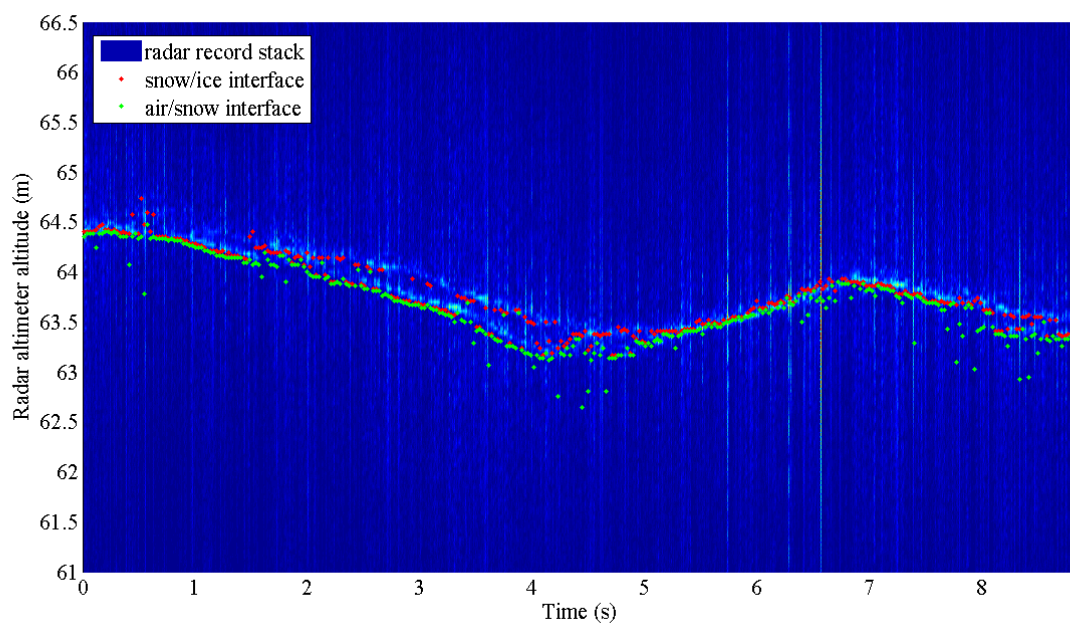


(b) The results of the picking algorithm overlaid on the 100 m nominal altitude Pass.

Figure 6.19: The raw radar data collected over a Pass at 100 m altitude, with the results of the picking algorithm overlaid.



(a) A spectrogram of the radar returns for a Pass at 50 m nominal altitude.



(b) The results of the picking algorithm overlaid on the 50 m nominal altitude Pass.

Figure 6.20: The raw radar data collected over a Pass at 50 m altitude, with the results of the picking algorithm overlaid.

Once identified, a further condition was applied that the two peaks must remain in the same location for as long as there is a correlation between the radar returns. The number of chirps that could be assumed to sample a similar surface (and hence be correlated) was found by calculating the decorrelation distance, (after *Walsh*, 1982) for an active area of radius r , and found to be equal to:

$$d = 0.305R\lambda/r \text{ [m]},$$

where R is the radar altitude, and λ is the radar wavelength. Using this decorrelation distance and the radar velocity, the maximum CRF at which independent sampling of the surface was made, was calculated to be:

$$CRF = \frac{v}{d} \text{ [Hz]},$$

$$\approx \begin{cases} 87 \text{ at } 50 \text{ m,} \\ 62 \text{ at } 100 \text{ m,} \end{cases}$$

At an operational CRF of 335 Hz, a conservative condition that the peaks identified as the air/snow and snow/ice interfaces remained in the same location for three consecutive radar returns - was applied. Figure 6.21 plots an example of three consecutive radar returns where the peaks are found to be in identical locations.

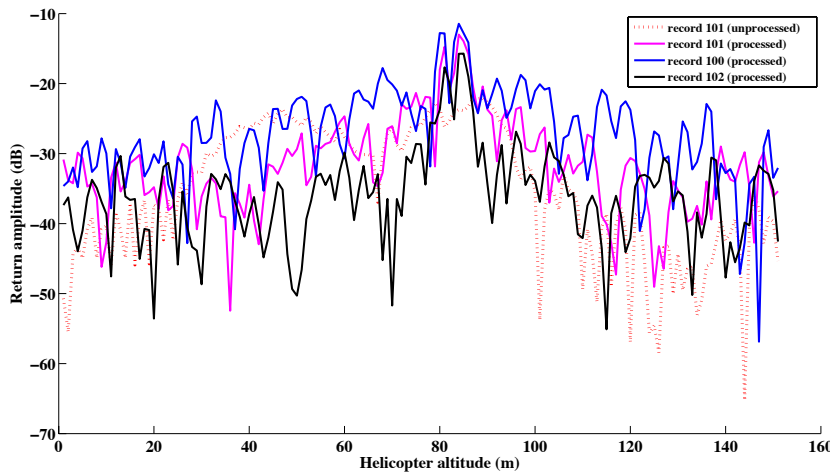


Figure 6.21: The raw radar data, and the corrected radar data for three consecutive returns showing the same peak location. Additionally, the performance of the non-linearity algorithm is shown: the dotted line represents the un-corrected radar record, where the interface peaks are completely unidentifiable.

Figures 6.19(b) and 6.20(b) demonstrate the results of the peak picking algorithm overlaid on the radar spectrogram for two sample Passes. The first thing to observe is the general nature of the radar waveforms - they are such as one would expect to come from a surface of low roughness. This is in agreement with the laser estimations of RMS height and correlation length. However, additionally one must observe that while the correlation length estimated from the laser data is ≈ 27 m, due to the pulse-limited operation of the radar it is the active area length that determines the effective length of the surface that the radar senses affecting the range of scattering angles that the radar receives.

The second observation is that due to the assumption that the snow/ice peak was always the peak of highest amplitude, the algorithm fails to detect the correct snow thickness. The figures (6.19(b) and 6.20(b)) demonstrate that there are areas where the picking is not very successful, as an example consider the zoomed in segment of the 50 m Pass shown in figure 6.22. Two records are selected from this segment - one which appears to be a successful pick, and one which is not. The corresponding individual radar records are plotted in figure 6.23. The assumption that the snow/ice interface will have the stronger return is not satisfied, this may be due to signal losses in the snow (products of wetness, salinity or volume scattering) and further work is necessary to explore methods of improving the picking criteria.

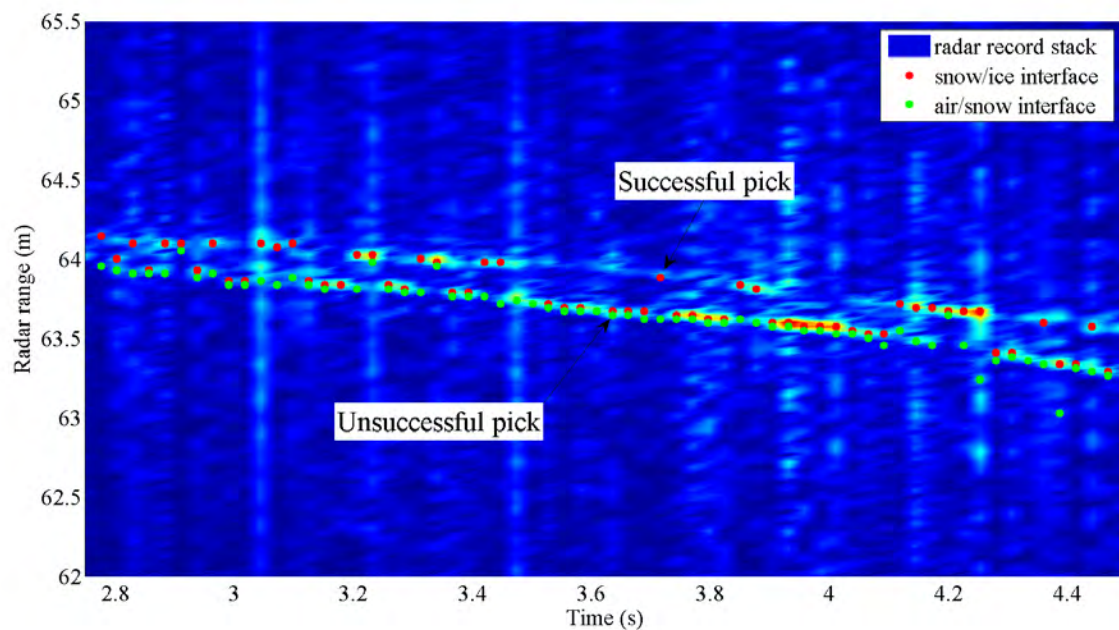


Figure 6.22: Closer demonstration of the results of the picking algorithm, in areas where the eye generally sees two surfaces, the picking algorithm is not successful.

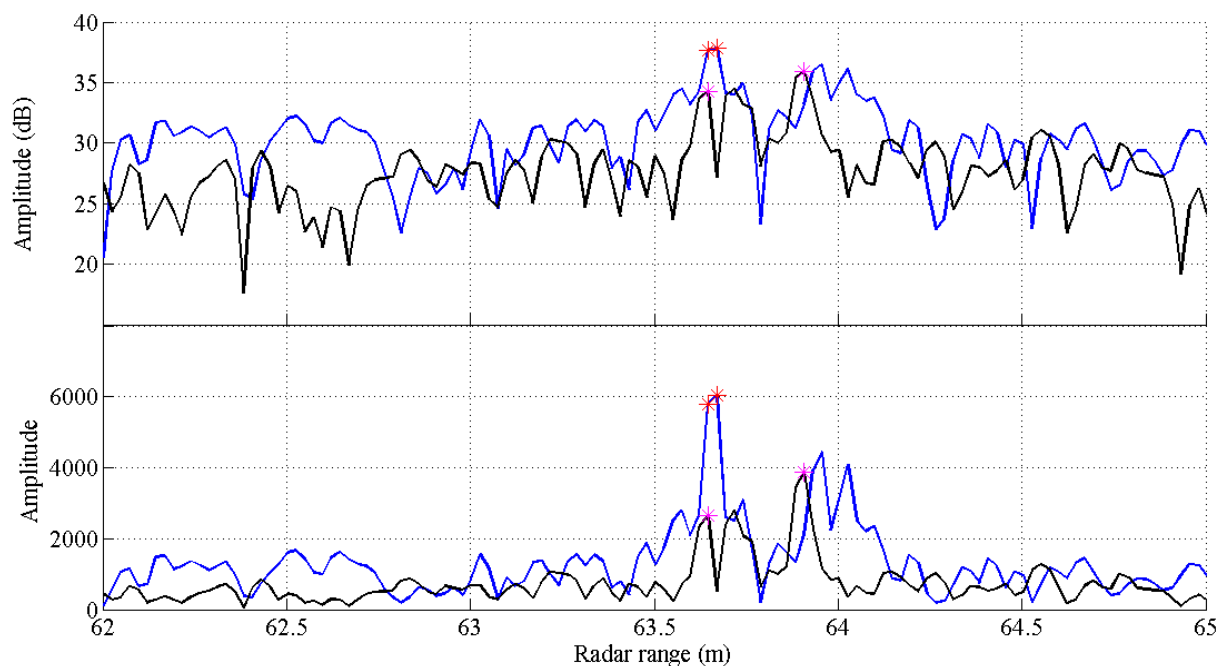


Figure 6.23: Closer demonstration of the results of the picking algorithm, comparison between a successful and unsuccessful pick result.

6.3.6 Converting peak separation to snow thickness

Considering that the snow pack was dry, an approximation for its refractive index can be made from measurements of its density, using the following formula (*Ulabay et al.* [1986b], pp 2062):

$$n_{snow} = \sqrt{1 + 1.9 (\rho_{ds}/\rho_w)}, \quad (6.3)$$

where ρ_{ds} is the density of the snow pack; and ρ_w is the density of water. Table 6.5 summarises the density values measured for the Line A transect, and the corresponding velocity factors derived.

An examination of the distribution of density and its effect on the velocity factor, in combination with *in-situ* snow thickness measurements demonstrates that it is not necessary to take the changing velocity factor across the transect into account. To account for it leads to less than a single range bin change in the radar signal. This is illustrated by figure 6.24, where the expected range bin number is calculated over the sampled area for the ten tracks that contributed to Line A. The red line plots the range-bin number calculated using a changing velocity factor over the 200 m distance, and the range-bin number (in blue) is calculated using the mean average velocity factor across the complete sampled area. Differencing these two lines results in less than a range bin change.

Distance [m]	Density (kg/m^3)	Permittivity	Velocity factor
0	244.2	1.46	0.83
20	371.4	1.71	0.77
40	424.8	1.83	0.74
60	504.9	1.96	0.71
80	504.3	1.96	0.71
100	501.5	1.95	0.72
120	512.5	1.97	0.71
140	503.2	1.96	0.71
160	nan	nan	nan
180	231.9	1.44	0.83
200	519.5	1.99	0.71
Mean	443.1	1.84	0.74
Std.Dev.	105.6	0.21	0.05

Table 6.5: *In-situ* measured snow density, and calculated corresponding velocity factor.

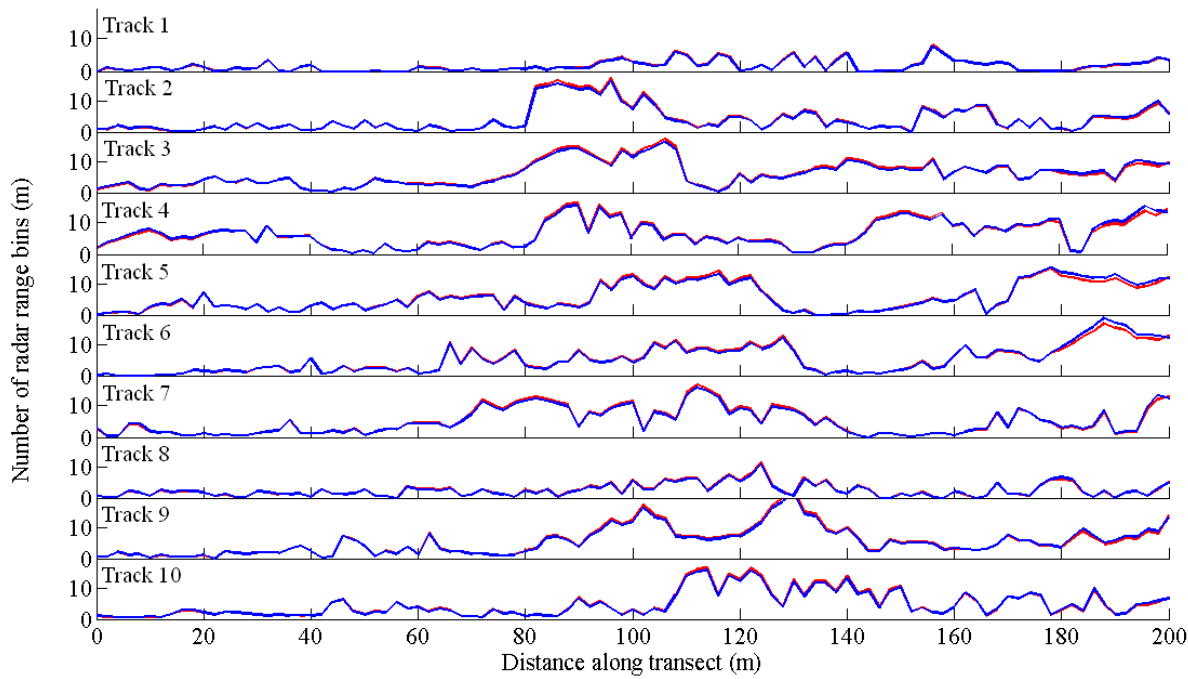


Figure 6.24: Approximate number of range bins calculated across the transect lines, using a changing velocity factor (red line), or a mean velocity factor (blue line).

6.3.7 Results

The aforementioned processing allowed for a comparison of the radar data and *in-situ* measured snow thickness estimates to be considered possible. Figures 6.25 and 6.26 plot the radar derived snow thickness as a function of distance for the three Passes at 100 m and 50 m altitudes respectively. Similarities between the Passes are easily observed. However, Pass 5 has anomalously large snow thickness values not consistent with the pattern observed in the other two passes (4 and 6), see figure 6.26. This could possibly be explained by the larger deviation from the flight path made during the Pass 5 flight between the flags, refer to figure 6.18. Perhaps the anomalous track line is symptomatic of larger than normal attitude changes of the helicopter, resulting in larger than normal off-nadir pointing of the radar. Consequently, Pass 5 is not used in further processing.

One final step is necessary prior to a direct comparison between the radar and *in-situ* data sets. This is due to the fact that the radar data is available at equal time intervals and not at equal distances along the transect. Consequently it needs to be mapped onto a distance axis. This is done by averaging the radar data into 5 m along track intervals.

Figures 6.27 and 6.28 plot the result after averaging and mapping for the 100 m and 50 m Passes. To generate this comparison, the snow thickness derived from the three Passes was averaged, and the average smoothed with 5-point moving average filter. The filter is applied in order to smooth out the high frequency variability in the radar data. Note, that the *in-situ* thickness (plotted in red) differs between the two Passes due to their 4 m separation which was taken into account when generating the average thickness. This comparison demonstrates a definite likeness between the radar and *in-situ* snow thickness values; a significant correlation of 0.88 is calculated for the Passes 1, 2 and 3, and 0.84 for the Passes 4, and 6. The lower performance observed in the 50 m altitude passes compared with the 100 m passes is probably the product of higher deviations of the helicopter from a straight line track. These significant correlation values support the notion that the radar is sufficiently sensitive to the snow thickness over the fast ice, and that the values it reports are geophysically significant.

A linear regression analysis, shown in figures 6.29 and 6.30, shows a likeness between the *in-situ* and radar derived datasets, with similar residual norms of 110.4 and 102.5 mm. The gradient of the regression could be expected to be 1.0, however, it deviates from this value. This could be due to an incorrect selection of the mapping coefficient between the range bin values of the radar, and the *in-situ* measured snow thickness values. However, when this coefficient is changed to force a 1.0 gradient, the residual error increases. This indicates that the result of the gradient deviation from 1.0 is not a result of this parameter, but rather a general bias in the radar data towards a smaller range bin selection, the cause of which could be explained by either lack of penetration of the signal to the ice surface completely, or selective losses at the higher frequencies (due to salinity or other dispersive properties of the snow pack), also crusty layers above the “true” ice surface could have reflected the signal. All these features of the snow pack are undetectable to the *in-situ* observer, yet affecting the radar signal.

A correlation of 1.0 should not be sought, and could rarely be achieved in practice. The reason for this is that the radar’s *view of the world* and a ruler measurement of snow thickness are not theoretically in one-to-one correspondence. The radar signal may be affected by conditions that humans cannot detect, such as icy layers or wetness within the snow pack. As such the above assessment undertaken demonstrates a correlation coefficient that is sufficient for the purposes of validation.

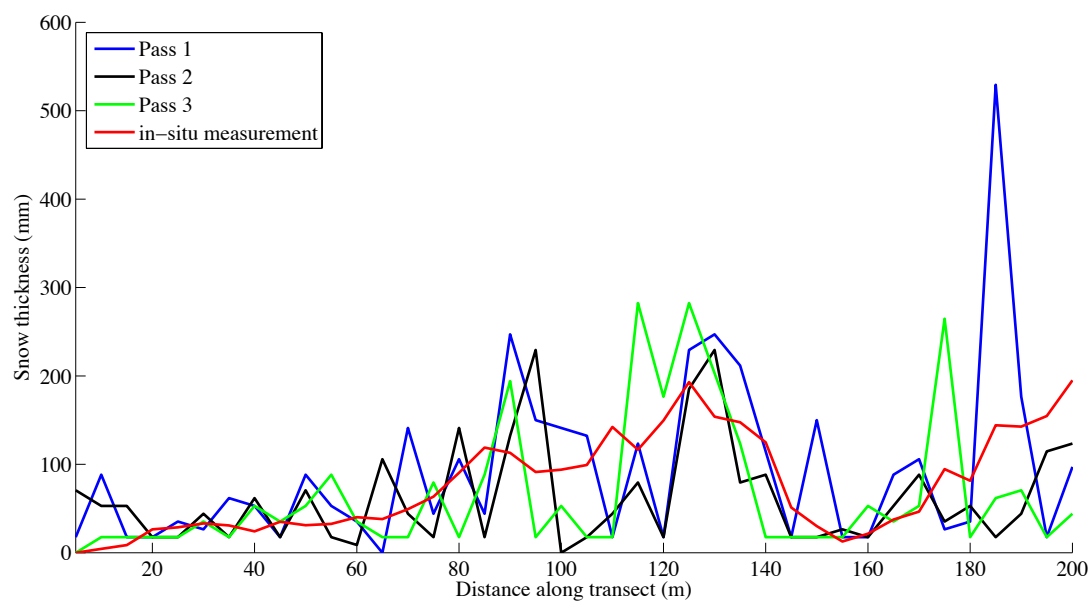


Figure 6.25: Snow thickness retrieved from the individual Passes: 1, 2, and 3.

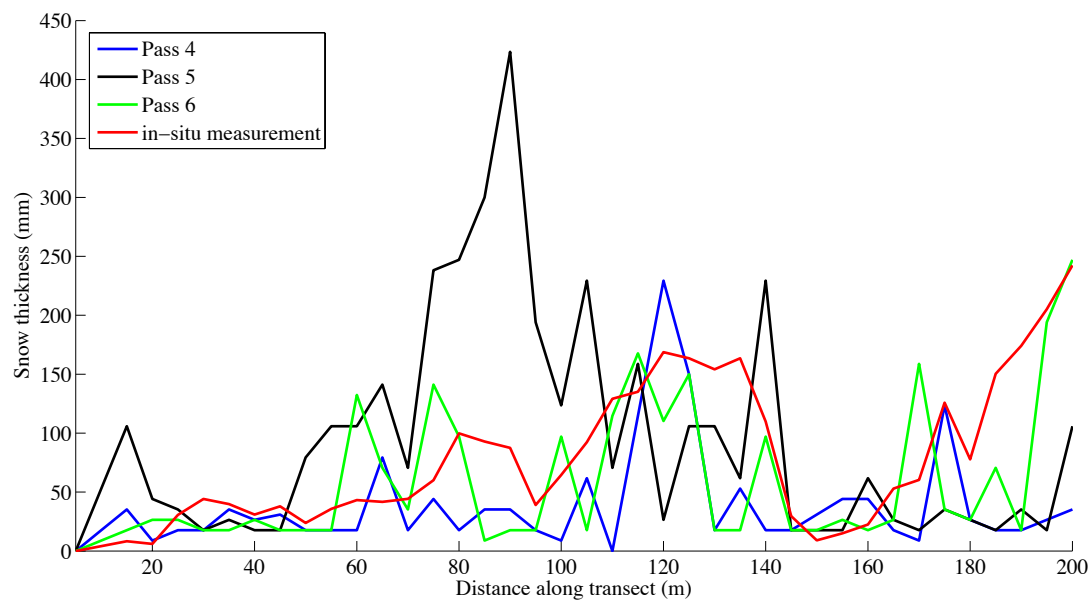


Figure 6.26: Snow thickness retrieved from the individual Passes: 4, 5, and 6. (Pass 5 snow depth retrieval is poor due to helicopter path deviations from flight line.)

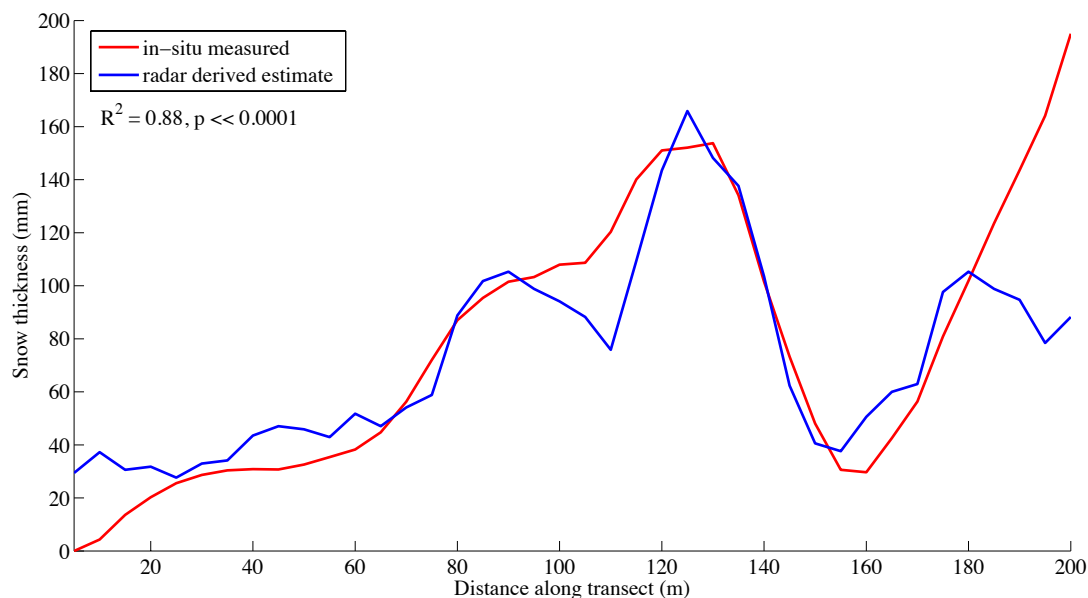


Figure 6.27: Comparison between the *in-situ* measured snow thickness, and the average radar derived snow thickness for the passes at 1, 2 and 3.

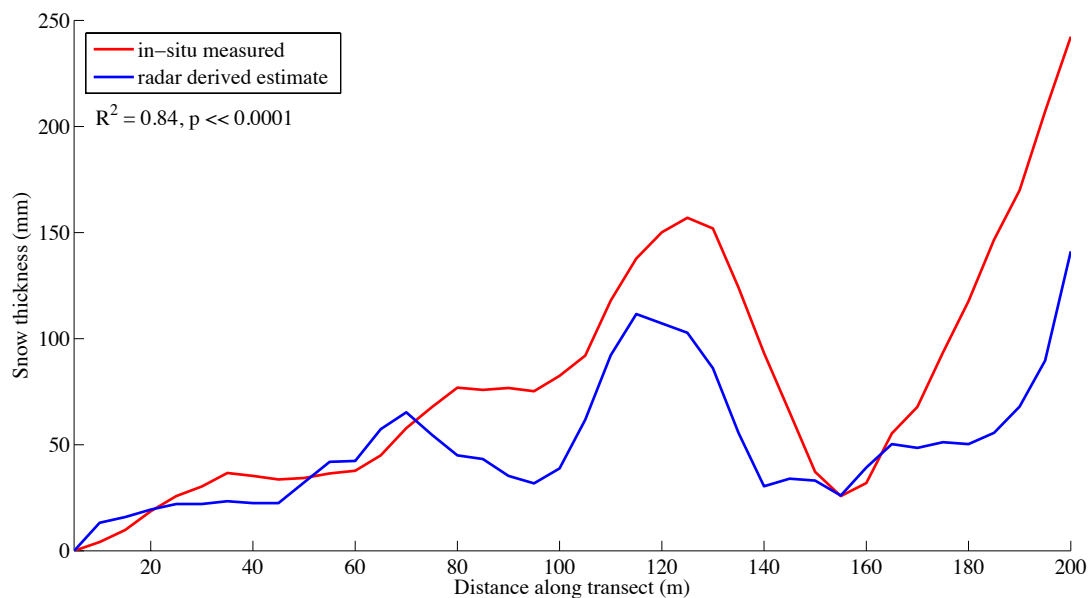


Figure 6.28: Comparison between the *in-situ* measured snow thickness, and the average radar derived snow thickness for the Passes 4 and 6. (Pass 5 is excluded from the average due to its high deviation from the flight path.)

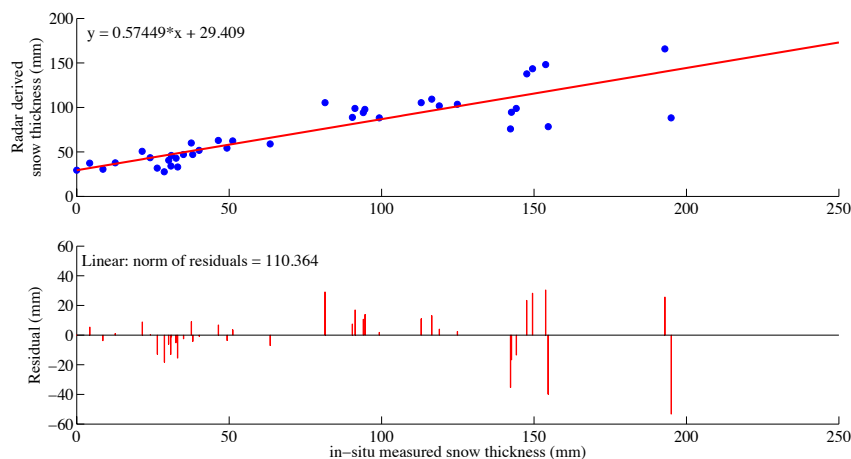


Figure 6.29: Scatter plot of the *in-situ* measured snow thickness versus the radar derived snow thickness. A linear least-squares fit to the data points is overlaid. It could be expected for the gradient of this line to be 1.0, and offset to be zero. However this is not the case. The smaller gradient value indicates that the radar under-estimates the snow thickness, which could be explained by the presence of undetected icy layers in the snow pack, or salinity at the bottom of the snow pack which was not measured. The bias value of 29.409 mm is less than the radar range resolution, and consequently the result of the resolving capacity of the radar system.

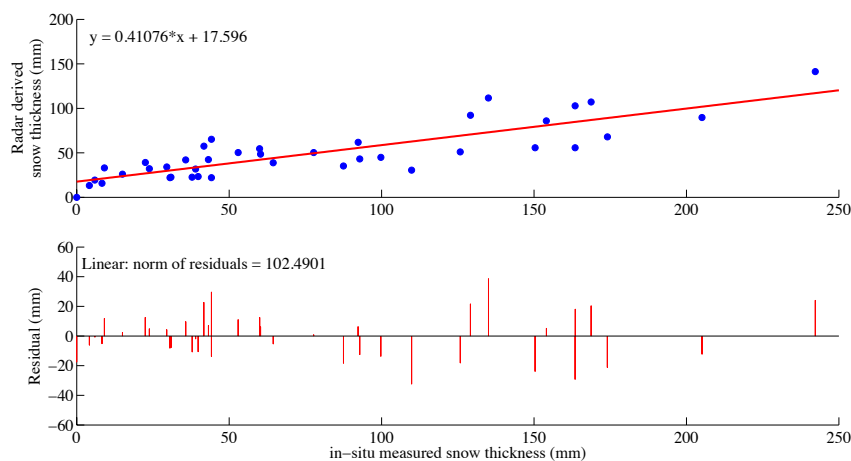


Figure 6.30: As in figure 6.29, the gradient deviation from 1.0 is the result of the radar underestimating the snow thickness. The differences between the two regression curves for the two lines (A and B) could be indicative of the differences in snow properties such as density and grain size, which were not measured separately for the two lines. In future experiments, it would be preferable to measure the density profile of both (or more) lines and if the salinity of the snow pack.

6.3.8 System Error Estimate

The availability of *in-situ* data for the flights allowed an estimate of radar accuracy. The percentage error between the *in-situ* and radar derived snow thickness estimates was calculated and plotted in figure 6.31, as a function of averaging area from 1 m - 100 m. The point-to-point performance of the radar is poor, at 70 %. However, it is encouraging that the difference in mean snow thickness estimates between the two methods is $\approx 20\%$. This error is representative of the *complete system* errors, including: vibration, off-nadir attitude of the helicopter, residual non-linearities, clutter, and processing errors.

6.4 Summary

This chapter provided a description of the radar helicopter platform and estimated the surface conditions encountered during operation. A step-by-step analysis of the validation procedure of the radar data is presented. The comparison and correlation between the radar derived and *in-situ* data are shown to be significant. Hence the radar operation for snow thickness extraction is validated. The 100 m mean accuracy of the helicopter-borne radar as a snow thickness retrieval system is calculated to be 20%.

Finally, exploiting the fact that the radar is receiving returns from the air/snow and snow/ice interface separately, it is possible to calculate the RMS height of the snow surface and underlying sea ice surface as *seen* by the radar. Just as was done with the laser data, the RMS height of the surface is calculated over increasing lengths. Figure 6.32 shows this estimated surface height as a function of increasing integration length, showing that the air/snow interface is rougher than the underlying ice, which was observed over the regions studied, and could be expected over fast ice in Antarctica. The *absolute* values of the calculated standard deviation are not considered to be representative of the actual surface features as it is not clear that the peak-picking algorithm selects the correct snow/ice peak. In future, with improvements to the radar system, and peak-picking algorithm it may be possible to derive estimates of surface and sub-surface roughness.

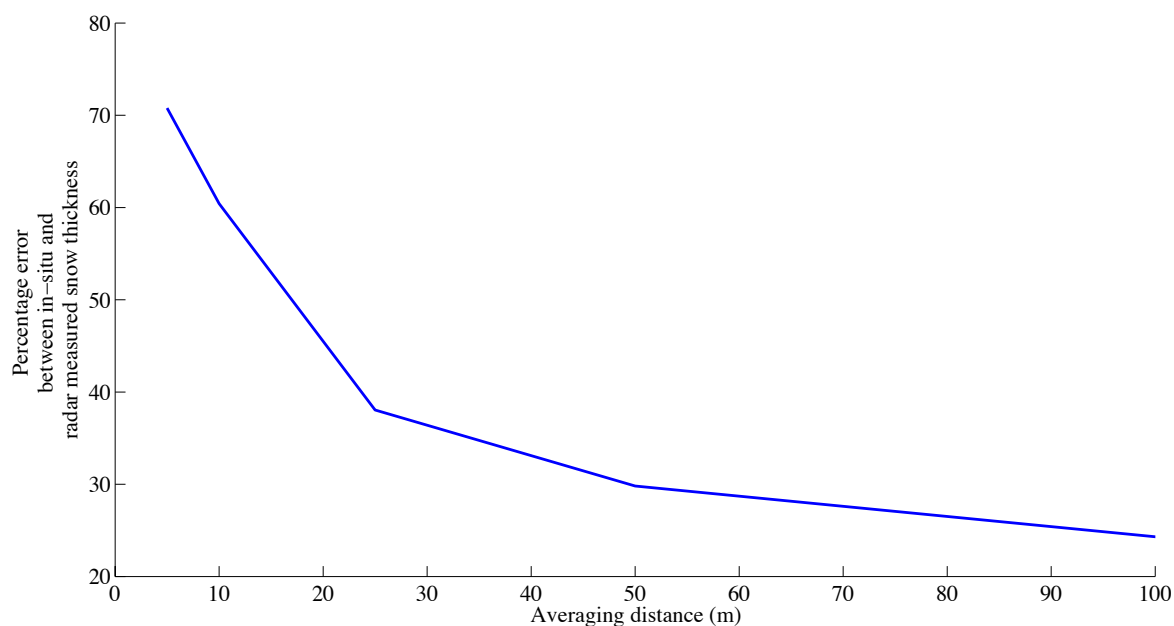


Figure 6.31: Error in helicopter data estimates as a function of averaging interval.

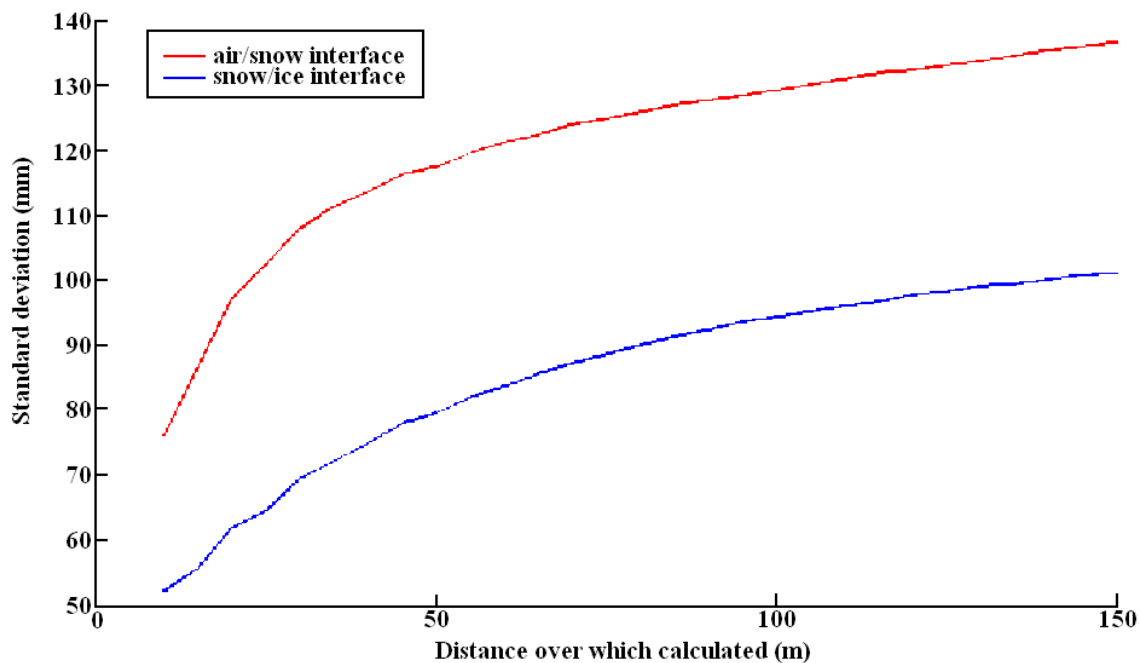


Figure 6.32: Estimated roughness (as RMS height) derived from the radar data for the air/snow and snow/ice interfaces.

Chapter

7

Conclusions and Recommendations

The objective of this thesis was to investigate the possibility of measuring snow thickness over sea ice in Antarctica with a helicopter-borne 2 - 8 GHz Frequency Modulated Continuous Wave (FMCW) radar, and to attempt to validate the radar data with coincident *in-situ* measurements. Thus, demonstrating the practical capacity of the FMCW radar to conduct comprehensive assessments of the region's sea ice snow cover in future, larger-scale work.

At the time of writing, Antarctic sea ice snow thickness cover measurements taken by radar from an airborne platform have not been validated with *in-situ* data. The difficulty in doing so has been a function of the geophysical properties of sea ice, its snow cover, and instrumentation restrictions. The first of these relates to the highly variable nature of snow cover: it can be wet, icy, rough, and can be quite thin (in the order of tens of centimeters). As a result, an instrument with a small viewing aperture, high vertical resolution, and high incident power is required. Unfortunately, these are competing demands that a single instrument finds difficult to satisfy. Moreover, it is challenging to obtain centimeter-scale vertical resolution measurements from a radar mounted on an inherently unstable (helicopter) platform, and then to validate this collected data.

This radar was provided by the Centre for Remote Sensing of Ice Sheets, Kansas University. The design was based on a radar which had successfully been used from a sled for snow thickness estimation over sea ice in Antarctica in 2003 (*Kanagaratnam et al.*, 2007).

A number of difficulties were encountered during the first airborne campaign (SIPEX'07), which subsequently led to a reassessment of the radar hardware and software. The main problems were due to vibration of the radar in the boot of the helicopter, and the systematic error contribution of the frequency generator to degrade the vertical range resolution of the radar. In preparation for second field trials (V1'08), both problems were addressed: the vibration effects on the hard-disk drives were minimised by use of an anti-vibration mount, and the systematic error was recorded for subsequent removal in post-processing of data.

The modification of the radar hardware to include a reference target for a *post factum* assessment of the non-linearities allowed for a signal processing algorithm to be developed to improve the quality of the data. The development of this algorithm is an essential element of this work, as it allowed for the identification of the air/snow and snow/ice interfaces. The second airborne campaign was successful in gathering airborne data and *in-situ* measurements to validate the radar.

Galin et al., (in press), summarise the work presented in this thesis, of the first *in-situ* validated results of snow thickness over Antarctic sea ice derived from airborne FMCW radar. To date, while it is theoretically assumed possible, *in-situ* validated snow thickness extraction over sea ice in Antarctica from an airborne platform has not been demonstrated. This is a function of the geophysical features of sea ice and its snow cover, and instrumentation difficulties. The first of these relates to the highly variable nature of the snow cover. It can be wet, icy, rough, and is typically relatively thin (order of tens of centimetres). As a result, an instrument with a small viewing aperture, high vertical resolution and high incident power is required. Unfortunately, these are all competing demands, which are difficult to satisfy with a single instrument. A helicopter is a highly unstable platform, and the second problem refers to difficulties in obtaining centimetre scale vertical resolution from a radar on this platform, and subsequent validation of these data. Overcoming these difficulties, this work presents analysis of the complete radar system, and the validation method of the radar with *in-situ* measured snow thickness. The validation results over a 200 m transect (over which snow thickness ranged from 0 - 300 mm) demonstrate that the radar was able to retrieve a mean snow thickness over 100 m with a 20% error. The error of the radar over its 5 m footprint is much greater, at approximately 75%.

7.1 Discussion

Admittedly, a 200 m transect for validation on a radar that is intended for regional studies of snow thickness is limiting. Unfortunately, time constraints, and circumstances prevented further data assessment. Furthermore, due to the vast area covered by sea ice in Antarctica, it should be acknowledged that in all probability no one regional validation campaign will provide results that will be application over the whole Antarctic sea ice extent. In future, it is foreseen that various satellite products and instruments will be tuned to regional sectors and seasons of the Antarctic.

Detailed analysis of the interactions of the 2 - 8 GHz chirp with the snow is outside the scope of this thesis. However, the overview presented in this thesis demonstrated that the interactions of

the 2 GHz frequency with the snow are quite different to that of the 8 GHz frequency. Generally speaking it is not yet well understood how a radar signal will interact with the snow cover over sea ice¹. This is supported by finding of *Leuschen et al.*, 2008 and *Willatt et al.*, 2008, as well as the findings of this thesis from both sled and airborne gathered data. For example, the analysis of the performance of the peak picking algorithm showed that there are times when the return from the snow/ice interface is not always stronger than that from the air/snow interface. Suggesting that perhaps penetration into the complete snow pack did not occur at all, prevented by flooding and/or brine wicking into the snow.

These findings do beg the question however: what is “snow depth” on sea ice? Accuracy of measurement of the instruments refers to the degree to which they are representative of the *truth*. However, in the case of snow over sea ice, this is not a clear concept. As a first attempt at a definition; snow should be defined as a measure of precipitation onto the sea ice. However, while the thickness of snow cover on sea ice is most certainly indicative of this process, it by no means provides a direct measure of it. This is due to the fact that once snow has fallen, it may be subject to aeolian distribution as well as metamorphic processes such as compaction, ice layer formation, depth hoar creation, basal flooding, and brine wicking. Consequently, once it has fallen it is difficult to unambiguously define where snow ends and ice starts. This is unlike terrestrial snow where there is a clear defining line between what is snow or ice, and what ground is, be it earth, gravel, cement, tundra, etc.

As the radar is an instrument sensitive to dielectric contrasts, perhaps a way forward on this issue is to redefine the problem by characterising the nature of the dielectric range which may be encountered in the snow cover over sea ice in Antarctica, and tuning the radar sensitivity according to the specific snow type within this range.

Such attempts however, may be further complicated by the features of small- and large-scale roughness of the snow cover. These features have been reported to cause the poor performance of a number of remote sensing instruments, for example: AMSR-E (*Markus et al.*, 2011), EM induction sounding (*Worby et al.*, 1999), airborne laser-altimeter (*Peterson et al.*, 2008), and airborne radar-altimeter (this work). Coupled with reports that a large volume of ice is locked in ridges and deformed areas (especially in Antarctica *Worby et al.*, 1998) this issue needs further

¹Especially an ultra-wide band signal where definition of centre-frequency are superfluous.

research. Snow and ice surface properties are not stationary in time, or spatially, and assuming ergodicity is not possible. These considerations are currently lacking in analysis of the radar signal interpretation, and admittedly in this thesis also, but in future work should be considered.

The considerations of both heterogeneity of the snow pack, and its spatial and temporal variability prevents a consensus of the required accuracy of snow depth retrieval over regional or global scales to be reached. Further work into the characterisation of the snow pack, its physical and dielectric properties is required.

7.1.1 Suggested Technical Improvements

Undoubtedly more fieldwork, direct observations and studies of Antarctic sea ice and its snow cover are needed. Additionally, based on the findings of this work, the suggested parameters for a FMCW radar that will avoid intensive post-processing of the data, and consequently improve snow thickness estimates are explored in *Galín*, [2010].

Improving the performance of the radar hardware is necessary for future work. The suggested changes are listed here in order of priority:

- (i) Use antennas with a narrower beamwidth. The wide beamwidth of the current antennas, apart from contributing to ambiguity in resolution of the air/snow and snow/ice interfaces, leads to sub-optimal use of power. Additionally, increase the usable bandwidth of the antennas to correspond to the full generated frequency range.
- (ii) Change the frequency generation method, which depending on the budget, and time constraints could take the following forms:
 - (a) if the oscillator had to remain in open loop operation, efforts should be made to hermetically seal it together with its driver in order to achieve the best possible temperature stability, and hence output frequency linearity, or
 - (b) if alterations to the setup were possible, place the oscillator within a negative feedback loop, i.e. a 3rd order Phase Locked Loop (*Nash*, 2006) to achieve zero error in tracking to quadratic changes in phase, or

- (c) use a Direct Digital Synthesiser (*Griffiths*, 1990) configuration (e.g. based on the AD9956 board, capable of generating up to 2.7 GHz (*Analog Devices*, 2004) to synthesise a coherent, highly linear, and most importantly repeatable chirp. However, due to the digital nature of the technique the contribution of phase noise to adjacent range bins would need to be considered.
- (iii) A second receive antenna, polarised in the same plane as the current transmit/receive antenna pair could be added to facilitate a second simultaneous measurement of snow depth, but from a slightly different angle. This second independent measurement could allow for the calculation of the snow density, and hence could facilitate Snow Water Equivalent (SWE) retrieval. This would be an invaluable gridded product for modellers.
- (iv) Alternatively, a completely different radar architecture could be considered, namely a step-frequency radar (*Iizuka et al.*, 1984; *Kawamura et al.*, 2006), which would relax the stringent linearity condition, while still maintaining the high vertical resolution. Such a radar has previously been demonstrated to measure saline ice thickness (*Iizuka et al.*, 1988). However, due to slow switching times these have so far been limited to hand-held/sled operation. It is envisaged that if not current, then future technology will make this possible.
- (v) Additionally, due to the large apparent unambiguous range (150 m), a high sampling frequency was used (12.5 MHz), consequently demanding high storage capacity (120 Gbytes/hr). This is not the case, however, as the maximum actual unambiguous range, at a highly conservative estimate, is a maximum of 5 m (i.e. maximum thickness of snow cover). Hence, with some adjustment to the nature of sampling or inducing delay to the transmitted chirp before mixing, this strain on storage capacity and post-processing tasks can be eliminated.

7.2 Related Work and Outlook

Massom, R.A., H. Eicken, C. Haas, M.O. Jeffries, M.R. Drinkwater, M. Sturm, A.P. Worby, X. Wu, V. Lytle, S. Ushio, K. Morris, P.A. Reid, S.G. Warren and I. Allison [2001] state that snow will play an increasingly important role in the environments of the polar regions if changes in Earth's climate result in greater high-latitude precipitation. Ultimately satellite platforms should provide snow thickness data, for both accumulation assessment, and sea ice thickness estimation. The

immediate future use of this radar should be toward the validation of satellite data, such as that reported by the AMSR-E instrument, and possibly extended to interpretation of other satellite data such as the Envisat radar altimeter.

The importance of remote sensing snow on sea ice on a regional and global scale is increasingly recognised by the science community (*Breivik et al.*, 2009). To achieve this additional satellite missions have been planned: CryoSat-2, launched on the 8th of April, 2010, as well as the continuation of the ICESat mission with ICESat2 planned for launch in 2015.

Even during the relatively short lifetime of ICESat, its data has provided such an important contribution to improving our understanding of the polar regions that in the time until 2015 NASA is investing in two airborne field campaigns per year (NASA - ICEBridge) for monitoring changes in the Arctic and Antarctic. One of the instruments on board the fixed-wing aircraft is a snow thickness FMCW radar (*Panzer et al.*, 2010), thus increasing the relevance of this work, and its potential contribution. Future satellite proposals highlight measuring sea ice thickness, growth, snow accumulation, heat exchange and momentum as goals, (*Rott et al.*, 2008).

In the Integrated Global Observatory Strategy (IGOS) Cryosphere theme report of 2007, emphasis has been placed on the integration of experimental data from different methods for the mutual benefit of research conducted into the nature of the polar regions. The benefit of having data from various sources is that no current or future dataset is ever likely to satisfy all desired criteria. *Drinkwater* [1989], *Remund et al.* [2000], *Askne* [2002], and *Dozier and Painter* [2004], all stress the usefulness of using a multisensor approach to the solutions of global monitoring problems.

Appendix



RAdar for Antarctic Snow Thickness Investigation (RAASTI)

A.1 Introduction

This appendix summarises the adaptation of the 2 - 8 GHz FMCW radar for estimating snow thickness over sea ice in Antarctica to operation from a helicopter. The radar was generously loaned by CReSIS to the AAD in 2007 and 2008 for installation and operation from a helicopter platform for the purpose of gathering snow thickness over sea ice. However, initial testing determined that it did not meet the strict requirements necessary for successful operation and data collection from a helicopter platform. Hence, a number of changes were made to the hardware and software; these changes and laboratory work performed are summarised in the following sections. Additionally, after the SIPEX'07 voyage, the radar underwent further evolution in attempts to compensate and minimise the sources of error which were noticed during this first field trial; section A.3 describes these changes.

A.2 SIPEX'07, Radar Version 1.0

A block diagram of the basic components of the radar used during SIPEX'07 is provided in figure A.1. The following modifications were made to the radar (the blocks to which the modifications apply are outlined in blue in the above figure):

- (i) initially a separate power supply box was provided for the RF box of the radar. This required three 19-inch racks in total to be installed into the boot of the helicopter. To remove this box the two PXI-4110 precision power supply boards were wired in parallel, and programmed to supply power to the RF box: $\pm 15 \text{ V @ } 3 \text{ A}$.
- (ii) the original *main coil driver* (voltage to current converter) to the YIG was tested and found to be noisy, figure A.2 shows the schematic of this driver. It was replaced with a driver

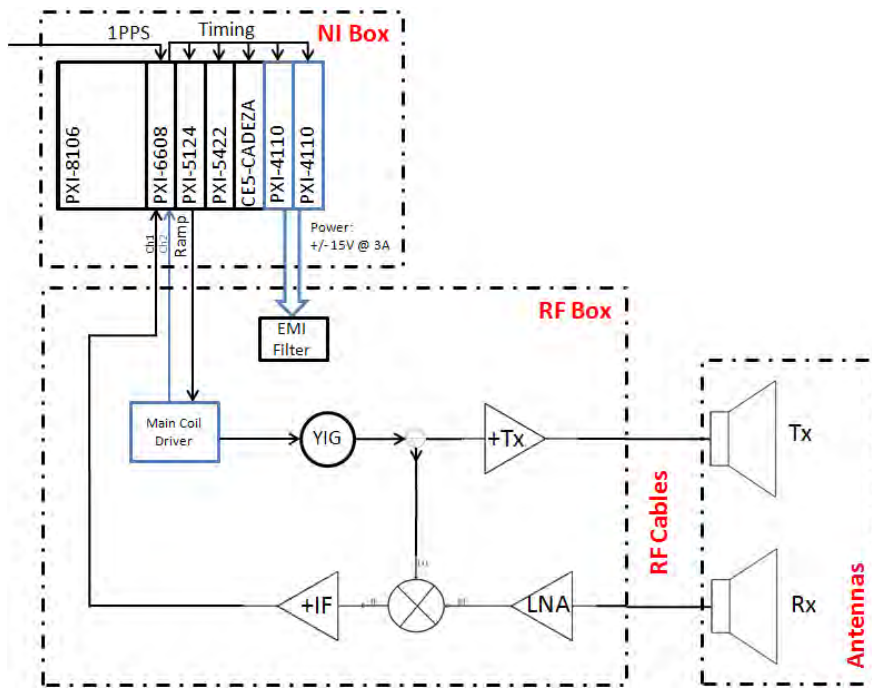


Figure A.1: RAASTI v1.0, the SIPEX'07 radar block diagram.

whose schematic is shown in figure A.3. Figures A.4 and A.5 compare the test results of the IF frequency generated with a delay line target by the original driver and the replacement. A comparison of the frequency response demonstrates that the original driver generated noise in the 1 MHz region, which would interfere with any signal that was received at that frequency. In the modified driver this noise is absent.

In the sections to follow a description of the blocks of the radar, and laboratory work performed to verify operation are described.

A.2.1 Antennas

The airborne tests were conducted with a set of custom built TEM horn array antennas (from CReSIS), which were flight approved and mounted between the skids of the helicopter as shown by the photographs of figures A.6 and A.7.

Aircraft Mounts

Figure A.8 is the technical drawing of the aviation approved mounts designed and constructed at the AAD to secure the antennas between the skids of the helicopter.

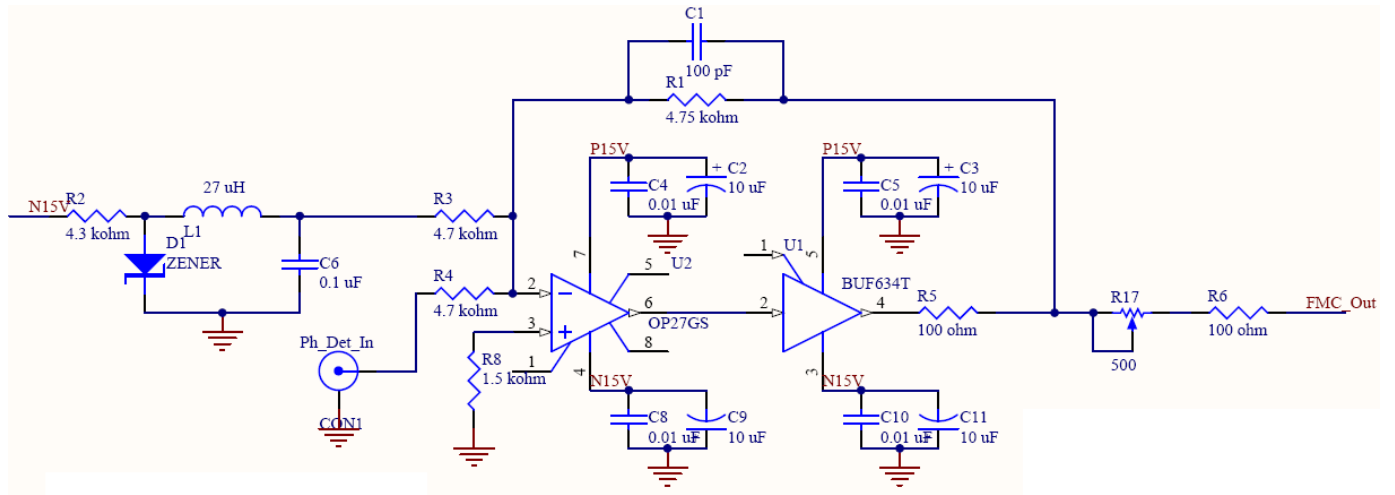


Figure A.2: Original YIG main coil driver, *courtesy of CREsis*.

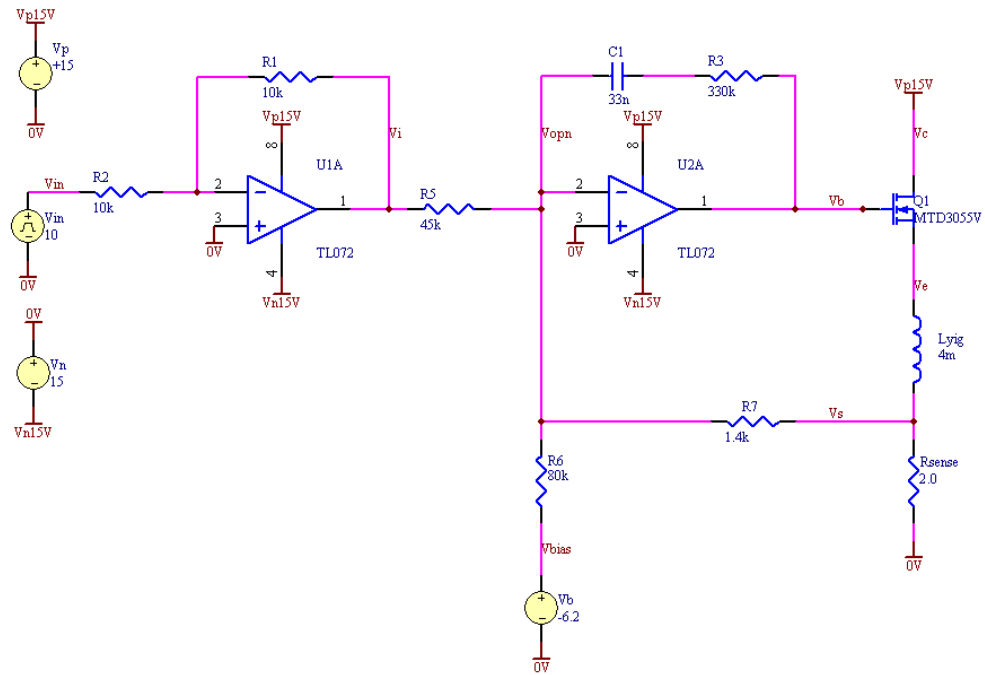


Figure A.3: Modified YIG main coil driver, *courtesy of P.Jansen (STS-AAD), adapted from MicroLambda Inc..*

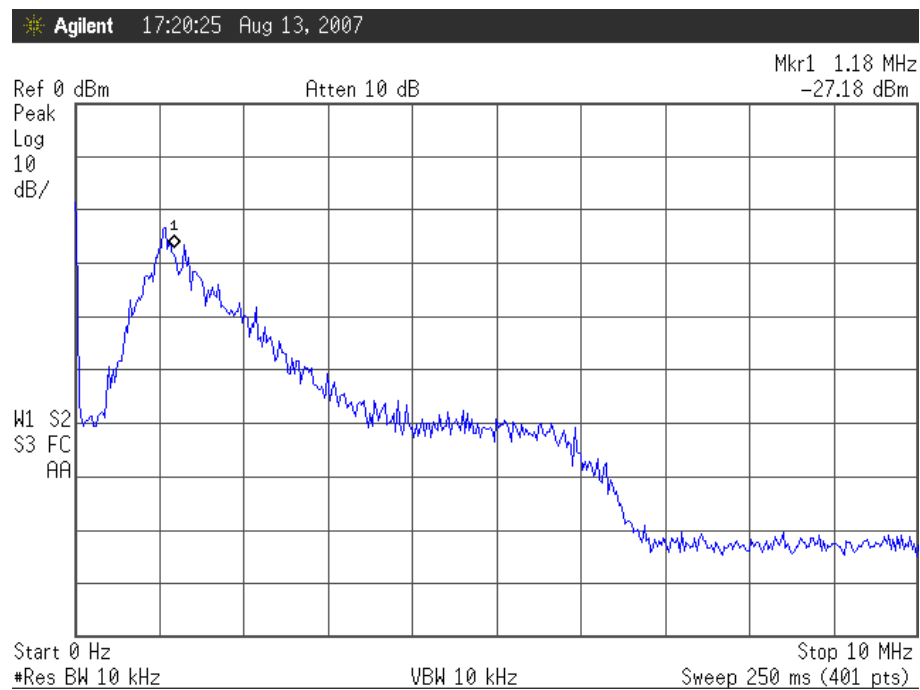


Figure A.4: Frequency response: original YIG main coil driver.

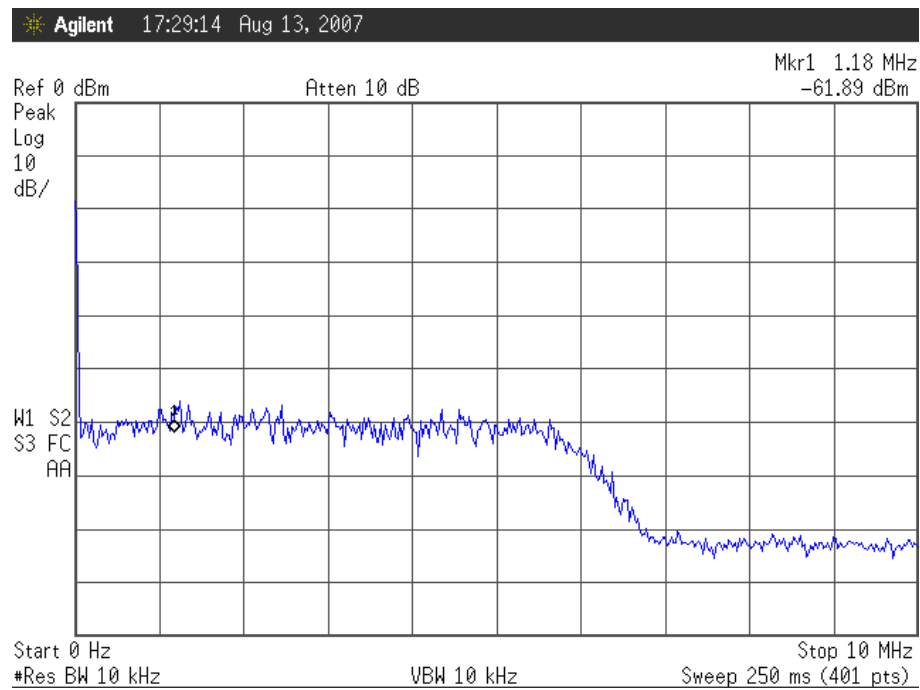


Figure A.5: Frequency response: modified YIG main coil driver.



Figure A.6: Custom designed 8 - element TEM horn array for helicopter operation, shown here within radome (PelicanTM 1700 case).



Figure A.7: Custom designed 8 - element TEM horn array in radome, attached between helicopter skids.



Figure A.8: Technical drawing of the antenna mounts for helicopter operation. *Courtesy of S. Whiteside, AAD.*



Figure A.9: Array antennas attached to cage pallet for crane tests.

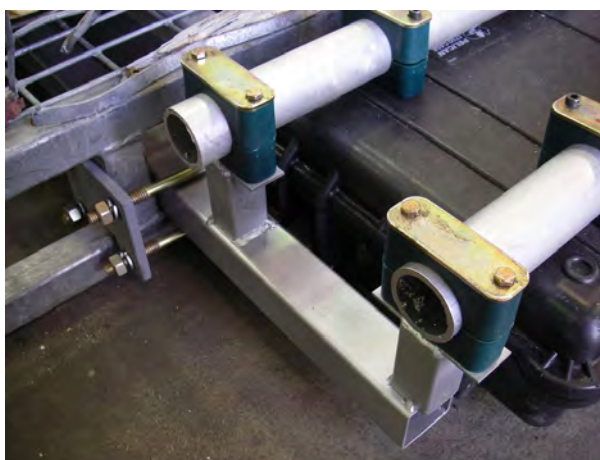


Figure A.10: Close-up: Array antennas attached to cage pallet for crane tests.

Crane Mounts

The array antennas had to be attached to a cage pallet for experiments from the ships crane. Figures A.9 and A.10 show the method of attachment of the antennas to a cage pallet.

A.2.2 YIG –Yttrium Iron Garnet Current Controlled Oscillator

Company: Micro Lambda Wireless Inc.

Model: MLMH-0208X

Serial No: 22845

The **X** suffix indicates that the YIG is specially designed to comply with the Military standard: MIL-STD-810E.

A.2.3 YIG Main Coil Driver

A replacement to the original current to voltage converter was built to interface between the National Instruments Arbitrary Waveform Generator (AWG - PXI-5422) and the YIG oscillator. The driver design was taken from the Micro Lambda application notes, and figure A.11 shows the schematic for the driver. For debugging purposes, to capture the nature of the signal sent to the YIG from the AWG, the voltage level across the resistor - R9 is tapped, and recorded on channel 1 by the digitiser (PXI-5124) board.

Current Stability:

For radar performance, the most important characteristics of the driver are its linearity and response time. The YIG oscillator is reported as having frequency sensitivity to main coil current of: 10 MHz/mA, combining this with the required frequency resolution of 800 Hz, the controlling current must be stable to within:

$$\frac{10[\text{MHz}]}{1[\text{mA}]} = \frac{800[\text{Hz}]}{x},$$

$$x = 80[\text{nA}].$$

For a fixed current through R9 to affect the current flow by 80 nA the resistance needs to change by:

$$V = RI,$$

$$dV = \Delta RI,$$

$$\Delta R = \frac{dV}{I} = \frac{\Delta IR}{I}, \text{ for}$$

$$0.2 \leq I \leq 0.8 [\text{A}],$$

$$1200 \times 10^{-9} \geq \Delta R \geq 300 \times 10^{-9} [\Omega].$$

The temperature coefficient of resistance (TCR) is 50 ppm/°C for R9, which means that the temperature change of the resistor must be less than 6°C at 0.8 A, and less than 24°C at 0.2 A. At these currents the resistor dissipates between 0.12 W and 1.92 W. Provided that the thermal resistance of the component is 3.3°C/W (as quoted in the datasheet) means that the temperature across the component will increase to somewhere between 0.4°C to 6.3°C as the driver sweeps

across the voltage. This is just low enough to prevent R9 from drifting in resistance so much as to go above the current drift requirements of less than 80 nA.

Noise Level:

Noise can and is introduced onto the control signal line by the amplifier (AD708). The datasheet quotes this noise signal level as 0.23 uVp-p on average. Examining the second stage of the driver schematic, the change in signal voltage experienced at point **B**, due to a change in current of 80 nA at point **A**, is calculated as:

$$\Delta V = \frac{R_7 + R_9}{R_6 + R_7} (80 \times 10^{-9}),$$

$$\approx 0.23[\mu V].$$

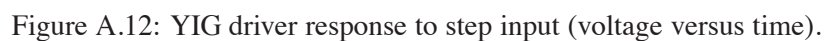
This is equal to the input voltage noise of the amplifier, and hence this noise contributes to degradation of the achievable frequency resolution. It should be considered however, that this noise is given over the frequency range 0.1 –10 Hz, which is a slow changing signal when compared with the 400 Hz of the input voltage. Hence, it should not affect the quality of the signal within each waveform, only the ability to add waveforms together (coherent integration). Amplifier input voltage noise values are also provided for frequencies up to 1 kHz, but their values are in the pV region and are too low to affect the signal voltage waveform.

Response Time:

The step response of the driver was calculated to confirm that the driver was capable of driving the YIG with a current sweep from 200 mA to 800 mA in the desired time (1.25 ms), and that it was capable of maintaining this rate at, at least 400 Hz. To test this, the driver response to a step and ramp input was tested and the voltage across R9 monitored with an oscilloscope. The waveforms showing a step response with a rise time of 221 us, and a delay of 36 us during ramp were recorded and displayed in figures A.12 and A.13, respectively. The 3 dB bandwidth of the driver was found to be 3.8 kHz.

YIG Linearity Tests

To achieve the required 25 mm range resolution, the frequency stability at the YIG output is required to be within 800 Hz. From the above calculations, it is found that the supplied voltage



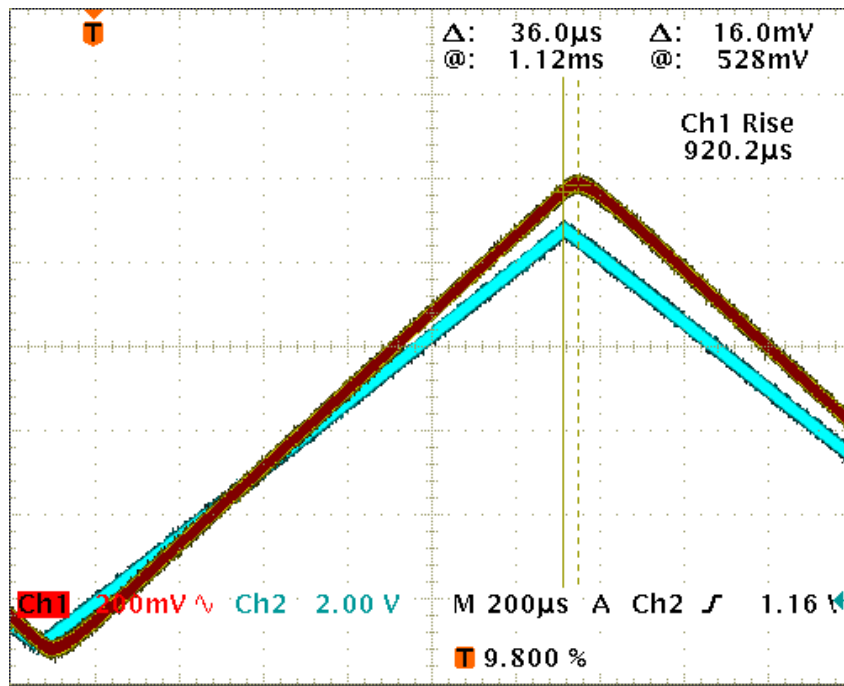


Figure A.13: YIG driver response to ramp input (voltage versus time).

and the voltage-to-current converter circuit were within specification for this. However, the YIG internal temperature is another strong contributor to the stability of its output. To gauge the level of drift in the YIG due to temperature, the YIG output frequency was recorded as a function of driver input voltage, and recorded to vary within 1 MHz, see figure A.14. Consequently, it is assumed that if spurious frequency jumps due to spikes in temperature could be minimised, the drift of frequency with current during chirping will be controlled to within the required level.

A.2.4 Laboratory Experiments

This section briefly summarises the components used, and laboratory experiments conducted (at the AAD) to characterise the radar performance.

Directional Couplers

Three directional couplers are present in the system, one is from an unknown company:

Narda 4244: -6 dB coupling,

Narda 4202B: -10 dB coupling.

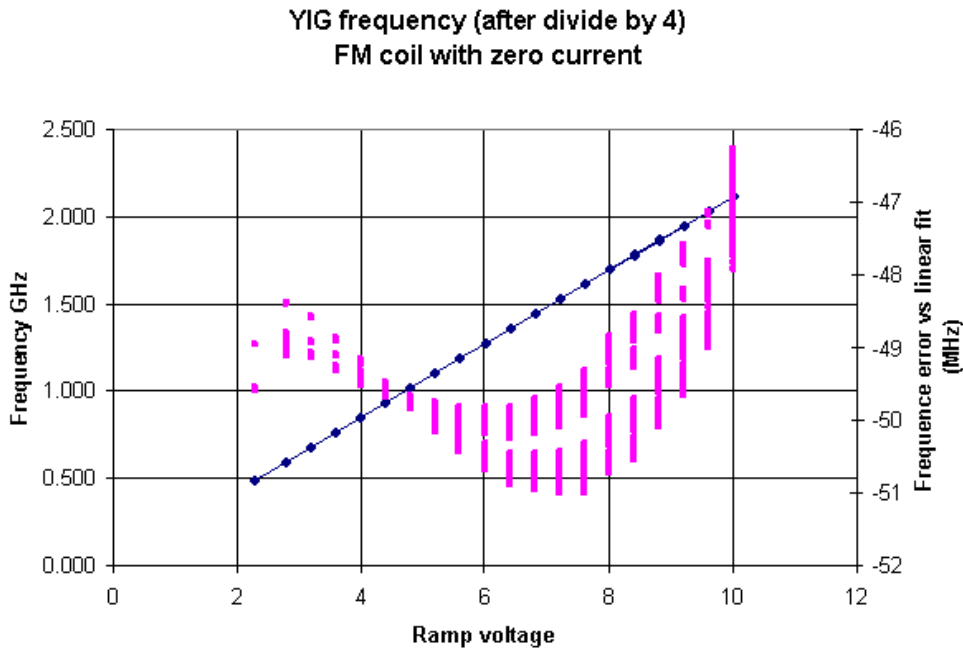


Figure A.14: YIG long term frequency drift. (YIG output monitored through a “divide-by-four” circuit.)

Transmit Power Amplifier

The Mini-Circuits ZVE-8G power amplifier was used to amplify the chirp signal before transmission. The linearity of the amplification to frequencies in the range 2 - 8 GHz is measured, and results are shown in figure A.15. The maximum output of 31.0 dBm occurs at a YIG driver voltage of 2 V (i.e. 3.2 GHz) and the minimum of 27.3 dBm occurs at a drive voltage of 10 V (i.e. 8 GHz). It was noticed, that even with a relatively constant transmit power of 30 dBm across the frequencies of interest, the Intermediate Frequency (IF) waveform is highly attenuated at the higher frequencies, see figure A.16 for an illustration. At first this was suspected to be caused by the lower cross over area of antennas, hence contributing to lower received power. However, even when the antennas were directed at each other (eliminating this possibility) the returned signal (IF) was still highly attenuated. This attenuation can be explained by the effective area of the antenna decreasing as the frequency is increased, this effect is discussed in detail in appendix E.

Low Noise Amplifier (LNA)

The MITEQ AMF-10-020080-35-13P low noise amplifier was used. The noise power in 1 Hz of measured bandwidth at 294 K, due to only white noise generated by the components in the system

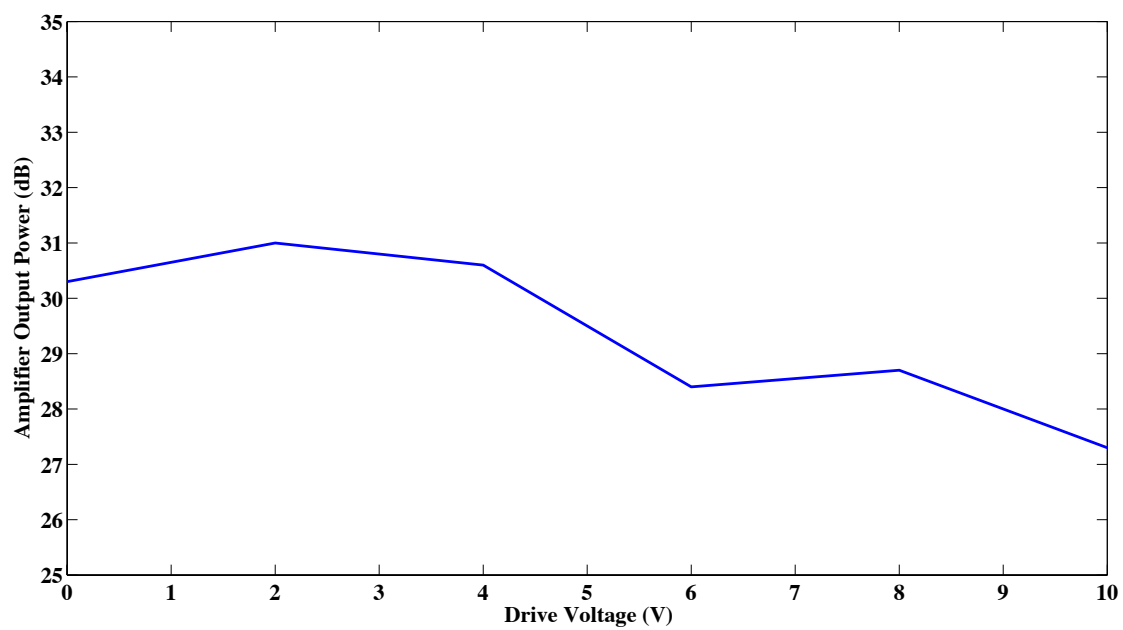


Figure A.15: Power at the output of the transmit power amplifier.

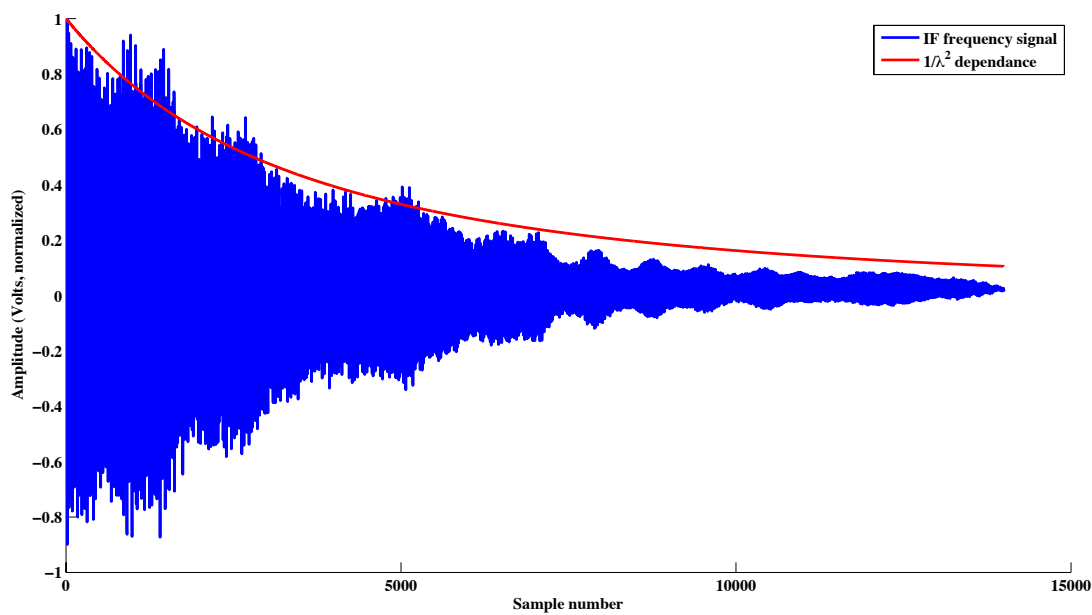


Figure A.16: Attenuation in IF observed at higher frequencies.

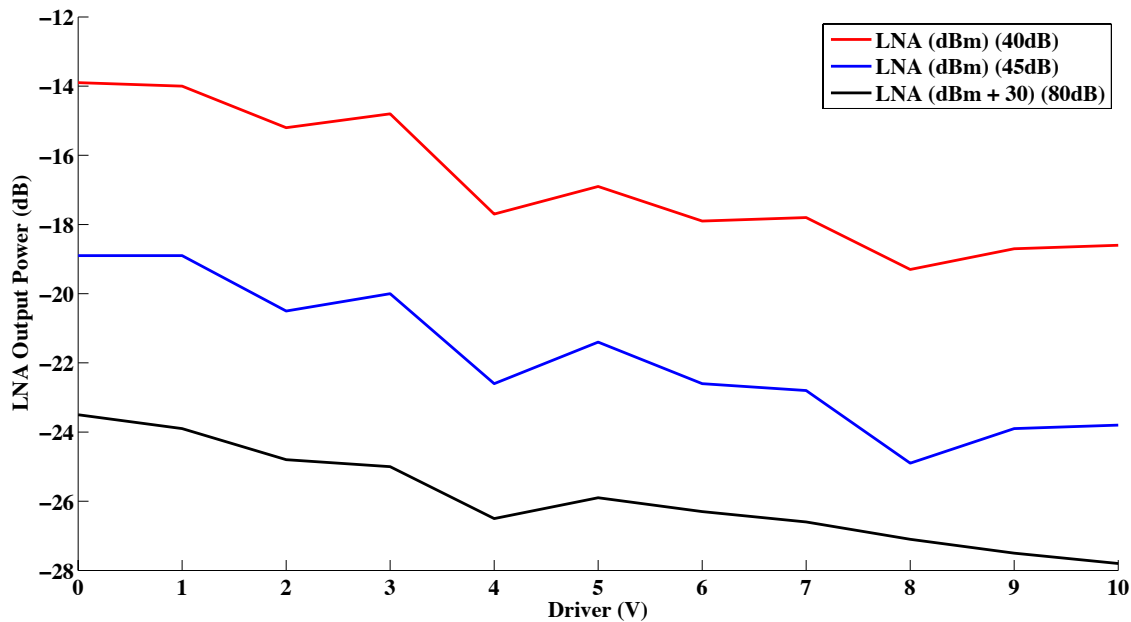


Figure A.17: LNA sensitivity test results.

is equal to: $kTB = -174$ dBm. The noise power contributed by the full 6 GHz bandwidth is: 98 dB. Using these values, cable attenuation and noise figure of the LNA, the minimum detectable signal (MDS) is computed as:

$$-174\text{dBm} + 98\text{dB} + 0.5\text{dB} + 3.5\text{dB} = -72.0\text{dBm}.$$

LNA Sensitivity Test

The LNA was tested for linearity as well as sensitivity across the driver voltages 0 - 10 V (i.e. the full range of output frequencies). The LNA was supplied with the attenuated YIG output, and figure A.17 shows a plot of the output of the LNA at attenuations of: 40, 45 and 80 dB (attached at the YIG output). The power meter when not connected gave a reading of - 62 dBm, hence it is assumed that the values recorded are valid. The experiment shows that that LNA is capable of amplifying very low power signals.

Mixer

The MITEQ DB0218LA1 mixer was used. The conversion loss was measured and found acceptable and within specification of the mixer.

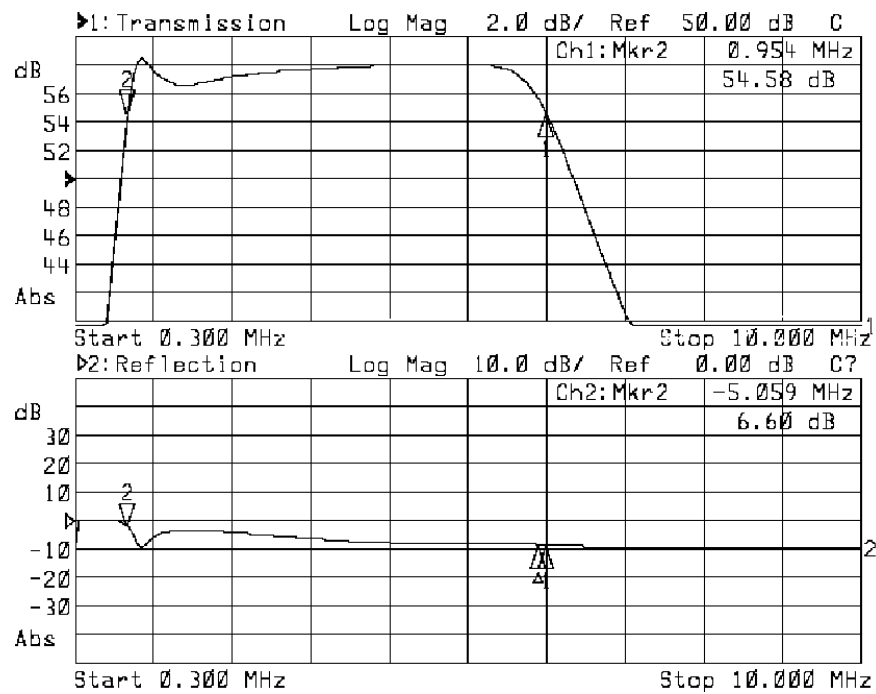


Figure A.18: Frequency response of the IF amplifier.

IF Filter/Amplifier

An IF amplifier (designed by CReSIS) was used which incorporated a 1 MHz high-pass and a 5 MHz low-pass filters. The operational amplifier on which the filter is based is the OP847, unfortunately no schematic is supplied. The frequency response of the IF amplifier as measured by a network analyser is presented in figure A.18, with the pertinent characteristics summarised below:

- Gain: 50 dB,
- Low-pass cut-off: 5 MHz,
- High-pass cut-off: 1 MHz.

EMI Filters

The Filter Concepts DT62 EMI filter was used to attenuate any possible spurious signals which may be coupled onto the cables supplying power to the RF box.

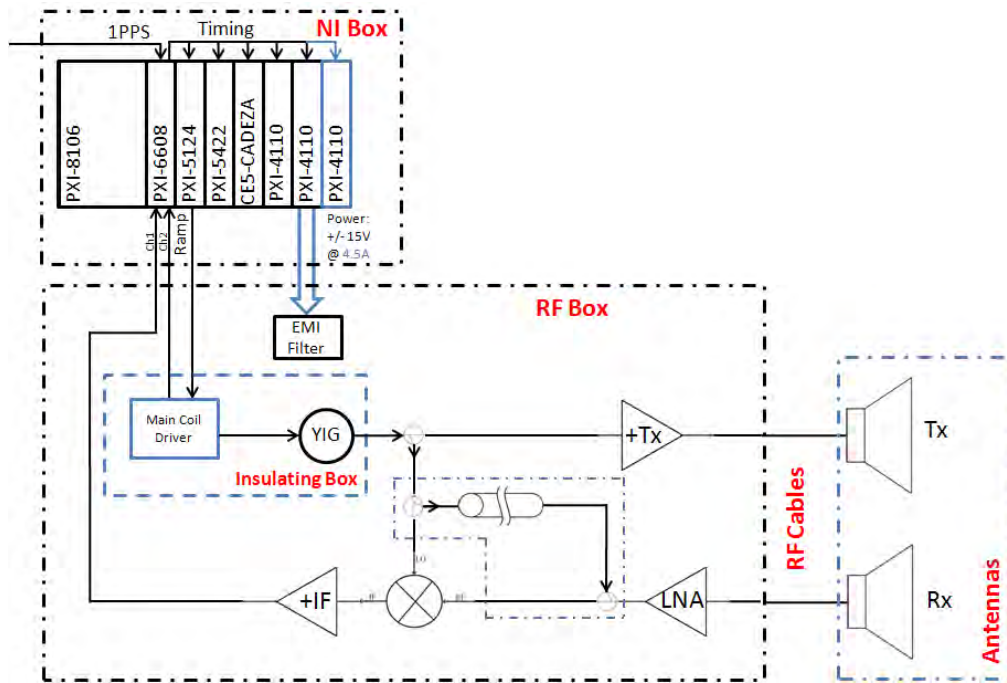


Figure A.19: RAASTI v2.0, the V1'08 radar block diagram.

A.3 V1'08, Radar Version 2.0

A number of further modifications were made to the radar, see figure A.19. The sections which were modified are outlined in blue, and summarised below:

- vibration problems of the hard-disk drives were eliminated, as described in appendix C,
- an extra precision power supply (PXI-4110) was added to power the radar RF box,
- the YIG main coil driver was updated,
- attempts were made to stabilise the YIG temperature to achieve frequency linearity,
- a delay line target was added to the radar to capture the non-linearities of the YIG,
- radar absorbing material was added to the helicopter antennas,
- the radar was adapted for sled-based operation,
- mount was built to minimise overall vibrations to the radar system.

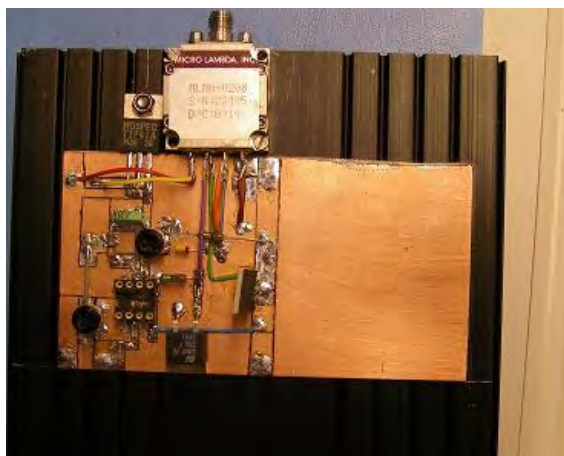


Figure A.20: The initial layout of the updated YIG mail coil driver. (Used during SIPEX'07.)

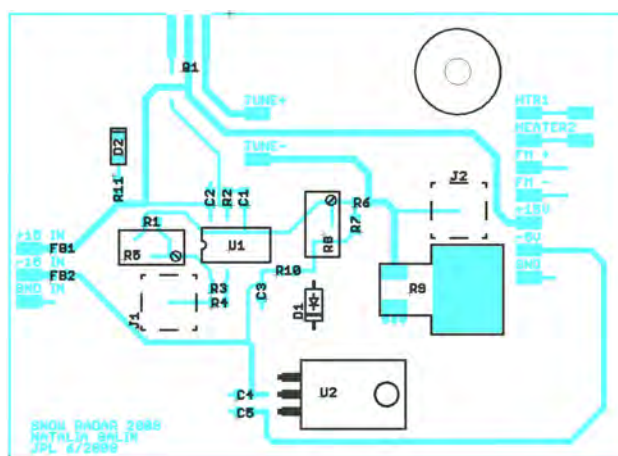


Figure A.21: The final layout of the updated YIG mail coil driver. (Used during V1'08.)

A.3.1 YIG Main Coil Driver

Due to time constraints the driver built for the SIPEX'07 experiments was mounted on a single copper plate, and the required tracks drilled out around the components, see figure A.20. In 2008, CReSIS provided the resources to update the driver schematic layout. It was laid out on a circuit board, and manufactured, see figure A.21. No changes were made to the driver schematic itself, and the performance remained the same.

A.3.2 YIG Heater Tests

The output frequency of the YIG oscillator depends primarily on two parameters: coil current, and temperature. As seen from the previous calculations, for the frequency deviation to be ± 400

Hz it is necessary for the coil current to be accurate to ± 40 nA, which is found to be achievable, especially under continuous sweeping conditions.

As to the temperature drift, the MLMH-0208 data sheet specifies a maximum frequency drift of 15 MHz over the operating temperature range of 0 – 65°C (personal correspondence with Micro Lambda engineer). To achieve less than this frequency drift with temperature, it is necessary to stabilise the temperature of the YIG core, this cannot be achieved as no direct access to the YIG coil is provided. However, the YIG has an internal heater which, when connected to a power source draws current to stabilise the YIG core, and maintain the internal temperature at around $85^{\circ}\text{C} \pm 1^{\circ}\text{C}$ to prevent spurious jumps.

The operating environment (inside the helicopter boot) is expected to be at an ambient temperature of around 20°C or less. The ambient temperature is much lower than the YIG temperature, consequently in these conditions the YIG will continuously be dissipating heat to the environment and may never reach the desired internal temperature. To prevent the YIG from continuously dissipating heat it was necessary to isolate the YIG and driver from the external environment. This was achieved by mounting the YIG on a temperature insulating material, and encapsulating the YIG and its driver within a separate box. To test the effectiveness of this isolation the temperature of the YIG case was monitored and the temperature data recorded. Figure A.22 shows a plot of the recorded case temperature as a function of flight time. The graph demonstrates that the temperature compensation of the YIG was not completely effective, and the case never achieved a strictly stable temperature. Hence, the effects of the temperature on the YIG output frequency must be considered in the data gathered.

A.3.3 Internal Delay Lines

There were four semi-rigid copper coaxial lines available to use as delay lines for testing the radar, see figure A.23, the fourth one is not seen here, was installed in the radar to provide a reference signal. The approximate lengths of the delay lines were measured and are listed in table A.1, (assuming a velocity factor of 69.5%).

Internal Delay Line Distortion

A power amplifier was used to increase the signal level prior to passing the signal to the internal delay line. The Mini-Circuits ZRON-8G was used for this purpose. In order to characterise any

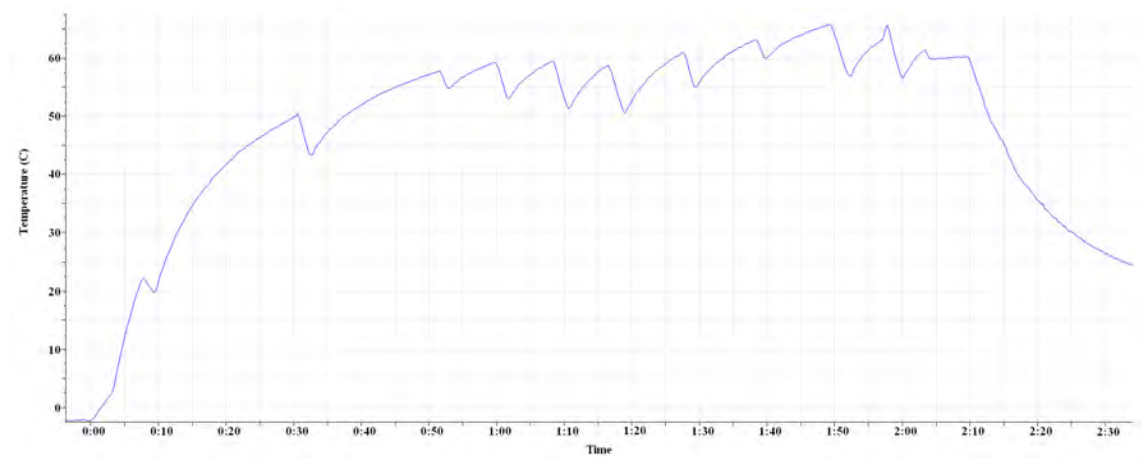


Figure A.22: YIG case temperature during first flight.



Figure A.23: Delay lines used in testing.

Delay Line:	A	B	C	D
Length (m):	6.6	8.8	31.7	36.1

Table A.1: Delay Line Lengths

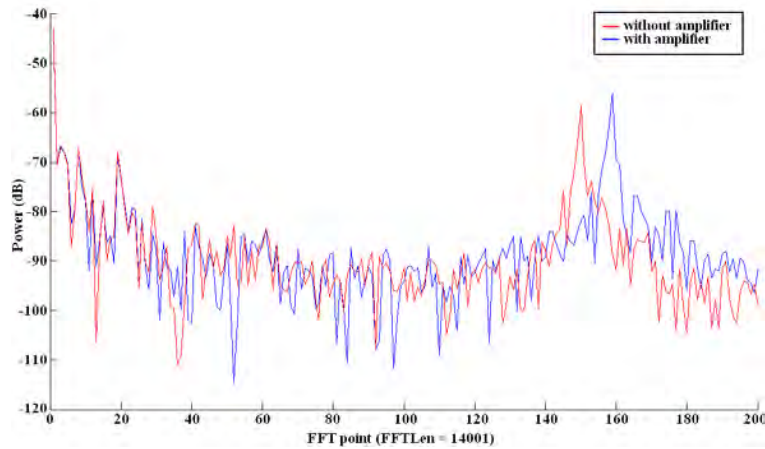


Figure A.24: Internal delay line distortion test.

distortion on the delay line signal that this power amplifier may cause, the return signal from the delay line was recorded with and without the power amplifier. Figure A.24 shows little distortion to the signal as it passes through the amplifier.

A.3.4 Antenna Interference

In order to minimise the cross coupling of the antennas, as well as reflections from the underside of the helicopter interfering with the signal, RF Absorbing Material (RAM, Cumming Microwave LF-75) was placed in the lid of the two Pelican[®] cases housing the TEM horn arrays.

A.3.5 Sled-based Radar Operation

To perform sled-based radar experiments a sled mount was made for the radar, see figure A.25. The antennas used for these experiments were ETS -3115, 2 - 18 GHz antennas from *ETS-Lindgren*. The gain of the antennas is approximately 10 dB, and beamwidth approximately 60° across 2 - 8 GHz. These antennas were secured to the radar sled, and the dimensions (also labelled in figure A.25) of the setup are:

- Height: 1.6 m above the surface.

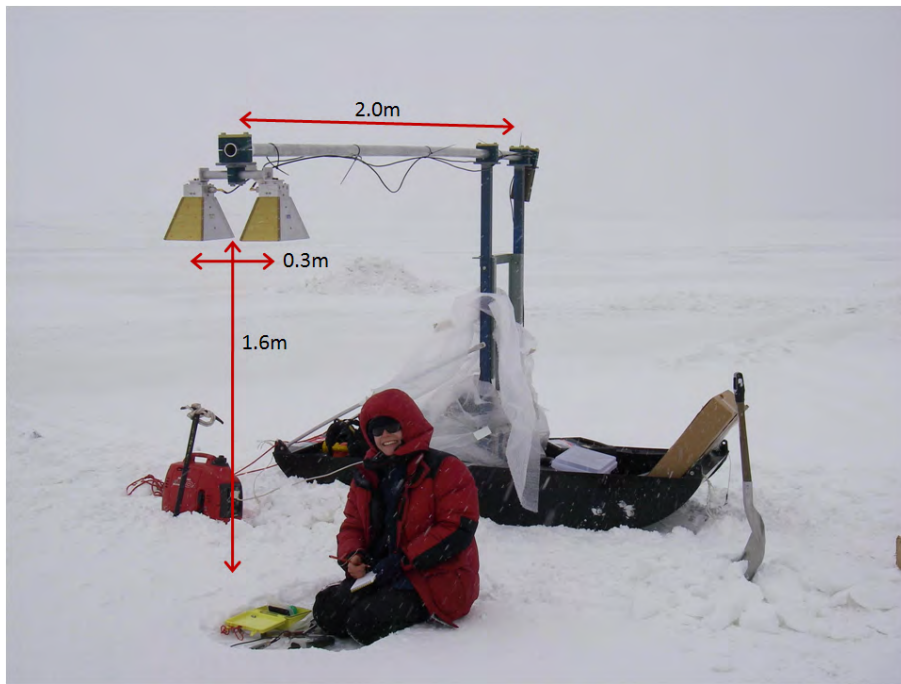


Figure A.25: Sled-based radar operation. *Photo courtesy K.Newbery.*

- Length: 2.0 m away from the sled.
- Width : 0.3 m separation between the transmit and receive antenna.

A.3.6 Helicopter Boot Vibration Tests

Vibrations inside the boot of the helicopter were characterised using a tri-axial digital accelerometer, from *Summit Instruments*. Figure A.26 plots the vibrations of the radar for 160 seconds during flight. The four major peaks are (amplitude averaged across time):

- (i) $F(1) = 20.9\text{Hz} @ 0.7 \text{ G}$
- (ii) $F(2) = 35.8\text{Hz} @ 0.3 \text{ G}$
- (iii) $F(3) = 103.5\text{Hz} @ 0.15 \text{ G}$
- (iv) $F(4) = 121.5\text{Hz} @ 0.27 \text{ G}$

The results show that the inside the boot, the instruments are subject to low frequency vibrations. The results can be used in future experiments to minimise detrimental effect on the radar

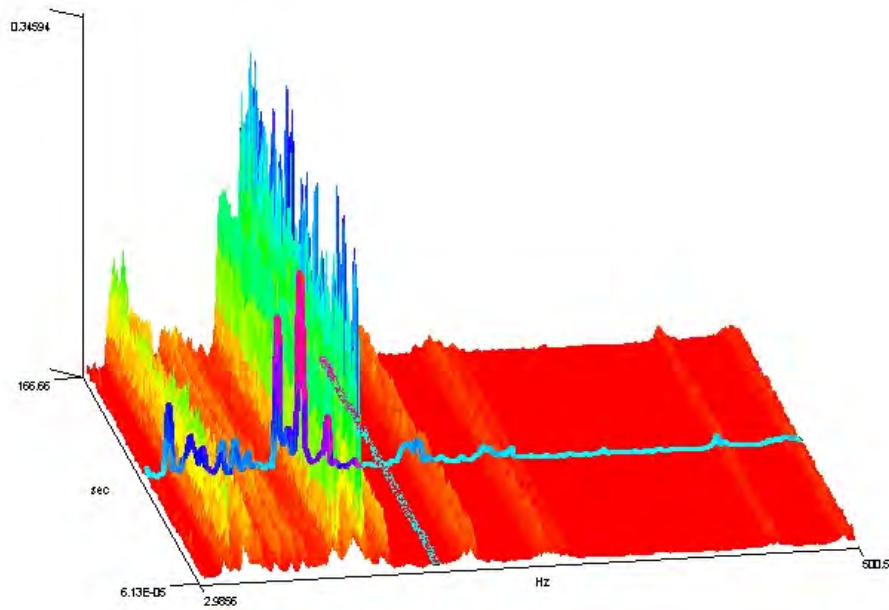


Figure A.26: Accelerometer measured vibrations inside the boot of the helicopter. (Courtesy: K. Newbery, STS - AAD).

performance. In order to minimise the transmission of the vibrations of the boot to the radar, a mount was constructed for it placing it on shock absorbing rubber (*Sorbothane Inc.*) caps. Figures A.27 and A.28 provide show the setup of the radar as it is to be fitted inside the boot of the helicopter. The NI box is standing on the sorbothane caps, and the metal case surrounding the radar is padded with the caps also.

A.4 National Instruments

This section provides a summary of the NI components supplied by CReSIS for the digital data acquisition and signal processing of the radar data, as well as a description of the software written (by the author) to coordinate the interaction of the boards in LabVIEW 8.5.

A.4.1 Hardware

The instruments used in the National Instruments box are:

- (i) Chassis: PXI - 1044

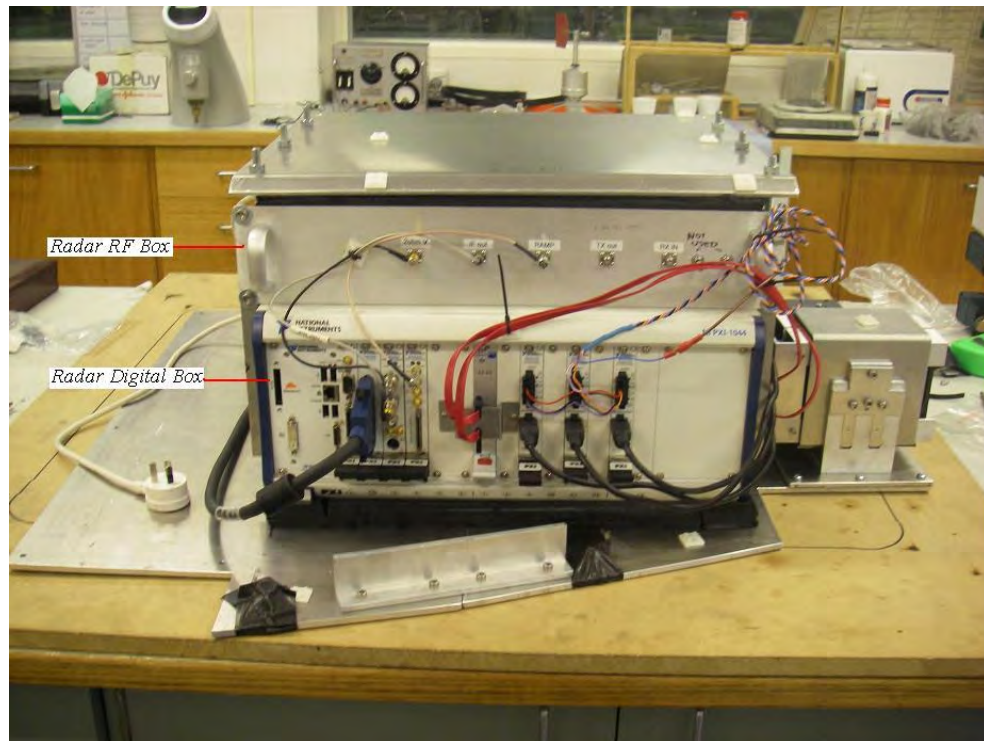


Figure A.27: Radar system setup, front.

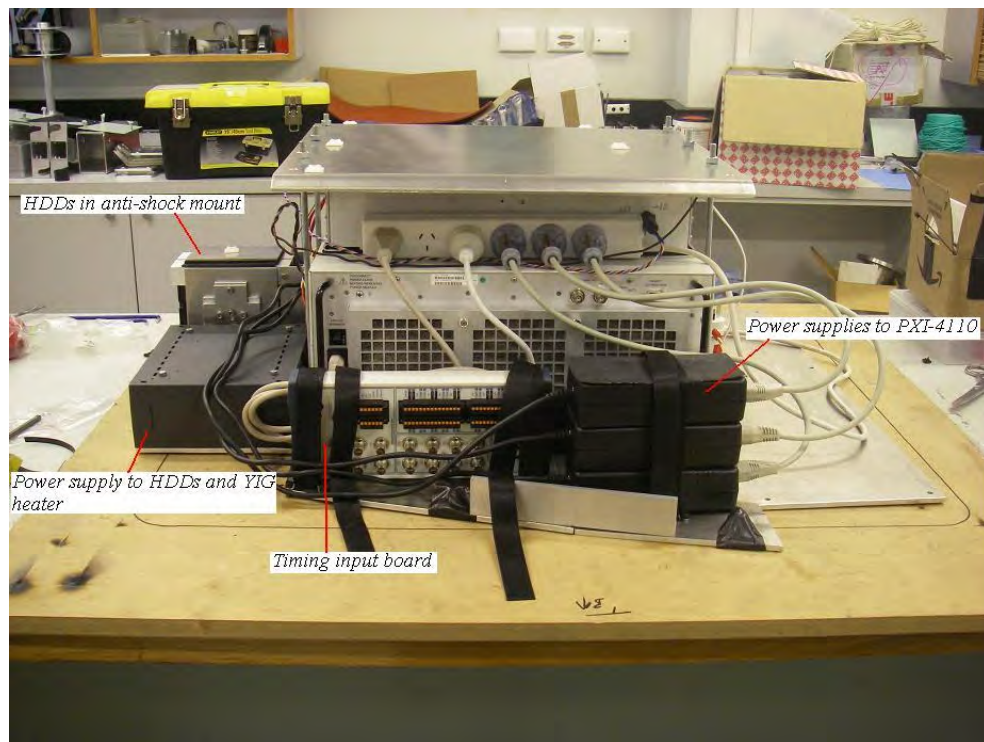


Figure A.28: Radar system setup, back.

(ii) Controller: PXI - 8106

(iii) Timer: PXI - 6608

The timing board was used to provide a means for synchronisation of the system with the INS and GPS units on the helicopter. This was achieved by routing the 1PPS signal as a global trigger input to all the radar signal paths.

(iv) AWG: PXI - 5422

The AWG provided the voltage ramp to the YIG driver, and as specified in the Micro Lambda technical specifications for the driver, the voltage sweep required to produce a 2 - 8 GHz output from the YIG is 0 - 10 Volts.

(v) SCOPE: PXI - 5124

The digitiser (A/D converter) used is capable of a maximum sampling rate of 200 Ms/sec and has 12-bit resolution. Two sampling ports are available, the IF signal was digitised, as well as the 2 ohm voltage (across the R9 resistor) in order to monitor any hysteresis or drift in the YIG output frequency.

(vi) SATA Controller: CE5 - H1 - CADENZA

Is used to connect the external SATA hard-disk drives for storage of radar data collected during flight.

(vii) DC Power Supplies: PXI-4110

The radar RF box requires ± 15 V, and draws approximately 3 A at highest frequency transmission. This power was supplied by the three PXI-4110 DC precision power supply boards, each had a maximum current delivery capacity of 1 A, and were hence they were wired in parallel to meet the 3 A requirements.

(viii) HDD Power Supply:

Artesyn - NFS110 - 7602PJ used for powering the external hard disks and YIG heater.

A.4.2 Software

The software to operate the National Instruments hardware of the radar was written in LabVIEW version 8.5. The graphical user interface (GUI) of the software is displayed figure A.29, and can

be split into four logical sections.

- (i) **Power indicators:** provide a display of the real-time voltage levels supplied to the RF box of the radar and the current drawn. The values are updated at a one second interval.
- (ii) **Main radar control buttons:** these control the overall radar operation, and are identified by the push buttons:
 - a. *Power On/Off:* controls the power output from the three PXI-4110 modules, which are powering the RF box. No radar operation is possible without activating this control button.
 - b. *Internal 1PPS On:* controls whether the radar receives the 1PPS signal from the PXI-6608 module. If this is not activated, the 1PPS signal is simulated (internally generated). This is necessary during laboratory testing, and also to achieve independence from the INS module during times when there is a problem with signal flow between the IMU and radar.
 - c. *Transmit On/Off:* controls the output of the AWG. Without this button active, the AWG does not produce a waveform to run the YIG driver. In addition, no trigger signal is supplied to the scope for data acquisition.
 - d. *Start/Stop File Write:* controls whether the acquired data is added to the FIFO queue for subsequent storage to the HDD. This was necessary because it was found that when the system crashed due to a buffer overrun, the acquired data which was temporarily stored in RAM before feeding to the FIFO was flushed. This button allows the radar operator to stop data from being queued when it is detected that the FIFO is approaching maximum capacity. Consequently, the data which is already in the queue is not lost and has a chance to be stored to the HDD.
- (iii) **Input and display of values:** for the scope and trigger waveforms provide the operator with some control over the file recording during flight, used mainly for debugging purposes. Generally, these values are preset before flight and are used to record the current flight mode in the data file.
- (iv) **Display of the acquired data:** supplied in real-time, in both the time and frequency domains, to provide the operator with a visual display of what the data being acquired by the radar.

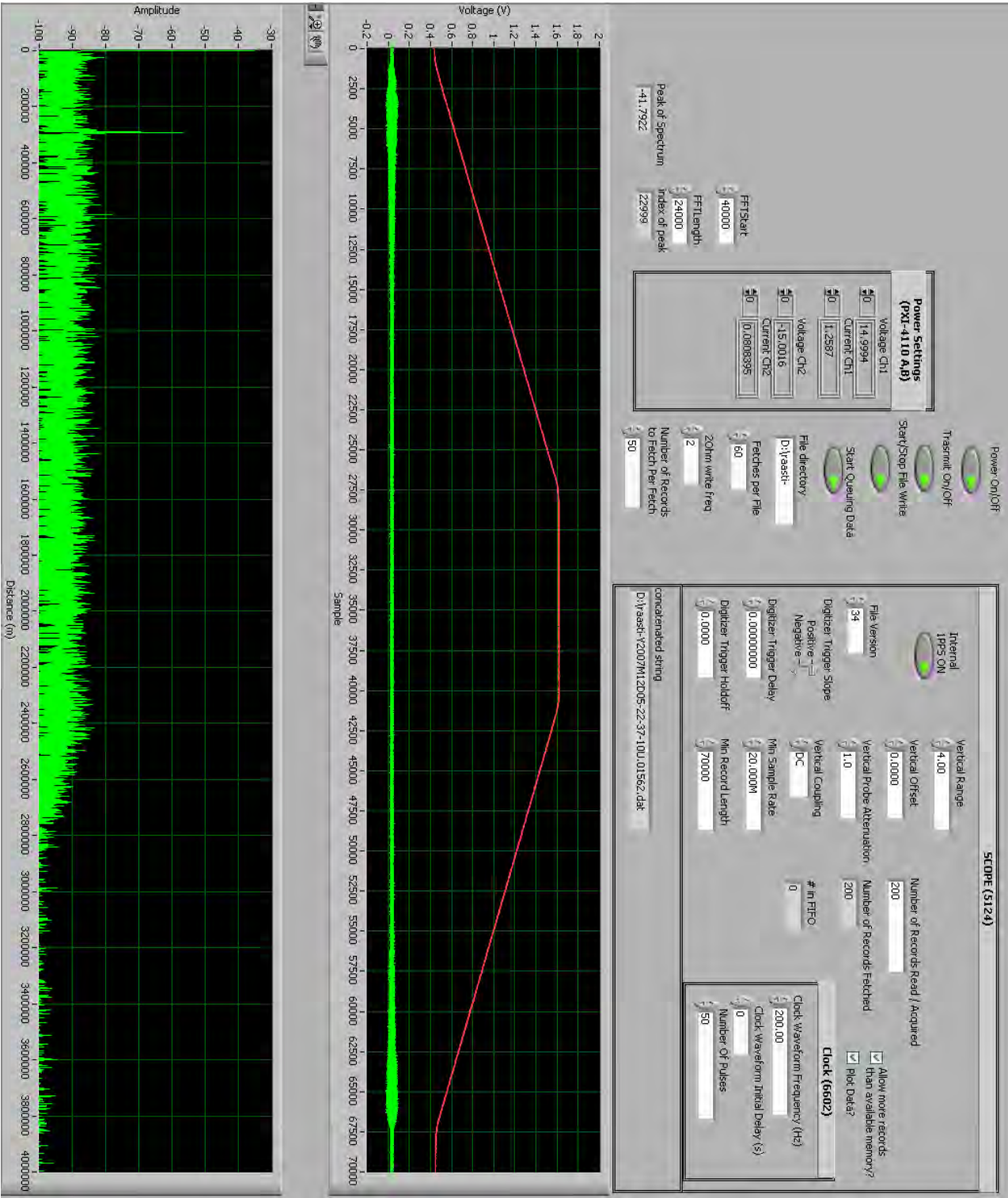


Figure A.29: RASTI GUI.

A.4.3 RAASTI File Format

The RAASTI file format evolved during the first SIPEX'07 voyage, and before deployment in 2008 in order to incorporate more accurate timing information from the onboard IMU. The main header length was maintained at 1024 bytes, each radar data record has a 36 byte header, and each radar sample is 16 bits wide. The field values of the file formats of all three versions are included here for completion, see figure A.30 and table A.2 for a description of the fields.

bytes	version 27	version 33	version 49
4	10 00 00 00	10 00 00 00	10 00 00 00
16	N a t a l i a ' s R A A S T I	N a t a l i a ' s R A A S T I	N a t a l i a ' s R A A S T I
4	1B 00 00 00	21 00 00 00	31 00 00 00
8	Timestamp	Timestamp	Timestamp
8	x++	x++	CRF
8	offset	offset	#pulses
8	gain	gain	VIG s/n
4	EF CD 00 00	CRF	VIG freq_low
4	BC 30 00 00		VIG freq_high
	00	#pulses	Fetch/file
	.. 00	#rec/fetch	2ohm freq
 960..	VIG s/n	MinSampRate
 00	Fetch/file	
	00 00 00 00	#rec/fetch	
8	Timestamp	2ohm freq	EF CD 00 00
		EF CD 00 00	A8 30 00 00
8	absInitX	39 80 00 00	00
		00 00
8	relInitX	.. 00 936..
	 920.. 00
4	actSmpls 00	00 00 00 00
		00 00 00 00	RecType
		Timestamp	ActSamp
		absInitX	absInitX
		absInitX	relInitX
		relInitX	Gain
		actSmpls	Offset
			msInMin

Figure A.30: RAASTI file format.

Field name	Type	Description
string length	int32	length of string to follow
string	array of bytes8	"Natalia's RAASTI"
software version	int32	version of the software used
timestamp	double64	current system time with micro-second accuracy
x++	double64	time in seconds between two samples acquired
offset	double64	offset factor for the given channel, for scaling binary data: $voltage = binary\ data \times gain\ factor + offset$
gain	double64	gain factor for the given channel, (see above)
end of header	int32	indicator for end of main header: 0xFEDC
string length	int32	length of string to follow
filler	byte8	filter bytes, to keep main header 1024 bytes long
record type	int32	indicates type of data record to follow: '1' indicates return signal data, '2' indicates 2ohm voltage data.
timestamp	double64	current system time with micro-second accuracy
absInitX	double64	timestamp in seconds of the first fetched sample that is comparable between records and acquisitions
relInitX	double64	time in seconds from the trigger to the first sample in fetched waveform
actSmpls	int32	number of samples in record to follow
trig freq	double64	frequency of the trigger waveform
#pulses	int32	number of trigger pulses used per second
YIG s/n	int32	serial number of the YIG used
YIG freq0	double64	starting frequency of the YIG
YIG freq1	double64	stopping frequency of the YIG
fetch/file	int32	number of record fetches for a file
#rec/fetch	int32	number of records per fetch
2ohm freq	int32	frequency of the 2ohm waveform recording

Table A.2: RAASTI File Format

Appendix

B

SIPEX'07 RAASTI Flight Summary

B.1 Introduction

The Sea Ice Physics and Ecosystem eXperiment (SIPEX) is one of Australia's major contributions to the International Polar Year (IPY). The SIPEX'07 expedition was made up of 45 scientists from 8 different countries, each focused on a particular aspect of sea ice including but not limited to: physics, ecology, meteorology and biogeochemistry. The expedition explored the sea ice zone around Antarctica in September - October 2007 and investigated the relationships between the physical sea ice environment and the structure of Southern Ocean ecosystems. Over 16 ice stations were conducted, with a suite a measurements taken, including: snow and ice properties, ice cores, meteorology, underwater remote vehicle experiments for krill studies, as well as oceanography measurements of water current and temperatures, and iron concentration studies.

RAASTI flew and recorded data on 19 flights, figure B.1 shows the locations of these flights. Due to hardware and software difficulties however, the data gathered is not readily usable, and not suitable for validation purposes of the radar. This appendix presents a summary of the flights, and debugging efforts. Table B.1 summarises the flights and lists the describing section.

Section	Flight Name
B.2.1	Alpha
B.2.2	Bravo, Charlie, Delta
B.2.3	Golf
B.2.4	Hotel, India, Juliet
B.2.5	Mike, November, Oscar
B.2.6	Papa
B.2.7	Sierra
B.2.8	Uniform
B.2.9	Victor, Crane Test
B.2.10	Yankee, Zulu, Zulu Two

Table B.1: Flight summary.

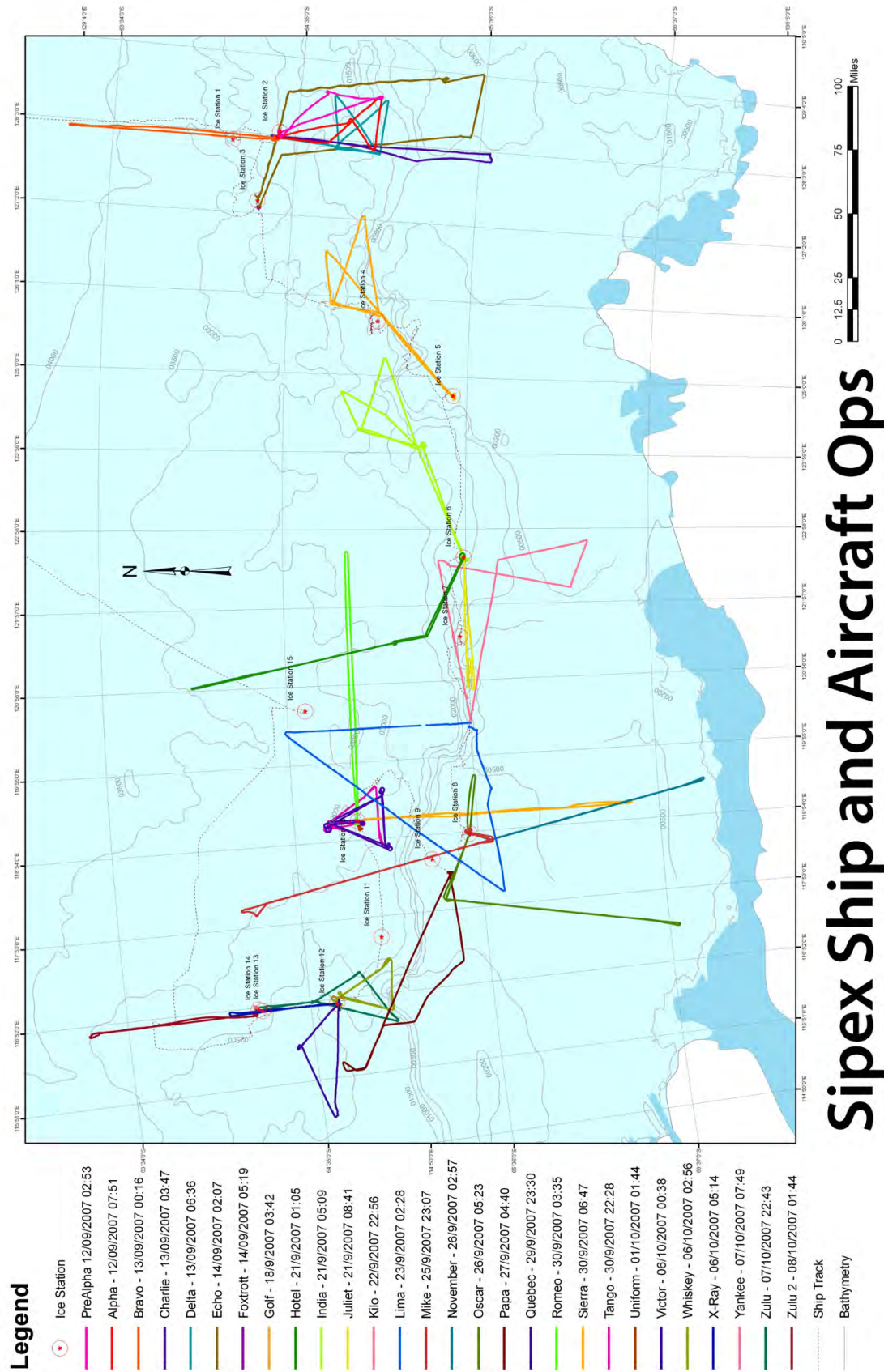


Figure B.1: Location of flights made during SIPEX'07. Image courtesy of J.Lieser.

B.2 Flight Details

B.2.1 Alpha

Date: 12/Sept/07

Duration: 85 minutes (07:47 - 09:12)

Notes Laboratory testing showed that the radar could maintain the required data rate (40MBytes/sec) successfully. However, during flight this was not possible.

Examining the radar data gathered, the most obvious discrepancy is between the timestamp difference of the last and first timestamps of the file, and the first and last indices written for each record. The discrepancy of the timestamps can be explained by the fact that the HDD takes longer to write the data record.

It was believed that vibration of the helicopter caused the HDD to err when writing data as it had to request the same data multiple times, causing the increased delay and buffer overruns that were observed during the flight. Figures B.2 and B.3 show the performance of operation of the HDD on the ground and during flight, respectively.

These two graphs illustrate the degradation in operating capacity of the hard disk drive during flight. Given that it is the only mechanical device (except for the YIG oscillator which may also be considered as having some mechanical movement) it was considered the primary culprit in the data throughput problems.

B.2.2 Bravo/Charlie/Delta

Date: 13/Sept/07

Duration:

Bravo: 130 minutes (00:15 - 02:25)

Charlie: 118 minutes (03:47 - 05:45)

Delta: 109 minutes (06:38 - 08:27)

Notes: Vibration problems affected the data throughput.

The Charlie flight saw an added problem with the radar which was not present in the previous flights (Alpha and Bravo). A spreading of the return signal was observed, which was labelled

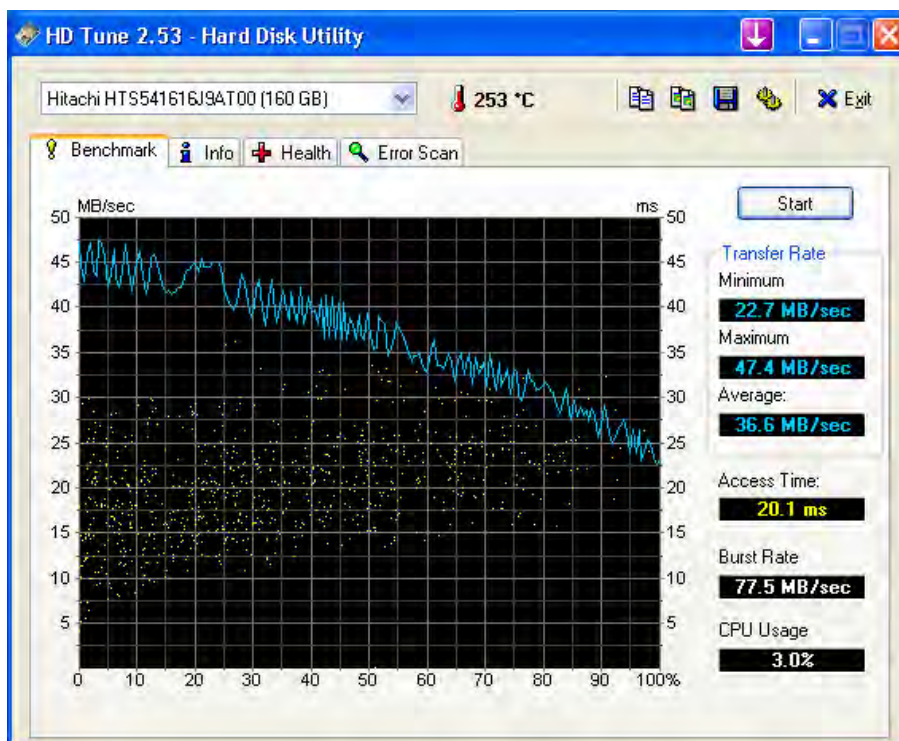


Figure B.2: Hard disk performance in the helicopter running on ground power.

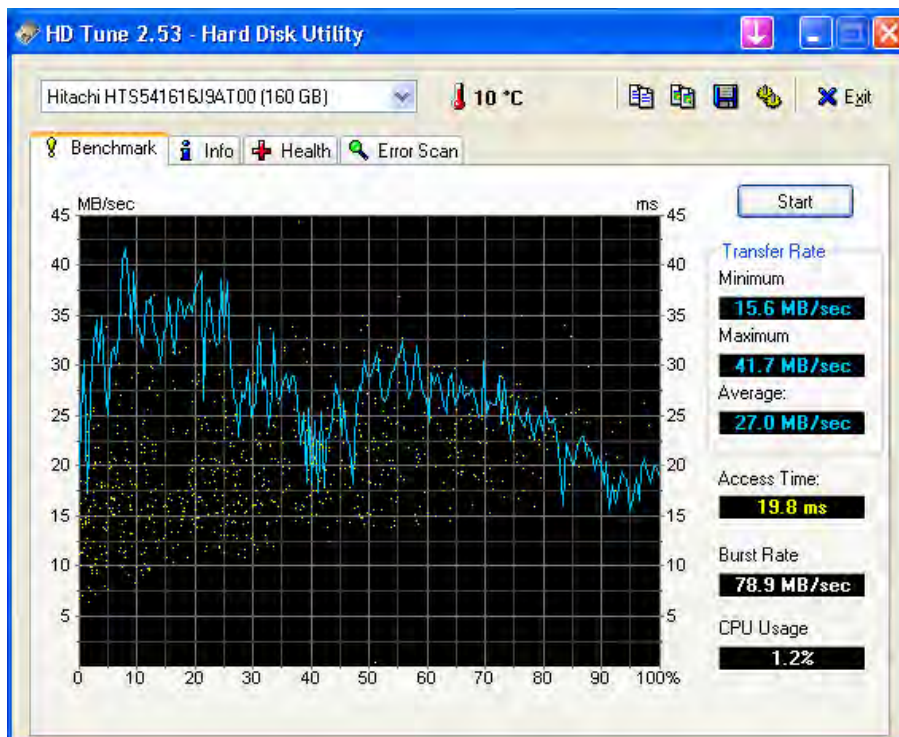


Figure B.3: Hard disk performance during flight.

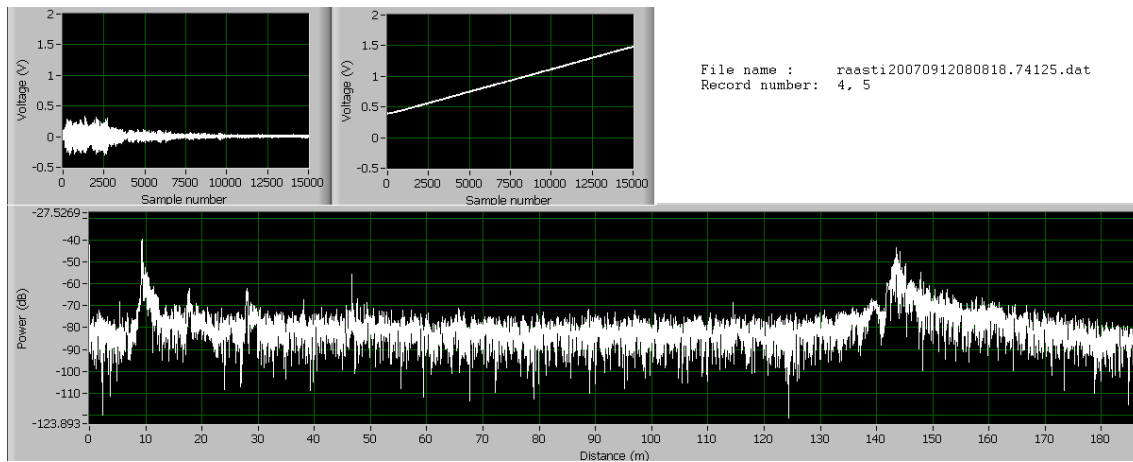


Figure B.4: Expected sharp return, seen here at approximately 145 m.

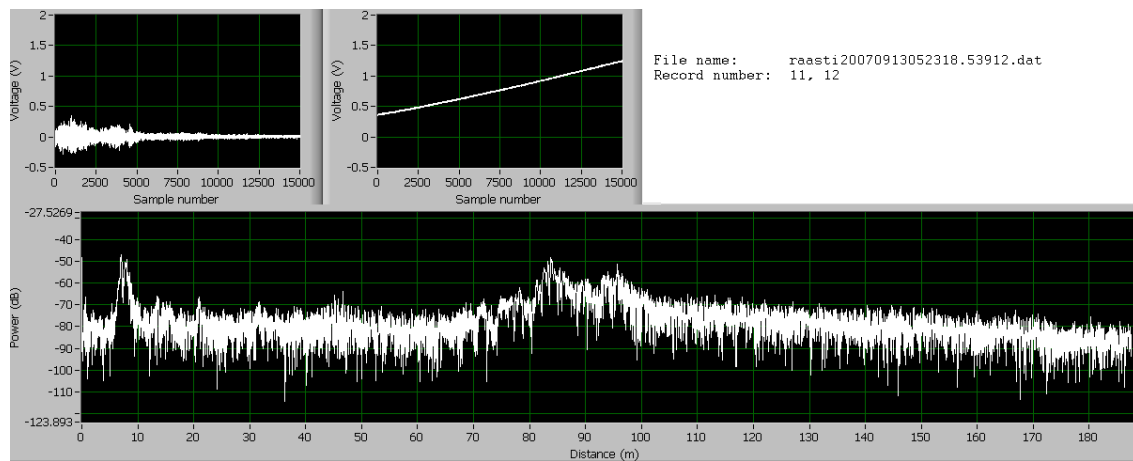


Figure B.5: "Diffuse return", seen here at approximately 85 m.

"diffuse return", figures B.4 and B.5, compare data from the start of the flight where a peak in the return is observed, and later in the flight (second figure) demonstrates the diffuse return.

On examination of the 2ohm waveform the cause for the spreading in the frequency spectrum becomes clear: the voltage supplied to the YIG oscillator not linear. The cause of this is unclear at this stage need to examine the driver. (It was not possible to replicate the error in the laboratory; hence it is possible that vibrations are a cause of it.)

The software parameters were modified to only transmit 10 (out of 335 Hz) pulses per second, which would allow time for the hardware to process the collected data, and store it to the hard disk. However, this of course lead to the fact that the radar did not image the entire surface it flew over, but only short sections of it.

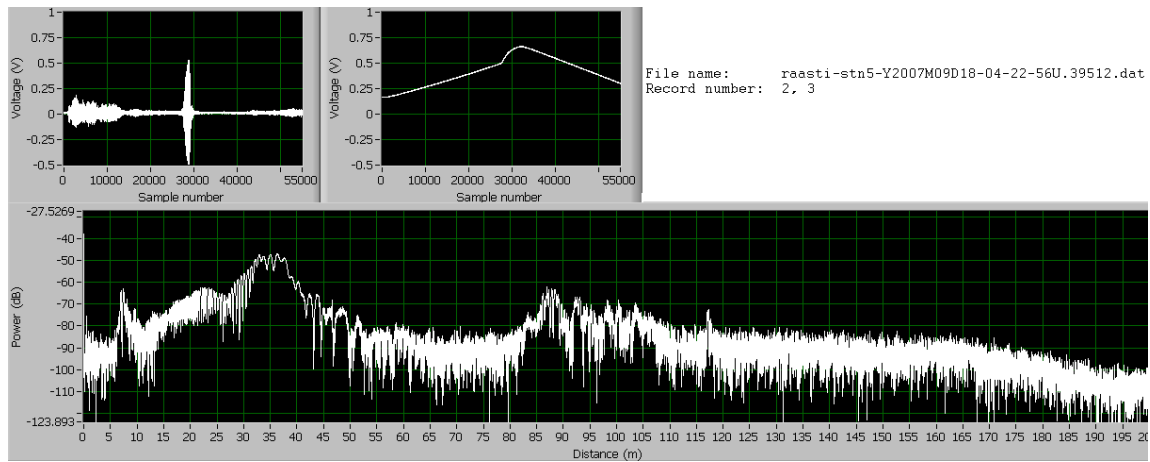


Figure B.6: Kinks in the 2ohm voltage, and affect on radar return.

B.2.3 Golf

Date: 18/Sept/07

Duration: 149 minutes (03:46 - 06:15)

Description: NA

Notes: Large “kinks” were observed in the 2ohm voltage waveform (see figure B.6), which contributed to large amounts of noise in the return signal and testing during flight showed that this noise was not a function of range. Consequently, it was believed that the YIG driver may be generating this noise as it is also present at high altitude operation when there can be no return from the ground, see figure B.7.

The kinks observed during this flight were considered as a degradation of the diffuse effect observed during Charlie. Given the behaviour of the signal, it was believed that the YIG driver was responsible for this error.

B.2.4 Hotel/India/Juliet

Date: 21/Sept/07

Duration:

Hotel: 149 minutes (01:08 - 03:37)

India: 158 minutes (05:13 - 07:51)

Juliet: 81 minutes (08:52 - 10:03)

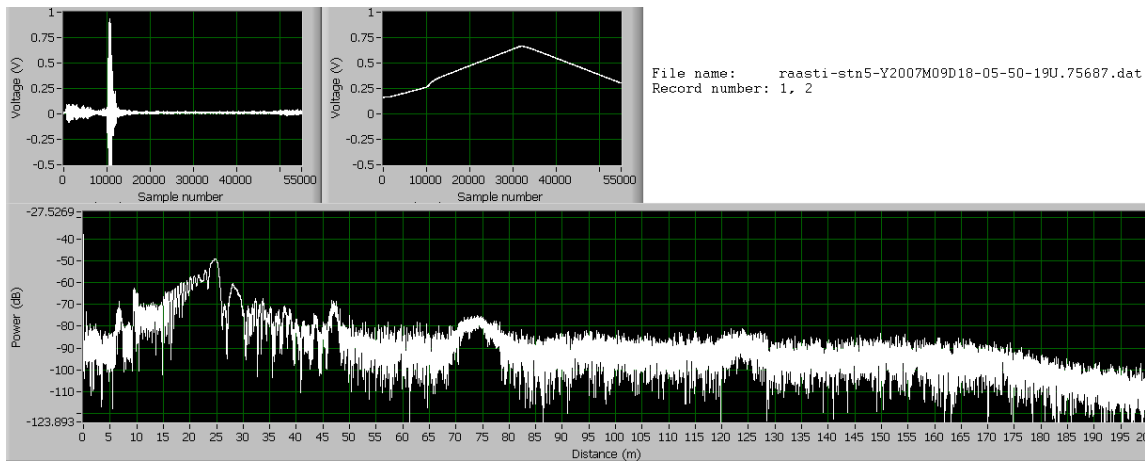


Figure B.7: Apparent return of the radar at high altitude.

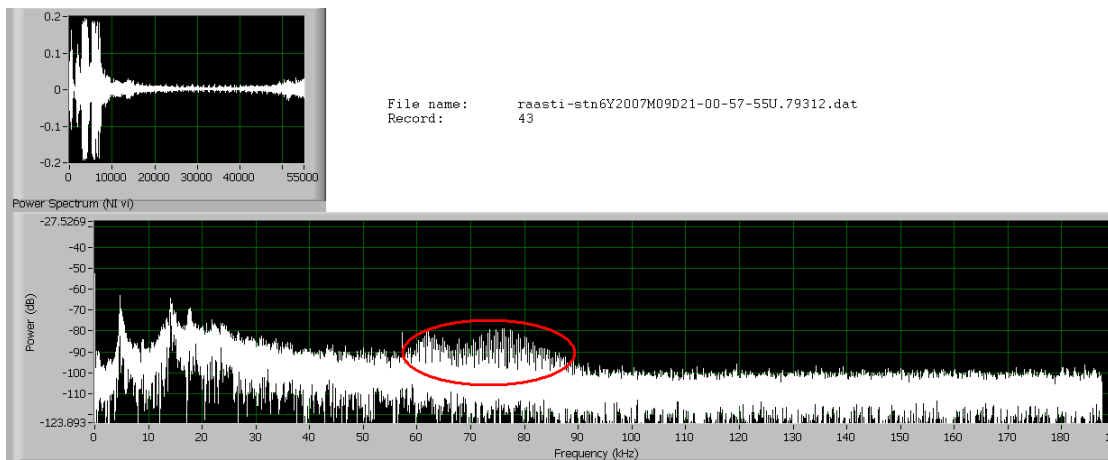


Figure B.8: First signs of “broadband” noise.

Notes: Another fault in the radar system developed during these flights, and was termed “broadband noise”, as it was noise that was spread over a large frequency range, as illustrated in figure B.8.

In order to eliminate the kinks in the 2ohm voltage, and their ramifications on the radar return, the YIG and YIG driver were replaced with the spare (set B).

Updates were also made to the software, changing the way the ramp voltage waveform was generated. In the new software, instead of a continuous stream of triangle waveforms, the waveform was modified to give the YIG time to settle at the lowest (2 GHz) and highest (8 GHz) frequencies (compare the top and bottom graphs in figure B.9).

It was noticed that the current drawn by the RF box which included the YIG and driver was

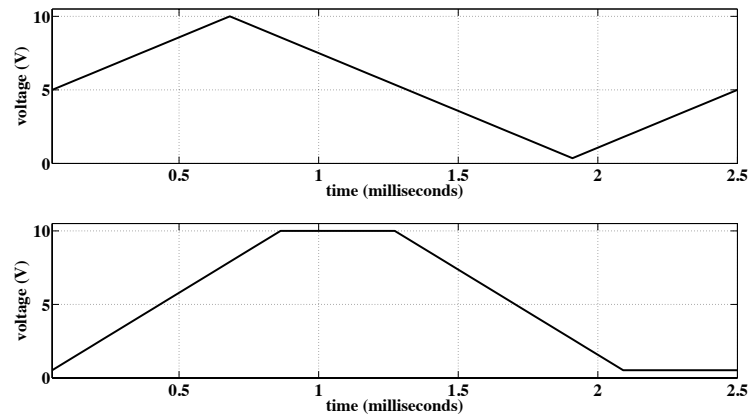


Figure B.9: Changes made to the YIG driver voltage waveform.

marginally close to the maximum current sourcing capacity of the two NI DC power supplies (PXI-4110) used to power the RF box. Hence, to avoid this possibly contributing to the noise problems in the radar, an external power supply was fitted into the boot.

B.2.5 Mike/November/Oscar

Date: 26/Sept/07

Duration:

Mike: 140 minutes (21:10 - 01:30)

November: 109 minutes (03:00 - 04:49)

Oscar: 150 minutes (05:25 - 07:55)

Notes: During this flight no kinks were present in the received signal, two reasons for this are identified: replacement of the YIG and driver, or use of the external power supply.

An interesting behaviour of the broadband noise was observed (figure B.10), namely that its amplitude was unaffected by the radar altitude. Coupled with the fact that it was not present on the 2ohm voltage, it was concluded that it was generated internally by the radar, either by the IF amplifier, or the LNA.

Laboratory testing could not replicate the broadband noise however, further testing revealed that it was present when the helicopter was stationary and running on ground power with the receive antenna port (figure B.11) disconnected, but absent when the radar was powered from the ship's AC power supply (figure B.12). The main difference in these two scenarios is that when it was

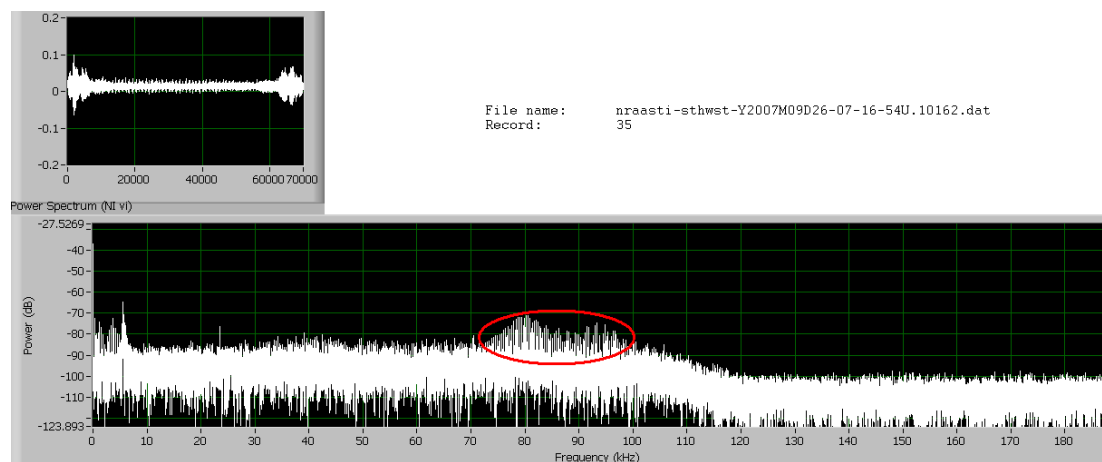


Figure B.10: Broadband noise present at on return, even at high radar altitude.

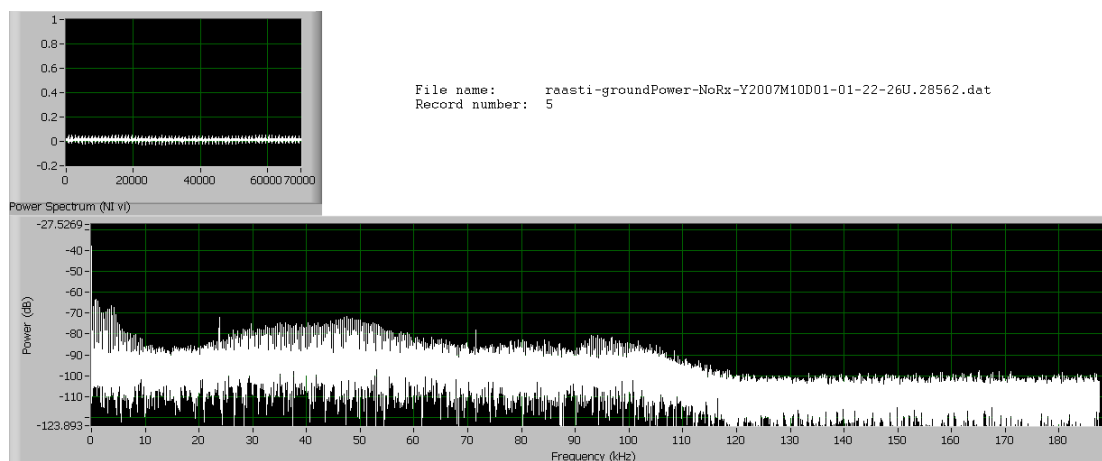


Figure B.11: Broadband noise present when running on ground power with receive antenna port disconnected.

running on ground power, the radar was powered through the inverter, consequently it is possible that the inverter had become faulty.

B.2.6 Papa

Date: 27/Sept/07

Duration: 122 minutes (04:40 - 06:42)

Notes: None.

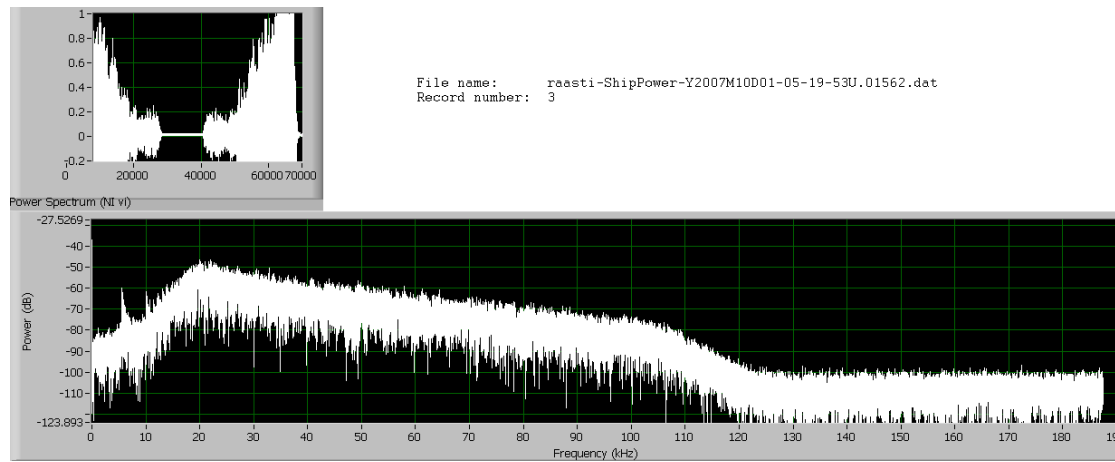


Figure B.12: Absence of broadband noise when running from a ship source of AC.

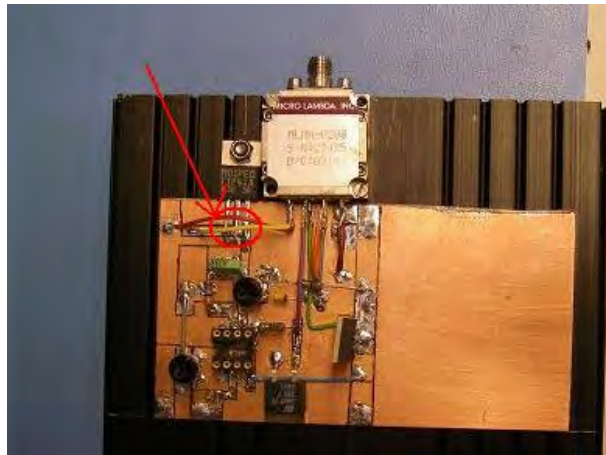


Figure B.13: YIG and YIG driver, illustrating the loose component.

B.2.7 Sierra

Date: 30/Sept/07

Duration: 114 minutes (06:49 - 08:43)

Notes: At the start of the flight something had gone wrong with the YIG and YIG driver because no voltage was detected on the 2ohm resistor.

Laboratory tests of the YIG and its driver revealed that the emitter of the current driving transistor (circled in figure B.13), had snapped off the board. Re-soldering the transistor fixed the problem.

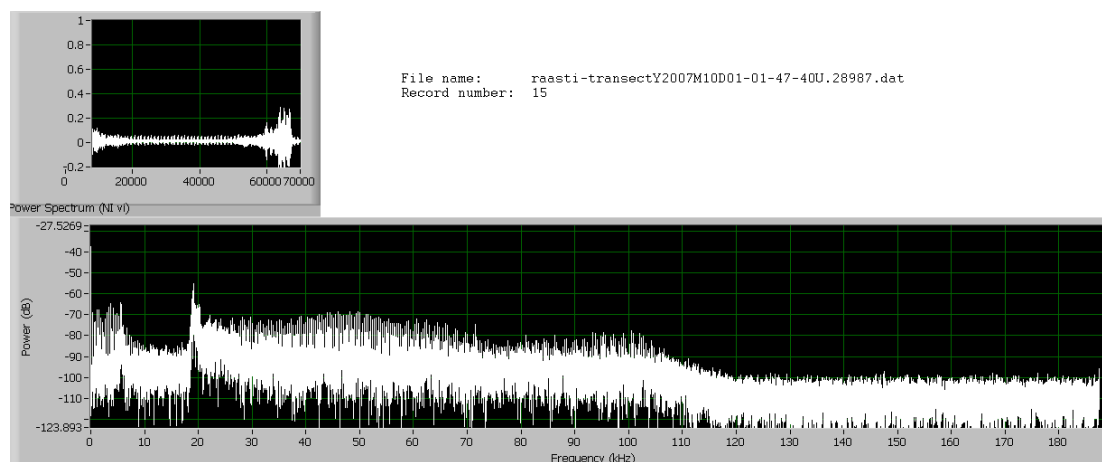


Figure B.14: Significant contribution of broadband noise, almost covering the full radar spectrum.

B.2.8 Uniform

Date: 01/Oct/07

Duration: 45 minutes (01:44 - 02:39)

Notes: It is believed that data was collected without problem, however the presence of the broadband noise corrupted the signal excessively, see figure B.14.

B.2.9 Victor and Crane Test

Date: 06/Oct/07

Duration:

Victor: 58 minutes (00:39 - 01:37)

Crane Test: 46 minutes (07:39 - 08:25)

Notes: The Crane Test from the preliminary analysis shown in figure B.15 indicates that the radar does indeed see the air/snow and snow/ice interfaces: the peaks at approximately 13 m are seen to move across the screen.

Spot testing of the area under the radar during the crane test revealed a snow depth of 150 mm on average which is consistent with a first-hand look at the data presented above in figure B.15.

B.2.10 Yankee/Zulu/Zulu Two

Date: 07/Oct/07

Duration:

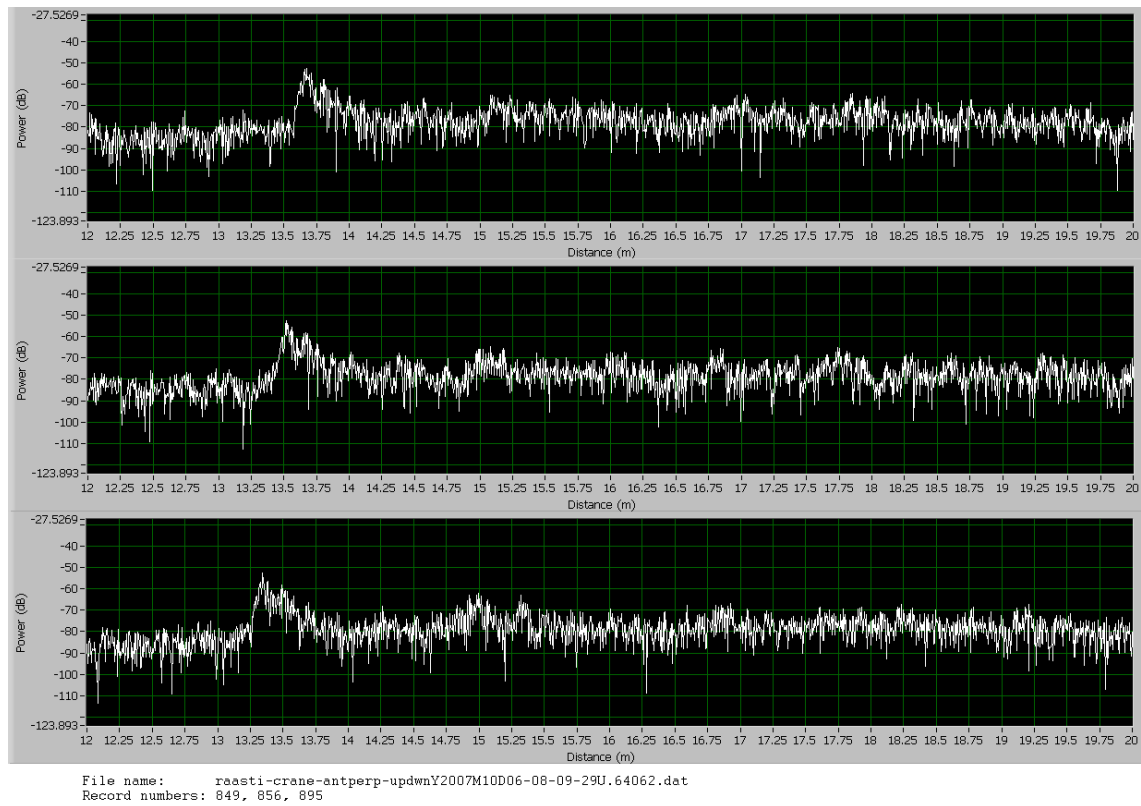


Figure B.15: Crane test results.

Yankee: 56 minutes (07:57 - 08:53)

Zulu: 116 minutes (22:43 - 00:39)

Zulu Two: 86 minutes (01:42 - 03:08)

Notes: The helicopter also hovered above a marked site whose average snow thickness was then measured to compare with the radar data. The average thickness was found to be 120 mm. The radar results over this site are shown in figure B.16. Due to the helicopter noise, it is difficult to extract the air/snow and snow/ice interfaces.

The data from the first flight (Yankee) showed that the radar was seeing the air/snow and snow/ice returns at lower altitudes (< 50 m), at higher altitudes the inverter noise was too large to detect any peaks.

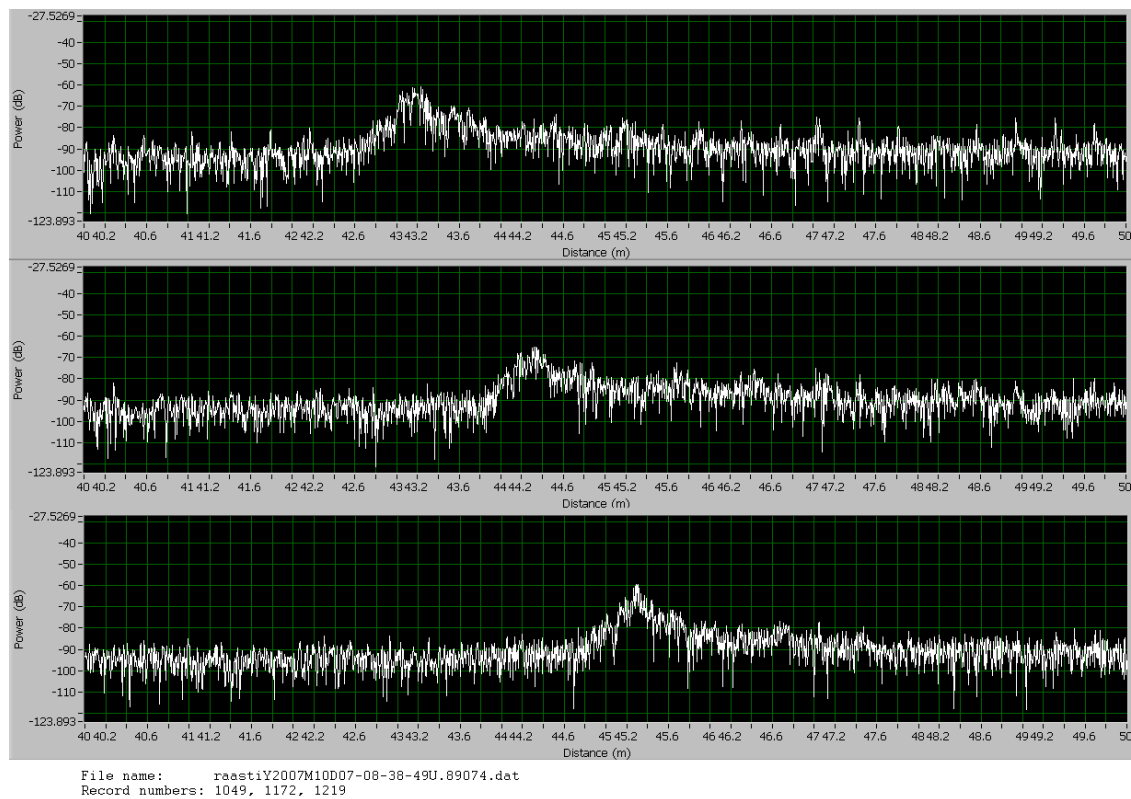


Figure B.16: Helicopter hover over marked area.

Appendix

C

Hard Disk Drive Anti-Vibration Tests

Three hard disk drives (HDD) of the radar system were tested for performance under vibration, during helicopter flight. The three drives were connected to the CE5-CADENZA (*EKF Systems*) board, installed in slot #7 on the National Instruments component of the radar, they are:

- internal Parallel ATA (PATA) drive on the Serial ATA (SATA) board: Hitachi, HTS541616J9AT00 (160 GBytes),
- external SATA drive A: WDC, WD1500ADFD-00NLR5 (150 GBytes),
- external SATA drive B: WDC, WD1500ADFD-00NLR5 (150 GBytes).

Note: all three were formatted as FAT32. All three were horizontally oriented during format, and vertically oriented during operation, this has been reported to affect performance.

The two external SATA drives (A and B) were mounted inside an anti-vibration casing designed at the Australian Centre for Field Robotics, Sydney University. Figures C.1 and C.2 show the anti-vibration mount designed to fit two 3.5 inch hard disk drives.

The software *HDTune* (*EFD-Software*) was used to test the performance on the ground, and in the air for performance comparison purposes.

C.1 Results

The figures mentioned below have write speed plotted as a function of the radius of the disk platter where the write function is taking place. It is expected, that unless the write performance is limited by the bandwidth of the connecting bus or cable, it would decrease with increasing distance away from the centre of the platter.

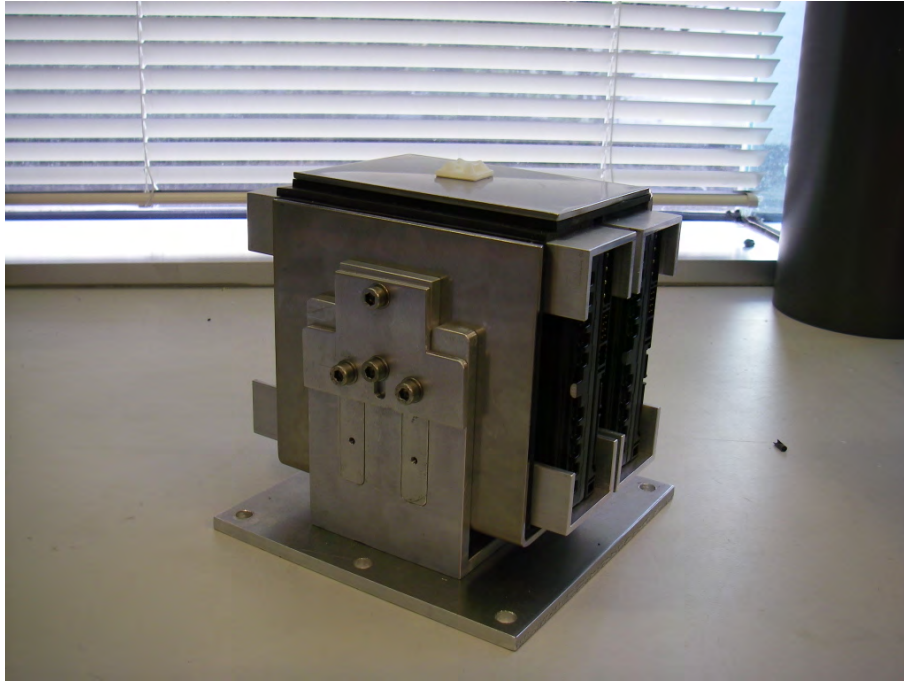


Figure C.1: Anti-vibration mount, side 1.

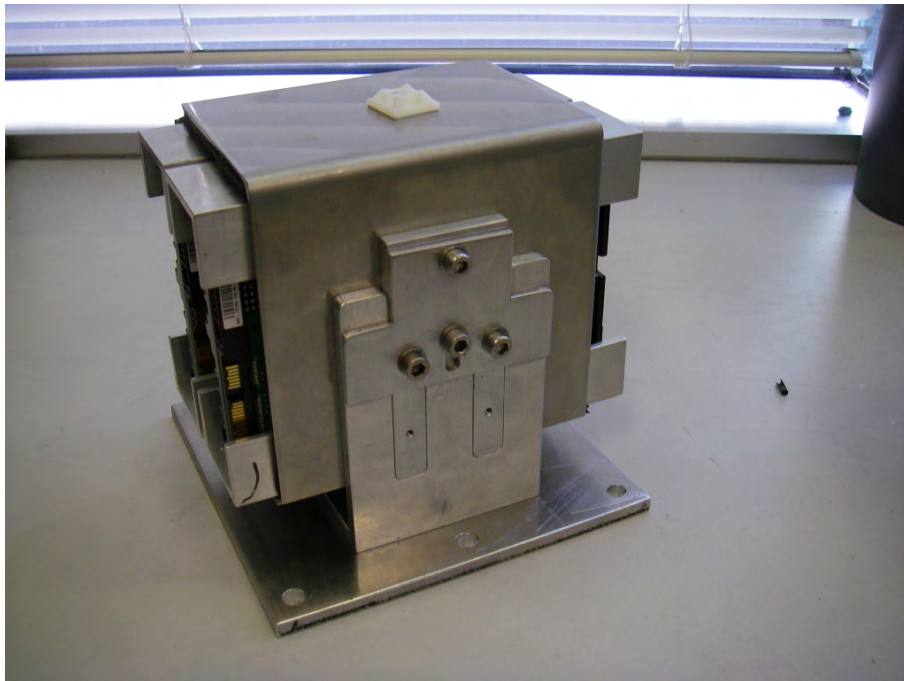


Figure C.2: Anti-vibration mount, side 2.

- Figures C.3 and C.4 compare the performance of the internal PATA drive on the ground and during flight.
- Figures C.5 and C.6 compare the performance of the external SATA drive (A) on the ground and during flight.
- Figures C.7 and C.8 compare the performance of the external SATA drive (B) on the ground and during flight.

The required data rate for the radar is approximately 40Mbytes/sec, and both the external drives are able to maintain this rate during the flight test. The internal drive however, is greatly affected by vibrations inside the helicopter, with minimum write speed decreasing from 23Mbytes/sec to 5Mbytes/sec.

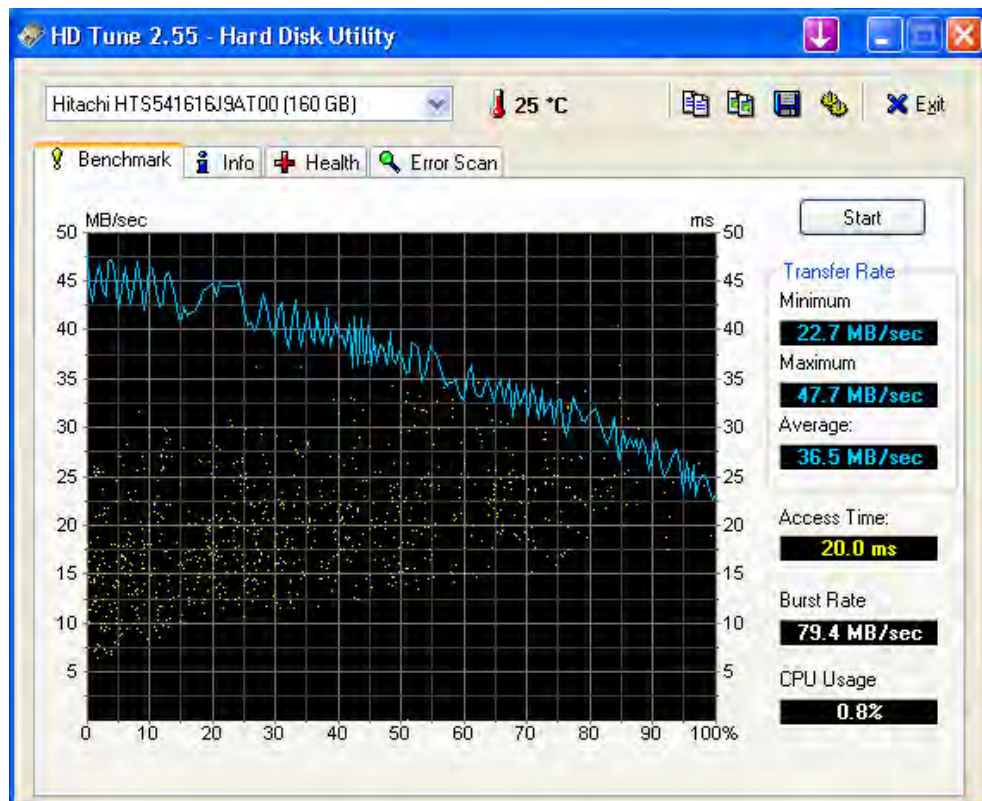
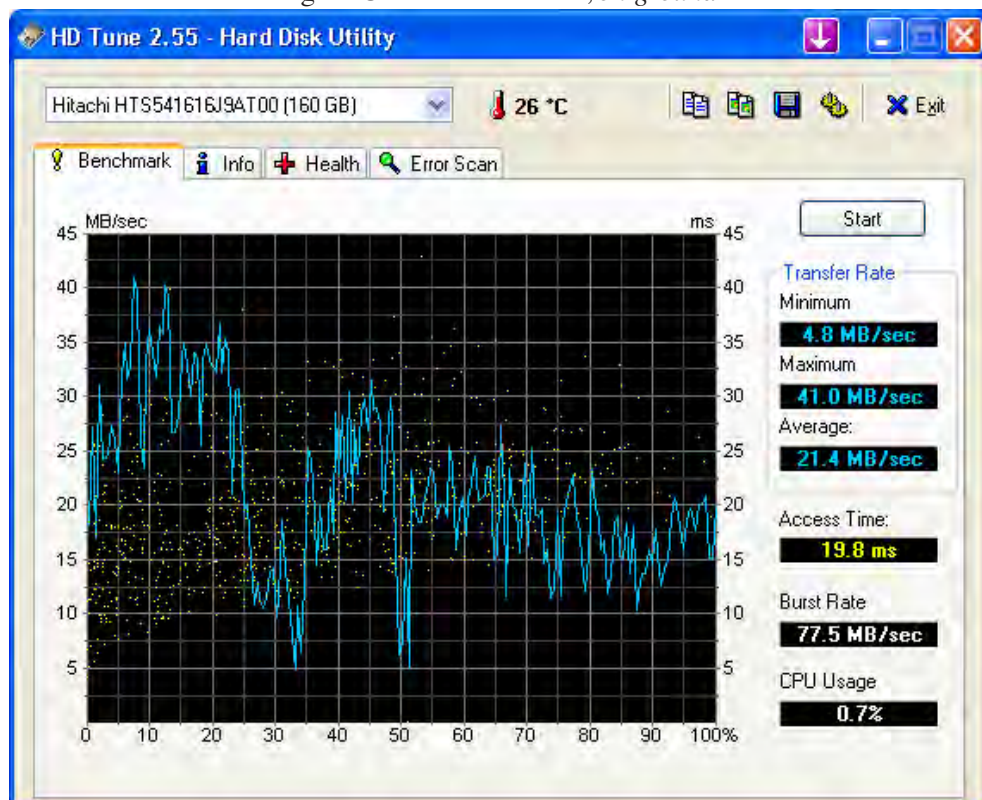
C.2 Discussion

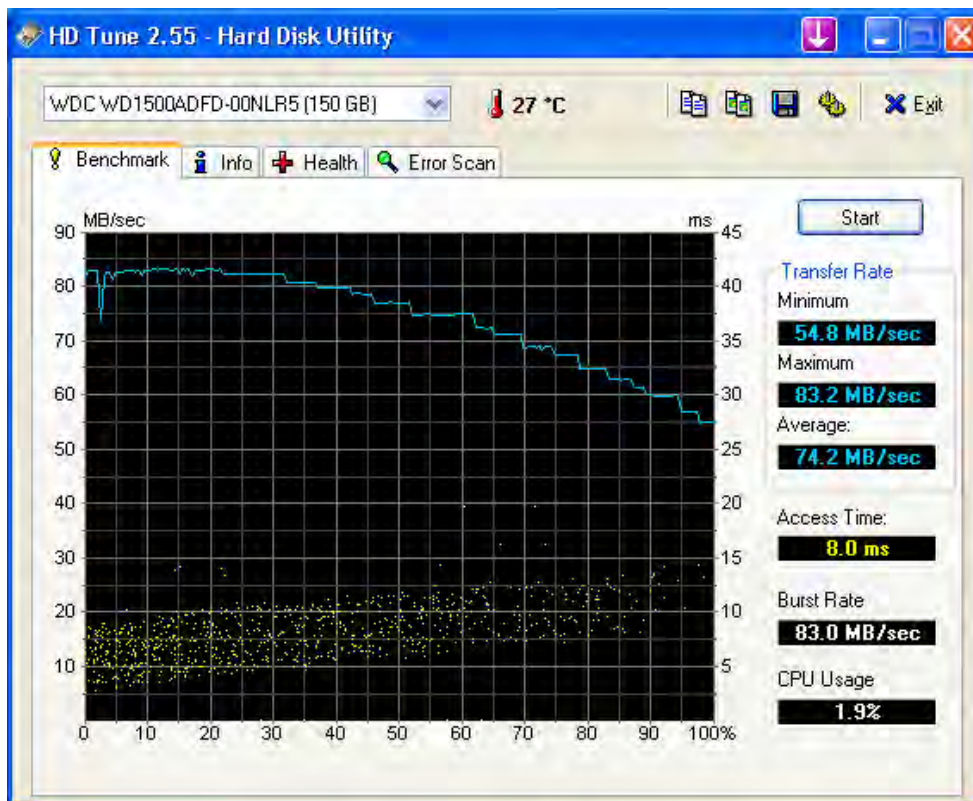
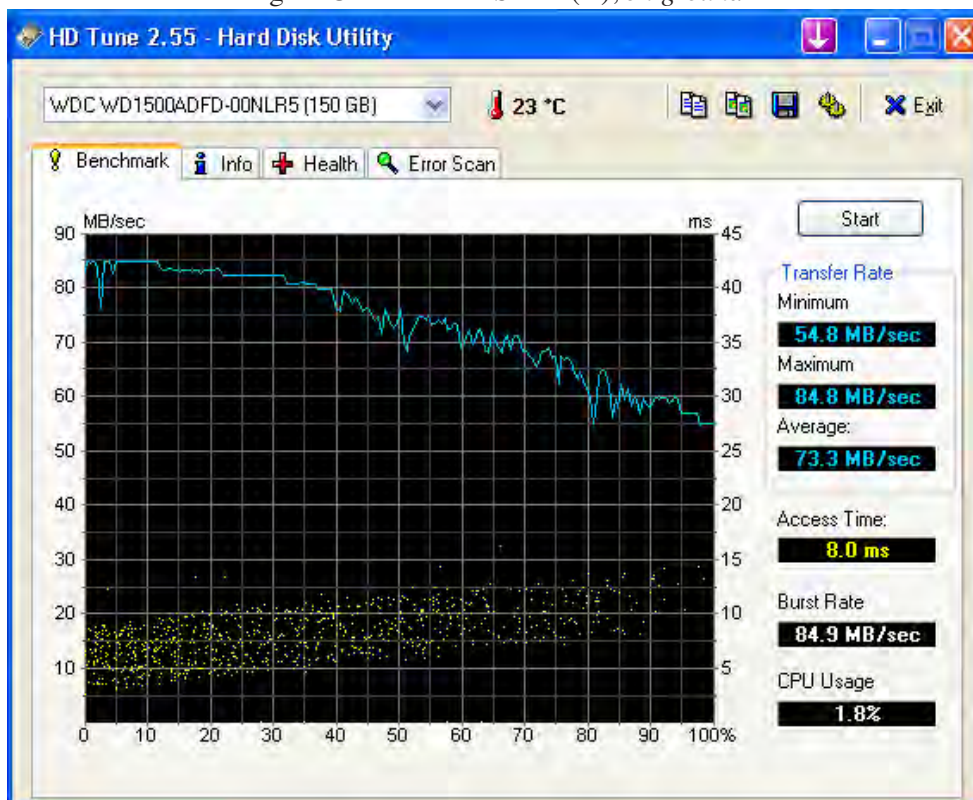
Two factors are believed to have improved the performance of the external drives in comparison with the internal drive, they are: use of the anti-vibration mount, and higher vibration rating on the external drives.

The table C.1 compares the HDD write speed on the ground and during flight. While the performance of the SATA drives is not directly comparable to PATA performance, as different methodology/structure of the connecting data bus limits the theoretical maximum write speed, the column indicating the percentage change is useful in assessing the effect of the anti-vibration mount. This table demonstrates that the required write speed can be maintained during flight by the HDD inside the anti-vibration mount.

HDD Type	Min (Mb/sec)	Max (Mb/sec)	Ave (Mb/sec)	Δ Ave (%)
SATA (A) Flight	54.8	84.8	73.3	98.9
SATA (A) Ground	54.8	83.2	74.2	100.0
SATA (B) Flight	44.4	83.1	68.1	94.5
SATA (B) Ground	50.4	83.4	72.1	100.0
PATA Flight	4.8	41.0	21.4	58.6
PATA Ground	22.7	47.7	36.5	100.00

Table C.1: Summary of HDD write speed performance.

Figure C.3: Internal PATA, *on ground*.Figure C.4: Internal PATA, *in flight*.

Figure C.5: External SATA (A), *on ground*.Figure C.6: External SATA (A), *in flight*.

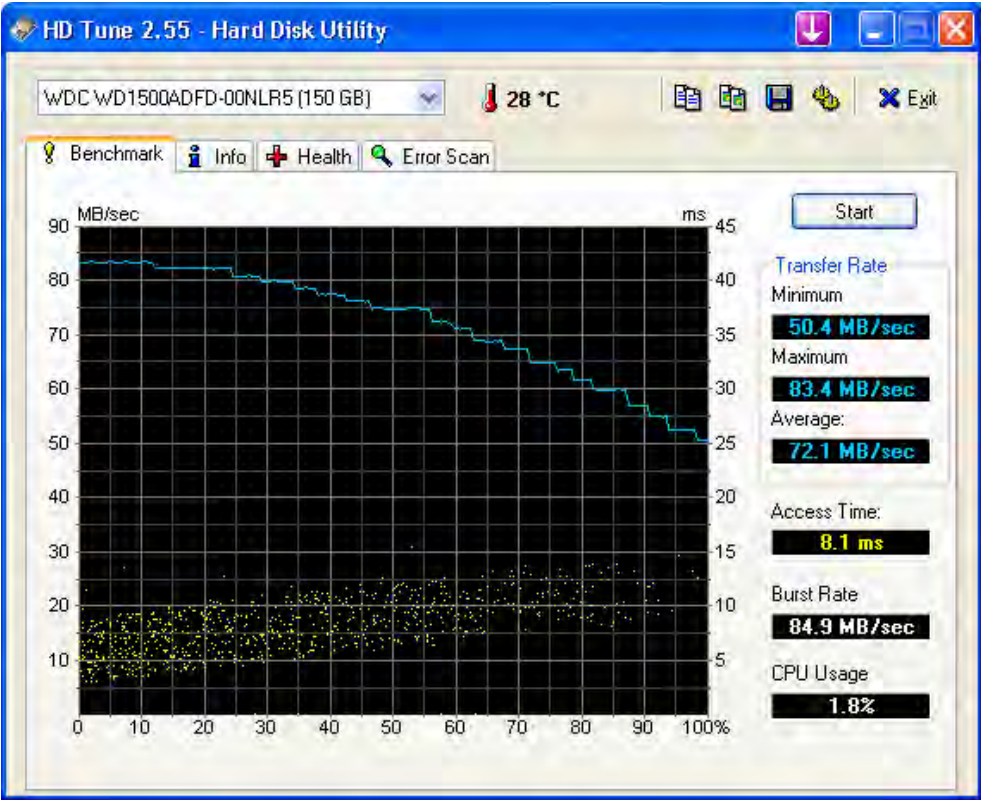


Figure C.7: External SATA (B), *on ground*.

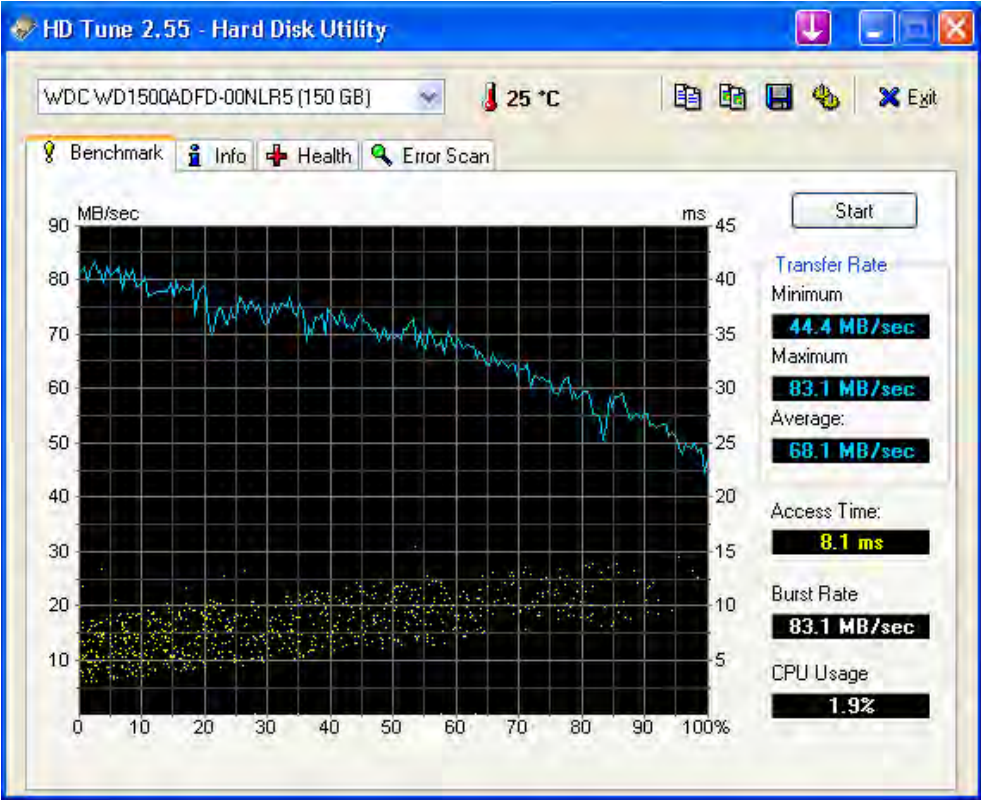


Figure C.8: External SATA (B), *in flight*.

Appendix

D

Characterisation of the 8-Element TEM Horn Antennas

This appendix details the anechoic chamber tests of the 8-element TEM horn antennas conducted at the NASA/Goddard Space Flight Centre test facility. The tests conducted characterise the performance of the ultra-wideband 8-element TEM horn antennas used as the transmit and receive antennas of a 2 - 8 GHz FMCW radar (RAASTI - see appendix A) mounted on a helicopter for the purposes of regional study of snow thickness over sea ice in Antarctica.

D.1 Background

Figure D.1 shows a model of a single-element of the antenna, and figure D.2 a photograph of the actual antenna element. figure D.3 shows the array antenna assembled and mounted in the radome which is a 1700 PelicanTM case. (It should be mentioned that the antennas are created in the air-space separating an array of these elements.) Figure D.4 shows the antennas mounted across the skids of the helicopter (Eurocopter AS 350 “Squirrel”): one antenna acting as the transmit and the other as the receive antenna for the radar which is installed in the boot of the helicopter.

D.2 Motivation

The theoretical ability of the radar to differentiate between closely spaced returns is directly a function of the receiver bandwidth. The antennas provide the last point of contact between the generated and subsequently received electromagnetic energy and the air. They are the *eyes* of the radar system, knowing their characteristics is imperative to quantifying the limiting (maximum) performance of the system.

D.3 Method

The antenna testing facility at NASA/Goddard Space Flight Centre was used to conduct the testing of the array antenna. Every test was performed with reference to a standard gain horn; the

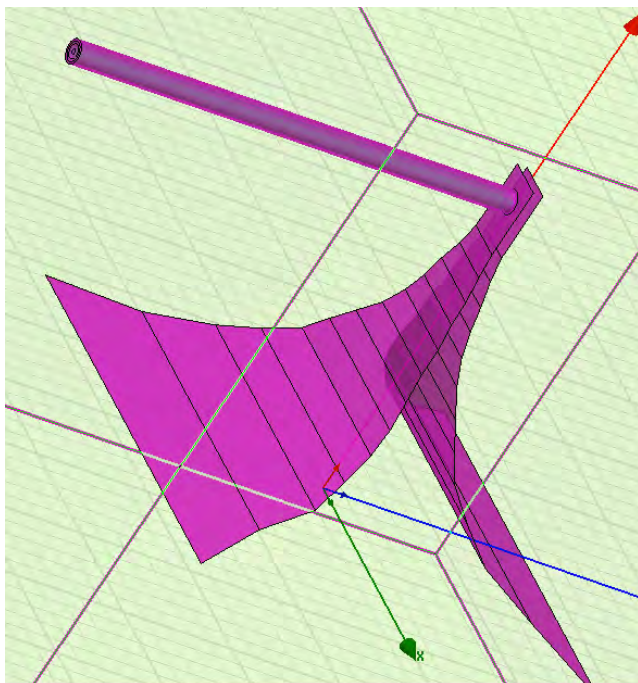


Figure D.1: Model of a single element of the antenna array, *Gunbatar* [2007].

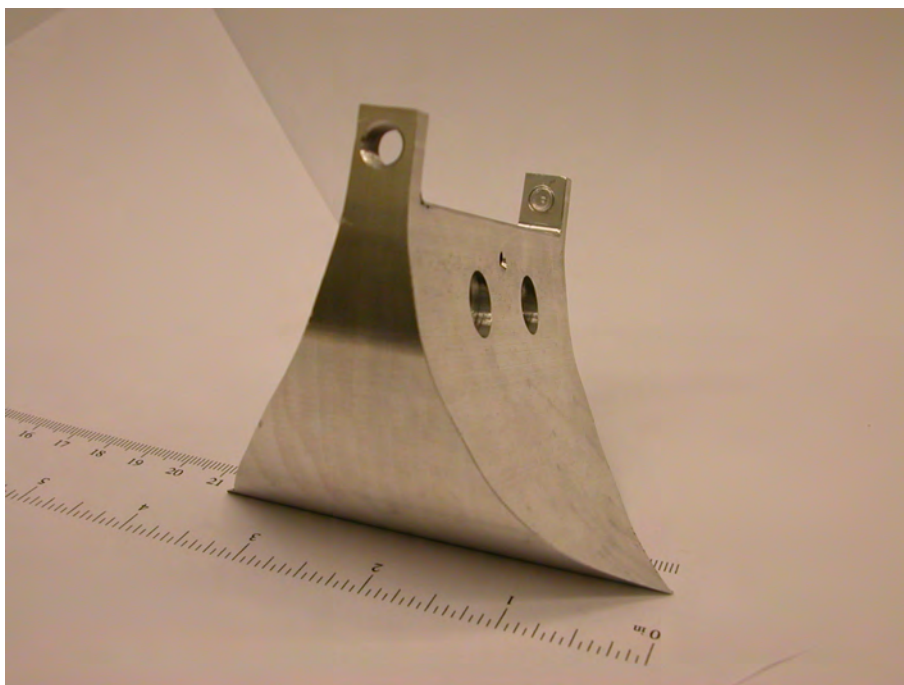


Figure D.2: Single antenna element, *Gunbatar* [2007].

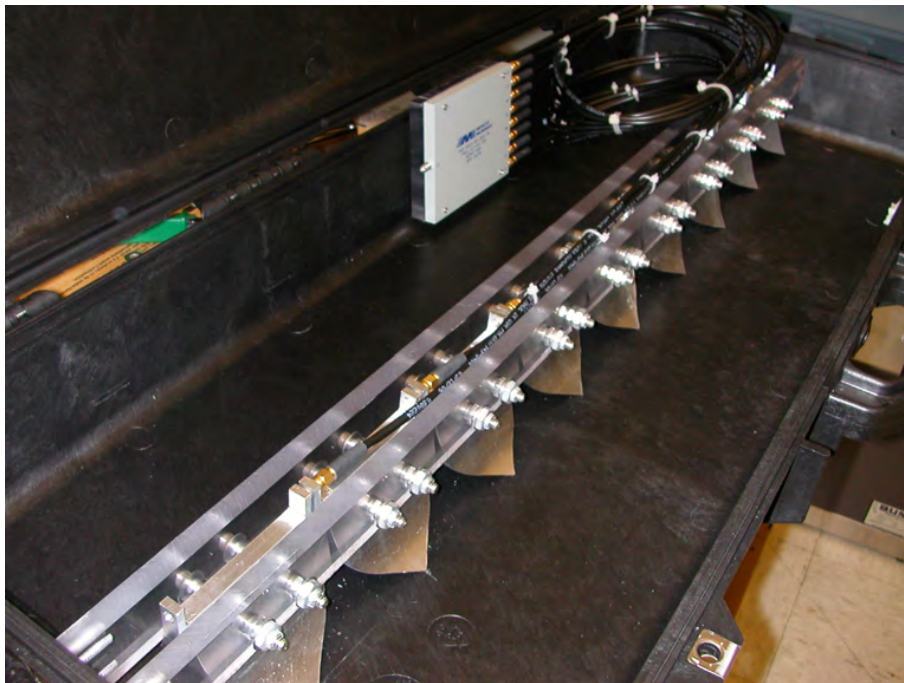


Figure D.3: Antenna array assembled and installed in the radome.



Figure D.4: Antennas in radomes, mounted between the skids of the Squirrel helicopter.

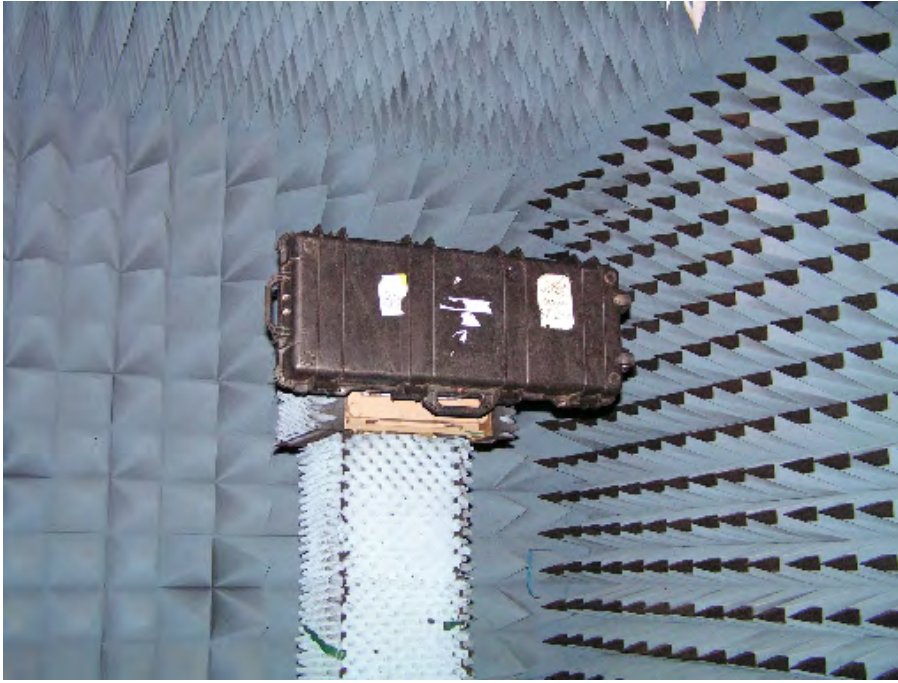


Figure D.5: Antenna with radome mounted on testing frame.

frequency bands tested are summarised in table D.1, and each test was performed from -180 to $+180$ degrees at 1° intervals. The antenna was tested with (configuration (a)), and without (configuration (b)) the radome to capture the effect of the radome for future applications.

Frequency band (GHz)	Frequency spacing of test points (GHz)
1.7 - 2.6	0.1 (10 points)
2.6 - 4.0	0.1 (15 points)
4.0 - 5.8	0.2 (10 points)
5.8 - 8.2	0.2 (13 points)

Table D.1: Antenna testing points.

D.4 Results

- The bore-sight gain of the antenna in configuration (a) plotted in figure D.7.
- The 3dB beamwidth (across the array - across track in helicopter operation) for configuration (a) is plotted in figure D.8.
- The bore-sight gain of the antenna with the radome removed (configuration (b)) is plotted in figure D.9. The blue line is the gain of the antenna with the radome for easy comparison of its affect.

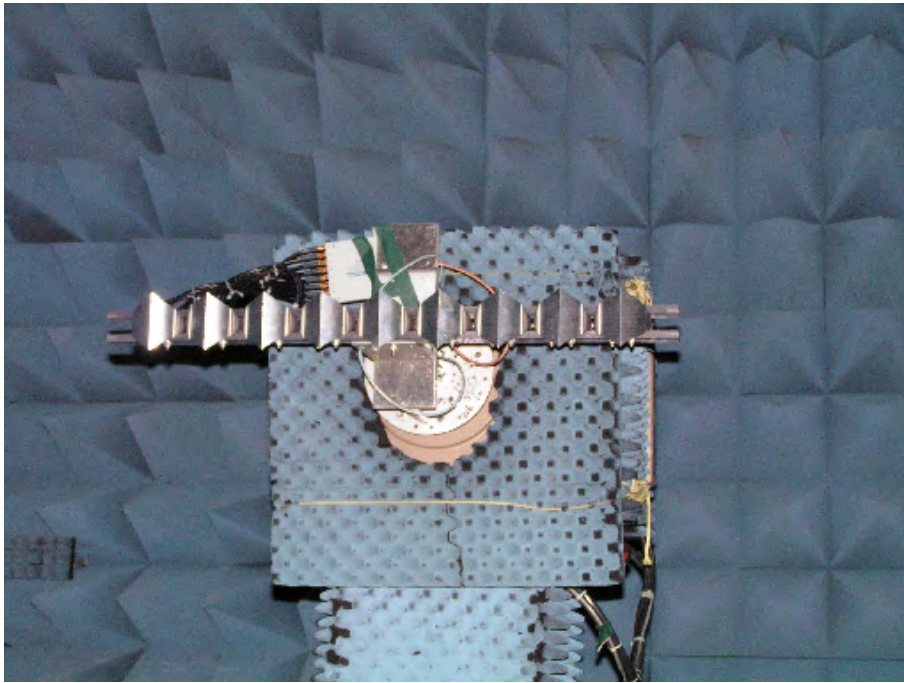


Figure D.6: Antenna without radome mounted on testing frame (bore sight).

- The 3dB beamwidth (across the array) for configuration (b) is plotted in figure D.10. The blue line is the beamwidth of the antenna with the radome for easy comparison of its affect.

D.5 Summary

The results show that the usable bandwidth of the antenna is: 2 - 6 GHz. The narrowing of the 3dB beamwidth as a function of frequency explains the chirp tapering. The effect on the resolution and SNR of the receive signal is the subject of Appendix E. The effect of the radome is found to be negligible, except at 7 GHz, however by comparison with the antenna performance at that frequency it does not detrimentally affect the system as it is already quite poor. It is possible that the radome magnifies the resonance present at this frequency, but it does not generate it.

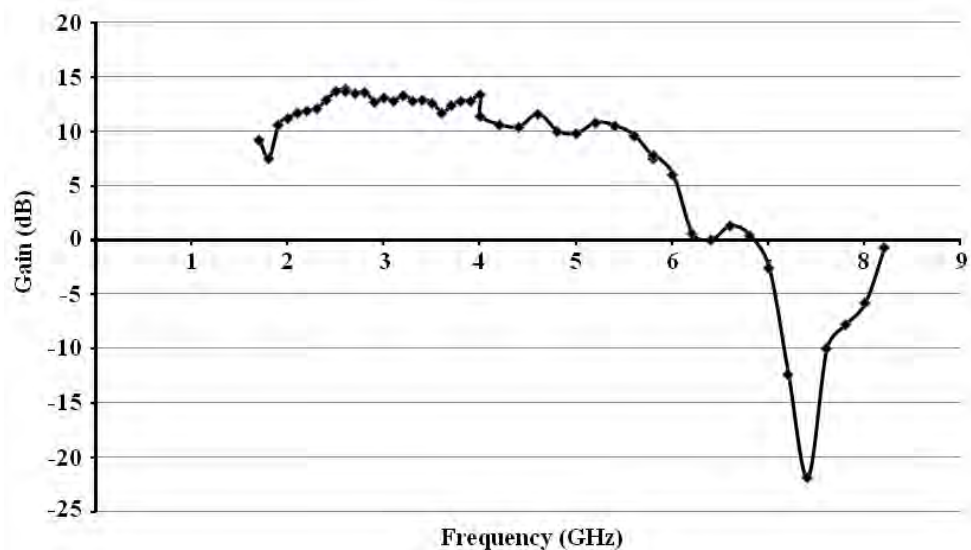


Figure D.7: Antenna Gain (dB) versus Frequency (GHz).

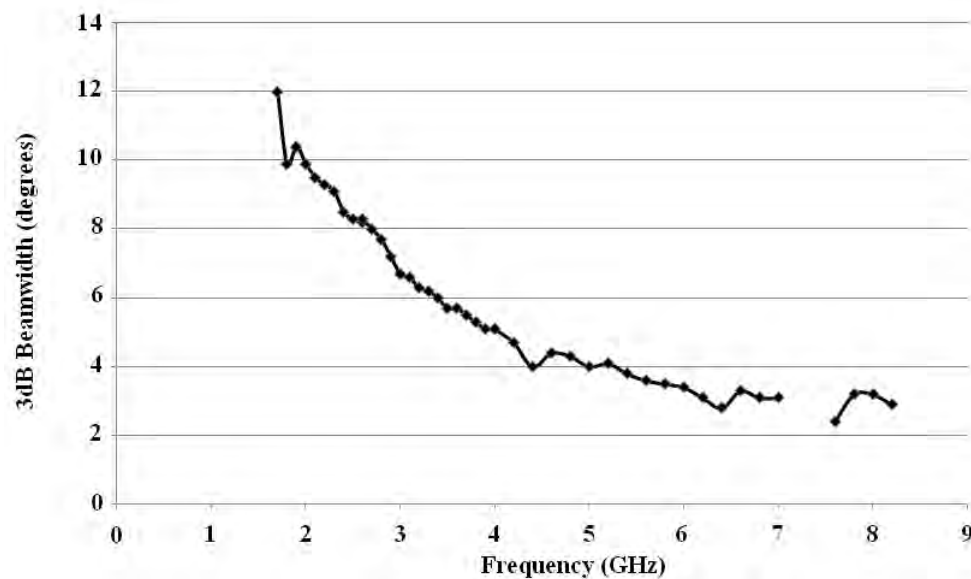


Figure D.8: Antenna full 3dB beamwidth (degrees) of antenna versus Frequency (GHz).

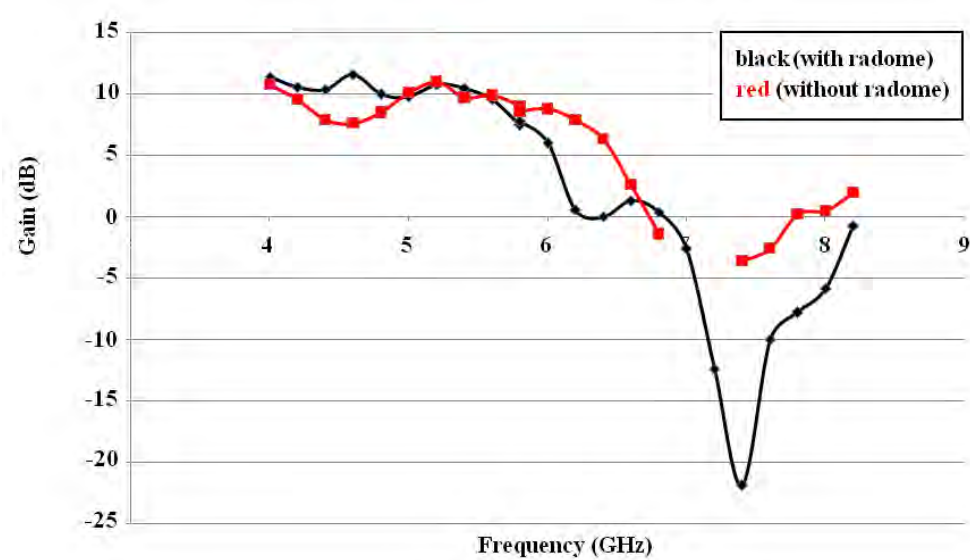


Figure D.9: Antenna Gain (dB) versus Frequency (GHz) - blue (with radome), red (without radome).

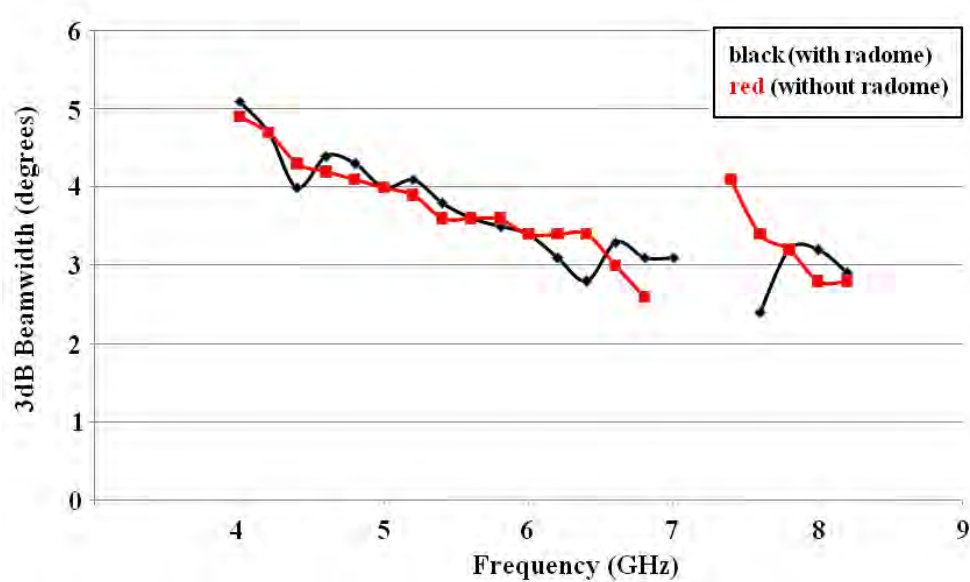


Figure D.10: Antenna 3dB beamwidth (degrees) versus Frequency (GHz) - blue (with radome), red (without radome).

Appendix

E

The Effect of Constant Antenna Gain on UWB Radar Systems.

E.1 Overview

In Ultra-Wide Band (UWB) or carrier-free radar the median/centre frequency is not a meaningful way of characterising the system. This is because the bandwidth is the same order of magnitude as the median frequency, and this must be considered when applying the radar range equation to calculate the maximum operating range and signal-to-noise ratio for example. The variation in wavelength across the bandwidth employed leads necessarily to amplitude suppression at the higher frequencies when a constant gain antenna is used for reception of the received signal. Here a quantitative analysis, simulation, and experimental results of this affect for a FMCW radar are presented.

E.2 Introduction

Examining the common form of the radar range equation (*Skolnik*, 1970):

$$P_r = \frac{P_t G_t G_r \lambda^2 \sigma}{(4\pi)^3 R^4}.$$

This equation is successfully applied to radar systems that have a carrier frequency, in which case there is no ambiguity in the wavelength (λ) to use, as the bandwidth leads to such a small change in wavelength, that its affect on the radar and target performance does not need to be considered. Careful assessment however, must be made when employing this equation to determine system performance for carrier free radar or UWB radar defined by: $0.25 < h < 1$, where h is given by *Harmuth* [1981]:

$$h = \frac{f_H - f_L}{f_H + f_L},$$

where f_H and f_L refer to the start and end of the frequency bandwidth used. In the case of the UWB radar, most parameters in the radar equation are no longer constant over the signal

bandwidth as presented in *Taylor* [2001]: all the parameters are constantly changing, instantaneous and vary over the bandwidth of the pulse/chirp.

Constant gain antennas may be employed in simple radars for convenience, this however degrades performance of the UWB radar, as constant gain indicates that the effective area of the antenna must be changing with frequency, as it is related to the gain by (*Balanis*, 1977):

$$A_{eff} = \frac{\lambda^2}{4\pi} G. \quad (E.1)$$

As G is designed to be constant, and λ varies, A_{eff} must be changing as well. The effect of this change is to decrease the maximum attainable range-resolution and SNR.

E.3 Problem Setup

In UWB radar careful consideration is made when applying the standard radar range equation for performance calculations. These considerations are made easier as there is controlled sweep over the bandwidth (i.e. a FMCW radar), and the instantaneous signal voltage which is passed to the transmit antenna, and amplified by a constant gain across the frequencies can be written as:

$$s_t(t) = \text{Re} \left(\exp(j2\pi(f_L t + \frac{1}{2}\alpha t^2)) \right), \quad (E.2)$$

valid over the interval $0 < t < T$, where T is the chirp repeat interval (CRI), and α is the frequency sweep rate, given by the ratio of the bandwidth transmitted and the CRI.

Assuming a lossless system and a constant gain antenna, the effective area of the antenna must be changing with frequency. Hence, the instantaneous signal voltage at the output of the receive antenna is:

$$s_r(t) = A(t) \text{Re} \left(\exp(j2\pi(f_L(t - \tau) + \frac{1}{2}\alpha(t - \tau)^2)) \right), \quad (E.3)$$

where τ is the time delay (proportional to range) of the object from which this signal is reflected, and $A(t)$ is the amplitude modulation imposed by the changing effective area of the antenna:

$$\begin{aligned} A(t) \equiv A_{eff}(t) &= \frac{\lambda^2}{4\pi} G, \\ &= \left(\frac{c}{f_L + \alpha t} \right)^2 \frac{G}{4\pi}, \end{aligned} \quad (E.4)$$

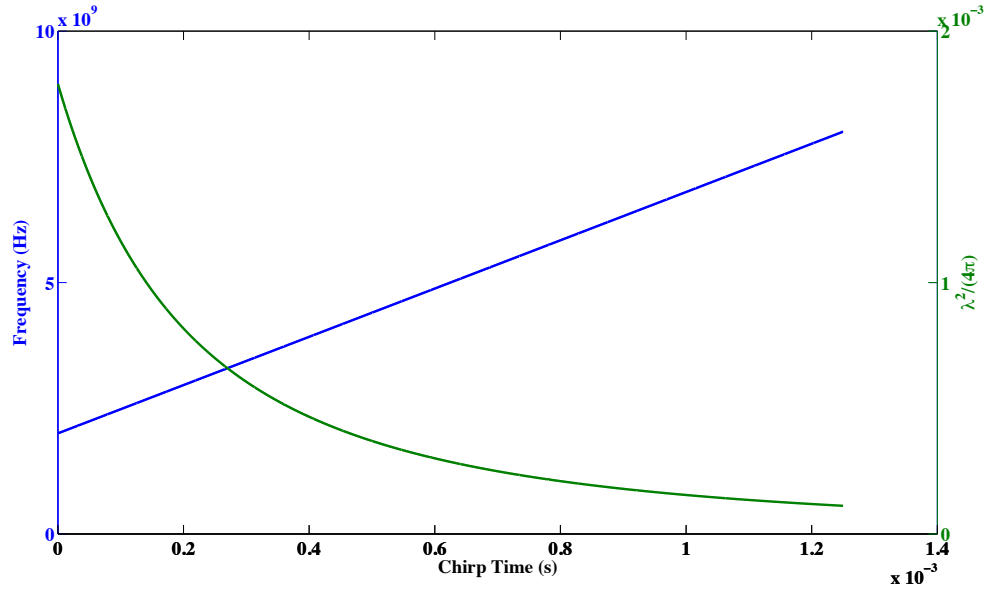


Figure E.1: Variation of A_{eff} as a function of frequency and chirp period.

Taking the product of E.2 and E.3 and consequently deriving the intermediate frequency:

$$s_{IF}(t) = A(t) \Re \left(\exp(j2\pi(f_L \tau + \alpha t \tau - \frac{1}{2} \alpha \tau^2)) \right), \quad (\text{E.5})$$

it becomes clear that the $A(t)$ term is effectively a *windowing* operation applied to the receive signal, and degrading the SNR and frequency resolution, which ultimately, of course affects the range resolution of the radar.

Figure E.1 illustrates the change in frequency over the chirp duration, plotted alongside this change in $A(t)$ over the same time interval.

E.4 Quantitative Analysis and Simulation

The degradation in SNR can be quantified by calculating the effective power received, and comparing it with the expected power received under no amplitude modulation conditions.

The total RMS power received under the inherent amplitude modulation condition, implied by a constant antenna gain is found by:

$$P_{rms}(t) = \sqrt{\frac{1}{T} \int_0^T A^2(t) dt}. \quad (\text{E.6})$$

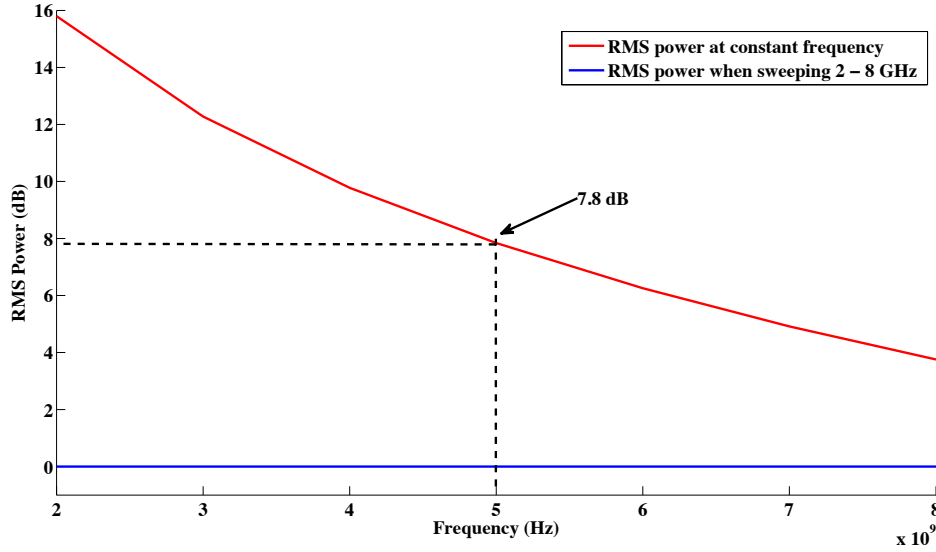


Figure E.2: RMS power as a function of centre frequency.

Performing this integration leads to the result that the received power is approximately 7.8 dB lower than it would be if the median frequency of 5 GHz was transmitted, or no such suppression occurred. Figure E.2 plots the RMS power in dB as a function of centre frequency (red line), relative to the RMS power that this suppression achieves (blue line - at 0 dB).

In order to determine the effect that this amplitude modulation has on the maximum obtainable frequency resolution, the Fourier transform of $s_{IF}(t)$ under the amplitude modulation/suppression condition must be found:

$$\mathcal{F}(\omega) = \int A(t) s_{IF} \exp(-j\omega t) dt. \quad (\text{E.7})$$

This is not a trivial integration however, and the degradation in range resolution is best illustrated by a simulation where the amplitude modulation effect is viewed as a window that is applied to the signal prior to processing. Figure E.3 illustrates the window effect of $A(t)$ in comparison with the rectangular window. Using MATLAB® *window simulation* toolbox, table E.1 compares a few of the window performance parameters for the two windows. Additionally, the main lobe width compared with the rectangular window is 1.14, which indicates a degradation in resolution ability of the frequency, and consequently the range resolution of the radar.

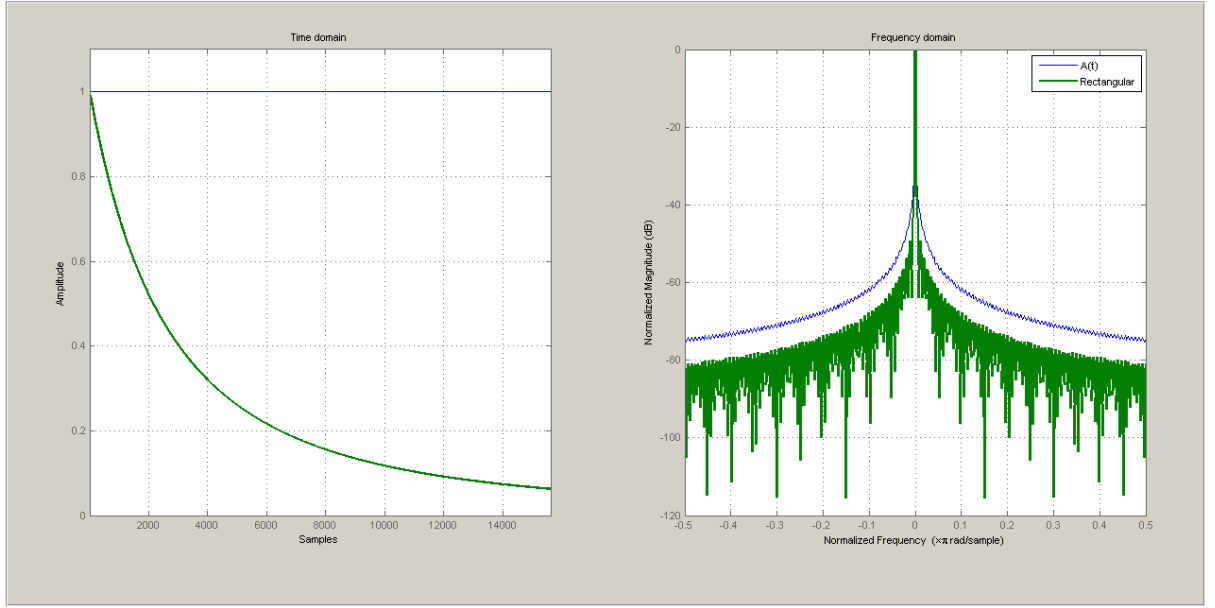


Figure E.3: Comparison of the rectangular and $A(t)$ (“amplitude suppression”) windows.

Window	Leakage factor (%)	Sidelobe attenuation (dB)	Main lobe width (relative)
Rectangular	9.17	-13.3	1.0
$A(t)$	19.44	-11.8	1.14

Table E.1: Window performance parameters.

E.5 Experimental Results

This effect was first noticed when processing the data obtained from a 2 - 8 GHz FMCW radar designed to estimate snow thickness on sea ice in Antarctica (*Galin et al.*, 2008). Figure E.4 shows the IF frequency of the radar with the $A(t) = 1/\lambda^2$ amplitude modulation plotted in red, illustrating the close correspondence.

The 6 GHz bandwidth is necessary for fine range resolution, and the antennas were designed to have constant gain across the bandwidth (*Gunbatar*, 2007), see appendix D.

E.6 Summary

The use of a constant gain antenna on receive leads to overall loss in SNR of ≈ 8 dB and slight degradation in resolution (by a factor of 1.14). It is important to consider that it is not possible to correct for this degradation in SNR in post processing due to the fact that this effect limits the receiver bandwidth. To avoid this in future a variable gain receive antenna design should be considered.

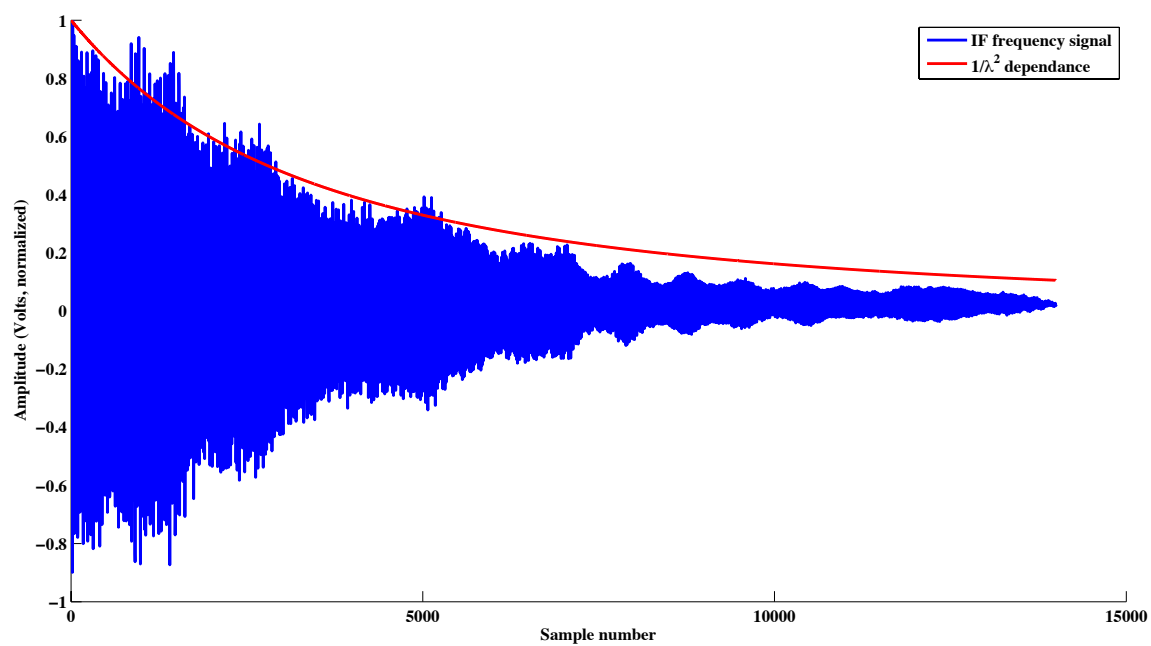


Figure E.4: Amplitude modulation effects on the IF frequency.

References

- Aagaard, K., and E. Carmack, The Role of Sea Ice and Other Fresh Water in the Arctic Circulation, *Journal of Geophysical Research*, 94, 485–498, 1989.
- Allison, I., R. Brandt, and S. Warren, East Antarctic sea ice: Albedo, thickness distribution, and snow cover, *Journal of Geophysical Research*, 98(C12), 12,417–12,429, 1993.
- Analog Devices, 2.7 GHz DDS-Based AgileRF Synthesiser, *Tech. rep.*, 2004.
- Andreas, E., and K. Claffey, Air-ice drif coefficients in the western Weddell Sea 1. Values deducted from profile measurements, *Journal of Geophysical Research*, 100, 4821–4831, 1995.
- Askne, J., Remote Sensing using Microwaves, <http://www.rss.chalmers.se/rsg/Education/RSUM/>, 2002.
- Axelsson, S., Area Target Response of Triangularly Frequency-Modulated Continuous-Wave Radars, *IEEE Transaction on Aerospace and Electronic Systems*, 14, 266–277, 1978.
- Balanis, C., *Antenna Theory: Analysis and Design*, Wiley, New York, NY, 1997.
- Barber, D., A. Fung, T. Grenfell, S. Nghiem, R. Onstott, V. Lytle, D. Perovich, and A. Gow, The role of snow on microwave emission and scattering over first-year sea ice, *Geoscience and Remote Sensing, IEEE Transactions on*, 36, 1750–1763, 1998.
- Beaven, S., G. Lockhart, S. Gogineni, A. Hosseinmostafa, K. Jezek, and A. Gow, Laboratory measurements of radar backscatter from bare and snow-covered saline ice sheets, *International Journal of Remote Sensing*, 16, 851–876, 1995.
- Beckmann, P., and A. Spizzichino, *The Scattering of Electromagnetic Waves from Rough Surfaces*, Pergamon Press, New York, NY, 1963.
- Bitz, C., M. Holland, and M. Eby, Simulating ice-thickness distribution in a coupled climate model, *Journal of Geophysical Research*, 106, 2441–2463, 2001.
- Blake, L., *Radar Range-Performance Analysis*, Artech House, 1986.

- Born, M., and E. Wolf, *Principles of Optics: Electromagnetic Theory of Propagation, Interference and Diffraction of Light*, third ed., Pergamon, New York, NY, 1965.
- Brandt, R., S. Warren, A. Worby, and T. Grenfell, Surface Albedo of the Antarctic Sea Ice Zone, *Journal of Climate*, 18, 3606–3622, 2005.
- Breivik, L., et al., Remote sensing of sea ice, White paper, Ocean Obs'09, 2009.
- Brooker, G., Understanding Millimeter Wave FMCW Radars, *International Conference on Sensing Technology, ICST*, pp. 152–157, 2005.
- Brooker, G., *Introduction to Sensors for Ranging and Imaging*, SciTech, 2009.
- Carsey, F. (Ed.), *Microwave Remote Sensing of Sea Ice*, American Geophysical Union, Washington D.C., 1992.
- Cavalieri, D., and T. Markus, EOS Aqua AMSR-E Arctic Sea-Ice Validation Program: Arctic2006 Aircraft Campaign Flight Report, *Tech. rep.*, NASA, 2006.
- Cavalieri, D., and C. Parkinson, Antarctic sea ice variability and trends, 1979–2006, *Journal of Geophysical Research*, 113, C07,004, 2008.
- Chapman, W., and J. Walsh, Recent Variations of Sea Ice and Air Temperature in High Latitudes, *Bulletin of the American Meteorological Society*, 74, 33–47, 1993.
- Chylek, P., J. Zhan, and R. Pinnich, Absorption and Scattering of Microwaves by Falling Snow, *International Journal of Infrared and Millimeter Waves*, 14, 2295–2310, 1993.
- Comiso, J., and C. Parkinson, Satellite-Observed Changes in the Arctic, *Physics Today*, 61(3), 70–76, 2004.
- Comiso, J., D. Cavalieri, and T. Markus, Sea ice concentration, ice temperature, and snow depth using AMSR-E data, *IEEE Trans. Geosci. Remote Sens.*, 41, 243–252, 2003.
- Crocker, G. B., and P. Wadhams, Breakup of Antarctic Fast Ice, *Cold Regions Science and Technology*, 17, 61–76, 1989.
- Curry, J., J. Schramm, and E. Ebert, Sea Ice-Albedo Climate Feedback Mechanism, *Journal of Climate*, 8, 240–247, 1995.
- de Wit, J., Development of an Airborne Ka-band FM-CW Synthetic Aperture Radar, Ph.D. thesis, Delft Technical University, 2005.

- Dozier, J., and T. Painter, Multispectral and Hyperspectral Remote Sensing of Alpine Snow Properties, *Annual Review of Earth and Planetary Sciences*, 32, 465, 2004.
- Drinkwater, M., LIMEX '87 Ice Surface Characteristics: Implications for C-Band SAR Backscatter Signatures, *IEEE Transactions on Geoscience and Remote Sensing*, 27, 147–158, 1989.
- Eicken, H., The role of sea ice in structuring Antarctic ecosystems, *Polar Biology*, 12, 3–13, 1992.
- Eicken, H., M. Lange, and P. Wadhams, Characteristics and distribution patterns of snow and meteoric ice in the Weddell Sea and their contribution to the mass balance of sea ice, *Annales Geophysicae*, 12, 80–93, 1994.
- Emery, W., C. Fowler, and J. Maslanik, Satellite-derived maps of Arctic and Antarctic sea ice motion: 1988 to 1994, *Geophysical Research Letters*, 24, 897–900, 1997.
- ETS-Lindgren, *3115 Double-Ridged Guide Antenna*.
- Feynman, R., *The Feynman Lectures on Physics: Volume 3*, vol. 3 of *The Feynman Lectures on Physics*, Addison-Wesley, Boston, 1963.
- Fichefet, T., and M. Morales Maqueda, Modelling the influence of snow accumulation and snow-ice formation on the seasonal cycle of the Antarctic sea-ice cover, *Climate Dynamics*, 15, 251–268, 1999.
- Fichefet, T., B. Tartinville, and H. Goosse, Sensitivity of the Antarctic sea ice to the thermal conductivity of snow, *Geophysical Research Letters*, 27(3), 401–404, 2000.
- Foster, T., and E. Carmack, Frontal zone mixing and Antarctic Bottom Water formation in the southern Weddell Sea, *Deep-Sea Research*, 23, 301–317, 1976.
- Frolov, A., and Y. Macheret, On dielectric properties of dry and wet snow, *Hydrological Processes*, 13, 1755–1760, 1999.
- Galin, N., RADar for Antarctic Snow Thickness Investigation (RAASTI), *Internal report*, Australian Antarctic Division, Channel Highway, Kingston, Tasmania, 7050, Australia, 2010.
- Galin, N., A. Worby, R. Massom, G. Brooker, C. Leuschen, S. P. Gogineni, and P. Jansen, 2 - 8 GHz FMCW radar for estimating snow depth on Antarctic sea ice, *2008 International Conference on RADAR, Adelaide, Australia*, pp. 276–281, 2008.

- Galin, N., A. Worby, T. Markus, C. Leuschen, and S. P. Gogineni, Validation of airborne FMCW radar measurements of snow thickness over sea ice in Antarctica, *IEEE Transactions on Geoscience and Remote Sensing*, p. in press, 2011.
- Galley, R., M. Trachtenberg, A. Langlois, D. Barber, and L. Shafai, Observations of geophysical and dielectric properties and ground penetrating radar signatures for discrimination of snow, sea ice and freshwater ice thickness, *Cold Regions Science and Technology*, 57, 29–38, 2009.
- Giles, B., R. Massom, and V. Lytle, Fast-ice distribution in East Antarctica during 1997 and 1999 determined using RADARSAT data, *Journal of Geophysical Research*, 113, C02S14, 2008a.
- Giles, K., and S. Hvidegaard, Comparison of space borne radar altimetry and airborne laser altimetry over sea ice in the Fram Strait, *International Journal of Remote Sensing*, 27, 3105–3113, 2006.
- Giles, K., S. Laxon, D. Wingham, D. Wallis, W. Krabill, C. Leuschen, D. McAdoo, S. Manizade, and R. Raney, Combined airborne laser and radar altimeter measurements over the Fram Strait in May 2002, *Remote Sensing of Environment*, 111, 182–194, 2007.
- Giles, K., S. Laxon, and A. Worby, Antarctic sea ice elevation from satellite radar altimetry, *Geophysical Research Letters*, 35, L03,503, 2008b.
- Gleitz, M., M. Rutgers v.d. Loeff, D. Thomas, G. Dieckmann, and F. Millero, Comparison of summer and winter inorganic carbon, oxygen and nutrient concentrations in Antarctic sea ice brine, *Marine Chemistry*, 51, 81–91, 1995.
- Gloersen, P., D. Campbell, D. Cavalieri, J. Comiso, C. Parkinson, and H. Zwally, *Arctic and Antarctic sea ice, 1978-1987: Satellite passive-microwave observations and analysis*, vol. 511, NASA Special Publication, Washington, DC, 1992.
- Gogineni, S., and G. Prescott, Validation of AMSR-E snow depth on sea ice retrievals using an airborne pulse radar, *Tech. rep.*, Radar Systems and Remote Sensing Laboratory, 2001.
- Gogineni, S., K. Wong, S. Krishnan, P. Kanagaratnam, T. Markus, and V. Lytle, An Ultra-wideband Radar for Measurements of Snow Thickness Over Sea Ice, in *Geoscience and Remote Sensing Symposium, 2003. IGARSS'03. Proceedings, 2003 IEEE International*, vol. 4, pp. 2802–2804, 2003.

- Gogineni, S., C. Leuschen, A. Patel, F. Rodriguez-Morales, and T. Satyanarayana, Validation of AMSR snow depth on sea ice retrievals using an airborne pulse radar, *Tech. rep.*, Center for Remote Sensing of Ice Sheets, 2009.
- Goldsetzer, T., A. Langlois, and J. Yackel, Dielectric properties of brine-wetted snow on first-year sea ice., *Cold Regions Science and Technology*, 58, 47–56, 2009.
- Griffiths, H., New ideas in FM radar, *Electronics and Communication Engineering Journal*, 2, 185–194, 1990.
- Griffiths, H., The Effect of Phase and Amplitude Errors in FM Radar, *IEE Colloquium on High Time-Bandwidth Product Waveforms in Radar and Sonar*, pp. 9/1–9/5, 1991.
- Gunbatar, Y., Eight-Element Tapered Horn Antenna, Master's thesis, The University of Kansas, 2007.
- Haas, C., Evaluation of ship-based electromagnetic-inductive thickness measurements of summer sea-ice in the Bellingshausen and Amundsen Seas, Antarctica, *Cold Regions Science and Technology*, 27, 1–16, 1998.
- Hallikainen, M., F. Ulaby, and M. Abdelrazik, Dielectric Properties of Snow in the 3 to 37 GHz Range, *IEEE Transactions on Antennas and Propagation*, 34, 1329–1340, 1986.
- Harmuth, H., *Nonsinusoidal Waves for Radar and Radio Communication*, Academic Press, New York, NY, 1981.
- Harris, F., On the use of windows for harmonic analysis with the discrete fourier transform, *Proceedings of the IEEE*, 66, 1978.
- Helm, V., D. Steinhage, R. Dietrich, and A. Rulke, CryoVEx08/09 - Antarctica: Data Acquisition and Final Processing Report, *Tech. rep.*, Alfred Wegener Institute, 2009.
- Holland, M., and C. Bitz, Polar amplification and climate change in coupled models, *Climate Dynamics*, 21, 221–232, 2003.
- Holland, M., C. Bitz, E. Hunke, W. Lipscomb, and J. Schramm, Influence of the Sea Ice Thickness Distribution on Polar Climate in CCSM3, *Journal of Climate*, 19, 2398–2414, 2006.
- Holland, M., M. Serreze, and J. Stroeve, The sea ice mass budget of the Arctic and its future change as simulated by coupled climate models, *Climate Dynamics*, 34, 185–200, 2008.

- Holmgren, J., M. Sturm, N. Yankielun, and G. Koh, Extensive measurements of snow depth using FM-CW radar, *Cold Regions Science and Technology*, 27, 17–30, 1998.
- Houghton, J. T., Y. Ding, D. Griggs, M. Noguer, P. van der Linden, X. Dai, K. Maskell, and C. Johnson, *Climate Change 2001: The Scientific Basis*, Cambridge University Press, Cambridge CB2 2RU, United Kingdom, 2001.
- IGOS, ., Integrated Global Observing Strategy Cryosphere Theme Report - For the Monitoring of our Environment from Space and from Earth, *Tech. Rep. WMO/TD-No. 1405*, Geneva: World Meteorological Organization, 2007.
- Iizuka, K., A. Freundorfer, K. Wu, H. Mori, H. Ogura, and V. Nguyen, Step-frequency radar, *Journal of Applied Physics*, 56, 2572–2583, 1984.
- Iizuka, K., A. Freundorfer, D. Wilson, G. Tzang, and W. Haras, Measurement of saline ice thickness using a step frequency radar, *Cold Regions Science and Technology*, 15, 23–32, 1988.
- Jacka, T., and W. Budd, Detection of temperature and sea-ice-extent changes in the Antarctic and Southern Ocean, *Annals of Glaciology*, 27, 553–559, 1998.
- Jordan, R., E. Andreas, and A. Makshtas, Heat budget of snow-covered sea ice at North Pole 4, *Journal of Geophysical Research*, 104, 7785–7806, 1999.
- Kanagaratnam, P., T. Markus, V. Lytle, B. Heavey, P. Jansen, G. Prescott, and S. Gogineni, Ultra-wideband radar measurements of thickness of snow over sea ice, *Transaction on Geoscience and Remote Sensing*, 45, 2007.
- Kawamura, T., H. Wakabayashi, and S. Ushio, Growth, properties and relation to radar backscatter coefficient of sea ice in Lutzow-Holm Bay, Antarctica, *Annals of Glaciology*, 44, 163–169, 2006.
- Kim, Y., R. Onstott, and R. Moore, The Effect of a Snow Cover on Microwave Backscatter from Sea Ice, *IEEE Journal of Oceanic Engineering*, 9, 383–388, 1984.
- Kingsley, S., and S. Quegan, *Understanding radar systems*, SciTech Publishing, 1999.
- Koh, G., N. Yankielun, and A. Baptista, Snow cover characterisation using multiband FMCW radars, *Hydrological Processes*, 10, 1609–1617, 1996.
- Krishnan, S., Modelling and Simulation Analysis of an FMCW Radar for Measuring Snow Thickness, Master's thesis, University of Kansas, 2007.

- Kwok, R., and G. Cunningham, ICESat over Arctic sea ice: Estimation of snow depth and ice thickness, *Journal of Geophysical Research*, 113, C08S010, 2008.
- Kwok, R., H. Zwally, and D. Yi, ICESat observations of Arctic sea ice : a first look, *Geophysical Research Letters*, 31, L16,401, 2004.
- Laxon, S., N. Peacock, and D. Smith, High interannual variability of sea ice thickness in the Arctic region, *Nature*, 425, 947–950, 2003.
- Ledley, T., *Sea ice: A Factor in Influencing Climate on Short and Long Time Scales, Ice in the Climate System*, Springer-Verlag Berlin Heidelberg, 2003.
- Lentz, H., W. Borisch, and H. Braun, Concept and realization of an Airborne SAR/Interferometric Radar Altimeter System (ASIRAS), *Geoscience and Remote Sensing Symposium, Proceedings of*, 6, 3099–3101, 2002.
- Leuschen, C., R. Swift, J. Comiso, R. Raney, R. Chapman, W. Krabill, and J. Sonntag, Combination of laser and radar altimeter height measurements to estimate snow depth during the 2004 Antarctic AMSR-E Sea Ice field campaign, *Journal of Geophysical Research*, 113, C04S90, 2008.
- Maksym, T., and M. Jeffries, A one-dimensional percolation model of flooding and snow ice formation on Antarctic sea ice, *Journal of Geophysical Research*, 104, 313–331, 2000.
- Makynen, M., and M. Hallikainen, Simulation of ASIRAS Altimeter Echoes for Snow-Covered First-Year Sea Ice, *Geoscience and Remote Sensing Letters, IEEE*, 6, 486–490, 2009.
- Manabe, S., and R. Stouffer, Sensitivity of a global climate model to an increase of CO₂ in the atmosphere, *Journal of Geophysical Research*, 85, 5529–5554, 1980.
- Manabe, S., R. Stouffer, M. Spelman, and K. Bryan, Transient Responses of a Coupled Ocean-Atmosphere Model to Gradual Changes of Atmospheric CO₂. Part I: Annual Mean Response, *Journal of Climate*, 4, 785–818, 1991.
- Markus, T., and D. Cavalieri, Snow Depth Distribution over Sea Ice in the Southern Ocean from Satellite Passive Microwave Data, *Antarctic Sea Ice: Physical Processes, Interactions and Variability. Antarctic Research Series*, 74, 19–39, 1998.
- Marshall, H., and G. Koh, FMCW radars for snow research, *Cold Regions Science and Technology*, pp. 118–131, 2008.

- Marshall, H., K. Birkeland, K. Elder, and T. Meiners, Helicopter-based microwave radar measurements in alpine terrain, *Proc. of the 2008 Int. Snow Science Workshop*, 2008a.
- Marshall, H., G. Koh, and M. Sturm, Ultra-broadband portable microwave FMCW radars for measuring snow depth, snow water equivalent, and stratigraphy: practical considerations, *Remote Sensing of the Cryosphere, International Union of Radio Science (URSI) General Assembly*, 2008b.
- Martinson, D., and C. Wamser, Ice Drift and Momentum Exchange in Winter Antarctic Pack Ice, *Journal of Geophysical Research*, 95, 1741–1755, 1990.
- Massom, R., M. Drinkwater, and C. Haas, Winter snow cover on sea ice in the Weddell Sea, *Journal of Geophysical Research*, 102(C1), 1101–1117, 1997.
- Massom, R., A. Worby, V. Lytle, T. Markus, D. Yi, K. Tateyama, H. Enomoto, A. Steer, and J. Zwally, Early Springtime Snow Cover on East Antarctic Sea Ice, ARISE 2003: Variability and Satellite Validation, *Annals of Glaciology*, 44, 288–296, 2003.
- Massom, R.A., H. Eicken, C. Haas, M.O. Jeffries, M.R. Drinkwater, M. Sturm, A.P. Worby, X. Wu, V. Lytle, S. Ushio, K. Morris, P.A. Reid, S.G. Warren and I. Allison, Snow on Antarctic Sea Ice, *Rev. Geophys.*, 39, 413–445, 2001.
- Maykut, G., and N. Untersteiner, Some Results from a Time-Dependent Thermodynamic Model of Sea Ice, *Journal of Geophysical Research*, 76, 1550–1575, 1971.
- McMinn, A., C. Ashworth, and K. Ryan, Growth and productivity of Antarctic sea ice under PAR and UV irradiances, *Botanica Marina*, 42, 401–407, 1999.
- Meiners, K., Sea-ice communities: structure and composition in Baltic, Antarctic and Arctic Seas, Ph.D. thesis, University of Kiel, Germany, 2002.
- Meta, A., P. Hogeboom, and L. Ligthart, Signal Processing for FMCW SAR, *Geosciences and Remote Sensing, IEEE Transactions on*, 45, 3519–3532, 2007.
- Moore, R., and C. J. Williams, Radar Terrain Return at Near-Vertical Incidence, *Proceedings of the IRE*, pp. 228–238, 1957.
- Nash, G., Phase-Locked Loop Design Fundamentals, *Tech. rep.*, Freescale Semiconductor, 2006.
- Nghiem, S., R. Kwok, S. Yueh, and M. Drinkwater, Polarimetric signatures of sea ice 1. Theoretical model, *Journal of Geophysical Research*, 100, 665–679, 1995a.

- Nghiem, S., R. Kwok, S. Yueh, and M. Drinkwater, Polarimetric signatures of sea ice 2. Experimental observations, *Journal of Geophysical Research*, 100, 681–698, 1995b.
- Nicol, S., T. Pauly, N. Bindoff, S. Wright, D. Thiele, E. Woehler, G. Hoise, and P. Strutton, Ocean circulation off East Antarctica affects ecosystem structure and sea-ice extent, *Nature*, 406, 504–507, 2000.
- Panzer, B., C. Leuschen, A. Patel, T. Markus, and S. Gogineni, Ultra-wideband radar measurements of snow thickness over sea ice, *Geoscience and Remote Sensing Symposium*, pp. 3130–3133, 2010.
- Parkinson, C., and D. Cavalieri, A 21 year record of Arctic sea-ice extents and their regional, seasonal and monthly variability and trends, *Annals of Glaciology*, 32, 441–446, 2002.
- Perovich, D., T. Grenfell, J. Richter-Menge, B. Light, W. Tucker III, and H. Eicken, Thin and thinner: Sea ice mass balance measurements during SHEBA, *Journal of Geophysical Research*, 108(C3), 8050, 2003.
- Powell, D., T. Markus, D. Cavalieri, A. Gasiewski, M. Klein, J. Maslanik, J. Stroeve, and Sturm, Microwave signatures of snow on sea ice: modelling., *IEEE Transactions on Geoscience and Remote Sensing*, 44, 3091–3101, 2006.
- Proakis, J., and D. Manolakis, *Digital Signal Processing: Principles, Algorithms, and Applications*, Pearson, Education. Third Edition, 2004.
- Rayner, N., D. Parker, E. Horton, C. Folland, L. Alexander, D. Rowell, E. Kent, and A. Kaplan, Global analyses of sea surface temperature, sea ice, and night marine air temperature since the late nineteenth century, *Journal of Geophysical Research*, 108, 4407, 2003.
- Rees, G., *Remote Sensing of Snow and Ice*, CRC Press, 2006.
- Remund, Q., D. Long, and M. Drinkwater, An iterative approach to multisensor sea-ice classification, *IEEE Transactions on Geoscience and Remote Sensing*, 38, 1843–1856, 2000.
- Rignot, E., and H. Thomas, Mass Balance of Polar Ice Sheets, *Science*, 297, 1502–1506, 2002.
- Rink, T., P. Kanagaratnam, D. Braaten, T. Akins, and S. Gogineni, A Wideband Radar for Mapping Near-Surface Layers in Snow, *Proceedings of IGARSS, Denver, CO*, pp. 3655–3657, 2006.
- Rintoul, S., C. Hughes, and D. Olbers, *Ocean circulation and climate*, chap. 4. The Antarctic Circumpolar Current System, International geophysics series, Academic, New York, 2002.

- Rothrock, D., Y. Yu, and G. Maykut, Thinning of the Arctic sea-ice cover, *Geophysical Research Letters*, 26, 3469–3472, 1999.
- Rott, H., et al., Scientific Preparations for COREH20, a Dual Frequency SAR Mission for Snow and Ice Observations, *IEEE International Geoscience and Remote Sensing Symposium*, 2008.
- Shepherd, A., D. Wingham, D. Wallis, K. Giles, S. Laxon, and V. S. A., Recent loss of floating ice and the consequent sea level contribution, *Geophysical Research Letters*, 37, L13,503, 2010.
- Skolnik, M., *Radar handbook*, McGraw-Hill, New York, NY, 1970.
- Smetacek, V., and S. Nicol, Polar ocean ecosystems in a changing world, *Nature*, 437, 362–368, 2005.
- Stove, A., Linear FMCW radar techniques, *Radar and Signal Processing, IEE Proceedings F*, 139, 343–350, 1992.
- Stroeve, J., T. Markus, J. Maslanik, D. Cavalieri, A. Gasiewski, J. Heinrich, and J. Holmgren, Impact of Surface Roughness on AMSR-E Sea Ice Products, *IEEE Transactions on Geoscience and Remote Sensing*, 44, 3103–3118, 2006.
- Sturm, M., K. Morris, and R. Massom, *Antarctic Sea Ice: Physical Processes, Interactions and Variability*, *Antarctic Research Serial*, vol. 74, chap. The winter snow cover of the West Antarctic pack ice: Its spatial and temporal variability, pp. 19–40, AGU, Washington D.C., 1998.
- Taylor, J. (Ed.), *Ultra-Wideband Radar Technology*, CRC Press, 2001.
- Ulaby, F., R. Moore, and A. Fung, *Microwave Remote Sensing Active and Passive, Vol.II*, Artech House, Dedham, MA, 1986a.
- Ulaby, F., R. Moore, and A. Fung, *Microwave Remote Sensing Active and Passive, Vol.III*, Artech House, Dedham, MA, 1986b.
- Van de Berg, W., M. Van den Broeke, C. Reijmer, and E. Van Meijgaard, Characteristics of the Antarctic surface mass balance, 1958-2002, using a regional atmospheric climate model, *Annals of Glaciology*, 41, 97–104, 2005.
- van de Hulst, H., *Light scattering by small particles.*, New York: Wiley, 1957.
- Vancoppenolle, M., T. Fichefet, H. Goosse, S. Bouillon, G. Madec, and M. Morales Maqueda, Simulating the mass balance and salinity of Arctic and Antarctic sea ice. 1. Model description and validation, *Ocean Modelling*, 27, 2009.

- Vossiek, M., P. Heide, M. Nalezinski, and V. Magori, Novel FMCW radar system concept with adaptive compensation of phase errors, *Proc. EuMC, Prague, Czech Republic*, p. 135139, 1996.
- Wade, U., Airborne Measurement of Snow Thickness over Sea Ice, *Geoscience and Remote Sensing Symposium, Proceedings of*, pp. 222–225, 2008.
- Wadhams, P., W. Tucker, W. Krabill, R. Swift, J. Comiso, and N. Davis, Relationship between sea ice freeboard and draft in the Arctic basin, and implications for ice thickness monitoring, *Journal of Geophysical Research*, 97, 20,325–20,334, 1992.
- Walsh, E., Pulse-to-pulse correlation in satellite radar altimeters, *Radio Science*, 17, 786–800, 1982.
- Warren, S., I. Rigor, and N. Untersteiner, Snow Depth on Arctic Sea Ice, *Journal of Climate*, 12, 1814–1829, 1999.
- Washington, W., and C. Parkinson, *An introduction to three-dimensional climate modeling*, University Science Books, 2005.
- Webster, J. (Ed.), *Wiley Encyclopedia of Electrical and Electronics Engineering*, John Wiley and Sons, Inc., 1999.
- Willatt, R. C., K. Giles, S. Laxon, L. Stone-Drake, and A. Worby, Field Investigations of Ku-Band Radar Penetration Into Snow Cover on Antarctic Sea Ice, *IEEE Transactions on Geoscience and Remote Sensing*, 48, 365–372, 2010.
- Willyard, R., Airborne Radar for Measuring Snow Thickness over Sea Ice, Master's thesis, The University of Kansas, 2006.
- Wingham, D., C. Francis, S. Baker, C. Bouzinac, D. Brockley, and R. Cullen, CryoSat: A mission to determine the fluctuations in Earth's land and marine ice fields, *Advances in Space Research*, 37, 841–871, 2006.
- Worby, A., P. Griffin, V. Lytle, and R. Massom, On the use of electromagnetic induction sounding to determine winter and spring sea ice thickness in the Antarctic, *Cold Regions Science and Technology*, 29, 49–58, 1999.
- Worby, A., G. Bush, and I. Allison, Seasonal development of the sea-ice thickness distribution in East Antarctica: Measurements from upward-looking sonar, *Annals of Glaciology*, 33, 177–180, 2001.

- Worby, A., C. Geiger, M. Page, M. Van Woert, S. Ackley, and T. DeLiberty, Thickness distribution of Antarctic sea ice, *Journal of Geophysical Research*, 113, C05S92, 2008a.
- Worby, A., T. Markus, A. Steer, V. Lytle, and R. Massom, Evaluation of AMSR-E snow depth product over East Antarctic sea ice using in situ measurements and aerial photography, *J. Geophys. Res.*, 113, C05S94, 2008b.
- Worby, A., et al., Regional-scale sea-ice and snow thickness distributions from in situ and satellite measurements over East Antarctica during SIPEX 2007, *Deep Sea Research Part II: Topical Studies in Oceanography*, 58, 1125–1136, in prep.
- Wu, X., W. Budd, and T. Jacka, Simulations of Southern Hemisphere warming and Antarctic sea-ice changes using global climate models, *Annals of Glaciology*, 29, 61–65, 1999.
- Xie, S., C. Bao, L. Zhang, and C. Hao, Interaction between Antarctic sea ice and ENSO events, *Proceedings of NIPR Symposium on Polar Meteorology and Glaciology*, pp. 95–110, 1994.
- Yankielun, N., An Airborne Millimeter-Wave FM-CW Radar for Thickness Profiling of Freshwater Ice, *Tech. rep.*, CRREL, 1992.
- Zhang, J., Increasing Antarctic Sea Ice under Warming Atmospheric and Oceanic Conditions, *Journal of Climate*, 20, 2515–2529, 2007.
- Zwally, H., C. Parkinson, and J. Comiso, Variability of Antarctic sea ice and changes in carbon dioxide, *Science*, 220, 1005–1012, 1983.
- Zwally, H., J. Comiso, C. Parkinson, D. Cavalieri, and P. Gloersen, Variability of Antarctic sea ice 1979-1998, *Journal of Geophysical Research*, 107, 3041, 2002.
- Zwally, H., D. Yi, R. Kwok, and Y. Zhao, ICESat measurements of sea ice freeboard and estimates of sea ice thickness in the Weddell Sea, *J. Geophys. Res.*, 113, C02S15, 2008.